Title

Resilience-Based Seismic Evaluation and Design of Reinforced Concrete Structures

Author

Ghotbi, Abdoulreza

Publication Date

2018

UNIVERSITY OF CALIFORNIA

Los Angeles

Resilience-Based Seismic Evaluation and Design of Reinforced Concrete Structures

A dissertation submitted in partial satisfaction of the
requirements for the degree Doctor of Philosophy
in Civil Engineering

by

Abdoulreza Ghotbi

2018

`

`

ABSTRACT OF THE DISSERTATION

Resilience-Based Seismic Evaluation and Design of Reinforced Concrete Structures

by

Abdoulreza Ghotbi

Doctor of Philosophy in Civil Engineering
University of California, Los Angeles, 2018
Professor Ertugrul Taciroglu, Chair

This dissertation addresses a wide spectrum of topics associated with resilience-based seismic evaluation and design of reinforced concrete structures. First, a comprehensive framework was developed enabling users to select, scale, and modify mainshock and aftershock ground motions (GMs) based on a set of different criteria. Various hazard-consistent target intensity measure metrices were utilized based on a set of conditioning criteria ($IM_j's$). Then, a statistical approach was utilized to pull realization samples from a multivariate distribution of multiple intensity measures (IM_i's) using both Monte-Carlo (MC) and Latin Hypercube Sampling (LHS) techniques. A comprehensive database of seismic records—namely, the PEER NGA-WEST2

database—was utilized to select those records whose $IM_i{}'$s match the conditioning targets by assigning a different set of weights to different $IM_i{}'$s in a least-squares sense.

The effects of different GM selection strategies on a range of engineering demand parameters ($EDPs$) were investigated for a pair of 4-, 8- and 12-story ductile and non-ductile reinforced concrete (RC) buildings. In such studies, a very large number of nonlinear response history analyses ($NRHAs$) is unavoidable. Therefore, the analyses were performed using a parallel computing approach, which was specifically designed for the task at hand and carried out at the Texas Advanced Computing Center's "Stampede2" supercomputer.

Another topic that was addressed in this dissertation has been the development of a novel framework to select earthquake records based on a *spectral shape matching* approach. The effects of different GM selection strategies based on a pre-existing spectral shape matching approach—namely, the *response spectrum matching* method—versus the newer approach developed in the present study was studied. The same ductile and non-ductile RC buildings mentioned above were utilized for this task and a variety of damage limit states (including the collapse) were used for comparison of fragility functions obtained using the two approaches.

Finally, an optimization framework was developed to reduce the effects of epistemic uncertainties associated with wide range of structural modeling parameters, on the probabilistic seismic responses of RC structures. To this end, a non-dominated sorting genetic algorithm ($NSGA-II$) was integrated with OpenSeesMP to determine optimal values of several design variables that minimize the median peak inter-story drift ratios ($IDRs$) at two different performance levels—namely, Immediate Occupancy (IO) and Collapse Prevention (CP)—simultaneously.

The dissertation of Abdoulreza Ghotbi is approved.

Jonathan Paul Stewart

George M. De Shazo

Oddvar O. Bendiksen

Ertugrul Taciroglu, Committee Chair

University of California, Los Angeles

2018

TABLE OF CONTENTS

LIST OF FIGURES

`

ACKNOWLEDGEMENTS

Financial support from the Department of Civil and Environmental Engineering at UCLA, through research & teaching assistantships and graduate fellowships, is gratefully acknowledged.

VITA

EDUCATION

M.Sc. in Structural Engineering, California State University, Long Beach (CSULB), May 2014.
M.Sc. in Geotechnical Engineering, Shahid Bahonar University of Kerman, 2007, Kerman, Iran.
B.S. in Civil Engineering, University of Mazandaran, 2004, Babol, Mazandaran, Iran.

SELECTED PUBLICATIONS

Ghotbi A. Performance-based seismic assessment of skewed bridges with and without considering soil foundation interaction effects for various site classes. *Earthquake Engineering and Engineering Vibration*, 2014, 13(3): 357–73.

Ghotbi A. Performance-based seismic assessment of a large diameter extended pile shaft in a cohesionless soil. *Earthquake Engineering and Engineering Vibration*, 2015, 14(1): 177–88.

Ghotbi A. Modal Pushover Analysis of Skewed Bridges—Case Study of Jack Tone Road On-Ramp Overcrossing. *KSCE Journal of Civil Engineering*, 2015, 1–10.

Ghotbi A. Response sensitivity analyses of skewed bridges with and without considering soil–structure interaction. *Structures*, 2016, (5): 219-232.

1 INTRODUCTION

1.1 BACKGROUND AND MOTIVATION

Earthquakes are among one of the major threats to the built environment across the globe. Given their unpredictably, they cannot be evaded, which is sometimes possible for other natural disasters such as floods or wildfires. Earthquakes are invariably more destructive in regions of the world where there is less preparation to encounter them. Lack of proper seismic codes, or lack of enforcement of such codes significantly increase life and material losses due to earthquakes.

There have been recurring/continuous efforts across the earthquake-prone regions of the world to improve the seismic resiliency of new/future infrastructure elements, and to assess the risks for those that already exist. These efforts can be categorized into to two main branches. One branch deals with reducing the uncertainties associated with seismic load (demand) predictions, which is primarily undertaken by seismologists who focus on, for example, factors that could trigger earthquake ground motions, fault rupture mechanisms, various causes that could amplify or de-amplify seismic motions, etc. These efforts have been producing outcomes such as ground motion prediction equations (GMPEs), and probabilistic seismic hazard assessment (PSHA) methods. Another main branch is populated by geotechnical and structural earthquake engineers who focus on developing predictive tools for quantifying the responses of structural/geotechnical systems.

These two main threads of earthquake research have resulted in significant progress, and—at least in the US—have been steadily converging towards a performance-based seismic assessment (PBSA) methodology that combines probabilistic evaluation of uncertainties associated with both estimated seismic motions as well as predictive models of structures.

This research aims at shedding more light on multiple areas associated with the probabilistic seismic risk assessment and design of reinforced concrete structures, which is one of the most commonly encountered type of structure in many regions of the world including the United States. The study specifically focuses on the probabilistic mainshock and aftershock ground motion selection as well as scaling and modification on the ground motions side. On the structural side, the focus will be on devising accurate—yet computationally efficient—numerical models of reinforced concrete structures, carrying out detailed sensitivity analyses with respect to various structural modeling and ground motion characteristics with the objective of reducing the epistemic variabilities with respect to their selection.

Specific research objectives and their brief descriptions are provided in the following sections of this chapter.

1.2 MAINSHOCK AND AFTERSHOCK GROUND MOTION SELECTION

Variabilities in the predicted responses of structures due to ground motion selection—and other associated procedures for conditioning/scaling the selected motions—have been recognized as one of the major sources of uncertainty in PBSA. This variability is often quantified by using a large number—i.e., a suite—of earthquake records for seismic analyses. There are already various ground motion selection methodologies by which one can select earthquake records for different *levels* of seismic hazard. However, neither the *efficiency* nor the *sufficiency* of the selected motions are matters that are deemed as settled by the research community. One of the main objectives of this research has thus been to make improvements in this area such that uncertainties/ dispersions in predicted structural performance due to record-to-record variability in earthquake records are reduced.

In this particular aspect of the dissertation, several methodologies are developed to generate a range of fully probabilistic and hazard-consistent targets with respect to different intensity measures representing various characteristics of earthquake records. Various conditioning criteria are considered to enforce the hazard consistency. Moreover, a ground motion selection, scaling, and modification (GMSSM) methodology is developed that uses multiple characteristics/measures of the candidate earthquake records rather than only one—i.e., spectral amplitude at a building's first period —, which is where the present state-of-the-art in GMSSM is at.

Furthermore, a stochastic aftershock GMSSM methodology is developed that enables users to select *hazard-consistent* aftershock ground motion records. The effect of time-lapse is incorporated into a temporal framework for aftershock PSHA, and an algorithm is developed to select the aftershock earthquake records.

These topics are presented and discussed in Chapters 2, and 3.

1.3 GROUND MOTION SELECTION BASED ON SPECTRAL SHAPE

Response-spectrum matching is arguably the most commonly used method for ground motion selection, which is based on picking ground motions whose response spectra match (in some manner) a hazard-consistent target response spectrum. This is achieved typically through a "spectral-shape matching," wherein the spectrum of a selected earthquake record matches all of the peaks and valleys of a target spectrum. This is nominally a difficult task given the limited number of available recorded ground motions.

To explore this problem more in depth, a new metric is developed in this dissertation to represent the spectral shape of a given earthquake record. Subsequently, a comprehensive study is carried out to compare structural response outcomes due to ground motion records selected based on the traditional spectral-shape matching method and on the new method devised herein.

This topic is presented and discussed in Chapter 4.

1.4 EFFECTS OF GROUND MOTION SELECTION ON THE VARIABILITY OF SEISMIC RESPONSES OF REINFORCED CONCRETE STRUCTURES

As previously mentioned, ground motion selection and conditioning is a major sources of variability in the predicted seismic responses of structures. This dissertation specifically investigates reinforced concrete structures in this regard, and quantitatively explores the dispersions of predicted structural responses due to various characteristics of the earthquake records.

This topic is presented and discussed in Chapter 5.

1.5 STRUCTURAL MODELING AND PARALLEL COMPUTING

This research utilizes state-of-the-art nonlinear models of both code-conforming (ductile) to none code-conforming (non-ductile) reinforced concrete structures. The models are analyzed through the probabilistic framework of PBSA, and various sampling techniques are utilized to draw realization samples from multivariate distributions of structural modeling parameters to increase computational efficiency without sacrificing accuracy. Moreover, since performing multitudes of nonlinear time-history analyses nominally bear high computational costs, parallel computing techniques are used. Both the high-fidelity nonlinear models of reinforced concrete structures and the parallel computing techniques devised in this study should be valuable to the broader research community.

These topics are presented and discussed in Chapters 4, 5, 6, and 7.

1.6 EFFECTS OF VARIABILITY IN STRUCTURAL MODELING PARAMETERES ON SEISMIC RESPONSES OF BUILDINGS

It is well established among both researchers and practitioners that variability in material and/or element modeling parameters cause dispersions in seismic demand responses, which is additional to dispersions due to the record-to-record variability of seismic input. Both types of dispersions need to be quantified and considered and this dissertation, therefore, explores an optimization framework that aims to reduces the uncertainties due structural modeling parameters.

This topic is presented and discussed in Chapter 7.

2 A GROUND MOTION SELECTION, SCALING, AND MODIFICATION FRAMEWORK

2.1 INTRODUCTION

One of the main tasks in performance-based seismic risk assessment and design of structures is the quantification of uncertainty in earthquake ground motion records. Ground motions have various characteristics such as amplitude, frequency content, and duration each of which can play significant roles in controlling diverse sets of structural responses. It is common to compile a ground motion suite (i.e., multiple earthquake records) that is broad enough to capture the inherent aleatoric variability in structural demands. On the other hand, if the record suite is too large, then it may not truly reflect the ground motions anticipated for the specific structure, rendering the performance assessment too conservative. Therefore, there is an optimal suite of GMs for each structure, selection of which can be an elusive task that is complicated by—among other things—the fact that structural behavior migrates into loading-path-dependent inelastic regimes as damage begins to accumulate.

2.2 SCOPE AND MOTIVATION

There have been a significant amount of influential works conducted in the area of GM selection, scaling and modification (GMSSM), which will be reviewed in the next section. While the broad strokes of work in this area have already been made, there are knowledge gaps, especially because GMSSM is coupled with the type and the response characteristics of the structure/facility that is being assessed or designed.

It is aimed, herein, to develop a comprehensive probabilistic framework to enable structural engineers to select ground motions based on a set of criteria for evaluating the expected performance of multi-story reinforced concrete buildings. The main tenet of this framework will be to minimize the uncertainty in structural demands imposed by earthquake records for a set of different hazard levels. The framework will also be hazard-consistent, which means that multiple fault rupture scenarios will be incorporated into the GM selection algorithm so that the actual/known seismicity of the region is captured. Moreover, ground motions will be selected with respect to multiple structural modal characteristics—but not only the first mode period—, which will significantly minimize dispersion in structural demands due to record-to-record variability.

The developed GMSSM framework yields hazard-consistent ground motions based on various conditioning criteria. First, a set of intensity measures ($IM_i{}'$s) are chosen to represent various earthquake characteristics such as amplitude and duration as well as cumulative metrics. Next a conditioning protocol is introduced based on single, double and multiple conditioning intensity measures ($IM_j{}'$s). The $IM_j{}'$s can be drawn from hazard curves for any given hazard levels. By using a disaggregation plot, which is a proxy to a seismic hazard curve, various rupture scenarios and their corresponding contributions to any IM_j level of interest can be defined and consequently incorporated into a conditioning multivariate distribution of IM_i vector consisting of several $IM_i{}'$s. This way, hazard consistency is fully enforced. Thus, a hazard-consistent conditioning multivariate distribution of multiple $IM_i{}'$s is defined by not only taking into correlation between all the $IM_i{}'$s in the IM_i vector with IM_j , but also the cross-correlation between various $IM_i{}'$s in the IM_i vector. Parameters of this distribution—namely, the median and the logarithmic standard deviation—can be defined using various ground motion prediction equations ($GMPEs$). Moreover, several empirical relationships that are proxies to $GMPEs$ are used for defining the correlations between various intensity measures.

Ultimately, any number of realization samples can be drawn from the marginal distribution of each IM_i in the IM_i vector for which a multivariate distribution was previously defined. In the present study this step is carried out using both the classical Monte Carlo technique and also the Latin Hypercube Sampling (LHS) method, which offers significant computational savings. These samples represent a target distribution for each IM_i in the IM_i vector for which ground motion records can be selected in a least-squares sense with or without amplitude-scaling. For this, a comprehensive ground motion database—namely, the PEER NGA-West2 database—is consulted to select earthquake records matching the target realization samples. These steps yield a GM suite whose empirical distribution match the target so that one can claim to have selected GMs that are hazard-consistent with respect to a target distribution that is drawn from a multivariate distribution of various $IM_i{}'$s in the IM_i vector.

Additionally, the GMSSM framework proposed herein is designed so that different weights can be assigned to each IM_i. This enables a ground motion suite to be compiled by giving more emphasis to amplitude-based characteristics rather than duration-based or cumulative measures of earthquake records, and vice versa.

2.3 A REVIEW OF PRIOR STUDIES

2.3.1 Background

In recent years, there have been significant efforts in the area of GMSSM. Baker (2011) developed a conditional mean spectrum (CMS) framework in which the conditioning intensity measure was set to be the spectral acceleration at the fundamental period of structure, which could be derived directly from hazard curve for a pre-specified rate of exceedance. Hazard-consistency was, however, implemented through a mean approach for all of rupture scenarios contributing to an IM_j level—rather than considering the contribution of each rupture scenario separately—and by summing over all of them with respect to corresponding probability of occurrence for each rupture scenario. In this approach, only the correlation between each IM_i in an IM_i vector—e.g., spectral acceleration at multiple periods (SAT's)—and IM_j $(e.g. SAT1)$ was considered and cross correlations between individual $IM_i{}'$s in the IM_i vector were not considered. (Lin, et al., 2013) extended the CSM approach to consider the contribution of multiple rupture scenarios to a conditioning SAT. This approach did not still incorporate cross correlations between different $IM_i{}'$s in the IM_i vector.

Jayaram et al. (2011) developed a framework to select ground motions matching both median and variance target response spectrum by incorporating a greedy optimization algorithm to enhance the selection and matching procedures. Baker and Lee (2018) extended this work to select ground motions to not only match the median and variance of the response spectrum but also match correlations between $SATs$ for various periods assuming a period range. They did so by statistically drawing samples from target distribution of $SATs$ at various periods given their mean vector and covariance matrix and then selecting ground motions to individually match each of the realization using an optimization algorithm to enhance the match-finding process. Baker and Cornell (2008) developed a vector-valued ground motion intensity measure metric consisting of other intensity measures such as spectral shape and also ε(i.e. the number of standard deviations by which each of the record's spectrum is away from the median target spectrum) in addition to SAT in order to see the effects on the dispersion in structural demands. Baker and Cornell (2005) used a vector-valued intensity measure consisting of SAT and ε, and concluded that failing to consider ε, which could be deemed as a proxy to spectral shape, would underestimate the structural response quite significantly.

Bradley (2010) developed a generalized conditional intensity measure ($GCIM$) approach using a multivariate distribution of an IM_ivector, conditioned on any desirable intensity measure

(IM_j), which is often drawn from the hazard curve. Bradley's (2010) method is the basis of this study as well and is a good way to narrow down several intensity measures (IMs) representing an earthquake record into a single one, while implicitly incorporating the effects of other IM_i's. In this method, marginal target distributions of various IM_i's can be obtained from a multivariate distribution, and earthquake records can be selected such that empirical distributions of their IM_i's match the targets so one can claim that the empirical multivariate distribution of the IM_i's of the selected records match the target multivariate distribution.

Bradley (2012) extended the $GCIM$ by selecting earthquake records to match target realization samples drawn from a conditional marginal distribution of various IM_i's for which a multivariate distribution was initially defined. An acceptable suite of earthquake records is the one that is deemed to have its empirical distributions of various IM_i's match the cumulative target distributions of target IM_i's drawn from the conditional multivariate distribution. Tarbali & Bradley (2015) extended the $GCIM$ to draw scenario-based realization samples from a conditional multivariate target distribution and to find earthquake records that match the target using an optimal amplitude scaling factor. They also studied the effects of various *importance weights* that can be assigned to different IM_i's, on the cumulative distributions of IM_i's belonging to the selected records. They concluded that consideration of only the spectral acceleration at various periods ($SATs$) in the selection phase may lead to the selection of records with poor representations of duration- and cumulative-based contents. Considering other IM_i's other than the SATs results in a ground motions suite that contains a better representation of those cumulative and duration-based IM_i's without significantly affecting the SAT ordinates.

Tarbali & Bradley (2016) also studied the effects of *causal* parameter bounds (e.g., magnitude, distance and site condition) on earthquake record selection through the $GCIM$

approach. They concluded that by considering wider bounds, ground motions could be selected whose causal parameters match those of the target. Considering narrower bounds led to a ground motions ensemble with a poor representation of the target intensity measure distribution due to the insufficient number of ground motions after enforcing restrictions on the causal parameter bounds.

Armstrong (2016) developed a ground motion selection algorithm to select earthquake records that match a set of different IM_i's. He did so by first scaling the records to match a conditioning IM target, and then by utilizing a semi-automated algorithm to trim the records down to a final set with better IM_i statistics with respect to those of targets. Wong & Chopra (2017) extended the $GCIM$ to generate target distributions conditioned on two IM_j's instead of one. The reason for this is that in most nonlinear response history analysis ($NRHA$) cases, the ground motions conditioned on a single IM_j do not have sufficient content to excite the structure at its various modes of vibration, especially as the structure undergoes some level of damage and experiences changes in its fundamental period. Therefore, it would be necessary to select multiple suites of ground motions conditioned on multiple single IM_j's, which increases the computational costs quite significantly. Using two or more conditioning IM_j's, however, would require users to select only a single suite of earthquake records, which would have sufficient content to be able to capture the nonlinear behavior of structures at several modes of vibration. This method will also be extended in the present study to devise a new target IM_i generation method based on a set of different IM_i's as well a new selection procedure to select records matching the target IM_i realizations conditioned on two IM_j's, rather than one.

Wong & Chopra (2016) compared various GMSSM procedures using conditioning spectrum (CS) and $GCIM$ to evaluate biases in the evaluation of seismic hazard demand curves ($SDHCs$) for a given structure at a specific site in comparison with a benchmark $SDHC$. Wong *et*

al. (2015) developed an algorithm to select unscaled ground motion records to evaluate $SDHCs$. Wong et al. (2015) used various methods to generate synthetic earthquake ground motion records to evaluate the effects of various GMSSM procedures on evaluating the $SDHCs$.

Kohrangi et al. (2017) employed a conditional IM_i target generation approach based on the adoption of an average of multiple SATs at various periods as IM_j, rather than a single conditioning IM_j . Ground motion records were subsequently selected to match the new conditioning target IM_i and were utilized in the $NRHA$s of structures, which ensured increased sufficiency and efficiency in estimation of response demands. Kohrangi et al. (2017) also studied the degree of site influence with respect to an adopted conditioning IM_j on the seismic responses of structures. They concluded that using a single IM_j as the conditioning IM results in significant variability in the seismic demand responses from site to site. In contrast, using an average IM_j—i.e. the average $SATs$ at multiple periods—helped decreasing the variability in response demand from site to site.

Dai et al. (2014) incorporated an optimization framework for the purpose of spectral matching to get a more robust *GM* suite matching a target spectrum. Wang (2011) proposed an algorithm to select GMs to match a target median, standard deviation and correlation matrix conditioned on specific causal properties. He concluded that *GMs* selected based on this procedure are more efficient and sufficient in seismic demand response evaluations. Ha & Han (2016) proposed a computationally efficient GMSSM algorithm to select earthquake records to match a target response spectrum's mean and standard deviation. Kottke & Rathje (2008) proposed a semi-automated GMSSM procedure for matching a target response spectrum while maintaining the variability between the records in the suite. According to this method, earthquake records are selected to match the target spectral shape and then to match the amplitude and standard deviation of the target through the adjustment of scale factors for each record.

(Weng, et al., 2010) proposed a ground motion selection and scaling method to consider dominating modes of structural seismic demand responses. To this end, they proposed multi-mode ground motion scaling methods to combine various seismic demand responses in different modes to compute the peak response.

Smerzini et al. (2014) selected displacement-spectrum-compatible real *GMs* especially for the sites in Italy by putting constraints on shorter and longer periods. Ebrahimian et al. (2012) compared various hazard-consistent GM selection methodologies based on different targets including the CMS and CS in a region with multiple seismic hazard sources. They also investigated the application of *GM*s selected to match a conditioning target, conditioned on average SATs at multiple periods. This method is extended, herein, to generate conditioning targets for various $IM_i{}'$s in an IM_i vector which are conditioned on average SATs as conditioning IM_j using novel sampling techniques and subsequently selecting ground motions to match the target $IM_i{}'$s.

2.3.2 The state of research

Selecting ground motions based on uniform hazard spectra (UHS) which is commonly used, is overly conservative and generally unrealistic. As such, ground motions selection based on a single conditioning IM_j have been gaining popularity, including CMS (Baker, 2011) and CS (Lin, et al., 2013). These methods are more realistic than (UHS) since the spectra of the GMs selected based on these methods are hazard-consistent only at the IM_j, which is typically the spectral acceleration at the fundamental period of structure (SAT1). At other period values, however, they will fall below the UHS. For most structures, most of the structural mass is mobilized at the first mode and therefore ground motions that have a more intense $SAT1$ will have sufficient content to excite the structure in that mode of vibration. However, in case that the structure undergoes some level of damage and therefore experiences changes to its dominant periods of vibration (or if there are many higher modes contributing to the overall response), then selecting GMs whose spectrum is intense only at a single IM_j (i.e. $SAT1$ in most cases) would not have sufficient content to capture the nonlinear behavior of the structure. Thus, one would have to select GMs based on multiple single IM_j's and then to take the maximum or the average of the responses obtained using multiple suites. This increases the computational burden quite significantly. Moreover, selecting GMs solely based on response spectrum will generate suites with dominant inertia contents, and duration and cumulative effects could be inadequately considered. This would result in an underestimation of structural responses for structures that exhibit significant cyclic degradation such as non-ductile reinforced concrete (RC) buildings, as they are inherently more sensitive to duration- and energy-based earthquakes intensity measures.

Attempts are made in the present study to address all of the aforementioned issues regarding GMSSM. Specifically, the $GCIM$ approach (Bradley, 2012) is extended first by generating IM_i target distributions via different sampling techniques—by drawing realization samples from a multivariate distribution of various IM_i's in the IM_i vector. Then, a new procedure to select GMs conditioned on two IM_j's is developed as a computationally efficient—and theoretically superior—alternative to the use of multiple single IM_j's for ground motion selection.

The method by Wong & Chopra (2017) is also extended to generate conditioning target distribution for IM_i's other than SATs. *GM*s are selected then to compile a suite whose empirical distribution matches that of the target conditioned on two IM_j's. Hazard consistency is implemented by estimating the contribution of each hazard source to two IM_j's simultaneously, using a novel approach, and then by summing over all of rupture scenarios based on the disaggregation of the seismic hazard curve. An additional method is introduced based on the use of an average IM_j—namely, the geometric mean of SAT at various periods— as an extension of the approach proposed by Ebrahimian et al. (2012).

2.4 ALGORITHMS FOR GROUND MOTION SELECTION

2.4.1 The generalized conditional intensity measure ($GCIM$) approach

The generalized conditional intensity measure ($GCIM$) approach developed by Bradley (2012) forms the basis of the framework proposed, herein. The idea is to select records to match hazard-consistent targets drawn from a multivariate distribution of various IM_i's. Accordingly, ground motions selected based on this method can feature cumulative and duration measures in addition to the conventional amplitude ones. The $GCIM$ algorithm is summarized in the following section and is extended such that users are enabled to utilize $GCIM$ based on two- IM_j and multiple- IM_j conditioning criteria.

2.4.1.1 Algorithm for a single IM_j

In Bradley's $GCIM$, first a vector of$IM_i's$ are populated, and then a multivariate distribution for various IM_i's in that vector are defined using statistical properties of each IM_i in the vector. The median and the logarithmic standard deviation of each IM_i can be obtained from various ground motion prediction equations (GMPEs). There are also empirical relationships that define the correlations between various IM_i's. Ultimately, the conditional density function of an arbitrary IM_i conditioned on an IM_j can be defined as:

$$f_{IM_i|IM_j} = \sum_{k=1}^{N_{rup}} f_{IM_i|Rup_{k,}IM_j} \, P_{Rup_k|IM_j} \tag{2.1}$$

where $f_{IM_i|IM_j} = f_{IM_i|IM_j}(im_i|im_j)$ is the conditional density function of an arbitrary IM_i conditioned on an IM_j, and $P_{Rup_k|IM_j}$ is the probability of rupture k. Hazard-consistency is enforced by considering a number of rupture scenarios ($N_{rup}'s$).

A lognormal distribution is assumed for various $IMi's$, whose probability density can be defined as

$$f_{IM_i|Rup,IM_j} = f_{IM_i|Rup_k,IM_j}\left(im_i\middle|rup_{k,}im_j\right) \sim LN(\mu_{lnIM_i|Rup,IM_j}, \sigma^2_{lnIM_{i|Rup,IM_j}}). \tag{2.2}$$

Here, $\mu_{lnIM_i|Rup,IM_j}$ is the conditional mean and $\sigma^2_{lnIM_{i|Rup,IM_j}}$ is the conditional variance for a given rupture scenario, which are defined as

$$\mu_{lnIM_i|Rup,IM_j} = \mu_{lnIM_i|Rup} + \sigma_{lnIM_i|Rup}\rho_{lnIM_i,lnIM_j|Rup}\varepsilon_{lnIM_j}, \tag{2.3}$$

$$\sigma_{lnIM_i|Rup,IM_j} = \sigma_{lnIM_i|Rup}\sqrt{1-\rho^2_{lnIM_i,lnIM_j|Rup}}. \tag{2.4}$$

where $\mu_{lnIM_i|Rup}$, and $\sigma_{lnIM_i|Rup}$ denote the logarithmic median and standard deviation of an IM_i for a given rupture scenario, respectively. $\rho_{lnIM_i,lnIM_j|Rup}$ is the correlation coefficient between IM_i and IM_j for a given rupture scenario, and ε_{lnIM_j} is defined as

$$\varepsilon_{lnIM_j} = \frac{lnIM_j - \mu_{lnIM_j|Rup}}{\sigma_{lnIM_j|Rup}}. \tag{2.5}$$

The correlation coefficients between various IM_i's can be defined first by introducing the i-th element of the mean and standard deviation vector as

`

$$\mu_{lnIM|Rup,IM_j}(i) = \mu_{lnIM_i|Rup,IM_j}, \tag{2.6}$$

$$\sigma_{lnIM|Rup,IM_j}(i) = \sigma_{lnIM_i|Rup,IM_j} \tag{2.7}$$

and then by deriving the *k*-th *e*lement of the correlation coefficient matrix as

$$\rho_{lnIM|Rup,IM_j}(i,k) = \frac{\rho_{ik} - \rho_{ij}\rho_{kj}}{\sqrt{1-\rho_{ij}^2}\sqrt{1-\rho_{kj}^2}} \tag{2.8}$$

where $\rho_{ik} = \rho_{lnIM_i,lnIM_{k|Rup}}$ is the correlation coefficient between lnIM_i and lnIM_k, given a rupture scenario, and so on and so forth for rest of the terms in Eq. (2.8)

Having the median and standard deviation vectors for all of the IM_i's in the IM_i vector and also the correlation coefficient matrix whose elements are derived using Eq. (2.8), the multivariate distribution of the IM_ivector can be defined. Then, any number of samples can be drawn from the marginal distributions of each IM_i.

2.4.1.2 Algorithm for two $IM_j's$

This section is devoted to generating hazard-consistent targets conditioning on two IM_j levels rather than one, which was covered in the previous section. Conditioning on two $IM_j's$ has several advantages over one IM_j which is briefly explained here. As a structure experiences some level of damage and undergoes changes in vibration periods, ground motions which are intense only at a single conditioning period would not have sufficient contents to capture actual behavior of the structure especially in the higher modes. Thus, there would be a need to use a few suites conditioned on multiple single-$IM_j's$ rather than one to compensate for this problem. This, however, would increase computational time, quite significantly. Setting the number of conditioning IM_j as two in generating hazard-consistent targets for a set of different IM_i's would mitigate this problem by generating targets which are hazard-consistent for a range of $IM_j's$ between IM_{j1} and IM_{j2}.

Details as to how the following equations are derived can be traced back to (Wong & Chopra, 2017). Though, this work is extended to generate targets for other IM_i's besides SATs by using a random realization sample generation. Besides, in addition to simultaneously considering correlation between each IM_i in the IM_i vector, and the two conditioning $IM_j's$, the conditional cross correlation between various $IM_i's$ will also be considered.

Eq.'s (2.3) and (2.4) are basis for this method as well, however since the number of IM_j are two, now, they are laid out as:

$$\mu_{lnIM_i|Rup,IM_{j1},IM_{j2}} = \mu_{lnIM_i|Rup} + \sigma_{lnIM_i|Rup}\varepsilon_i^* \tag{2.9}$$

$$\sigma_{lnIM_i|Rup,IM_{j1},IM_{j2}} = \sigma_{lnIM_i|Rup}\sqrt{1-\rho_i^*} \tag{2.10}$$

where, $\mu_{lnIM_i|Rup,IM_{j1},IM_{j2}}$ and $\sigma_{lnIM_i|Rup,IM_{j1},IM_{j2}}$ are the conditional logarithmic median and standard deviation of for an IM_i conditioned on two IM_j's. $\mu_{lnIM_i|Rup}$ and $\sigma_{lnIM_i|Rup}$ are the logarithmic median and standard deviation of the IM_i obtained from a corresponding GMPE. The terms ε_i^* and ρ_i^* denote the generalized epsilon and correlation for an IM_i with respect to two $IM_j's$, respectively, and are given by

$$\varepsilon_i^* = c_{i1}\varepsilon_{lnIM_{j1}} + c_{i2}\varepsilon_{lnIM_{j2}} \tag{2.11}$$

$$\rho_i^* = c_{i1}\rho_{lnIM_i,lnIM_{j1|Rup}} + c_{i2}\rho_{lnIM_i,lnIM_{j2|Rup}} \tag{2.12}$$

where ε is the number of standard deviations by which the record's IM_i is away from the target median, which can be computed in a similar manner as what's given in Eq. (2.5). The coefficients $c_{j1}$and c_{j2} are

$$c_{i1} = \frac{\rho_{lnIM_i,lnIM_{j1|Rup}} - \rho_{lnIM_{j1},lnIM_{j2|Rup}}\rho_{lnIM_i,lnIM_{j2|Rup}}}{1 - \rho^2_{lnIM_{j1},lnIM_{j2|Rup}}} \tag{2.13}$$

$$c_{i2} = \frac{\rho_{lnIM_i,lnIM_{j2|Rup}} - \rho_{lnIM_{j1},lnIM_{j2|Rup}}\rho_{lnIM_i,lnIM_{j1|Rup}}}{1 - \rho^2_{lnIM_{j1},lnIM_{j2|Rup}}} \tag{2.14}$$

where $\rho_{lnIM_i,lnIM_{j1|Rup}}$ is the correlation between lnIM_i, lnIM_{j1}; $\rho_{lnIM_i,lnIM_{j2|Rup}}$ is the correlation between lnIM_i, and lnIM_{j2}; and $\rho_{lnIM_{j1},lnIM_{j2|Rup}}$ is the correlation between lnIM_{j1} and lnIM_{j2}.

In addition to considering the correlation between each IM_i in the IM_i vector and the two $IM_j's$, the cross-correlation between various $IM_i's$ with respect to two conditioning $IM_j's$ is considered as well. The correlation matrix is, therefore,

$$\rho_{lnIM|Rup,IM_{j1},IM_{j2}}(i,k) = \frac{\rho_{lnIM_i,lnIM_{k|Rup}} - \rho_i^*\rho_k^*}{\sqrt{1-{\rho_i^*}^2}\sqrt{1-{\rho_k^*}^2}} \tag{2.15}$$

where ρ_i^*, ρ_k^* are defined in Eq. (2.12).

Having the median, standard deviation vector as defined by Eq.'s (2.9) and (2.10) and also the correlation coefficients matrix as defined in Eq. (2.15), the conditional multivariate distribution of various $IM_i's$ with respect to two $IM_j's$ can be defined.

The Eq. (2.9) to (2.15) are for a single rupture scenario whose simultaneous contribution to two $IM_j's$ can be computed as

$$\Pr(Rup|A_c = a_c) = \frac{f_{A_c|Rup}(a_c|Rup)\lambda_{Rup}(Rup)}{\sum_{k=1}^{N_{Rup}} f_{A_c|Rup_k}(a_c|Rup_k)\lambda_{Rup}(Rup_k)} \tag{2.16}$$

where $A_c = [IM_{j1}\ IM_{j2}]$ is a vector including two $IM_j's$, $f_{A_c|Rup}(a_c|Rup)$ is the multivariate lognormal probability density function of $\log(A_c)$ for any given rupture scenario. The denominator is the summation of contributions from all rupture scenarios that define the seismicity of the site for which the GM records are to be selected.

2.4.1.3 *Algorithm for multiple IM_j*

In this algorithm—which is based on studies by Ebrahimian et al. (2012) and Kohrangi et al. (2017) works—, IM_j is set to be a vector consisting of more than two conditioning intensity measures (e.g., $SATs$). Thus, for a range of SATs where $T = [T^{(1)}, T^{(2)}, T^{(3)} \ldots . T^{(n)}]$, which includes the structure's fundamental period as well, the geometric mean of the SAT vector is defined as

$$Sa_{avg} = Sa_{avg}\left(T^{(1)}, \ldots, T^{(n)}\right) = \left(\prod_{i=1}^{n} Sa(T^{(i)})\right)^{1/n}, \tag{2.17}$$

and the logarithmic median and standard deviation for a given rupture are given by

$$\mu_{lnSa_{avg|Rup}} = \frac{1}{n}\sum_{i=1}^{n} \mu_{lnSa|Rup(T^{(i)})} \tag{2.18}$$

$$\sigma_{lnSa_{avg}|Rup} = \frac{1}{n}\sqrt{\sum_{i=1}^{n}\sum_{j=1}^{n}\rho(lnSa(T^{i}), lnSa(T^{j})).\sigma_{lnSa(T^{(i)})|Rup}.\sigma_{lnSa(T^{(j)})|Rup}} \tag{2.19}$$

where, $\mu_{lnSa|Rup(T^{(i)})}$ is the logarithmic median of each $Sa(T^{(i)})$ for a given rupture, $\rho\big(lnSa(T^{i}), lnSa(T^{j})\big)$ is the correlation between $\ln Sa(T^{i})$ and $\ln Sa(T^{j})$, and $\sigma_{lnSa(T^{(i)})|Rup}$ and $\sigma_{lnSa(T^{(j)})|Rup}$ are the logarithmic standard deviations of $Sa\big(T^{(i)}\big)$ and $Sa\big(T^{(j)}\big)$ for a given rupture, respectively. Then, the logarithmic median and standard deviation of conditioning IM_i for any IM_i conditioned on $lnSa_{avg}$ can be obtained as

$$\mu_{lnIM_i|lnSa_{avg},Rup} = \mu_{lnIM_i|Rup} + \sigma_{lnIM_i|Rup}\rho_{lnIM_i,lnSa_{avg}|Rup}\varepsilon_{lnSa_{avg}|Rup} \tag{2.20}$$

$$\sigma_{lnIM_i|lnSa_{avg},Rup} = \sigma_{lnIM_i|Rup}\sqrt{1-\rho^{2}_{lnIM_i,lnSa_{avg}|Rup}} \tag{2.21}$$

where,

$$\varepsilon_{lnSa_{avg}|Rup} = \frac{lnSa_{avg} - \mu_{lnSa_{avg}|Rup}}{\sigma_{lnSa_{avg}}} \tag{2.22}$$

The terms $\mu_{lnSa_{avg|Rup}}$ and $\sigma_{lnSa_{avg}|Rup}$ can be obtained by using an appropriate GMPE and by utilizing Eq's (2.18) and (2.19).

The correlation between $\ln IM_i$ and $\ln Sa_{avg}$ for a given rupture is defined as

$$\rho_{lnIM_i,lnSa_{avg}|Rup} = \frac{\sum_{i=1}^{n}\rho\big(lnSa(T^{i}), lnSa(T^{j})\big).\sigma_{lnSa(T^{(i)})}}{\sqrt{\sum_{i=1}^{n}\sum_{j=1}^{n}\rho(lnSa(T^{i}), lnSa(T^{j})).\sigma_{lnSa(T^{(i)})}.\sigma_{lnSa(T^{(j)})}}}. \tag{2.23}$$

Since the cross-correlation between different $IM_i{}'s$ in the IM_i vector is also considered in addition to Eq. (2.23), the correlation matrix of the multivariate distribution of various $IM_i{}'s$ in the IM_i vector can be derived as

$$\rho_{lnIM|lnSa_{avg},Rup}(i,k) = \frac{\rho_{lnIM_i,lnIM_k|Rup} - \rho_{lnIM_i,lnSa_{avg}|Rup}\rho_{lnIM_k,lnSa_{avg}|Rup}}{\sqrt{1-\rho^2_{lnIM_i,lnSa_{avg}|Rup}}\sqrt{1-\rho^2_{lnIM_k,lnSa_{avg}|Rup}}} \quad (2.24)$$

Now, by having the logarithmic median, and the standard deviation vector via Eq's (2.20) and (2.21), and the correlation matrix via Eq. (2.25), the conditional multivariate distribution of various IM_i conditioning on multiple $IM_j{}'s$ can be derived. This, of course, is for a single rupture scenario whose contribution to IM_j—which is lnSa_{avg} in this case—can be obtained using Eq. (9) or (12) in (Ebrahimian, et al., 2012). By consulting the hazard disaggregation data for any given site and by summing over all of the potential rupture scenarios with respect to their contributions to lnSa_{avg}, a fully probabilistic and hazard-consistent conditional target can be computed.

2.4.1.4 Drawing realization samples from a conditional multivariate distribution

2.4.1.4.1 Mote Carlo sampling technique

Following Bradley (2012), a two-level approach will be adopted herein, to draw realization samples of each IM_i from conditional multivariate distribution of various IM_i's, which was defined in the previous sections based a single-, two-, and multiple-IM_j. This is done first by obtaining a random rupture probability (Rup^{nsim}) from a disaggregation density function. Then, to draw samples from a multivariate distribution, an uncorrelated standard normal random vector is defined (u^{nsim}) whose elements are drawn from a standard normal distribution, independently. Using this vector, a correlated vector can thus be defined as

$$v^{nsim} = Lu^{nsim} \tag{2.25}$$

where L is the Cholesky decomposition of the correlation matrix, which is

$$\rho_{lnIM|IM_{j,Rup}} = LL^T. \tag{2.26}$$

Using this, the realization sample for each IM_i can be obtained via

$$\ln IM_i{}^{nsim} = \mu_{lnIM_i|Rup,IM_j} + \sigma_{lnIM_i|Rup,IM_j} v_i{}^{nsim} \tag{2.27}$$

where $v_i{}^{nsim} = v^{nsim}(i)$ is the i-th element in the v^{nsim} vector, and $Rup = Rup^{nsim}$.

2.4.1.4.2 Latin Hypercube sampling technique

The Latin hypercube sampling (LHS) can be applied through a stratified sampling approach. In order to draw realization samples from a distribution of an IM_i , its domain is stratified into N equally-spaced and non-overlapping intervals. Next is to randomly draw a sample from each of the interval. Hence, by utilizing a random permutation approach, a set of random LHS samples can be obtained. As such, the application of LHS to draw samples from a theoretical multivariate distribution of multiple $IM_i's$ can be summarized as:

1. Sample from the actual marginal distribution of each IM_i using LHS (Zhang & Pinder, 2003).
2. Derive the correlation matrix of the sampled realizations of various $IM_i's$.
3. Get the Cholesky decomposition of a Hermitian positive-definite matrix (L) of the correlation coefficient matrix (see Eq. 2.26). If L is not positive definite apply methods such as the one introduced by (Higham, 2002) to find the nearest PD matrix.

`

4. Add dependency between the independent samples drawn using LHS by transforming their governing normal distribution into a uniform distribution (this transformation preserves the dependency between the variables).
5. Map each of the $IM_i's$ uniform distribution onto the associated probability distribution of each defined by a $GMPE$.
6. Obtain the correlation between the new realization samples in order to compare it with the original correlation of the multivariate distribution to make sure they are identical.

It is worth noting that due to the superior efficiency and accuracy of the LHS versus Monte Carlo (see Chapter 6), given the number of realization samples to be drawn from the corresponding distributions, LHS has been adopted for sampling purposes throughout this study.

2.4.2 Record selection

Once the properties of hazard-consistent target distributions are obtained and the realization samples are drawn, a database of ground motion records can be consulted to select the suitable ground motion records. The criterion in this selection process is to find earthquake records for which the empirical distributions of various IM_i's match those of the realization samples drawn from the multivariate target distribution. It is useful to note here that once a record is selected matching a realization target, then that record will be removed from the database and will not be used again. To begin the selection process, all of the available records' response spectra, should be scaled to match the IM_j at the conditioning intensity measure, after the restrictions on the causal bounds have been applied.

2.4.2.1 Scaling

For a single IM_j, the amplitude scale factor is given as follows

$$SF_m = \left(\frac{IM_j}{IM_j^{m,unscaled}} \right)^{1/\alpha} \tag{2.28}$$

where $IM_j^{m,unscaled}$ is the intensity measure (corresponding to IM_j) of an unscaled record. Here α is an integer, which for intensity measures such as peak ground acceleration (PGA), peak ground velocity, (PGV), and spectral acceleration (SA) that scale linearly with amplitude scale factor, is considered as 1. For intensity measures such as arias intensity (IA), which exhibits quadratic scaling, $\alpha = 2$. Significant duration (SD) is independent of the amplitude scale factor, so $\alpha = 0$ (Bradley, 2012). IMi for each record is, therefore, scaled using

$$IM_i{}^m = IM_i{}^{m,unscaled}(SF_m)^\alpha \tag{2.29}$$

In cases of using two-, or multiple $IM_j{}'s$ as the conditioning intensity measures, either of the following relationships can be used (Wong & Chopra, 2017)

$$SF_{average} = \frac{\sum_{j=1}^{N_p} SAT_{sGCMS}(T_j)}{\sum_{j=1}^{N_p} SAT(T_j)} \tag{2.30}$$

$$SF_{optimal} = \left[\prod_{j=1}^{N_p} \frac{SAT_{sGCMS}(T_j)}{SAT(T_j)} \right]^{1/N_p} \tag{2.31}$$

where SAT_{sGCMS} is the target spectral acceleration conditioned on two or multiple $IM_j{}'s$, $SAT(T_j)$ is the spectral acceleration of a record at the given period T_j, and N_p is the number of period points in the interval $[T_1\ T_2]$ corresponding to IM_{j1} and IM_{j2} (here, $SAT1$ and $SAT2$).

The selection algorithm adopted, herein, is a least-squares approach suggested by Bradley (2012), which uses the following objective function to minimize

$$r_{m,nsim} = \sum_{i=1}^{N_{IM_i}} w_i \left[\frac{lnIM_i^{\ nsim} - SF_{optimal}\, lnIM_i^{\ m}}{\sigma_{lnIM_i|Rup^{nsim},IM_j}} \right]^2 \tag{2.32}$$

where,

$$SF_{optimal} = \exp\left(\frac{\sum_{i=1}^{N_{IM}} \left(\frac{\alpha_i}{\sigma_{lnIM_i|Rup^{nsim},IM_j}{}^2} \right) ln\left(\frac{lnIM_i^{\ nsim}}{lnIM_i^{\ m}} \right)}{\sum_{i=1}^{N_{IM}} \left(\frac{\alpha_i}{\sigma_{lnIM_i|Rup^{nsim},IM_j}} \right)^2} \right) \tag{2.33}$$

and where $\ln IM_i^{\ nsim}$ is the logarithmic IM_i of the realization target, $lnIM_i^{\ m}$ is the logarithmic IM_i of the record and $\sigma_{lnIM_i|Rup^{nsim},IM_j}$ is the logarithmic standard deviation of a realization target. The term w_i is the normalized weight vector assigning importance weights to the IM_i's considered during selection phase. Eq. (2.35)—which was proposed by (Wong & Chopra, 2017) —can also be used to further scale the records using an optimization approach to better match the target.

2.5 APPLICATIONS

The application of the methods described in the preceding sections are presented here through an example involving a simple and generic inelastic structure. First, an IM_i vector has to be populated. As suggested by Bradley (2012), $IMi = \{SA(T), AI, CAV, Ds575, Ds595\}$ where $AI, CAV, Ds575, Ds595$ denotes the Arias intensity, cumulative absolute velocity, 5-75% significant duration, and 5-95% significant duration, respectively. For computation of $SA(T)$, 21 different periods identical to those for which hazard curves can be generated, have been chosen.

The GMPEs used to define distribution of each IM_i in the IM_i vector are developed by Boore & Atkinson (2008) for $SA(T), PGA,$ and PGV, Campbell & Bozorgnia (2012) for AI, Campbell & Bozorgnia (2010) for CAV, and Bommer et al. (2009) for $(Ds575, Ds595)$.

In order to generate the multivariate distribution of IM_i's in the IM_i vector, a correlation matrix defining the cross-correlations between various IM_i's should be defined in addition to the median and standard deviation of each IM_i. For this, the reader is referred to Table 1 in Bradley (2012).

In order to select the ground motion records, a hypothetical site in the city of Los Angeles, CA (LONG-118.43; LAT34.053) with average shear-wave velocity for the upper 30 m depth of 760 m/sec and a depth to a 2.5 km/sec shear-wave velocity horizon of $z_{2.5} = 1$ km has been chosen. Using the relationships developed earlier in the texts, a set of different GM suites are selected based on different conditioning criteria and IM_i importance weight factors. Various suites selected based on giving different weights to the different IM_i's in the IM_i vector. Thus, weight factors of $70\%, 99\%, 1\%$ for the $SAT's$ and consequently weight factors of $30\%, 1\%, 99\%$ for the non-$SAT's$ are considered. The weights to be assigned to either of $SAT's$ or non-$SAT's$ intensity measures are evenly distributed among them during the selection phase. For the causal parameters, the magnitude range of $M = [5, 8]$, the closest source-to-site distance of $R_{jb} = [0, 100]$ km and the $V_{s30} = [300, 1200]$ m/sec are adopted. The maximum scale factor is set to 4. It is worth noting that hazard-consistency is implemented by considering up to 2,000 rupture scenarios and their contributions to different types of conditioning intensity measures.

2.5.1 Selected ground motions based on single-IM_j

This section is based on the algorithm developed in section 2.4.1.1. To begin, a structural fundamental period of $T1 = 1.30$ sec is adopted as the period for which the conditioning IM_j—

`

which is $SAT1$ throughout this study—will be derived from a hazard curve assuming a 2% probability of exceedance in 50 years. The number of realization samples to be drawn from the conditional multivariate distribution of $IM_i's$ in the IM_i vector is set to $50.$ The NGA-WEST2 database (see Appendix A) is chosen to select the earthquake records from, following the instructions given in section 2.5.2 of (Bozorgnia, et al., 2014).

Figure 2.1(b) displays the response spectra after applying the scale factor based on section 2.5.2.1 (see Figure 2.1(a)) using 1% SAT and 99% non-SAT weight factors assigned to different $IM_i's$. The blue solid and dashed curves are the statistics of the realizations drawn from $GCIM$ distribution (shown in red). As previously stated, ground motion records are selected to match these realizations. As such, the median as well as the 16- and 84-percentile ranges of the selected records (shown in green) appear to almost match those of the targets (shown in blue), it can be claimed that the empirical distribution of the selected records matches the theoretical distribution of the target. However, after more closely looking into the empirical distribution of SAT at multiple periods, as can be observed in Figure 2.1(c) and Figure 2.1(d), it can be observed that there is a clear mismatch between the empirical distribution of the selected records and those of the target. Note that, in this selection procedure, a larger weight was given to the non-$SATs$, so it is expected to get some levels of mismatch in the $SATs$, as discussed previously. Also applying various restrictions to different parameters will limit the number of records in the database, so a perfect match would be a rather difficult task to achieve unless a more comprehensive database is available and/or the restrictions on causal and site properties are relaxed.

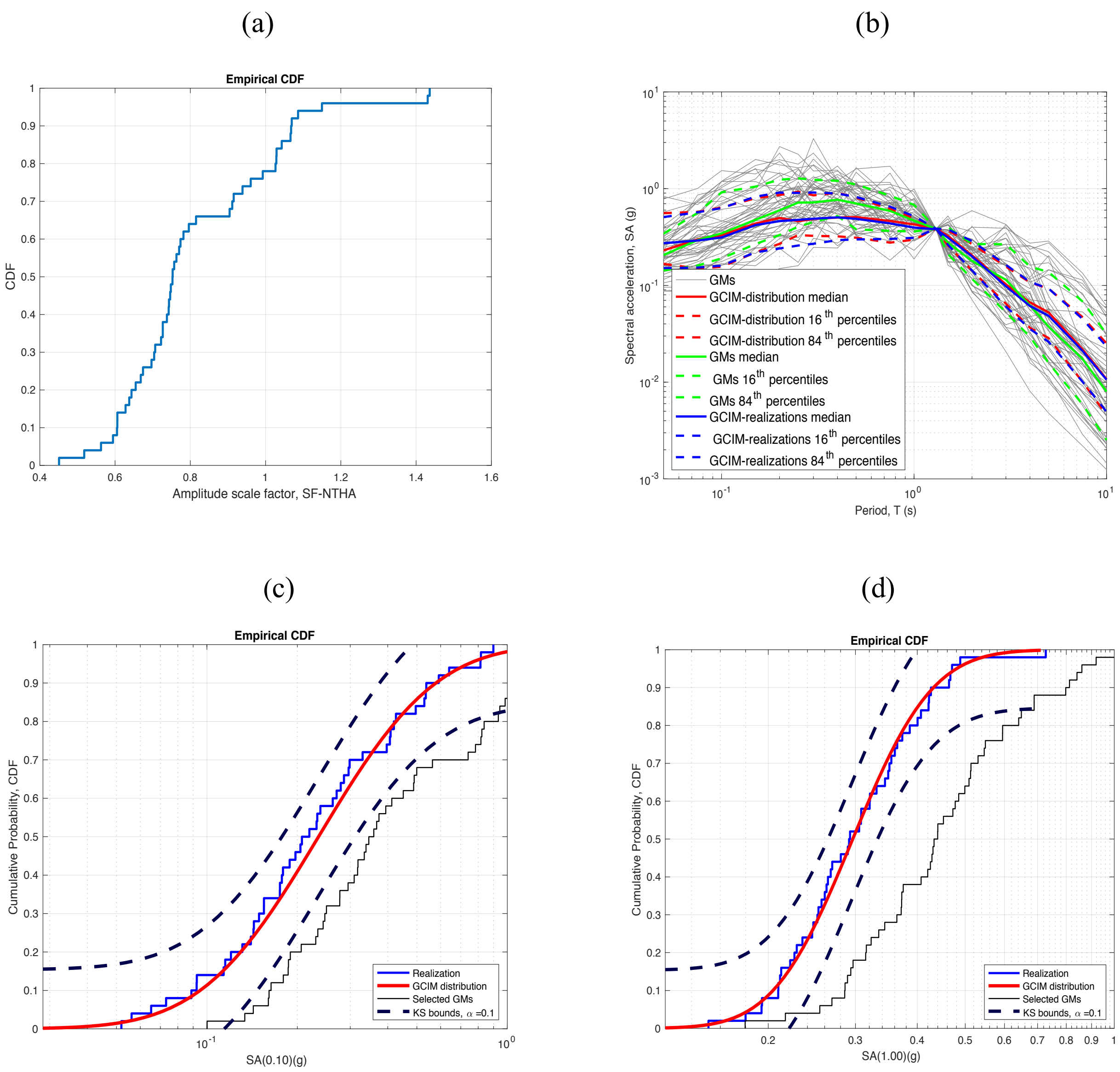

Figure 2.1. (a) Amplitude scale factor, (b) SAT of the selected records based on 1% SAT and 99% non-SAT weigth factors and cumulative probability distribution of selected records for (c) $SA(T = 0.10sec)$ and (d) $SA(T = 1.0sec)$.

For the cumulative and duration-based $IM_i{}'s$, Figure 2.2 displays the empirical distribution of various non-SAT $IM_i{}'s$—namely, CAV, AI, $Ds575$ and $Ds495$. Cumulative distribution of the realizations drawn from the theoretical distribution (median of which is shown in red) is shown in blue. As can be observed, there is a good match between empirical distribution of the selected records for all of the non-SAT intensity measures which are shown in black and those of the target which are shown in blue. This clearly shows that assigning a larger weight to the non-SAT intensity measures results in a GM set with records whose cumulative and duration-based characteristics closely match those of the hazard-consistent targets.

As can be observed, there is a good match between the empirical distribution of the selected records for all of the non-SAT intensity measures which are shown in black and those of the target which are shown in blue.

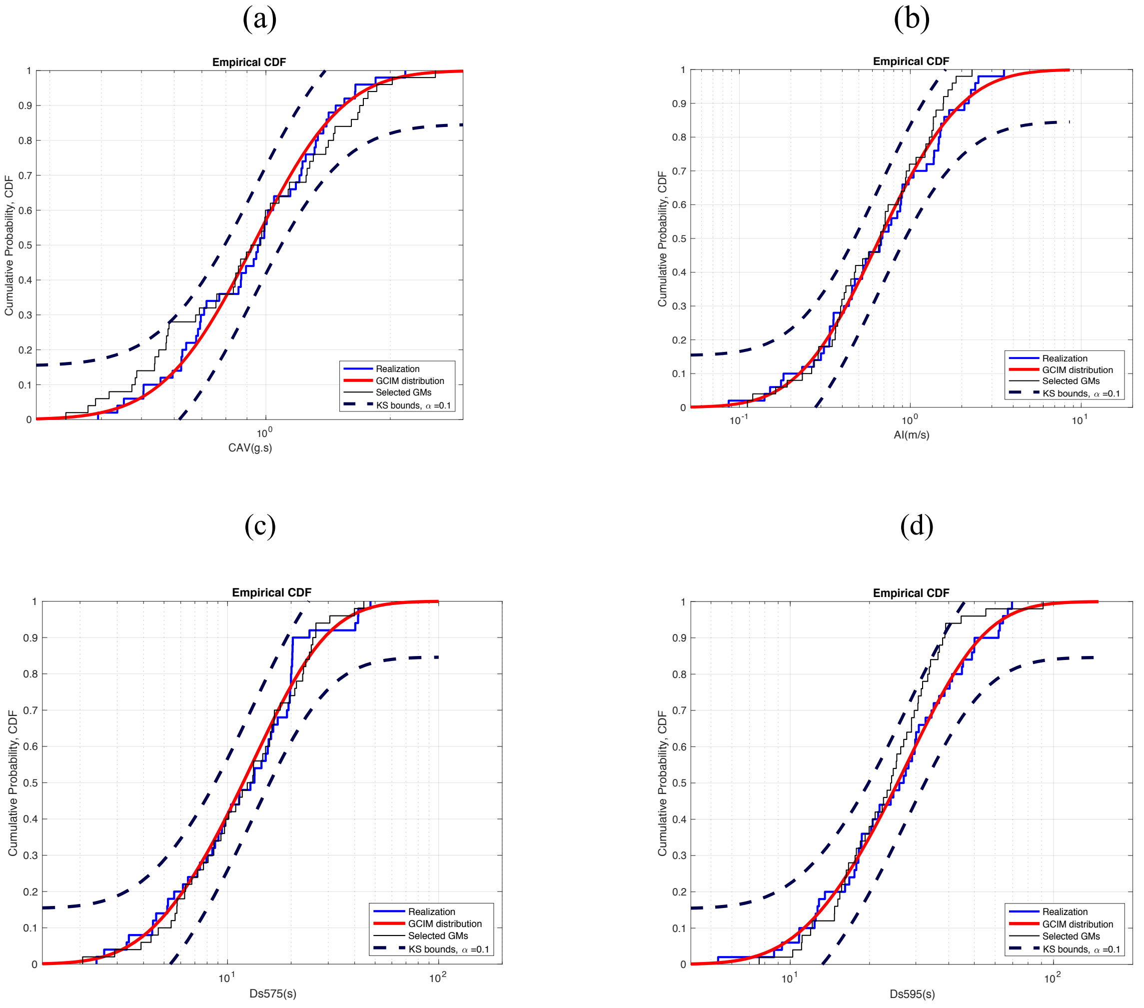

(a) (b)

(c) (d)

Figure 2.2. Cumulative probability distribution of selected records for (a) CAV, (b) AI, (c) $Ds575$ and (d) $Ds595$ based on 1% SAT and 99% non-SAT weigth factors.

For the other weight combinations considered, only a portion of the results are presented, for the sake of brevity. Figure 2.3 displays the response spectra and CAV of the selected records based on 70% SAT and 30% non-SAT weight factors.

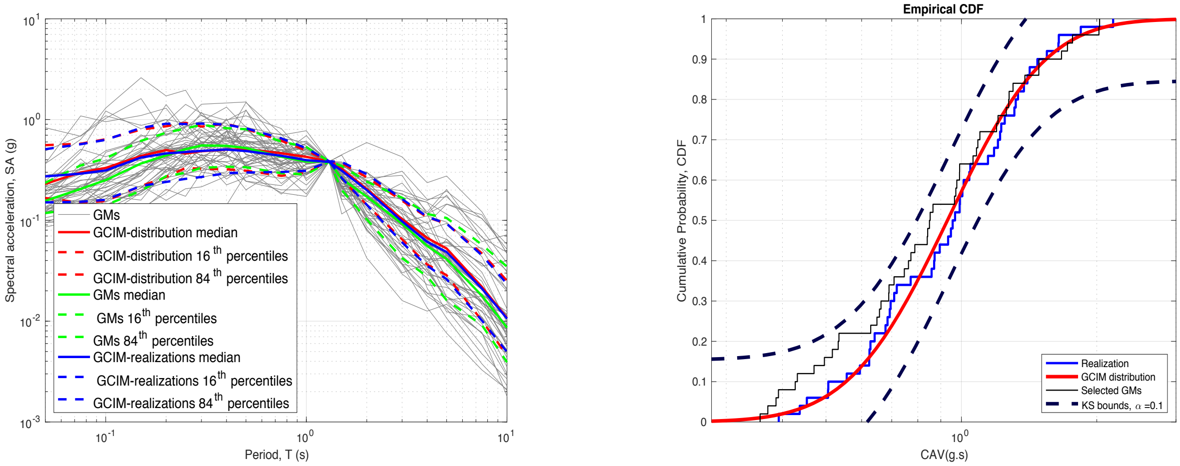
(a)

(b)

Figure 2.3. (a) SAT and (b) CAV of the selected records based on 70% SAT and 30% non-SAT weigth factors.

Assigning a larger weight to $SATs$ results in a better statistical property of the selected records with respect to those of the targets, which can be noticed in Figure 2.3(a) However, this choice will affect the empirical distribution of the selected records with respect to the cumulative intensity measures, which can be seen in Figure 2.3(b) Consequently, the distribution of the selected records (shown in black) does not closely match the distribution of the realizations (shown in blue), which was expected due to the weight factor used. However, the level of mismatch is not significant.

Figure 2.4 displays the response spectra and CAV of the selected records based on 99% SAT and 1% non-SAT weigth factors. Since the main goal was to select records based on matching the amplitude contents rather than cumulative ones, a better match can be observed in Figure 2.4(a) in the statistical properties of response spectra of the selected records with respect to those of the target. Figure 2.4(b). shows a clear mismatch in the cumulative distribution (shown in black) of the selected records with respect to the target (shown in blue). This is expected given the smaller importance weight given to the non-$SATs$.

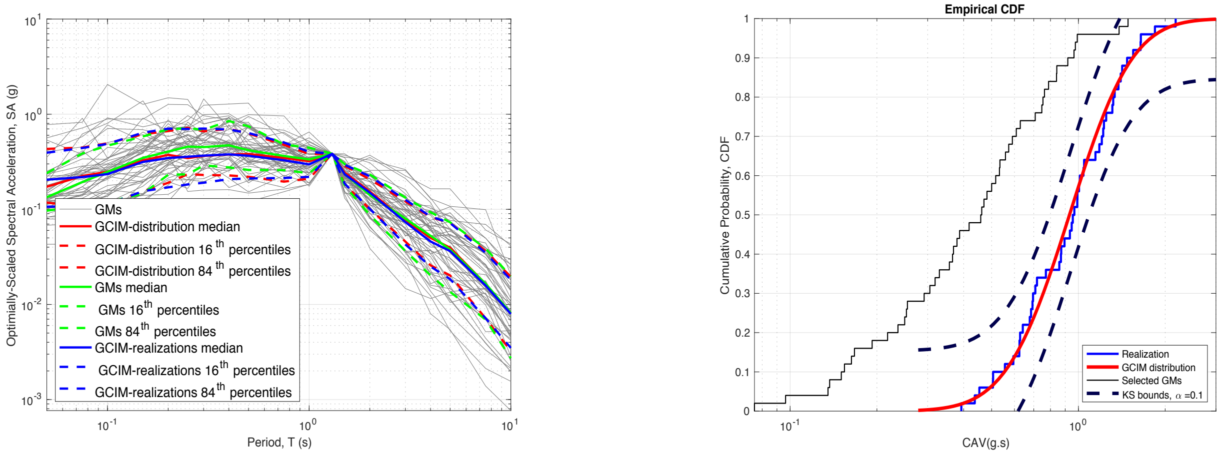
(a)

(b)

Figure 2.4. (a) SAT and (b) CAV of the selected records based on 99 % SAT and 1% non-SAT weigth factors.

2.5.2 Selected ground motions based on two-IM_j

This section is based on the algorithm developed in section 2.4.1.2. Lower and upper bound coefficients of 0.20 and 3.0 are applied to the structure's fundamental period of $T1 = 1.3$ sec in order to obtain IM_{j1} and IM_{j2} based on the study by Eads et al. (2016) and Chandramohan (2016). Thus, $T1$, $T2$ were set to 0.25 sec and 4.0 sec, respectively.

Figures 2.5(a) and 2.5(b) display the cumulative amplitude scale factor and the response spectra for the selected records for a conditional target conditioned on two-$IM_j's$—i.e., $SA(T = 0.25\,\text{sec})$ and $SA(T = 4.0\,\text{sec})$. When a smaller weight is assigned to $SATs$, the statistics of the selected records do not match those of the target especially at shorter and longer period ranges. This can be clearly observed from the cumulative distribution of two sample $SATs$ shown in

Figures 2.5(c) and 2.5(d). Based on that, empirical distributions (shown in black) of SAT at two different periods don't match those of the target (shown in blue). That's clearly the goal from the beginning to select ground motions with a stronger representation of cumulative rather than amplitude-based measures, which was enforced by assigning a larger weight factor to cumulative- as well as duration-based $IM_i's$.

Given that the records are selected here based on 1% SAT and 99% non-SAT weight factors, Figure 2.6 clearly shows that there is good match between the cumulative and duration-based characteristics of the selected records and those of the target. Therefore, it can be seen in all of the plots in Figure 2.6 that the empirical cumulative distributions of the selected records match those of the realization target quite closely, proving that assigning a larger weight factor to non-$SATs$ will result in a GM suite with stronger representation of cumulative and duration-based intensity measures.

(a) (b)

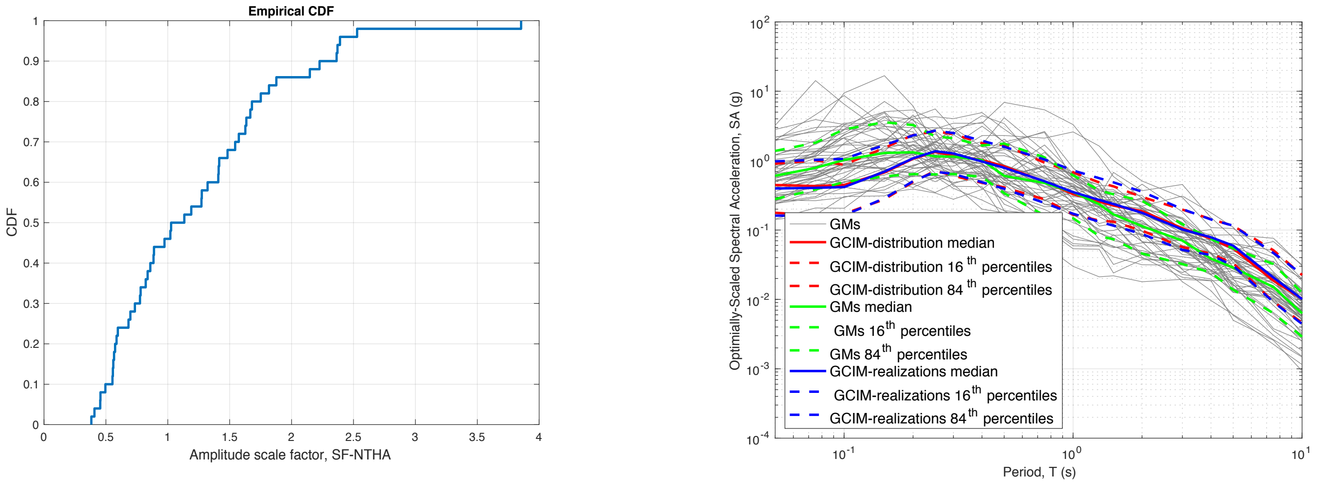

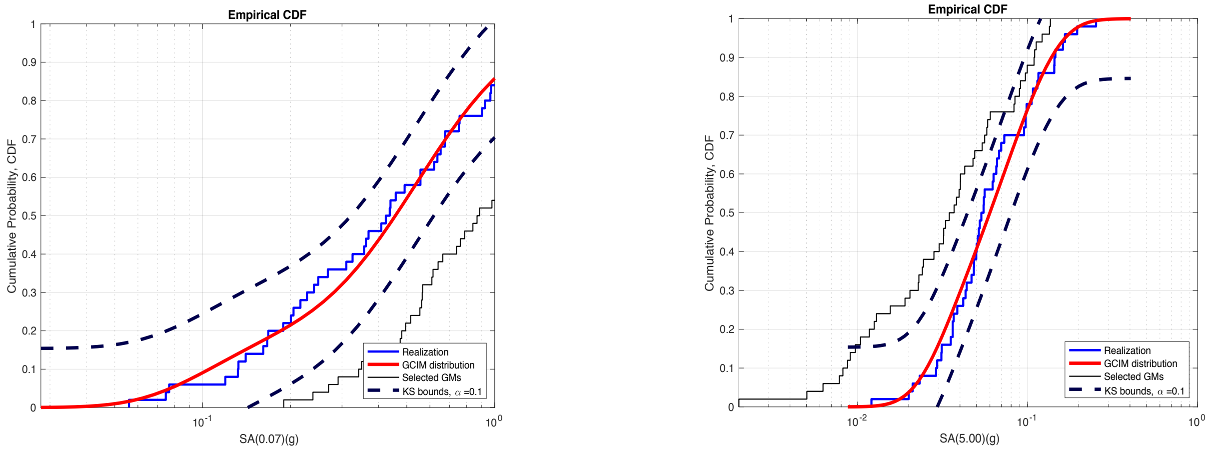
(c)

(d)

Figure 2.5. Amplitude scale factor, (b) SAT of the selected records based on 1% SAT and 99% non-SAT weigth factors and cumulative probability distribution of the selected records for (c) $SA(T = 0.07\,\text{sec})$ and (d) $SA(T = 5.0\,\text{sec})$.

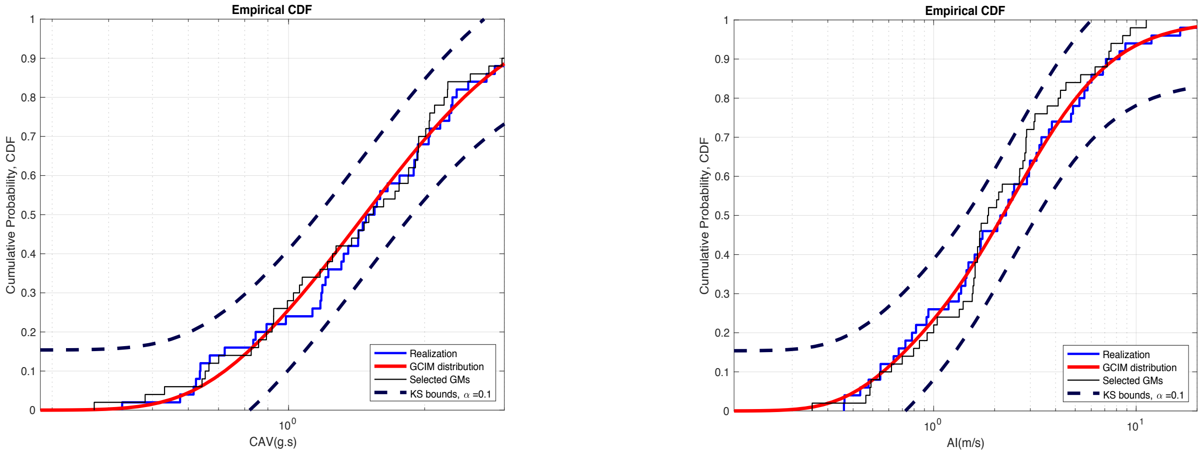
(a)

(b)

`

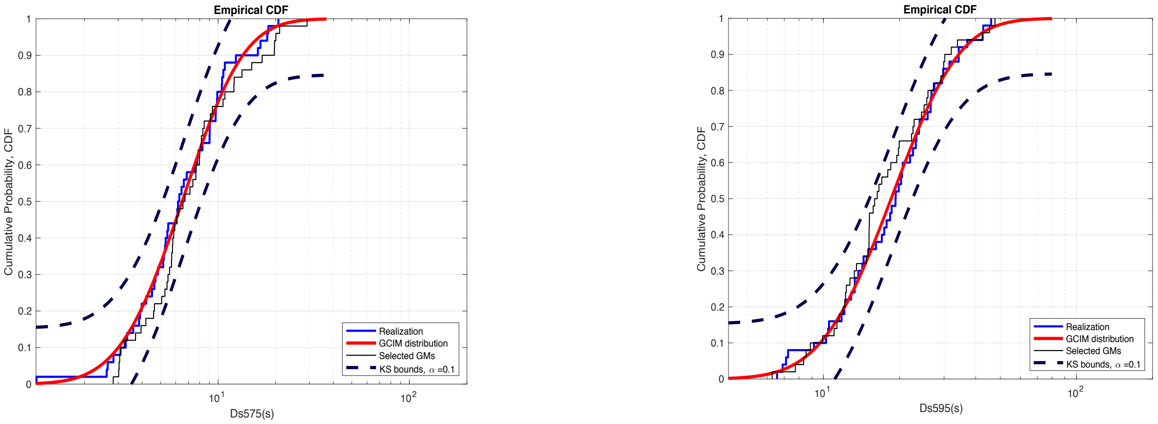
(c)

(d)

Figure 2.6. Cumulative probability distribution of selected records for (a) CAV, (b) AI, (c) $Ds575$ and (d) $Ds595$ based on 1% SAT and 99% non-SAT weigth factors.

Changing the weight factors to 70% SAT and 30% non-SAT will have some impact on the selected records. Figure 2.7(a) displays that the statistics of response spectra for the selected records match those of the targets quite closely, however when it comes to non-$SATs$, as seen in Figure 2.7(b), the empirical cumulative distribution of AI (shown in black) does not match the target (shown in blue). This is a direct consequence of the weight factors assigned for the purpose of record selection.

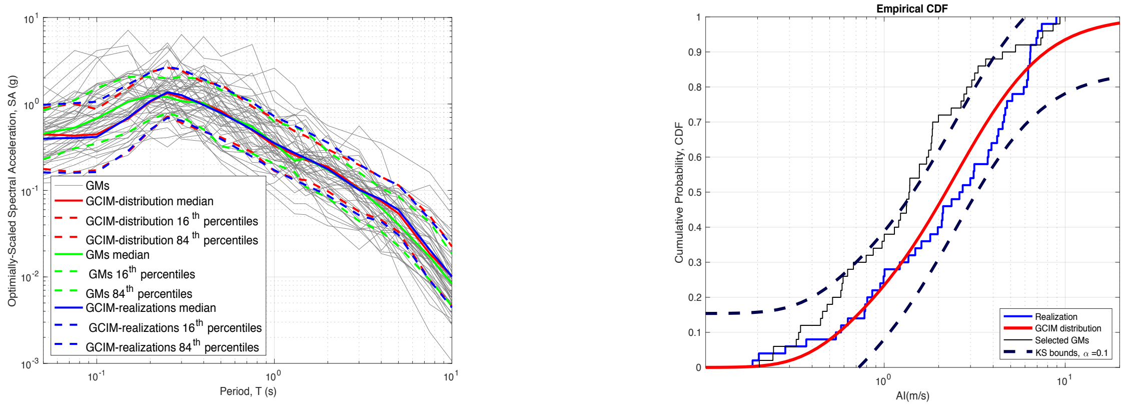
(a)

(b)

Figure 2.7. (a) SAT and (b) AI of the selected records based on 70% SAT and 30% non-SAT weigth factor.

`

Next, 1% SAT and 99% non-SAT weight factors are utilized to select records to match a conditional target conditioning on two $IM_j's$. Figure 2.8(a) shows that given the larger weight assigned to $SATs$ during the selection process, the statistics of the selected records' spectra match those of the target. However, as seen in Figure 2.8(b), the cumulative distribution of non-$SATs,$ of which only $Ds575$ results are presented here for brevity, does not match the target, and there is a significant mismatch which is due to the smaller weight initially assigned to non-$SATs$.

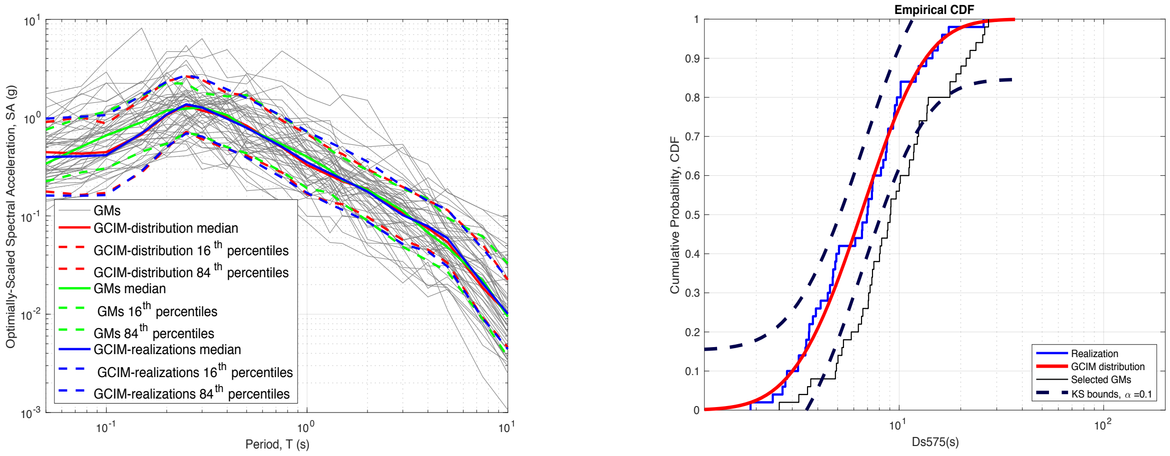
(a)

(b)

Figure 2.8. (a) SAT and (b) $Ds575$ of the selected records based on 99% SAT and 1% non-SAT weigth factor.

2.5.3 Selected ground motions based on Multiple-IM_j

This section is centered around ground motion selection based on the algorithm developed in section 2.4.1.3. The conditioning IM_j here is set to be Sa_{avg}, which is the geometric mean of multiple $SATs$ over the period interval of $[T1, T2]$. Lower and upper bound coefficients of 0.20 and 3.0 are applied to the structure's fundamental period of $T1 = 1.3$ sec in order to obtain IM_{j1} and IM_{j2} based on the study by Eads et al. (2016) and Chandramohan (2016). Thus, $T1$, $T2$ were set to 0.25 sec and 4.0 sec, respectively. The algorithm described in section 2.4.1.3 is then utilized to develop a hazard-consistent conditional target conditioned on $\ln Sa_{avg}$ and thereafter, the ground motion records are selected following section 2.4.2.

Figures 2.9(a) and 2.9(b) display the cumulative distribution of amplitude scaling factors and response spectra of the selected records based on 1% SAT and 99% non-SAT weigth factors, respectively. Given that the majority of weight has been assigned to non-$SATs$, the statistics of the selected records (shown in green) do not match well those of the target (shown in blue). The same can also be seen in Figures 2.9(c) and 2.9(d) where there is a clear mismatch between distributions of the selected records (shown in black) and those of the target (shown in blue) for $SA(T = 0.50\ \text{sec})$ and $SA(T = 1.50\ \text{sec})$, respectively.

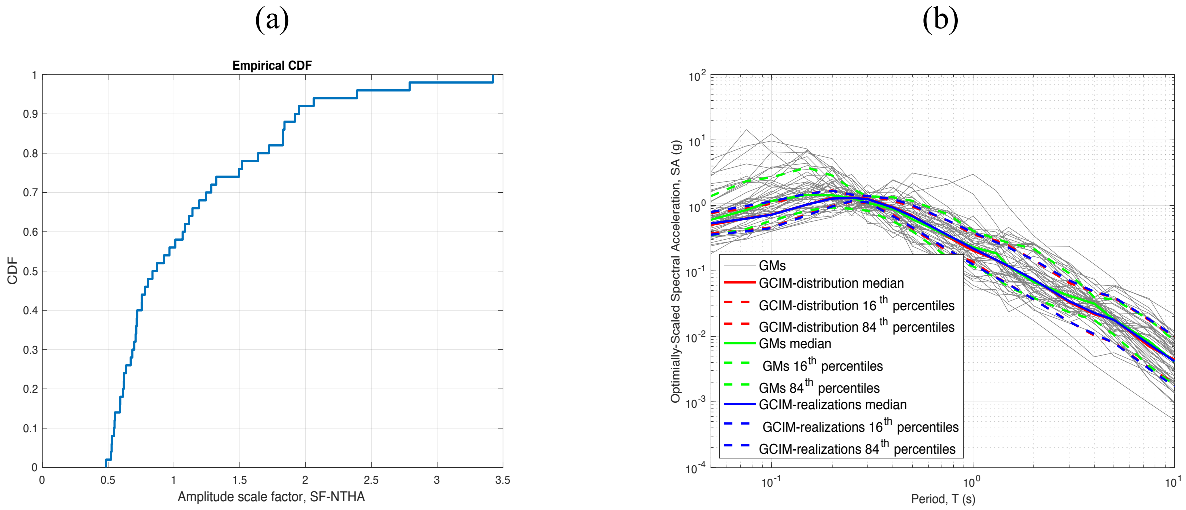

(c) (d)

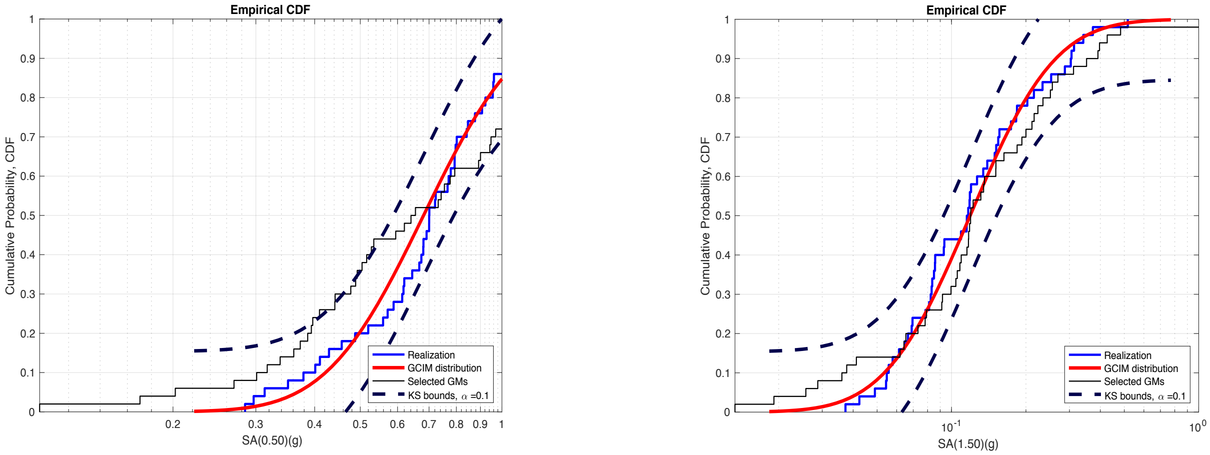

Figure 2.9. Amplitude scale factor, (b) SAT of the selected records based on 1% SAT and 99% non-SAT weigth factors and cumulative probability distribution of the selected records for (c) $SA(T = 0.50\,\text{sec})$ and (d) $SA(T = 1.50\,\text{sec})$.

While amplitude-based contents of the selected records do not match those of the target—due to the smaller weight factors assigned to them during the selection process—, cumulative-based characteristics *do*, as it can be observed in the plots of Figure 2.10.

(a) (b)

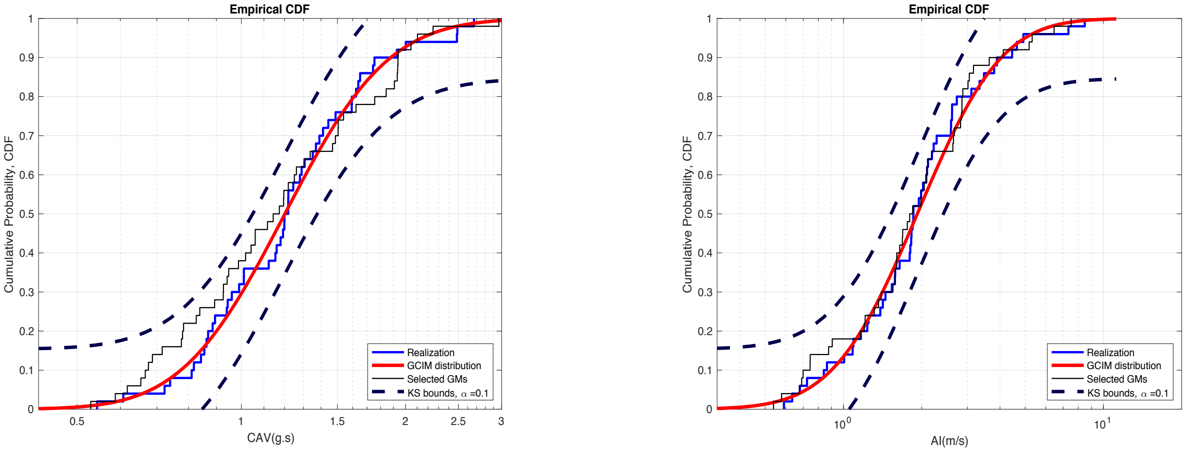

`

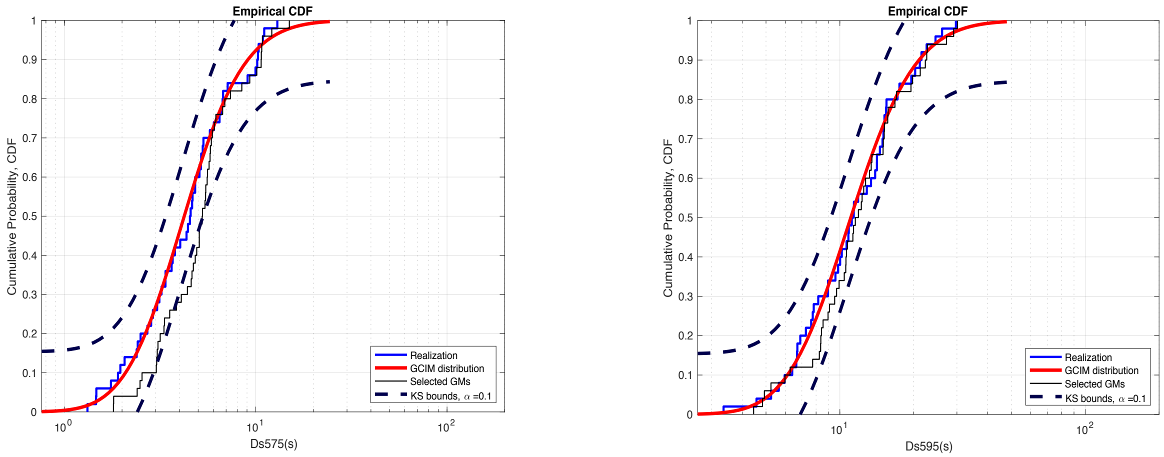
(c)

(d)

Figure 2.10. Cumulative probability distribution of selected records for (a) CAV, (b) AI, (c) $Ds575$ and (d) $Ds595$ based on 1% SAT and 99% non-SAT weigth factors.

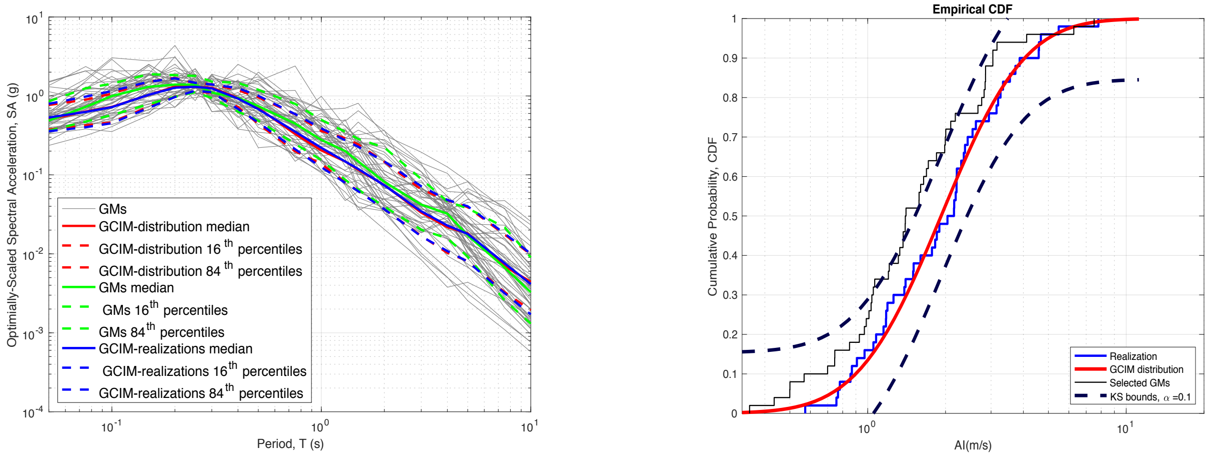
(a)

(b)

Figure 2.11. (a) SAT's and (b) AI of the selected records based on 70% SAT and 30% non-SAT weigth factors.

Another set of weights—i.e., 70% SAT and 30% non-SAT —is also considered to select ground motions matching conditional targets conditioned on $\ln Sa_{avg}$. As seen in Figure 2.11(a), assigning a larger weight to $SATs$ measures results in records whose statistics better match those of the target. However, as it can be seen in Figure 2.11(b), when it comes to non-$SATs$ (such as AI), there is a poor match between the cumulative distribution of the selected records (shown in black) and the conditional target (shown in red).

Another attempt is also made with 99% SAT and 1% non-SAT weight factors in order to select earthquake records with near full emphasis on amplitude-based contents. Figure 2.12(a) indicates that the statistics of the selected records match those of the target pretty closely, however cumulative distribution of the selected records (e.g., for AI) has a very poor match with respect to the target, as it can be seen in Figure 2.12(b).

(a) (b)

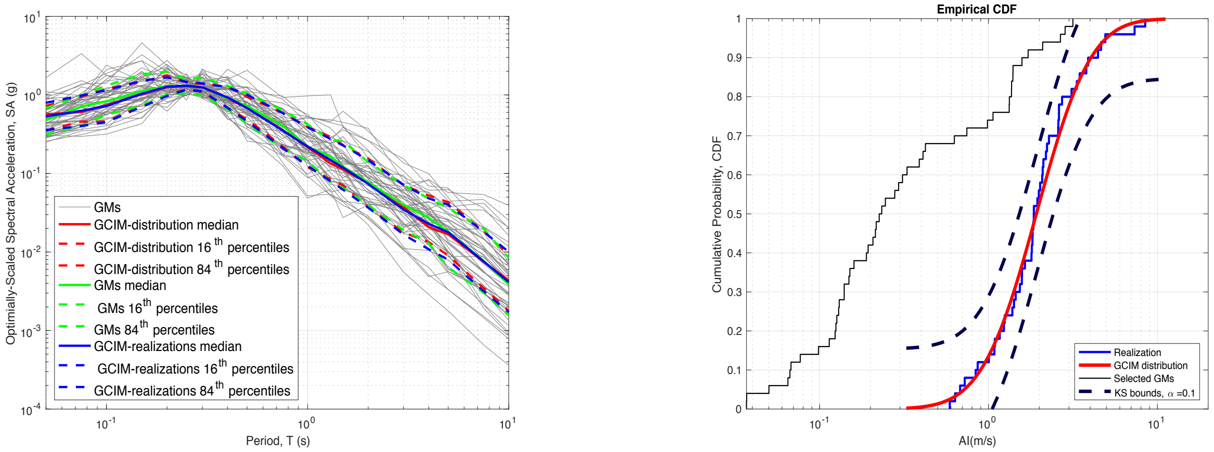

Figure 2.12. (a) SAT and (b) AI of the selected records based on 99% SAT and 1% non-SAT weigth factors.

2.6 DISCUSSION

Ground motion earthquake records are one of the main sources of variability in the estimates of structural responses when it comes to the performance-based seismic risk assessment. In these procedures an appropriate suite of ground motion records is required to capture the said uncertainties. Depending on the structural type and the selected performance objective, a structure may experience significant changes to its fundamental period of vibration or have multiple modes significantly contributing to its overall response. This, therefore, makes the structure sensitive to intensity measures of an earthquake motion other than the spectral amplitude/ordinate at the fundamental period of the structure (SAT1), which is what conventional methods for selecting GM suites are based on. Such selection procedures thus often produce structural demand/response estimates with large scatter (uncertainty).

In most cases, practicing engineers will prefer to use GMs selected to match a design spectrum recommended by various codes. As demonstrated in the preceding sections, ground motions selection procedures that give more emphasis to response spectrum may lack adequate representations of cumulative and duration-based intensity measures. This then may result in the underestimation of structural responses, especially for cases when structural nonlinearities are observed (e.g., for collapse estimates).

Several new GM selection methods were proposed in the preceding sections by considering correlations between various $IM_i's$ conditioned on various $IM_j's$ while incorporating hazard-consistency for various rupture scenarios.

It is well known that selecting ground motions matching a uniform hazard spectrum (UHS) is deemed to be overly conservative. UHS is obtained directly from the hazard curves for various $SATs$ over a range of periods. All of the ordinates of UHS are, therefore, hazard-consistent and have the same return period. In reality, only a few as-recorded earthquakes can produce a response spectrum that is hazard-consistent over all of its ordinates. The algorithms developed herein are able to produce a more reasonable set of hazard-consistent targets.

A quick comparison of the median response spectra obtained from various conditioning methods can be seen with the help of Figure 2.13, which is obtained for a hypothetical site in the city of Los Angeles, CA (LONG -118.43; LAT 34.053) with an average shear wave velocity of

760 m/sec for the upper 30m depth, varying towards 2.5 km/sec shear-wave velocity at a horizon of $z_{2.5} = 1 \text{ km}$. The structural fundamental mode period is set to be $T1 = 1$ sec.

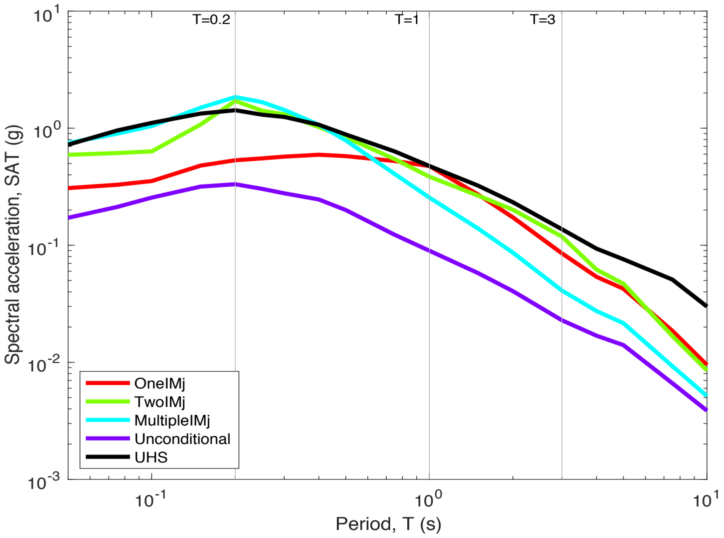

Figure 2.13. Comparison of median spectra obtained from various methods of conditioning target generation, with the target spectrum obtained based on UHS.

As it can be observed from this figure, selecting earthquake records matching the UHS target spectrum (shown in black) will result in a very conservative set of records, simply because these records are going to be very intense at the entire set of structural periods of vibration. On the other hand, the response spectrum obtained from the new methods proposed earlier, as well as the response spectrum using an unconditional approach, all fall below the UHS at most period values. However, record selection based on an unconditional approach is highly non-conservative and produces hazard-inconsistent $SATs$ for any period of vibration, and therefore it is not recommended. The target conditioned on a single intensity measure (shown in red) produces a target that is hazard-consistent at a single IM_j (i.e. $SAT = 1$ sec) and falls below UHS at all of the other $SATs$. Here, it can be argued that records selected matching this target spectrum may not be sufficient if the structure goes into a highly nonlinear phase. Therefore, one would have to repeat this process for a few times to generate conditional targets using new $IM_j's$ each time, which then increases the computational burden significantly.

Selecting records matching a target to be hazard-consistent over a range of conditioning periods—which has been the case for the proposed two-IM_j and multiple-IM_j methods—seems to have mitigated the aforementioned problems. As it can be observed in Figure 2.13, the target spectrum conditioned on two-IM_j (shown in green) intercepts the UHS over a range of periods between IM_{j1} and IM_{j2}— here, $SAT(T = 0.2\text{sec})$ and $SAT(T = 3.0\text{sec})$, respectively—, which necessarily brackets and includes $SAT1$ ($SAT = 1.0\ sec$). Thus, the selected records matching this target *will* have sufficient intensity to excite the structure at its many modes (controllable by selecting the IM_{j1} and IM_{j2}) rather than only $T1$. This, then, obviates the use of multiple suites, thereby reducing the computational burden significantly.

The records selected based on multiple-IM_j conditioning (shown in cyan in Figure 2.13) produces but a more intense spectrum at a lower vibration periods than other methods, but a less intense spectrum around $SAT1$, eventually diminishing into the unconditional spectrum at longer periods.

While a more comprehensive set of nonlinear time history analyses will be carried out on realistic (ductile and non-ductile multi-story reinforced concrete) structures in the Chapters 4 and 5, parametric studies carried out with a simple nonlinear structure should unveil the consequences of different GM selection methods. For this purpose, a SDOF structure, which approximates the typical concrete bridge pier (Chandramohan, 2016) is considered, which is shown in Figure 2.14.

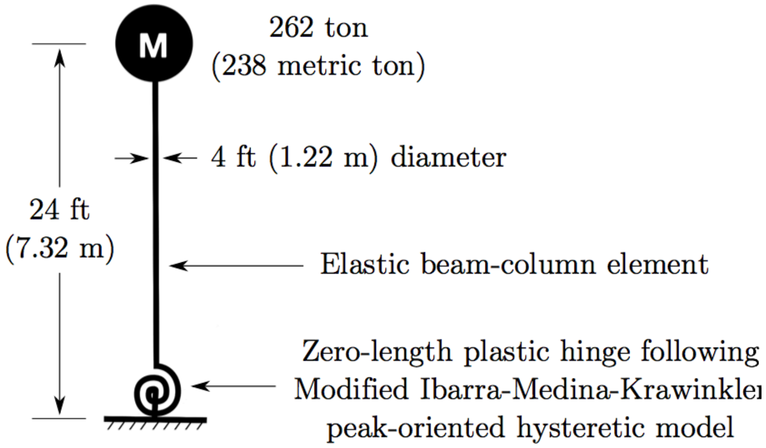

Figure 2.14. A ($SDOF$) structural system (adopted from (Chandramohan, 2016)).

Figure 2.15 displays the statistics of the top-node normalized displacement (Drift (%)) of the $SDOF$ system including the median as well as 16- and 84-percentile values obtained through the application of different GM selection algorithms (and importance weight factors therein). It is obvious that the medians decrease from Figure 2.15(a) to Figure 2.15(d), as the emphasis shifts away from the non-SAT intensity measures. It is evident that when non-$SATs$ weight is at a maximum (see Figure 2.15.a), the median drift is above 1%, whereas when it drops to 50%, 30% and eventually 1%, the median drift decreases (nearly linearly) and falls even below 1% as seen in Figure 2.15(d). These results clearly indicate the importance of the inclusion/consideration of cumulative and duration-based intensity measures when compiling GM suites for performance assessment.

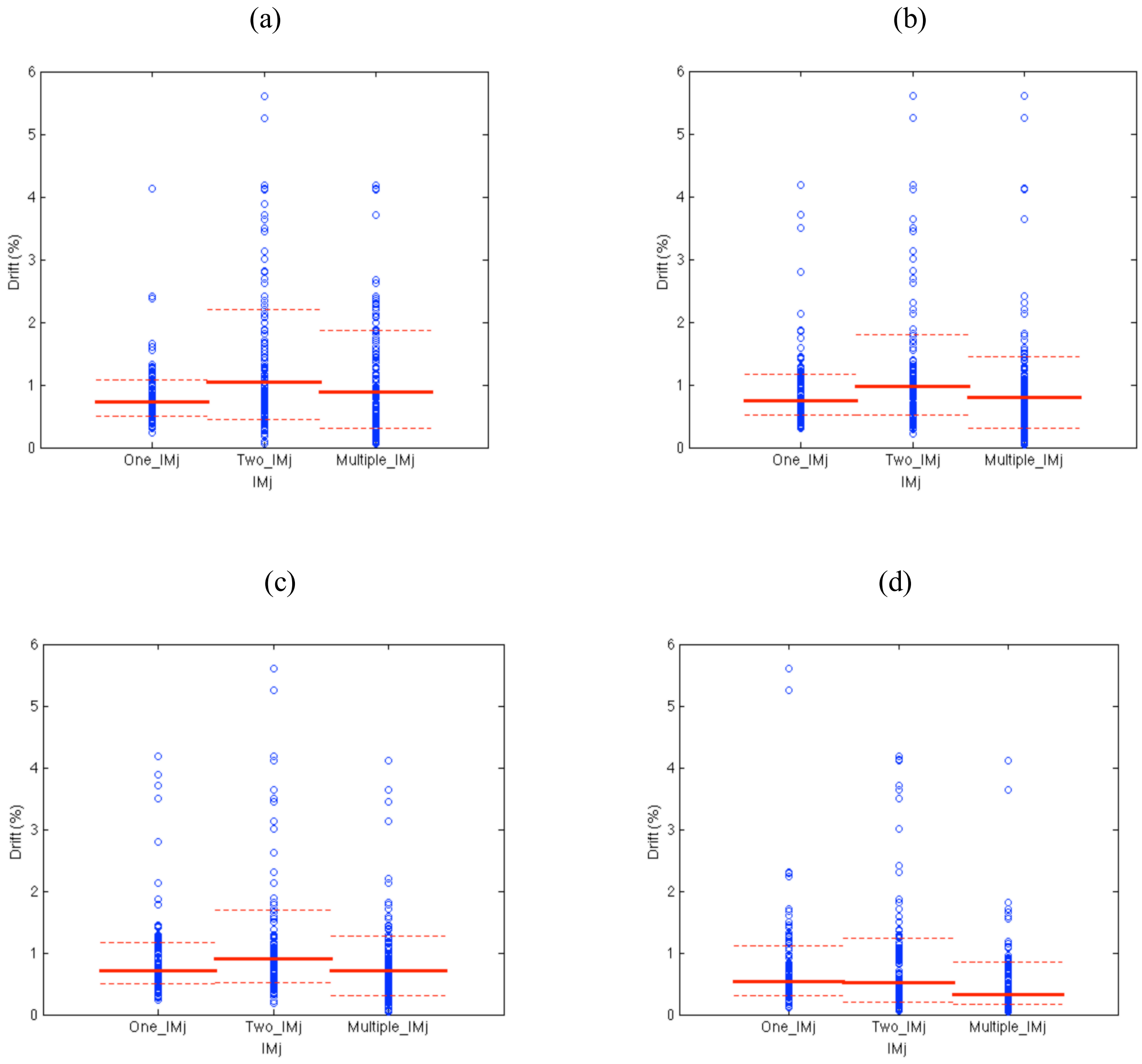

Figure 2.15. Comparison of a $SDOF$ seismic demand responses obtained using different GM suites selected based on various ground motion selection procedures with different weight factors: (a) 1% SAT and 99% non-SAT, (b) 50% SAT and 50% non-SAT, (c) 70% SAT and 30% non-SAT and (d) 99% SAT and 1% non-SAT.

Another set of comparisons can be made regarding the effect of the type of conditioning algorithm used—namely, those based on single, two or multiple-IM_j—on the statistics of the estimated responses. It is clear from Figures 2.15(a) to 2.15(c) that the median drift is higher for two-IM_j compared to the multiple-IM_j and single-IM_j, proving that the records selected matching targets conditioned on more than one IM_j will have sufficient contents to capture the response of a structural system in multiple modes of vibration. This clearly stands out when looking at the upper percentiles of the response as well, which stand higher for the case of two- and multiple-IM_j, as compared to single-IM_j. In Figure 2.15(d) where the non-$SATs$ weight was set to be very small, there is a balance in the median response, so the records selected based on single-IM_j seem to have sufficient contents to capture the demand. This is mainly due to the fact that the ground motions in this case were selected by giving more emphasis to SAT intensity measures, with the inertia-based effects dominating the response while duration and cumulative effects were not that pronounced.

2.7 CONCLUDING REMARKS

A comprehensive GMSSM framework was proposed. Most of the existing methods/frameworks are based on response spectrum matching, and the use of intensity measures other than spectral amplitudes is often not considered. Moreover, most of the algorithms developed thus far are based on a median approach, both in considering the effects of various rupture scenarios as well as spectral matching. Given these potential shortcomings in GMSSM, various new algorithms were developed here to generate hazard-consistent target intensity measure distributions using single-IM_j, two-IM_j, and multiple-IM_j as the conditioning intensity measures. Correlations among the intensity measures themselves, and those of the conditioning $IM_j's$ have been considered when drawing realization targets from a multivariate distribution of various $IM_i's$. Ground motion were then selected by first drawing a desirable number of realization samples from the target and then by interrogating a GM database to find earthquake records whose contents match those of the corresponding realizations. Different importance weight factors for the considered $IM_i's$ were examined, which enabled user-control in generating adequately diverse GM suites with records selected by assigning different weights to amplitude-, and duration- or cumulative-based intensity measures.

It was concluded that for structures that will experience some level of damage and go into a highly nonlinear phase, the selected ground motions should have sufficient duration or cumulative characteristics in order to sufficiently probe the probable structural responses. This approach incidentally resulted in reducing the uncertainty in estimated structural responses. Based on parametric studies carried out using a generic nonlinear SDOF structure, ground motion suites selected based on more than one conditioning intensity measure were observed to be more appropriate in capturing the structural behavior (less uncertainty). Moreover, assigning a larger weight factor to energy-based (duration- or cumulative-based) rather than amplitude-based intensity measures in the selection process resulted in a more realistic (conservative) estimation of the responses.

3 A STOCHASTIC FRAMEWORK FOR AFTERSHOCK GMSSM

3.1 INTRODUCTION

A mainshock earthquake is typically followed by a sequence of aftershocks, which exhibit a higher frequency of occurrence in first few days after the mainshock event. Due to the mainshock earthquake event, a given structure may already have undergone some level of damage. As such, aftershocks pose further risks and additional losses on an already-damaged building. It is known that earthquakes are quite unpredictable, however, if a mainshock has already taken place, it is reasonable to assume that there *will* be a sequence of aftershocks.

Past earthquakes remind us of both the financial and human losses due to mainshock-aftershock events. In current seismic codes and provisions, buildings are designed only for the mainshock event, and there are no requirements to evaluate the performance of structures for a sequence of aftershocks. This, in part, can be attributed to the lack of a comprehensive database of aftershock earthquake ground motion records and the relative complexity of fault rupture mechanisms causing aftershocks, which makes it difficult to simulate aftershock earthquake records. Consideration of aftershocks in any seismic design appears to be a task that cannot be overlooked.

3.2 SCOPE AND MOTIVATION

Consideration of aftershocks requires detailed understanding of the mechanisms that produce both the mainshock and the aftershock events. In practical terms, there is a need to equip researchers and engineers with relevant tools and methodologies to enable them to select ground motions both for mainshock and aftershock events that can be utilized during various stages of seismic evaluation. GM selection for mainshock events has been the topic of numerous prior studies (see Chapter 2), but studies on GM selection/characterization of aftershocks have been extremely scarce.

Given the lack of prior studies, this research is aimed at developing tools (i) to define the seismicity of a given region for aftershocks, (ii) for producing hazard-consistent targets for various intensity measures ($IM_i's$) for aftershock events, and subsequently (iii) for selecting as-recorded or simulated aftershock ground motion records. For achieving these objectives, a set of hypothetical fault rupture events will be devised to compute seismic hazard associated with aftershock events. In order to compute a seismic hazard curve for an aftershock event, aftershock magnitudes will be sampled from an existing magnitude density distribution in similar fashion with what is done for a mainshock event with the difference of setting the mainshock event magnitude as an upper bound limit for the aftershock event. For source-to-site distance computation, the epicenters of the mainshock and aftershock will be assumed to be the same, based on the fact that most of aftershocks will initiate within the same rupture area as the mainshock. Thus, by using existing relationships for computing the length of fault rupture as a function of magnitude, it will be possible to determine a probability distribution of distance. After having the magnitude and distance distributions for aftershock events, and given site conditions, it will be possible to generate a seismic aftershock hazard curve. This will be carried out in a manner that considers the difference between the frequency of occurrence of aftershock events and that of the mainshock. The overall method will thus produce aftershock hazard curves that are computed with respect to a specific elapsed time from the mainshock event, ranging from a day to several months. Additionally, disaggregation plots, which are proxies to hazard curves, will be computed and will be used for defining the contribution of each rupture scenario to any given level of any intensity measure (IM) of interest.

After computing the aftershock hazard curve—which will be computed for spectral acceleration (SAT) as the adopted IM of interest here—, the uniform hazard spectrum (UHS) will be derived for a specific return period. Finally, the GMSSM framework developed in Chapter 2 will be utilized for selecting hazard-consistent aftershock GMs. The steps will be similar to what was carried out in Chapter 2, and thus hazard-consistent conditional aftershock ground motion target distributions conditioned on single-, two- or multiple-$IM_j's$ will be produced first. Then, earthquake records will be selected from a database of recorded or synthetic earthquake records whose $IM_i's$ match those of the target(s).

Another objective will be to study the sensitivity of various key parameters involved in defining the aftershock seismicity—namely, the elapsed time from the mainshock during which a sequence of aftershocks will take place, multiple seismic sources, and the variations in upper-bound magnitude, which caps the aftershock magnitude interval. The main outcome of this research effort will thus be a stochastic framework that defines aftershock seismicity of a given site and enables aftershock ground motion selection for performance-based seismic assessment and design.

3.3 A REVIEW OF PRIOR STUDIES

3.3.1 Background

Research in the area of hazard-consistent aftershock GMSSM are presently very limited in scope and quantity. Although there have been some recent studies in the area of seismic risk evaluation of structures due to mainshock-aftershock events, the GMSSM-related aspects in these studies are highly simplistic. Since, ground motion earthquake records are the primary source of variability on the estimated structural responses, failing to select accurate aftershock ground motion records would, in principle, negatively affect the seismic risk evaluation of structures due to mainshock-aftershock sequences.

Yeo & Cornell's (2005) work in this area is one of the pioneering studies, which forms the basis of the present study. A good portion of their work is devoted to hazard characterization of aftershocks. However, aftershock hazard curves are developed using a deterministic rupture scenario. This shortcoming will be mitigated and enhanced in the present study by adopting a probabilistic approach to define the seismicity of a site due to aftershock events under a range of different fault rupture scenarios.

In a follow-up study, Yeo & Cornell (2009) performed a building life-cycle cost analysis due to mainshock-aftershock events by modeling mainshocks as a homogenous Poisson process with a constant rate of co-occurrence, as opposed to aftershocks that are modeled as non-homogenous Poisson processes with random magnitudes conditioned on the occurrence of a mainshock event. They introduced a general decision-making procedure based on stochastic dynamic programming wherein the main factor they considered was the time-varying effects of aftershocks. They proposed a method to develop aftershock hazard curves for SAT as the intensity measure of interest, similar to the approach that develops mainshock hazard curves through probabilistic seismic hazard analysis ($PSHA$). The main difference of an aftershock probabilistic seismic hazard analysis ($APSHA$) as opposed to $PSHA$ is that in $PSHA$, the rate of occurrence of mainshock event is considered as constant, whereas in $APSHA$ this rate varies with time and decreases as the elapsed time since the mainshock vent increases. Yeo and Cornell (2009) assumed—as is commonly done in other prior studies—that aftershocks are initiated due to a rupture scenario that is identical to that for the mainshock and that the location where aftershocks initiate is in the same zone as the mainshock. As stated above, Yeo and Cornell's works (2005, 2009) form the basis of the present study wherein their deterministic approach will be extended to a probabilistic one and will be utilized thereafter for aftershock GMSSM.

Other studies of note include that by Sunasaka & Kiremidjian (1993) who proposed a procedure to evaluate the seismic performance of structures under mainshock-aftershock sequences. They assumed that the probability density function of interval times of mainshock are Weibull or exponentially distributed, and that the number and magnitude of aftershocks depend on the same attributes of the mainshock. They used this information along with other assumptions to simulate aftershock ground motions using a method called "duration-independent envelope function." More recently, Burton and Sharma (2017) studied the reduction in the collapse safety of reinforced concrete buildings that are already are in different damage states due to mainshock-aftershock sequences. They used the same suite of ground motion records for both mainshock and aftershock events but incrementally scaled up the records to capture various states of post-mainshock damage of buildings. Burton et al. (2017) studied the aftershock collapse vulnerability of buildings using different parameters such as mainshock intensity, engineering demand parameter response, and various physical damage indicators. They used a similar strategy as what was used in (Burton & Sharma, 2017) to simulate the mainshock-aftershock sequences.

Most recently, Shokrabadi & Burton (2018) studied the post-mainshock seismic response of buildings due to mainshock-aftershock sequences by assuming various damage limit states for buildings after a mainshock event. They considered time-dependent nature of the aftershock events using a Markov risk assessment framework. They went on to develop a framework to estimate financial losses due to sequences of mainshock-aftershock events wherein they considered uncertainties associated with the time-varying nature of aftershock events and various damage states of buildings after the mainshock.

Li and Ellingwood (2007) studied the effects of mainshock-aftershock sequences on seismic damage of steel frames and Wang et al. (2017) on concrete gravity dams. The latter study used as-recorded mainshock-aftershock earthquake sequences and examined the effects of the correlation between mainshock and aftershock records on the seismic response of dams.

Goda et al. (2015) used a dataset of as-recorded mainshock-aftershock events in Japan and examined the seismic responses of an SDOF system by considering the variability in nonlinear structural parameters. Goda & Taylor (2012) used both as-recorded and simulated mainshock-aftershock events to study the nonlinear responses of an SDOF system wherein simulated sequences of aftershocks were generated to compensate when data were lacking.

Ebrahimian et al. (2014) proposed a performance-based framework for an adaptive aftershock seismic risk assessment for buildings in a post mainshock environment. They used an epidemic-type aftershock sequence model to simulate the spatio-temporal evolution of aftershocks. Jalayer & Ebrahimian (2017) proposed a methodology for aftershock seismic risk evaluation of structures by considering both time-dependent rate of aftershock occurrence and uncertainties in building damage state due to a mainshock event. Jeon et al. (2015) developed a framework by first creating mainshock-aftershock sequences of earthquake records and then by analyzing several buildings to develop aftershock damage fragility curves given a range of mainshock damage states.

Nazari et al. (2015) proposed a framework to incorporate the aftershock hazard into a performance-based framework through analytical studies using structural modeling parameters obtained from publicly available data on wood frame buildings. They developed aftershock fragility curves using an incremental dynamic analysis (IDA) approach in which the sequences of mainshock-aftershock earthquake records were utilized.

Raghunandan et al. (2015) performed damage fragility assessment of ductile reinforced concrete buildings using mainshock-aftershock sequences. They considered a range of damage states due to mainshock events and studied the effects on post-mainshock damage and collapse vulnerability of buildings. Han et al. (2015) studied the effects of mainshock-aftershock sequences using synthetic aftershock records to evaluate damage vulnerability of buildings. Ruiz-Garcia and Aguilar (2015) studied the effects of near-fault mainshock-aftershock sequences on seismic risk assessment of structures assuming various damage states the buildings sustained due to mainshock events. Yue et al. (2014) assessed the collapse vulnerability of steel buildings due to mainshock-aftershock sequences.

3.3.2 The state of research

As can be noticed from the literature review presented in the previous section, there is a need for tools that enable structural engineers to select temporally hazard-consistent aftershock ground motion records so that mainshock-aftershock sequences can be generated for seismic risk assessment of different structural types. By delving into literature and pervious works on this topic, it becomes evident that there is yet no tool that is equivalent to $PSHA$ in terms of rigor for $APSHA$ and for the subsequent task of aftershock GMSSM. The present work will aim towards that direction by introducing a framework for generating a set of probabilistic aftershock hazard curves and eventually by applying/extending the GMSSM framework developed in Chapter 2 to aftershocks.

3.4 AN ALGORITHM FOR AFTERSHOCK PROBABILISTIC SEISMIC HAZARD ASSESSMENT (*APSHA*)

The algorithms and required ingredients to develop an aftershock probabilistic seismic hazard assessment ($APSHA$) framework can be found in (Yeo & Cornell, 2009) and (Li & Ellingwood, 2007). These works are extended herein to simulate a range of fault rupture scenarios in developing aftershock seismic hazard by considering a range of elapsed times from mainshock event.

Eq. (3.1) generates a time-dependent aftershock hazard curve for a number of seismic sources (Num_{source}) given the lower- and upper-bound magnitudes, m_l, and m_m, respectively:

$$\lambda(im,T) = \sum_{i=1}^{Num_{source}} \mu^*\left(t,T;m_{m,i}\right) \iint_{m_l r_l}^{m_m r_m} P(IM > im|m_i\,, r_i\,) f_{R_i\,|M_i}\,(r_i\,|m_i\,). f_{M_i\,(m_i\,)} dmdr \tag{3.1}$$

the m_l is set to be 5.20 and the m_m is set to be the mainshock magnitude, $\lambda(im,T)$ denotes the mean number of aftershocks in $[t,T]$ exceeding the ground motion intensity measure (im), t is the elapsed time from the mainshock and T is the time window, which is usually set to be 1 year. $f_{M_i\,(m_i\,)}$ is the probability density, and $f_{R_i\,|M_i}(r_i\,|m_i\,)$ is the source-to-site distance distribution conditioned on the source magnitude (m_i). The terms r_l and r_m are the lower and upper bounds for closest source-to-site distance distribution. $\mu^*\left(t,T;m_{m,i}\right)$ is the mean number of aftershocks with magnitude range of $[m_l, m_m]$ in the time interval of $[t,T]$ following a mainshock magnitude of m_m, which is defined as

$$\begin{aligned} \mu^*(t,T;m_m) &= \int_t^{t+T} \mu(t;m_m)d\tau \\ &= \frac{10^{a+b(m_m-m_l)} - 10^a}{p-1}\left[(t+c)^{1-p} + (t+T+c)^{1-p}\right] \end{aligned} \tag{3.2}$$

Note that in a generic California sequence, $a = -1.67, b = 0.91, p = 1.08$ and $c = 0.05$. Also, when $\mu^{*}(t,T;m_m) = \lambda_{o,i}$ Eq. (3.1) can be used for $(PSHA)$, where $\lambda_{o,i}$ is the mean annual frequency of total earthquakes in a specific magnitude interval for a given source.

The last term in Eq. (3.1) that needs to be defined is $P(IM > im|m_i\,, r_i\,)$, which can be computed using

$$P(IM > im|m_i\,, r_i\,) = 1 - \varphi(\frac{\ln(im) - \overline{\log(IM)}}{\sigma_{\ln(\mathrm{IM})}}|m_i\,, r_i\,) \tag{3.3}$$

Here $P(IM > im|m_i\,, r_i\,)$ is the conditional probability of exceedance of a given intensity measure (im) conditioned on a given $m_i\,, r_i\,.\,\overline{\log(IM)}$ and $\sigma_{\ln(\mathrm{IM})}$ denote the logarithmic median and standard deviation, which can be obtained from a ground motion prediction equation $(GMPE)$, and finally, $\varphi(.)$ represents a standard normal cumulative distribution.

Eq. (3.1) represents the temporal aftershock seismic hazard of a site for a range of rupture scenarios which dominate the hazard at that site. In earthquake engineering, a rupture can be represented by the properties of the rupture including the epicenter, length of rupture and also various properties of the fault. Magnitude (m) is one of the parameters that can be correlated well with the physical properties of the rupture and is, therefore, adopted herein as one of the main parameters representing the rupture scenario, which will be used to develop site specific hazard curves. Another term that is key to developing hazard curves is the closest distance from source to site and often is denoted as R_{rup} .

In order to develop time-varying aftershock hazard curves for any given site of interest, one would use a magnitude distribution function to simulate a range of magnitude at a specific interval of $[m_l, m_m]$. A magnitude cumulative distribution function is

`

$$F_M(m) = \frac{e^{\beta m_m}(e^{-\beta m_l} - e^{-\beta m_a})}{(e^{\beta(m_m - m_l)} - 1)} \tag{3.4}$$

where β is a constant greater than zero which is related to the mainshock magnitude (m_m). For the mean and logarithmic standard deviation of β, one could use the following relationships developed by (Sunasaka & Kiremidjian, 1993),

$$\begin{gathered} E(\beta) = \exp(1.1130 - 0.135 M_m), \\ \sigma_{ln\beta|M_m} = 0.41. \end{gathered} \tag{3.5}$$

Sunasaka & Kiremidjian (1993) also studied the relationship between the number of aftershocks with magnitude greater than 3 and mainshock magnitude (M_m) whose mean and logarithmic standard deviation respectively are

$$\begin{gathered} E\big(N_a(3.0)\big) = \exp(-0.647 + 0.684 M_m), \\ \sigma_{lnN_a(3.0)|M_m} = 0.79. \end{gathered} \tag{3.6}$$

Having Eqs. (3.4) to (3.6), one could first draw sufficient number of realization samples for β and $N_a(3.0)$, then for any given β, randomly draw m_a samples from Eq. (3.4) and repeat this for the entire length of $N_a(3.0)$. Each time the procedure is repeated, the maximum m_a is restored and at the end a vector of m_a's realization samples can be obtained to be used in Eq. (3.1) to compute the hazard curve.

Another key parameter for computing the hazard curve using Eq. (3.1) is R_{rup}. It is assumed here that there is a correlation between m and rupture length (Wells & Coppersmith, 1994). In the present research, Table 2A in (Wells & Coppersmith, 1994) is used to get

$$\log(SRL) = -3.22 + 0.69M \tag{3.7}$$

where SL stands for surface rupture length. By plugging the magnitude realization samples derived by drawing samples from Eq. (3.4) into Eq. (3.7), one can obtain the realization samples for SRL. Following Figure 3.1, the realization samples for R_{rup} can be obtained using simple geometry relationships.

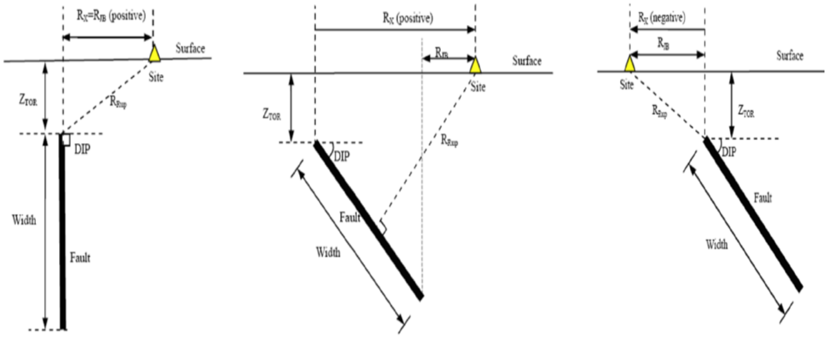

Figure 3.1. Computing the closest source-to-site distance given various rupture configurations. (adopted from CEE245 notes by Yousef Bozorgnia at UCLA)

In the next section, a practical example is provided to compute the mainshock and aftershock hazard curves for a hypothetical range of rupture scenarios using the information provided in this section.

3.5 *APSHA* FOR A HYPOTHETICAL RANGE OF RUPTURE SCENARIOS

3.5.1 A segmental rupture scenario

A hypothetical site in the city of Los Angeles, CA (LONG -118.43 LAT34.053) with average shear-wave velocity for the upper 30 m depth of $760\ \text{m/sec}$ and a depth to a $2.5\ \text{km/sec}$ shear-wave velocity horizon of $z_{2.5} = 1$ km has been chosen. For defining the seismicity for this site, a hypothetical range of faults with arbitrary dip angles (see definition in Figure 3.1) are picked. By using the sampling procedure that was laid out in section 3.4, and assuming an interval of $[5.5, 8]$ and $[5.2, 7]$ for the mainshock and aftershock magnitudes, respectively, the magnitude and closest source-to-site distance distributions to define the mainshock and aftershock seismic hazards for the given site are computed.

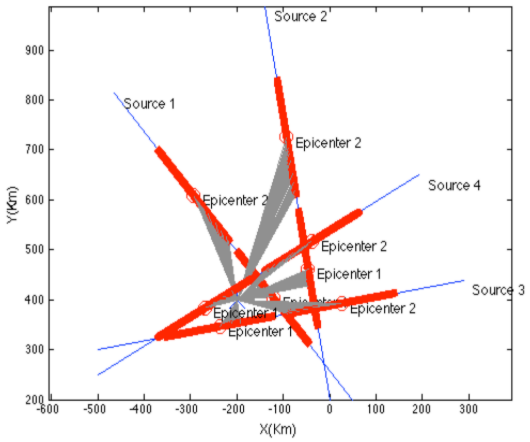

Figure 3.2. Source and rupture definition for a range of aftershock events.

Example results are shown in Figure 3.2, which displays a hypothetical representation of sources along with a set of different rupture scenarios with given rupture epicenters for an aftershock event. Here, it was assumed that the aftershock events are initiated from the same rupture zone as for the mainshock. Moreover, the probability of fault rupture for each of the sources shown in blue is equal, which is 25% for each. The probability of each rupture along with a source is also set to be equal which is 50% for each epicenter. With these assumptions and given the sampled magnitudes, a range of rupture lengths can be derived, which is shown in red in Figure 3.2. Then, the closest source-to-site distance (R_{rup}) can be computed (shown in grey) and ultimately the distribution of R_{rup} can be obtained, which is now fully correlated with the magnitude distribution.

An example of a mainshock magnitude m and $R_{rup\,,Aftershock}$ distribution is shown in Figure 3.3. These examples are provided only as a demonstration, and the rest of distributions are omitted for brevity.

`

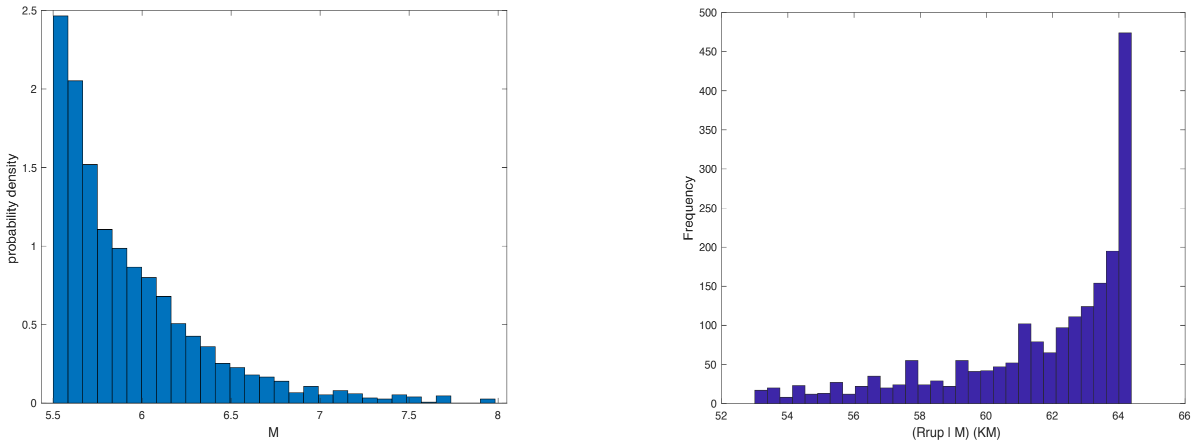

(a) (b)

Figure 3.3. (a) Mainshock magnitude distribution. (b) Aftershock $R_{rup\ ,Aftershock}$ distribution.

Figure 3.4 shows the cumulative distribution and histogram of the sampled aftershock magnitudes (m_a) with respect to m_m.

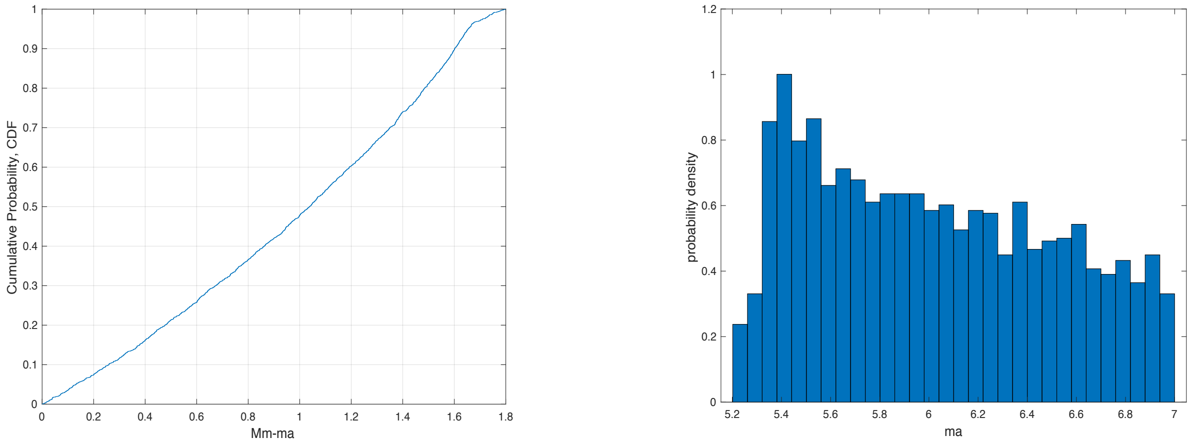

(a) (b)

Figure 3.4. (a) Cumulative distribution of the sampled aftershock magnitudes (m_a) with respect to the maximum mainshock magnitude (m_m). (b) Histogram of the sampled aftershock magnitude (m_a).

Having this information, one could use Eq. 3.1 to compute the hazard curves setting forth an intensity measure (IM) of interest, which, here, is set to be the spectral acceleration at multiple periods (SAT).

Figure 3.5(a) displays the hazard curves for SAT at multiple periods of vibration for both the mainshock and aftershock scenarios. Note that for both scenarios $T = 1$ year; however, in case of aftershock, since the time-varying nature of that was taken into account, an elapsed time of $t = 7$ days was considered to compute the $\mu^*\left(t, T; m_{m,i}\right)$ and ultimately to derive the hazard curves. It is also worth noting that in order to compute Eq. 3.3, the Boore & Atkinson (2008) GMPE was used to obtain $\overline{\log(IM)}$ and $\sigma_{\ln(\mathrm{IM})}$. Figure 3.5(b) shows the mainshock and aftershock uniform hazard response spectra (UHS) that corresponds to 2% probability of exceedance in 50 years, which were directly derived from Figure 3.5(a)

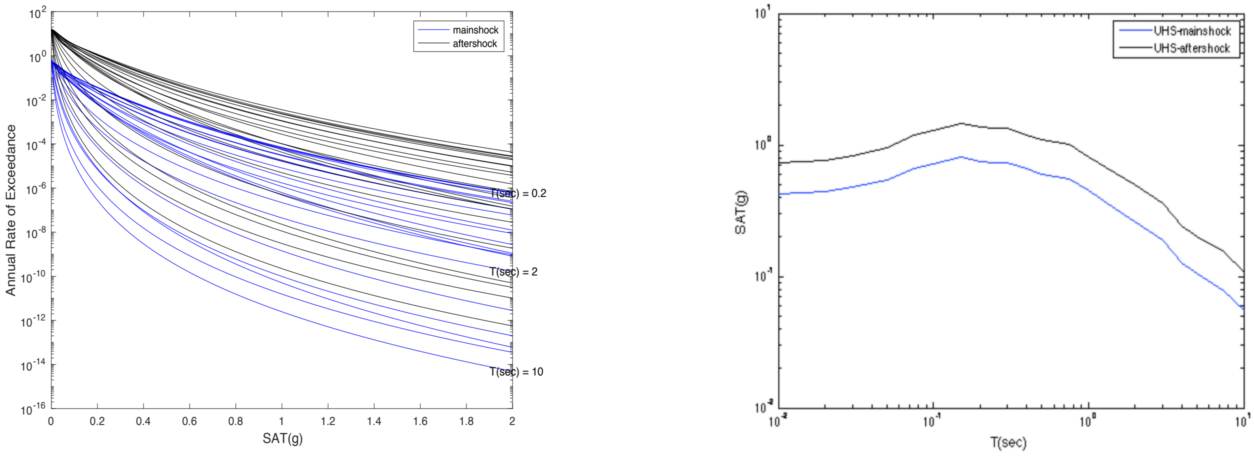
(a)

(b)

Figure 3.5. (a) Hazard curves for various $SATs$ for both mainshock and aftershock earthquake events assuming $T = 1\ year$ for both mainshock and aftershock events and $t = 7$ days for the aftershock event. (b) The mainshock and aftershock uniform hazard response spectrum (UHS) corresponding to 2% probability of exceedance in 50 years.

As can be easily observed from Figure 3.1(a), the aftershock hazard curves, which are shown in black, fall atop those of the mainshocks shown in blue, indicating that for a given SAT, they exhibit a higher rate of exceedance compared to the mainshocks. This is mainly due to setting the elapsed time as $t = 7$ days. During this timeframe, the frequency of aftershocks will be at its peak with a higher intensity and will eventually diminish as the elapsed time from the mainshock event increases. This also applies to UHS, so that the UHS corresponding to 2% probability of exceedance in 50 years is more intense for the aftershock (shown in black in Figure 3.5.b) than the mainshock (shown in blue). A similar conclusion was made in (Yeo & Cornell, 2009), however for a deterministic case.

The information developed here for the aftershock hazard curve will be used for the aftershock ground motion selection wherein the required conditioning intensity measures will be extracted from the aftershock-UHS developed here. To this end, and by assuming a structural fundamental period of $T1 = 1$ sec, the $SAT1$ will be used as the conditioning intensity measure (IM_j) for the case when a single-IM_j will be used. As assumed in Chapter 2, the lower and upper bound coefficients of 0.20 and 3.0 suggested by (Eads, et al., 2016) and (Chandramohan, 2016), will be used for multiplying $T1$, to obtain $T = 0.2$ sec and $T = 3.0$ sec, which will be used as IM_{j1} and IM_{j2} for the two- and multiple-IM_j cases.

Disaggregation plots demonstrating the contribution of all of the sources shown in Figure 3.2, to the conditioning $IM_j's$, namely $SA(T = 0.2$ sec), a $SA(T = 1.0$ sec), and $SA(T = 3.0$ sec), are presented in Figure 3.6. As seen, the rupture scenario that initiated from the epicenter 1 of source 3 has the highest contribution to all IM_j levels. After that, sources 1 and 4, which are both at epicenter 1, have the highest contribution, respectively. Looking back at the sources depicted in Figure 3.2, this is mostly due to R_{rup}, since an identical magnitude distribution at each epicenter was assumed.

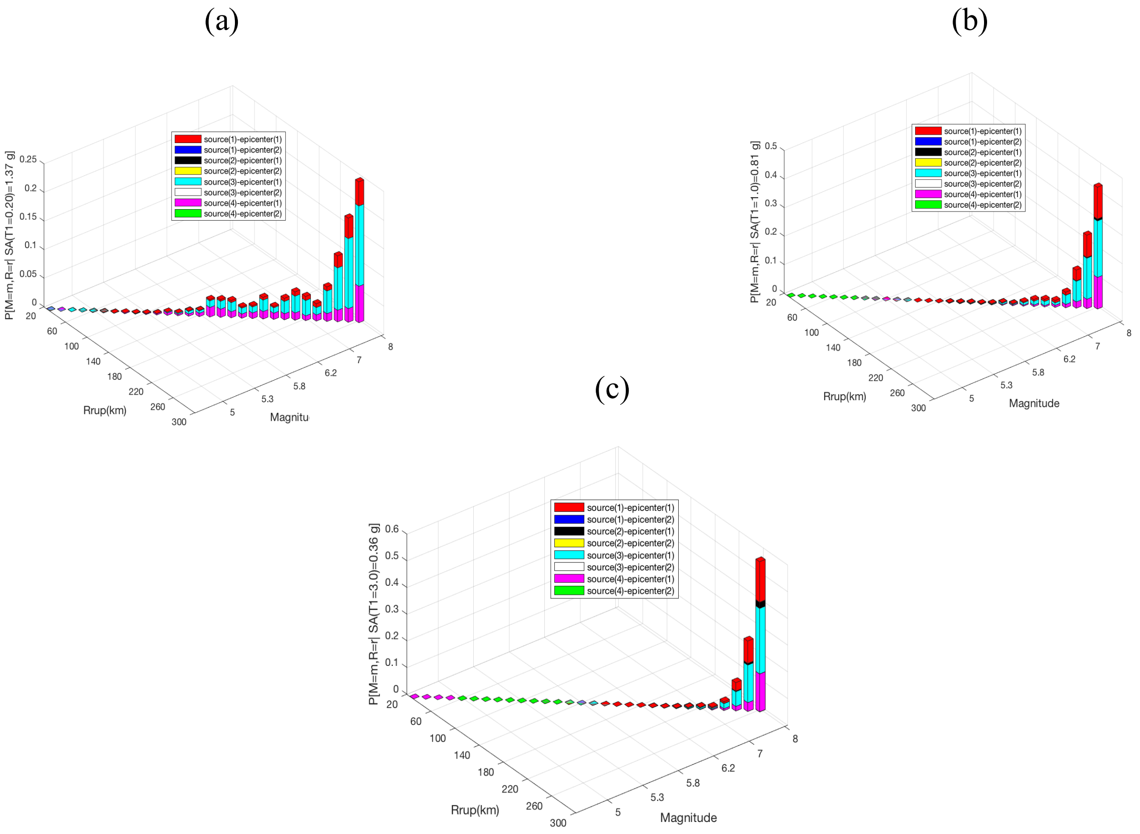

Figure 3.6. Disaggregation of seismic hazard. (a), (b) and (c) source contribution to $SA(T = 0.20 \text{ sec})$, $SA(T = 1.0 \text{ sec})$, and $SA(T = 3.0 \text{ sec})$, respectively.

3.5.2 A full-length rupture scenario

Everything that was carried out in section 3.5.1 is replicated here, however with an assumption that fault rupture can take place at any point along the fault length. Such full-length aftershock scenarios are depicted in Figure 3.7. The only difference, however, would be in the magnitude distribution which is different for the aftershocks compared to the mainshock. Moreover, according to this approach, magnitude and distance are independent of each other as distribution of distance was not obtained using the relationship that provides length of rupture as a function of magnitude, which was the case in the previous section.

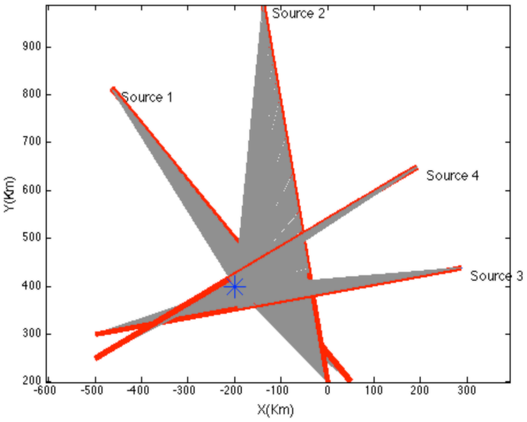

Figure 3.7. Source and rupture definition for a range of aftershock events.

Magnitude distribution remains the same as the section 3.5.1 case, however given a different layout for epicenters, R_{rup} distribution will change, which is the main reason of the subsequent difference in the hazard curve. Figure 3.8(a) displays the hazard curve for this rupture configuration and Figure 3.8(b) shows the UHS. As seen, the amplitudes of various curves in this case is a bit higher than those in Figure 3.5. Moreover, it can be noticed that the gap between the mainshock and aftershock UHS curves is wider in this case compared to Figure 3.5. The disaggregation plots are shown in Figure 3.9. It is evident that source 4 has an absolutely dominant contribution to all the IM_j levels, and that is mainly due to R_{rup}.

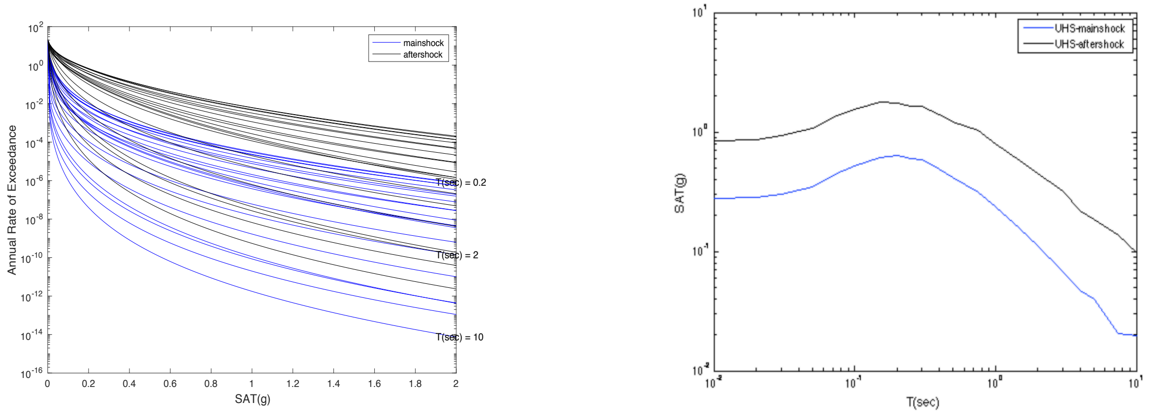
(a)

(b)

Figure 3.8. (a) Hazard curves for various $SATs$ for both mainshock and aftershock earthquake events assuming $T = 1$ year for both mainshock and aftershock events and $t = 7$ days for the aftershock

event. (b) The mainshock and aftershock uniform hazard response spectrum (UHS) corresponding to 2% probability of exceedance in 50 years.

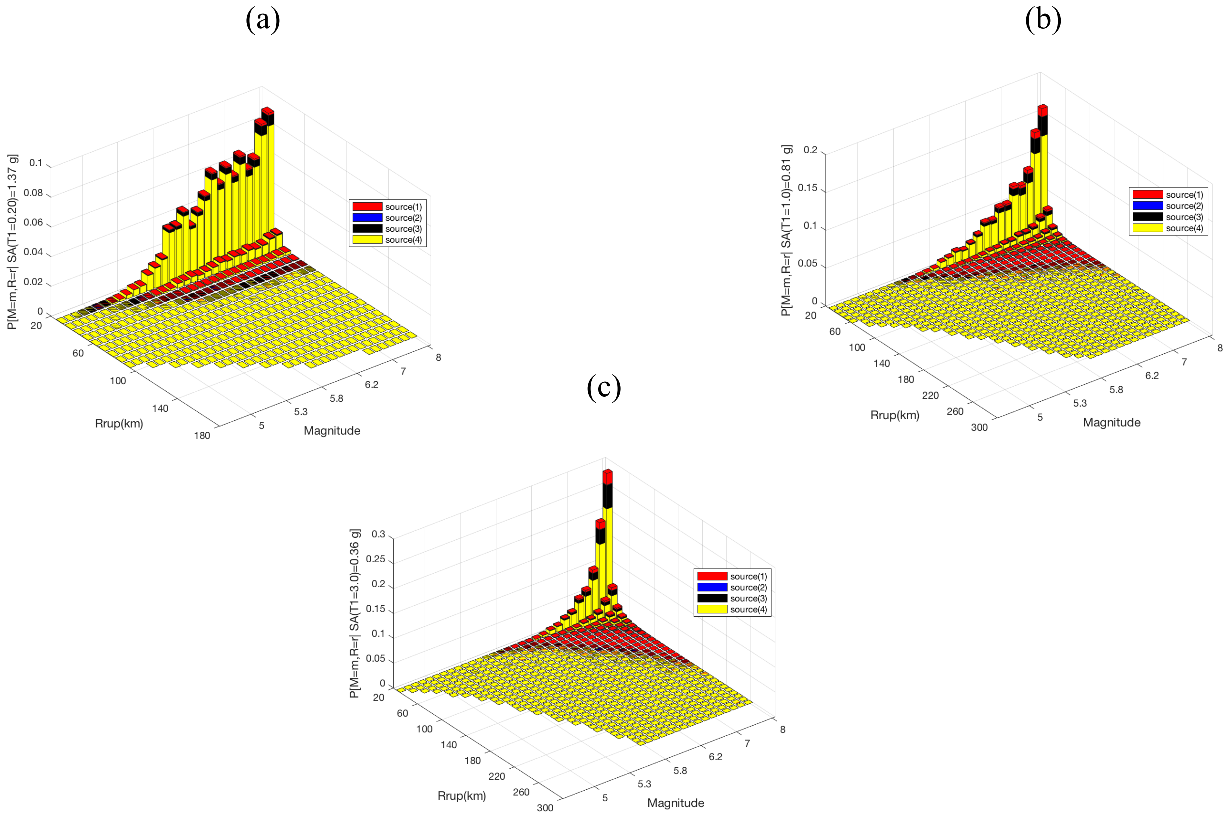
(a)

(b)

(c)

Figure 3.9. Disaggregation of seismic hazard: (a), (b) and (c) source contribution to $SA(T = 0.20 \text{ sec})$, $SA(T = 1.0 \text{ sec})$, and $SA(T = 3.0 \text{ sec})$, respectively.

It is worth noting that each fault in this case has a uniform rupture probability of 25%, which is even for all of the 4 sources.

3.6 AFTERSHOCK RECORD SELECTION, SCALING AND MODIFICATION

The comprehensive GMSSM algorithm developed in Chapter 2, will also be used here to select hazard-consistent aftershock GMs based a generalized conditional intensity measure ($GCIM$) approach with a set of different conditioning intensity measures ($IM_j's$) whose numeric values were computed in section 3.5.2 as $SA(T = 0.20 \text{ sec})$, a $SA(T = 1.0 \text{ sec})$, and $SA(T = 3.0 \text{ sec})$.

The same Los Angeles site (and properties) used in section 3.5.2 are used here. Also, the full-length rupture scenario discussed in section 3.5.2 is considered. For causal parameters, a magnitude interval of $[5.2,8]$, R_{rup} interval of $[0, 100]$ kilometers, and V_{s30} interval of $[400,1200]$ $\mathrm{m/sec}$, and maximum scale factor of 4 were used.

3.6.1 The single- IM_j approach

In this method, it is assumed that target realizations for various intensity measures ($IM_i's$) are drawn from a multivariate distribution and ground motions are selected from the $NGA-WEST2$ database (Bozorgnia, et al., 2014) to match the target IM_i realizations. As such, the aftershock ground motion records will be selected from a database of earthquake records consisting of both mainshock and aftershock records, however with respect to a set of different targets representing the characteristics of aftershock events.

Figure 3.10(b) displays the response spectra of the selected records as well as median, 16-, and 84-percent percentile of the selected records and those of the target $IM_i's$. Aftershock hazard-consistency is enforced by considering the contribution of various rupture scenarios to the IM_j, which is $SA(T = 1.0 \text{ sec})$, from the disaggregation plots that were discussed in the preceding sections. A 99-percent weight is assigned to SAT-based intensity measures, and therefore the rest of $IM_i's$ (i.e. Non- SATs) are assigned only a 1-percent weight. As such, this turns out to be a ground motion selection strategy that is solely based on response spectrum matching.

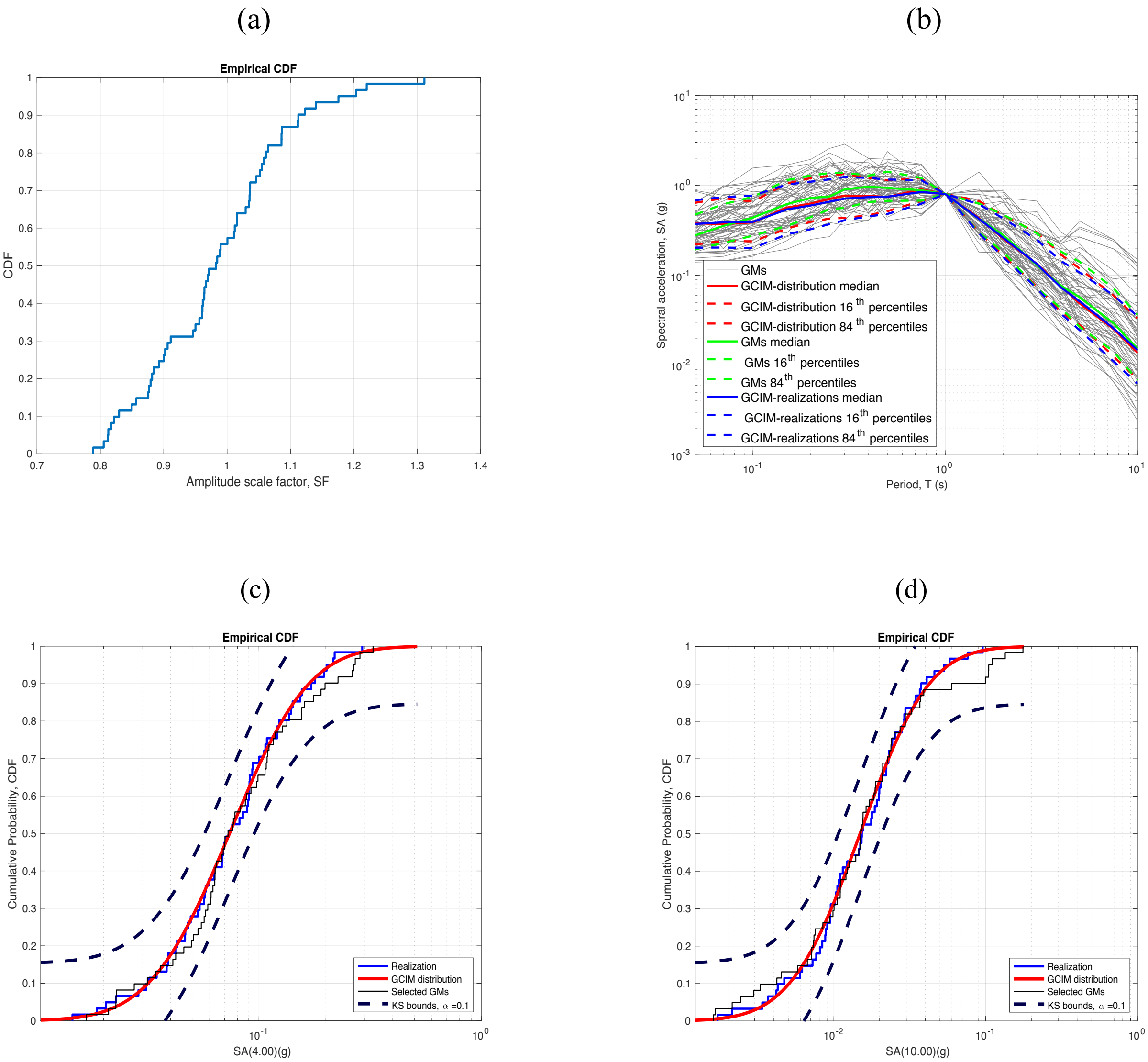
(a)

(b)

(c)

(d)

Figure 3.10. (a) Cumulative distribution (CDF) of amplitude scaling factor. (b) Conditional response spectrum conditioned on $SA(T = 1.0$ sec). (c) and (d) Empirical CDF of $SA(T = 4.0$ sec) and $SA(T = 10.0$ sec).

With the number of records set to 50 and given the emphasis to record selection based on response spectrum, as well as the amplitude scaling shown in Figure 3.10(a), near perfect matches can be seen in all of the plots in Figure 3.10. Figure 3.10(b) shows that the statistics of the selected records (shown in green) closely match those of the realization targets (shown in blue). Figure 3.10(c) and Figure 3.10(d) show that there is a good agreement between the empirical cumulative distribution of selected records shown in black and those of the realization targets shown in blue, for $SA(T = 1.0 \text{ sec})$ and $SA(T = 10.0 \text{ sec})$.

3.6.2 The two-IM_j approach

In an effort to select ground motions to be hazard-consistent, two conditioning intensity measures—namely, $SA(T = 0.20 \text{ sec})$ and $SA(T = 3.0 \text{ sec})$—will be used as $IM_j's$. Emphasis here is again given to spectrum matching just like the selection based on single$-IM_j$ conditioning approach discussed earlier.

Figure 3.11(b) shows that the statistics of the selected records conditioned on two $IM_j's$ shown in green, match those of the target shown in blue, with a little bit of amplitude scaling, of course, which is shown in Figure 3.11(a), proving that the algorithm resulted in a hazard-consistent suite of ground motion records based on the $GCIM$ approach. Figure 3.11(c) shows the cumulative distribution of $SA(T = 7.50 \text{ sec})$ shown in black which is in good agreement with target shown in blue. Herein, a non-SAT target intensity measure is included as well, which is the significant duration, $Ds575$. As can be observed from Figure 3.11(d), even though, a smaller weight was assigned to $Ds575$ during the selection phase, a reasonable agreement was still attained with respect to the empirical distribution of the selected records and the target.

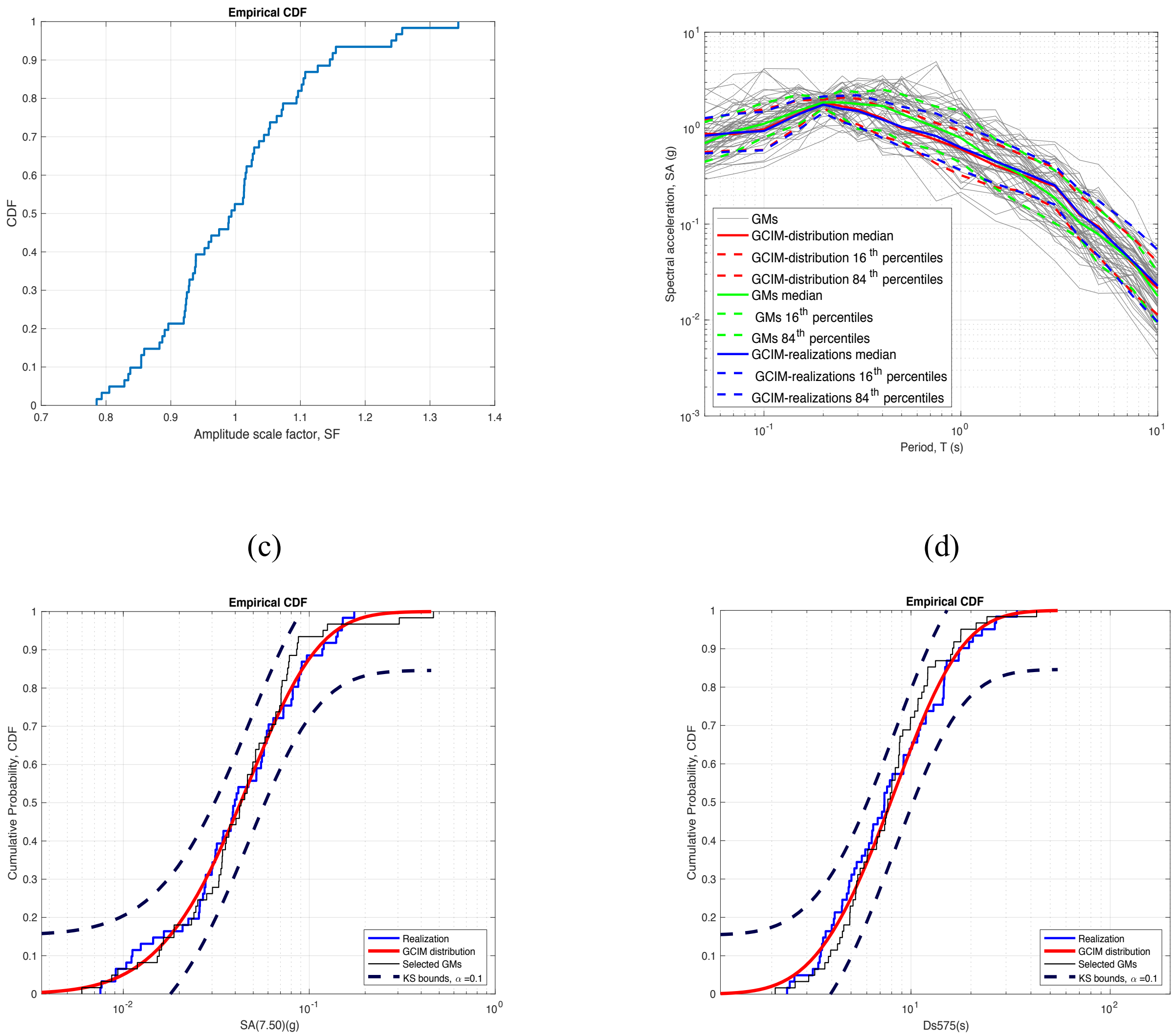

(a)

(b)

(c)

(d)

Figure 3.11. (a) Cumulative distribution (CDF) of amplitude scaling factor. (b) Conditional response spectra conditioned on $SA(T = 0.20 \text{ sec})$ and $SA(T = 3.0 \text{ sec})$. (c) and (d) Empirical CDF of $SA(T = 7.5 \text{ sec})$ and $Ds575(\text{sec})$.

3.6.3 The multiple-IM_j approach

Another conditioning criterion is used, herein, to select records matching targets conditioned on a range of intensity measures by setting the conditioning intensity measure as SA_{avg} as explained in Chapter 2. This is again an attempt to select records which have sufficient contents to excite a structure in multiple modes of vibration specially in case that the structure has undergone some level of damage. All the assumptions which were applied during the selection phase for the pervious sections, will be applied here too.

Figure 3.12(b) shows the statistics of the response spectra of the selected records shown in green which closely match those of the target shown in blue, with a little bit of amplitude scaling, of course (Figure 3.12(a)).

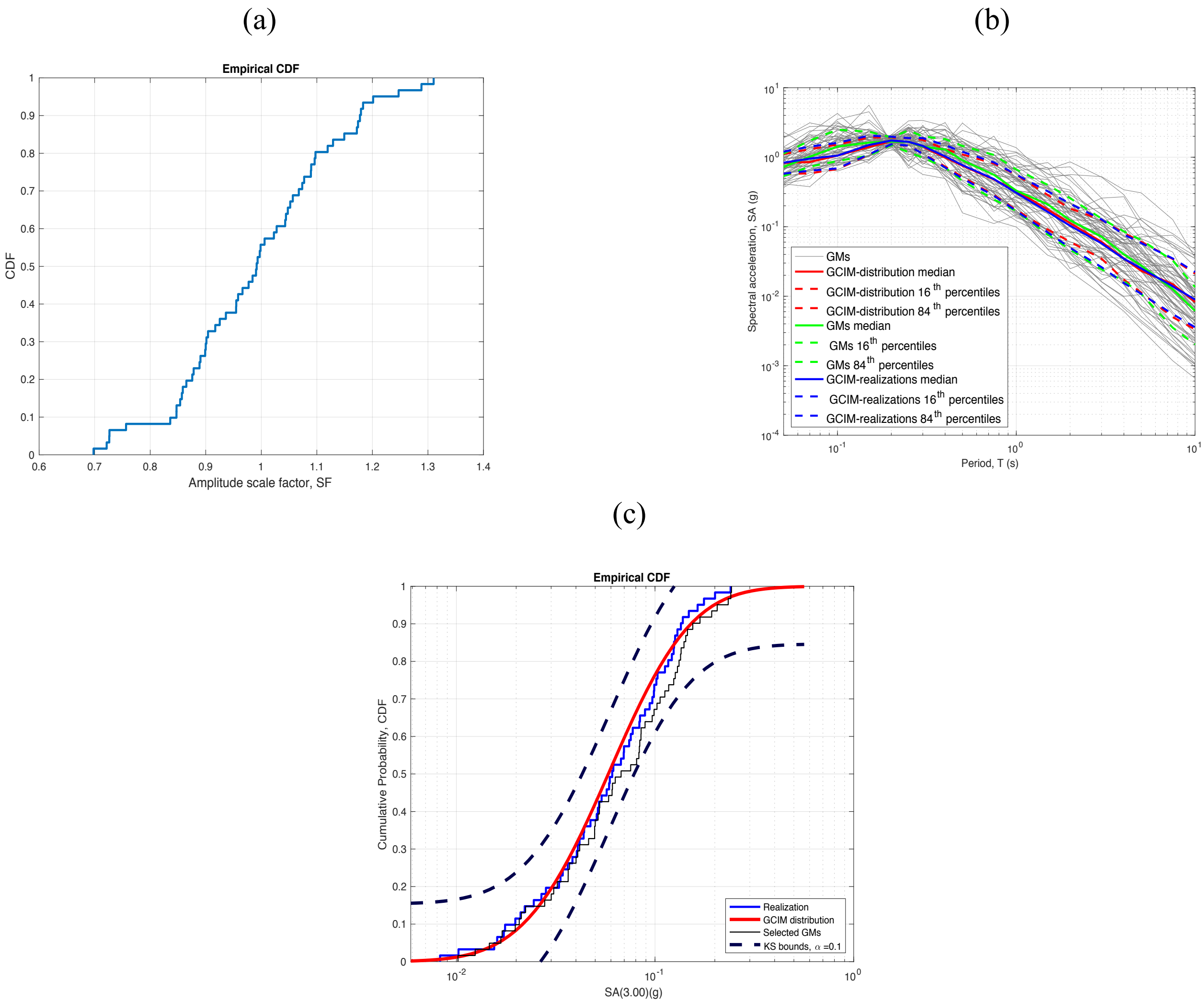
(a)

(b)

(c)

Figure 3.12. (a) Cumulative distribution (CDF) of amplitude scaling factor. (b) Conditional response spectra conditioned on SA_{avg} .(c) Empirical CDF of $SA(T = 3.0 \text{ sec})$.

Figure 3.12(c) shows the cumulative distribution of $SA(T = 3.0 \text{ sec})$ with a slightly different distribution for the selected records (shown in black) with respect to the target (shown in blue) which can still be deemed acceptable given the restrictions imposed on amplitude scaling factor, causal parameters, etc. during the selection phase.

3.7 DISCUSSION

Given a range of different parameters involved in the computation of time-varying aftershock hazard curves as laid out in section 3.5, a sensitivity analysis is carried out herein, to study the influence of each parameter on the seismic hazard, in a similar manner as the study by Yeo & Cornell (2009).

At first, a sensitivity analysis is carried out to study the effects of elapsed time (t) on the rate of exceedance of PGA, considering multiple levels of shaking. One can clearly notice from Figure 3.13 that for all levels of shaking, the annual rate of exceedance will decline gradually as the elapsed time increases. This indicates that, frequency of aftershocks is higher within days from the main event and as the time goes by, it declines which makes sense given past experiences with aftershocks. Moreover, as the level of shaking goes up, the annual rate of exceedance decreases indicating that stronger aftershocks are less frequent than the weaker ones. This can clearly be noticed from Figure 3.13 with respect to the hazard curves for different levels of $PGA(g)$.

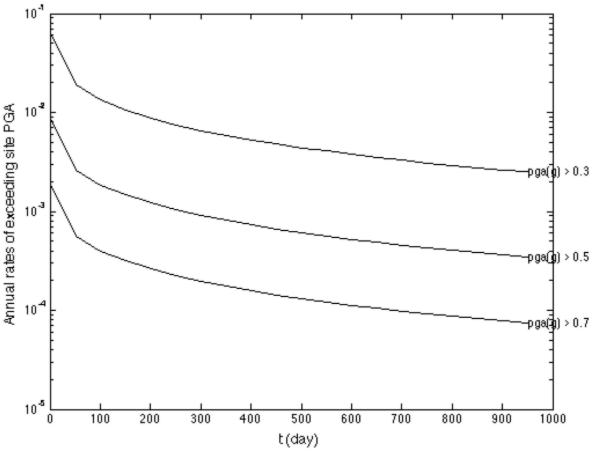

Figure 3.13. Sensitivity of temporal aftershock hazard curves for peak ground acceleration PGA (g) with various exceedance levels, as a function of elapsed time from the mainshock event, t (days).

Figure 3.14. shows the sensitivities of various sources' dip angles, which are laid out in a counter clockwise fashion from the x-axis to the right of the source which is atop all other sources, on the temporal aftershock hazard carve. Figure 3.14(a) shows sources with different dip angles, and Figure 3.14(b) shows the effects of considering different dip angles on the seismic hazard. As can be noticed from Figure 3.14(b), given the dip angles of various faults positioning from top to bottom in a counter clockwise fashion, the annual rate decreases which indicates a rise in the return period, as the fault tends to get farther away from the site (i.e. increase in R_{rup}), hence those faults tend to have less contribution to various levels of $PGAs$. As such, since sources with dip angles of 105 and 170 degrees are the farthest away from the site, thereby their contributions to the seismic hazard are the least.

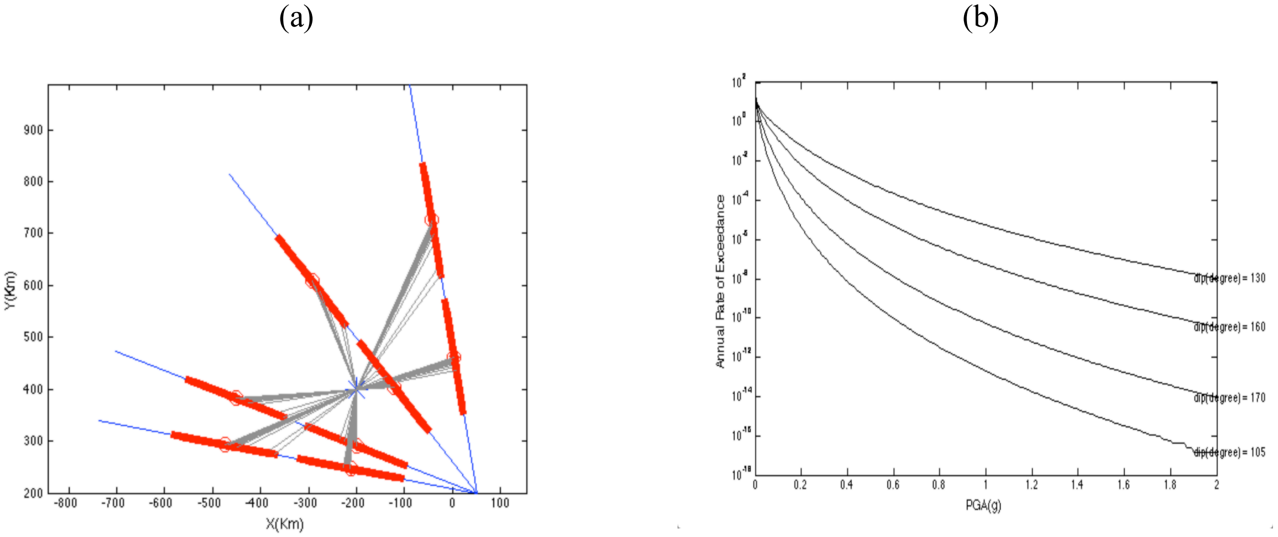
(a)

(b)

Figure 3.14. (a) Various source configurations with respect to the dip angle. (b) Effect of considering different dip angles on the aftershock hazard curve where $t = 7$ days.

Figure 3.15 shows the effects of considering various upper-bound aftershock magnitudes ($M_m's$) on the annual rate of aftershock exceedance for different PGA levels. As can be observed, as the M_m increases, the annual rate tends to increase as well, indicating that stronger aftershocks are more frequent within $t = 7$ days and their contribution to various levels of PGA is higher.

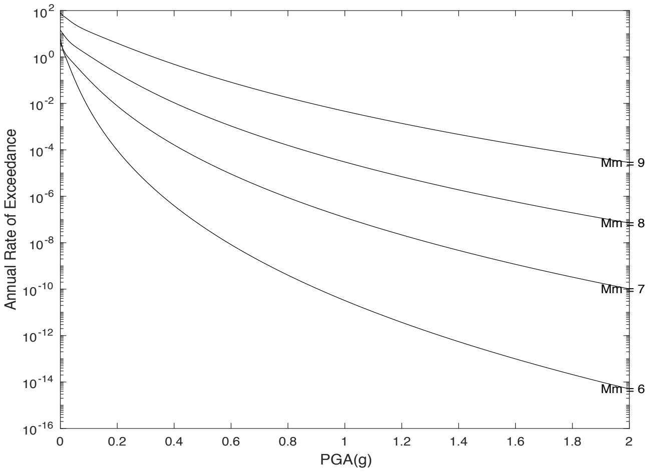

Figure 3.15. Sensitivity of temporal aftershock hazard where $t = 7$ days with respect to various upper bound aftershock magnitudes (M_m).

Figure 3.16 shows the influence of considering a set of different time windows ($T's$) on the mean number of aftershocks given a specific level of shaking (e.g. $PGA > 0.5g$) with respect to an increase in the elapsed time (t).

It is clear that aftershock hazard is higher, when T is longer. The difference between hazard given various $T's$ becomes more noticeable as t increases indicating that aftershocks are more frequent in a shorter elapsed time from the mainshock event, hence their frequency of occurrence will diminish as t increases. Therefore, at higher $t's$, difference between aftershock hazard for various $T's$ is more pronounced.

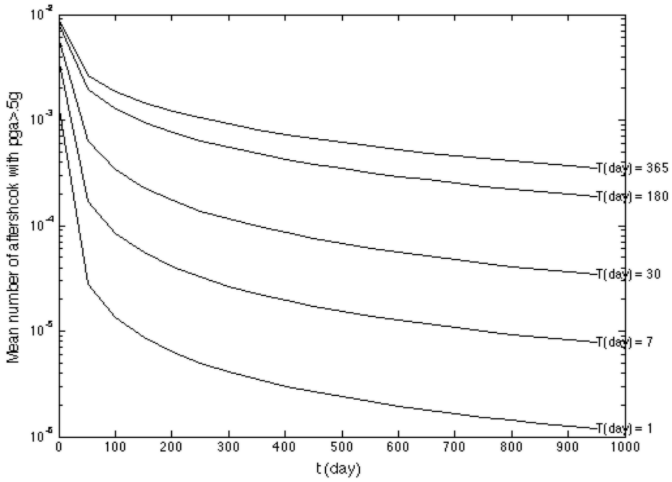

Figure 3.16. Sensitivity of considering effects of various time windows ($T's$) on the mean number of aftershocks given a specific level of shaking (e.g. $pga > 0.5(g)$) with respect to a range of elapsed times ($t's$) from the mainshock event.

Figure 3.17 shows the ratio of aftershock hazard to mainshock hazard with respect to different upper-bound aftershock magnitudes ($M_m's$), normalized based on the case of $M_m = 7$. The difference in the ratio is, to some extent, due to the difference between the mainshock and aftershock magnitudes which in case of aftershock is bounded by an upper-limit (e.g., M_m), which subsequently affects the R_{rup} distribution. Thus, at some point when the magnitude and R_{rup} for both mainshock and aftershock become identical, the ratio does not change as much which is clear from the figure since with the increase of pga the curves go flat from some point onward. Another potential cause of change in the ratio is the mean aftershock rate ($\mu^*(t, T; m_m)$) which was defined earlier. As can be noticed, for constant values of T and t , M_m is the main parameter changing the value of mean aftershock rate and therefore having influence on the ratios in Figure 3.17. This ratio shows also not to be that sensitive to PGA, from some point onward, as can be noticed from the figure.

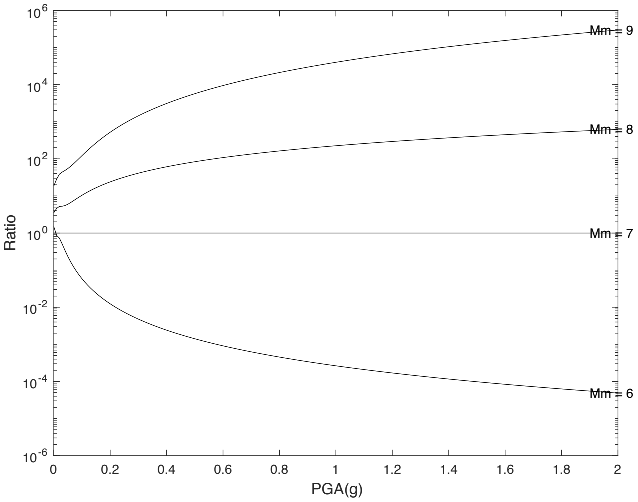

Figure 3.17. Ratio of aftershock hazard to mainshock hazard with respect to different upper-bound aftershock magnitudes ($M_m's$), given a range of $PGAs$.

Last but not the least, in order to render the effects of various ground motion selection strategies based a set of different conditioning criteria as discussed in section 3.6, Figure 3.18 displays the difference between conditioning median spectra conditioning on a range of $IM_j's$, with the UHS and the unconditional spectrum.

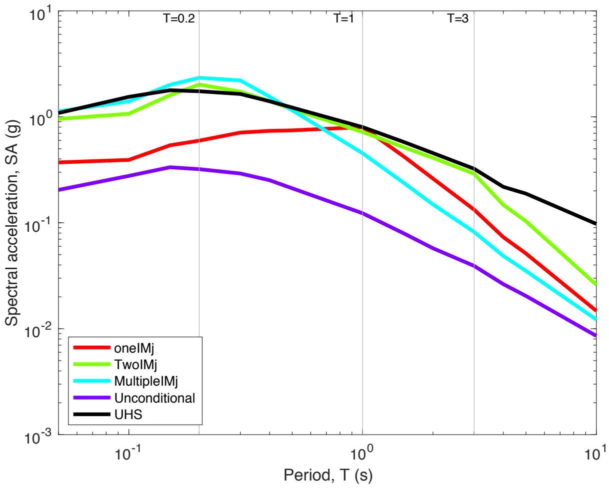

Figure 3.18. Comparison of the conditioning median spectra obtained from various methods of conditioning target generation, with the target spectrum obtained based on UHS.

`

As it can be observed from this figure, selecting earthquake records matching the UHS target spectrum (shown in black) will result in a very conservative set of records, simply because these records are going to be very intense at the entire set of structural periods of vibration. On the other hand, the response spectrum obtained from the new methods proposed earlier, as well as the response spectrum using an unconditional approach, all fall below the UHS at most period values. However, record selection based on an unconditional approach is highly non-conservative and produces hazard-inconsistent $SATs$ for any period of vibration, and therefore it is not recommended. The target conditioned on a single intensity measure (shown in red) produces a target that is hazard-consistent at a single IM_j (i.e. $SAT = 1$ sec) and falls below UHS at all of the other $SATs$. Here, it can be argued that records selected matching this target spectrum may not be sufficient if the structure goes into a highly nonlinear phase. Therefore, one would have to repeat this process for a few times to generate conditional targets using new $IM_j's$ each time, which then increases the computational burden significantly.

Selecting records matching a target to be hazard-consistent over a range of conditioning periods—which has been the case for the proposed two-IM_j and multiple-IM_j methods—seems to have mitigated the aforementioned problems. As it can be observed in Figure 3.18, the target spectrum conditioned on two-IM_j (shown in green) intercepts the UHS over a range of periods between IM_{j1} and IM_{j2}— here, $SAT(T = 0.2\text{sec})$ and $SAT(T = 3.0\text{sec})$, respectively—, which necessarily brackets and includes $SAT1$ ($SAT = 1.0\ sec$). Thus, the selected records matching this target *will* have sufficient intensity to excite the structure at its many modes (controllable by selecting the IM_{j1} and IM_{j2}) rather than only $T1$. This, then, obviates the use of multiple suites, thereby reducing the computational burden significantly.

The records selected based on multiple-IM_j conditioning (shown in cyan in Figure 3.18) produces but a more intense spectrum at a lower vibration periods than other methods, but a less intense spectrum around $SAT1$, eventually diminishing into the unconditional spectrum at longer periods.

3.8 CONCLUDING REMARKS

A new framework was proposed for an aftershock probabilistic seismic hazard assessment ($APSHA$). To this end, various hypothetical rupture scenarios were considered at a given site; and using a set of different relationships, aftershock hazard curves were computed in comparison with those of the mainshock for a set of different intensity measures. The time-varying nature of aftershock is one of the main parameters making the computation of aftershock hazard curves different than those of the mainshock, which was incorporated herein. Both uniform hazard spectrum (UHS) and disaggregation data were also generated. The obtained information was then used to select hazard-consistent aftershock ground motion records from a database of earthquake ground motion records.

Ground motions selection was carried out using $GCIM$ for a range of conditioning intensity measures to select records with sufficient contents to be able to excite a structure at its multiple modes of vibration and/or in case the structure experiences some level of damage. Given the fact that as-recorded aftershock ground motion earthquake records are limited, the present method paves the way to select identical hazard-consistent aftershock records from a database of both as-recorded mainshock and aftershock records.

Extensive sensitivity analyses were also carried out with respect to a set of different variables, which are key in performing $APSHA$. To this end, the effect of time window (T) as well as elapsed time (t) from the mainshock on the annual rate of aftershock hazard were thoroughly examined. The effect of upper-bound aftershock magnitude (M_m) on the ratio of mean number of aftershocks to mainshock was also studied for a range of hazard levels. Furthermore, the effect of source properties, such as dip angle on annual rate of aftershock hazard exceedance, was also studied and proper conclusions were drawn.

4 A PROBABILISTIC GM SELECTION ALGORITHM BASED ON SPECTRAL SHAPE AND A CASE STUDY ON REINFORCED CONCRETE STRUCTURES

4.1 INTRODUCTION

Due to the significant amount of variability in various aspects of earthquake engineering, a probabilistic approach should be utilized to estimate structural responses. The said variabilities could be due to source and fault rapture properties, site effects, ground motion attenuation characteristics, and so on and so forth. The presence of such variabilities makes it difficult to obtain an accurate suite of earthquake record to represent the seismicity of a given site. The number of records in the suite and the algorithm through which the records are selected play key roles in capturing and minimizing dispersions in estimated structural responses due to record-to-record variabilities in the selected ground motion suite.

It is also well established that depending on structural systems, different characteristics of ground motion records will be key in properly capturing the expected behavior of structures. These characteristics should be considered in the ground motion selection algorithm up-front, so that the selected earthquake records have sufficient content/features to probe and capture the variability in structural responses.

4.2 SCOPE AND MOTIVATION

One of the popular methods for ground motion selection is based on *target spectrum matching*. In doing so, a hazard-consistent target, which is usually a design spectrum has to be picked. GM records whose spectra closely match the target are then selected from an appropriately rich/large database of earthquake records. It should be noted that there is also some inherent variability in the adopted target, which is often neglected, and a median-based approach is adopted wherein the target variance is not considered. Moreover, a least-squares optimization approach is often utilized to select records within a reasonable confidence interval of the target spectrum. Due to the limited number of as-recorded ground motions, a perfect match is unlikely to be achieved even by using an aggressive amplitude scaling strategy. As such, the set of selected records typically do not represent the actual seismicity of the site.

The shape of a response spectrum for an earthquake record consists of numerous peaks and valleys, which represent the amplitude and frequency contents of the earthquake record. This could be taken as one of the factors as to how destructive a record could be. The spectral shape, however, is not often considered as an independent metric to represent an earthquake record. Hence, in engineering practice, the spectrum-matching is usually called record selection based on spectral shape, which is not quite the correct terminology.

In the absence of an independent metric to represent the effects of spectral shape of the selected ground motion records on seismic responses of structures, the present study aims at developing a probabilistic algorithm to select GM records based on spectral shape matching. To this end, a parameter is introduced to represent the spectral shape for which a hazard-consistent target will be developed using a probabilistic approach. The goal is then to select earthquake records whose spectral shapes, based upon the newly defined parameter, match those of the hazard-consistent target.

In order to study the relative consequences of GM records selected based on the newly defined parameter, namely the spectral shape, against those selected based on the common approach, namely response spectrum matching, a set of ductile and non-ductile reinforced concrete

(RC) buildings will be employed. These structures, which vary in height, will be analyzed using the GM suites compiled using different methods through nonlinear response history analyses ($NRHAs$) and incremental dynamic analyses ($IDAs$). These parametric studies are intended to unveil the effects of the two different GM selection strategies on estimate structural responses.

4.3 A REVIEW OF PRIOR STUDIES

4.3.1 Background

Previous works on independently considering the spectral shape as a metric in ground motion selection are not many. (Baker & Cornell, 2008) developed a vector-valued ground motion intensity measure metric consisting of other intensity measures such as spectral shape and also ε (i.e. the number of standard deviations by which each of the record's spectrum is away from the median target spectrum) in addition to spectral acceleration (SAT) in order to see the effects on the uncertainty in structural demands. (Baker & Cornell, 2005) used a vector-valued intensity measure metric consisting of SAT and epsilon (ε) and concluded that failing to consider ε which could be deemed as a proxy to spectral shape would underestimate the structural response, quite significantly. (Eads, et al., 2016) examined a set of different parameters that could represent the spectral shape and studied the effects on the collapse vulnerability of a given building with respect to those parameters. They showed that in case of using spectral acceleration at the fundamental period of the structure ($SAT1$) as the IM representative, records causing collapse at lower $SAT1's$ have a totally different spectral shape as opposed to others which wouldn't cause collapse until way higher $SAT1's$. $(\text{Kennedy, et al.}, 1984)$ studied relationship between $SAT1$ and an average-SAT for a lengthened period range with respect to the structural fundamental period , on nonlinear responses of structures. They concluded that when average-SAT is greater than $SAT1$, ground motions would need less scaling beyond the yield level to cause certain ductility demand in the structure as opposed to those records with smaller average-SAT.

(Sewell, et al., 1996) showed that damage potential of a record would be related to specific parameters such as spectral breath and slope, etc. which are obtained from spectral amplitudes at various frequencies of interest. They also concluded that for those records which were scaled to have the same $SAT1$, damage potential could be due to the slope of the spectrum at the fundamental period ($T1$). (Cordova, et al., 2000) considered $SATs$ at other periods longer than $T1$ in addition to $T1$ which ended up in reducing variability in structural demand response. (Vamvatsikos & Cornell, 2005) utilized one, two and three $SATs$ as well as a weighting sum average of $SATs$ normalized by $SAT1,$ for a period range of interest, in order to study the effects on structural demand responses. (Haselton, et al., 2011) studied the effects of spectral shape based on response spectrum matching approach on collapse probability of various types of structure and proposed to use the epsilon (ε) in lieu of the spectral shape. (Mousavi, et al., 2011) proposed another proxy to spectral shape called η which is a linear combination of ε's based on SAT and peak ground velocity. They showed that η was more effective than ε to predict the probability of collapse. (Bojórqueza & Iervolinob, 2011) concluded that using spectral shape as ratio of average $SATs$ in period interval of $[T1{,}2T1]$, to $SAT1$ could reduce dispersion in demand response by almost 70% compared to using $SAT1$ alone.

(Kohrangi, et al., 2017) employed a conditional IM_i target generation approach based on adoption of an average of multiple SATs at various periods as the conditioning intensity measure (IM_j) rather than a single conditioning IM_j. Ground motion records were subsequently selected to match the new conditioning target intensity measure (IM_i) and were utilized in $NRHA$s of structures which ensured increased sufficiency and efficiency in estimation of the demands.

(Kohrangi, et al., 2016) adopted a vector-valued probabilistic seismic hazard approach using several scaler and vector intensity measures such as $SATs$, ratio of $SATs$, and average of $SATs$ for a certain period range, in order to study the seismic response of buildings which were molded 3-dimentionally.

4.3.2 The state of research

Given a lack of state-of-the-art research on developing various metrices for ground motion spectral shape and considering its importance which was delineated in the handful number of works carried out in the past as reviewed in the previous section, the present study will try to shed some light on this topic. Hence, this research is proposed which is mainly based on (Chandramohan, 2016) who has developed a probabilistic framework to select ground motion earthquake records based on spectral shape and duration metrices. His work will be further extended, herein, by taking the spectral shape as an additional metric to SAT at multiple periods, to form a vector-valued intensity measure (IM). The elements of this IM are assumed to be correlated and by defining the median, standard deviation of those elements and also the correlation coefficients between them, a multivariate distribution will be defined. It is worth noting that the multivariate distribution will be conditioned on a single IM_j, namely $SAT1$.

Next, a desirable number of realization samples will be drawn from the multivariate distribution considering two sets of importance weight to be assigned to SAT and spectral shape metrices during the selection phase. Accordingly, first ground motion records will be selected by assigning larger weights to $SATs$. Next, they will be selected with respect to spectral shape metric so that this time a larger weight will be assigned to that. Using the selected records based on the aforementioned strategies, a set of different types of structural analyses will be conducted (e.g.

$NRHAs$ and $IDAs$) to compare seismic demand responses of a range of different ductile and nonductile RC buildings.

4.4 HAZARD-CONSISTENT GM SELECTION BASED ON SPECTRAL SHAPE

An algorithm is developed, herein, to select ground motion earthquake records to match a set of different hazard-consistent targets consisting of spectral shape as one of the intensity measure metrices (IM_i). To this end, the work by Chandramohan (2016) is extended to form a multivariate distribution of a set of different $IM_i's$ including the spectral shape as an independent metric. The algorithm will then enable users to draw a desirable number of realization samples from the marginal distribution of each IM_i. Hence, an empirical cumulative distribution of these realizations for each IM_i , including the spectral shape, can be obtained. The algorithm will be equipped with a novel ground motion selection, scaling and modification tool as discussed in Chapter 2, in order to select earthquake records whose empirical distribution of various $IM_i's$ match those of the hazard-consistent target drawn from a multivariate distribution. By assigning a set of different importance weight factors to different $IM_i's$ including the spectral shape, one could select records with respect to different contents of an earthquake record.

The IM vector representing the logarithmic of a set of different intensity measures (e.g. $IM_1, IM_2 \ldots$) is represented with

$$ln(IM) = \begin{Bmatrix} \ln(IM_1) \\ \ln(IM_2) \\ \vdots \\ \ln(IM_{n-1}) \\ \ln(IM_n) \end{Bmatrix}. \quad (4.1)$$

`

The distribution of each of the IM_i can be obtained from a respective ground motion prediction equation ($GMPE$) which can be represented with

$$\begin{aligned} \mu_{\ln(IM_i)|Rup} &= f(M|Rup, R|Rup, \Theta|Rup), \\ \sigma_{\ln(IM_i)|Rup} &= g(M|Rup, R|Rup, \Theta|Rup) \end{aligned} \tag{4.2}$$

where $\mu_{\ln(IM_i)|Rup}$ and $\sigma_{\ln(IM_i)|Rup}$ are the logarithmic median and standard deviation of the distribution and $M|Rup, R|Rup$ l and $\Theta|Rup$ are the magnitude, closest source-to-site distance and other site properties for a given rupture scenario, respectively.

Given the provided information, the covariance matrix can be obtained as

$$\Sigma_{\ln(IM)|Rup} = \sigma_{\ln(IM)|Rup}\rho_{IM|Rup}\sigma_{\ln(IM)|Rup} \tag{4.3}$$

where,

$$\sigma_{\ln(IM)|Rup} = \begin{bmatrix} \sigma_{\ln(IM_1)|Rup} & 0 & 0 \\ 0 & \ddots & 0 \\ 0 & 0 & \sigma_{\ln(IM_n)|Rup} \end{bmatrix} \tag{4.4}$$

and,

$$\rho_{IM|Rup} = \begin{bmatrix} 1 & \rho_{(IM_1,IM_2)|Rup} & \cdots & \rho_{(IM_1,IM_n)|Rup} \\ \rho_{(IM_2,IM_1)|Rup} & 1 & \vdots & \rho_{(IM_2,IM_n)|Rup} \\ \vdots & \vdots & \ddots & \vdots \\ \rho_{(IM_n,IM_1)|Rup} & \rho_{(IM_n,IM_2)|Rup} & \cdots & 1 \end{bmatrix} \tag{4.5}$$

where $\rho_{IM|Rup}$ is the correlation coefficient matrix whose off-diagonal elements (e.g., $\rho_{(IM_1,IM_2)|Rup}$) are the correlation coefficients between any given pair of $IM_i's$.

The conditional median vector consisting of the medians of different $IM_i's$ conditioning on an intensity measure (IM_j), which is chosen to be $SAT1$ herein, can be derived as

$$\mu_{\ln(IM)|\ln(SAT1),Rup} = \left\{ \begin{matrix} \mu_{\ln(IM_1)|Rup} + \rho_{(IM_1,SAT1)|Rup}\varepsilon_{\ln(SAT1)}\sigma_{\ln(IM_1)|Rup} \\ \mu_{\ln(IM_2)|Rup} + \rho_{(IM_2,SAT1)|Rup}\varepsilon_{\ln(SAT1)}\sigma_{\ln(IM_2)|Rup} \\ \vdots \\ \mu_{\ln(IM_{n-1})|Rup} + \rho_{(IM_{n-1},SAT1)|Rup}\varepsilon_{\ln(SAT1)}\sigma_{\ln(IM_{n-1})|Rup} \\ \mu_{\ln(IM_n)|Rup} + \rho_{(IM_n,SAT1)|Rup}\varepsilon_{\ln(SAT1)}\sigma_{\ln(IM_n)|Rup} \end{matrix} \right\} \tag{4.6}$$

where $\mu_{\ln(IM_1)|Rup}$, and $\sigma_{\ln(IM_1)|Rup}$, as an example, are the unconditional logarithmic median and standard deviation, obtained from Eq. (4.2) for a given rupture scenario; $\rho_{(IM_1,SAT1)|Rup}$ is the correlation between IM_1 and $SAT1$ and $\varepsilon_{\ln(SAT1)}$, which is the number of standard deviations by which $\ln(SAT1)$ of each record is away from $\mu_{\ln(SAT1)|Rup}$, is defined as

$$\varepsilon_{ln(SAT1)} = \frac{\ln(SAT1) - \mu_{\ln(SAT1)|Rup}}{\sigma_{\ln(SAT1)|Rup}} \tag{4.7}$$

Hence, the conditional covariance matrix can be derived as

$$\Sigma_{\ln(IM)|\ln(SAT1),Rup} = \Sigma_{\ln(IM)|Rup} - a_{\ln(IM)|Rup}{a_{\ln(IM)|Rup}}^T \tag{4.8}$$

where $\Sigma_{\ln(IM)|Rup}$ is the diagonal variance matrix of $IM_i's$ for a given rupture and $a_{\ln(IM)|Rup}$ is

$$a_{\ln(IM)|Rup} = \left\{ \begin{matrix} \rho_{(IM_1,SAT1)|Rup}\sigma_{\ln(IM_1)|Rup} \\ \rho_{(IM_2,SAT1)|Rup}\sigma_{\ln(IM_2)|Rup} \\ \vdots \\ \rho_{(IM_{n-1},SAT1)|Rup}\sigma_{\ln(IM_{n-1})|Rup} \\ \rho_{(IM_n,SAT1)|Rup}\sigma_{\ln(IM_n)|Rup} \end{matrix} \right\} \tag{4.9}$$

where ${a_{\ln(IM)|Rup}}^T$ is the transpose of $a_{\ln(IM)|Rup}$.

Having Eqs. (4.6) to (4.8), the conditional multivariate normal distribution of various $IM_i's$ can be defined for a single rupture scenario. For multiple rupture scenarios, however, the aforementioned equations can be defined as

$$\mu_{\ln(IM)|\ln(SAT1)} = \sum_{n=1}^{n_{Rup}} p_n \, \mu_{\ln(IM)|\ln(SAT1),Rup_n} \tag{4.10}$$

where n_{Rup} is the number of rupture scenarios contributing to the hazard-consistent conditional intensity measure (e.g. $SAT1$) for all the rupture cases and p_n is the probability associated with each rupture scenario, which can be obtained from hazard disaggregation information. Moreover, the hazard-consistent covariance matrix for a combination of rupture cases can be defined as

$$\Sigma_{\ln(IM)|\ln(SAT1)} = \sum_{n=1}^{n_{Rup}} p_n \left[\Sigma_{\ln(IM)|\ln(SAT1),Rup_n} + \Delta\mu_{\ln(IM)|\ln(SAT1),Rup_n} \Delta\mu_{\ln(IM)|\ln(SAT1),Rup_n}{}^{T}\right] \tag{4.11}$$

where

$$\Delta\,\mu_{\ln(IM)|\ln(SAT1),Rup_n} = \mu_{\ln(IM)|\ln(SAT1),Rup} - \mu_{\ln(IM)|\ln(SAT1)}. \tag{4.12}$$

4.4.1 An intensity measure for spectral shape

SA_{Ratio}, which is the ratio of the spectral acceleration at the first mode period to the average of spectral ordinates over a range of periods with an interval of $[T_{lb,}T_{ub}]$, is one of the metrics to represent the spectral shape, as was addressed in section 4.3.1 while reviewing previous studies. This metric is thus given by

$$SA_{Ratio}\left(T1, T_{lb,} T_{ub}\right) = \frac{SA(T1)}{SA_{avg}(T_{lb,} T_{ub})} \tag{4.13}$$

where $T_{lb,}$ and T_{ub} are the lower- and upper-bound periods, respectively; and $T1$ is the conditional period, which is often chosen to be the fundamental period of vibration of a given structure. $SA_{avg}(T_{lb,} T_{ub})$, which is the geometric mean of spectral ordinates over a range of periods with a period interval of $[T_{lb,} T_{ub}]$, can be computed using

$$SA_{avg}\left(T_{lb,} T_{ub}\right) = \left(\prod_{i=1}^{n} SA(T_i)\right)^{1/n} \tag{4.14}$$

which, in a logarithmic space, can be rearranged as

$$\ln(SA_{Ratio}) = \ln\left(SA(T1)\right) - \tfrac{1}{n}\textstyle\sum_{i=1}^{n} \ln\left(\, SA(T_i)\right). \tag{4.15}$$

Given these new terms, a new IM_i vector can be defined as

$$ln(IM) = \left\{\begin{array}{c} \ln(SAT_1) \\ \ln(SAT_2) \\ \vdots \\ \ln(SAT_{lb}) \\ \vdots \\ \ln(SAT_{lb}) \\ \vdots \\ \ln(SAT_{n-1}) \\ \ln(SAT_n) \end{array}\right\} \tag{4.16}$$

which can be reproduced after computing/adding the spectral shape metric (SA_{Ratio}) over the period interval of $[T_{lb,}T_{ub}]$, as follows

$$\ln(IM_{vector}) = \begin{Bmatrix} \ln(SA_{Ratio}) \\ \ln(SAT_1) \\ \ln(SAT_2) \\ \vdots \\ \ln(SAT_{lb}) \\ \vdots \\ \ln(SAT_{ub}) \\ \vdots \\ \ln(SAT_{n-1}) \\ \ln\,(SAT_n) \end{Bmatrix}. \tag{4.17}$$

Eq. (4.17) can be represented using an affine function. That is,

$$\ln(IM_{vector})|\ln\,(SAT1) = Aln(IM)|\ln\,(SAT1) + b \tag{4.18}$$

where *A* and *b* are defined as

$$A = \begin{bmatrix} 0 & 0 & \dots & -1/n & -1/n & \dots & -1/n & -1/n & \dots & 0 & 0 \\ 1 & 0 & \dots & 0 & 0 & \dots & 0 & 0 & \dots & 0 & 0 \\ 0 & 1 & \dots & 0 & 0 & \dots & 0 & 0 & \dots & 0 & 0 \\ 0 & 0 & \dots & 1 & 0 & \dots & 0 & 0 & \dots & 0 & 0 \\ \vdots & \vdots & \dots & \vdots & \vdots & \dots & \vdots & \vdots & \dots & \vdots & \vdots \\ 0 & 0 & \dots & 0 & 0 & \dots & 0 & 0 & \dots & 1 & 0 \\ 0 & 0 & \dots & 0 & 0 & \dots & 0 & 0 & \dots & 0 & 1 \end{bmatrix} \tag{4.19}$$

$$b = \begin{Bmatrix} SAT1 \\ 0 \\ \vdots \\ 0 \\ \vdots \\ 0 \\ \vdots \\ 0 \\ \vdots \\ 0 \end{Bmatrix}. \tag{4.20}$$

Given these, the conditional logarithmic median of IM_{vector} for a given rupture scenario is

$$\mu_{\ln(IM_{vector})|\ln(SAT1),Rup} = A\mu_{ln(IM)|\ln(SAT1),Rup} + b \tag{4.21}$$

and the conditional covariance is

$$\Sigma_{\ln(IM_{vector})|\ln(SAT1),Rup} = \mathrm{A}\Sigma_{ln(IM)|\ln(SAT1),Rup}A^T. \tag{4.22}$$

The conditional logarithmic median and standard deviation for any given IM_i (e.g. SAT_k) other than SA_{Ratio} in the IM_{vector}, can be obtained using

$$\begin{gathered} \mu_{\ln(SAT_k)|\ln(SAT1),Rup} = \mu_{ln(IM_{vector})|\ln(SAT1),Rup}(k) \\ \sigma_{\ln(SAT_k)|\ln(SAT1),Rup} = \sigma_{ln(IM_{vector})|\ln(SAT1),Rup}(k) \end{gathered} \tag{4.23}$$

the conditional logarithmic median for SA_{Ratio}, which is the first element of $\mu_{\ln(IM_{vector})|\ln(SAT1),Rup}$ to be obtained from Eq. (4.21), can be defined as

`

$$\mu_{\ln(SA_{Ratio})|\ln\,(SAT1),Rup} = \mu_{\ln(IM_{vector})|\ln\,(SAT1),Rup}(1) \tag{4.24}$$

and the conditional logarithmic standard deviation for that can be derived as follows, given that there is a correlation between the SAT ordinates over which the SA_{Ratio} is computed

$$\sigma_{\ln(SA_{Ratio})|\ln\,(SAT1),Rup}$$

$$= \sqrt{\sum_{i=1}^{n}(\frac{1}{n})^2\sigma^2_{\ln(SAT_i)} + \sum_{i=1}^{n}\sum_{j=i+1}^{n-1} 2\left(\frac{1}{n}\right) cov(\ln(SAT_i),\ln(SAT_j))\sigma_{\ln(SAT_i)}\sigma_{\ln(SAT_j)}} \tag{4.25}$$

where all the σ terms are based on a given rupture scenario and are conditioned on ln $(SAT1)$—e.g., $\sigma_{\ln(SAT_i)} = \sigma_{\ln(SAT_i)|\ln\,(SAT1),Rup}$, and so on and so forth. The standard deviation matrix can then be derived as

$$\sigma_{\ln(IM_{vector})|\ln\,(SAT1)} = \begin{bmatrix} \sigma_{\ln(SAT_1)} & 0 & 0 & 0 & 0 \\ 0 & \sigma_{\ln(SAT_2)} & 0 & 0 & 0 \\ \vdots & \vdots & \ddots & \vdots & \vdots \\ 0 & 0 & 0 & \sigma_{\ln(SAT_k)} & 0 \\ 0 & 0 & 0 & 0 & \sigma_{\ln(SA_{Ratio})} \end{bmatrix} \tag{4.26}$$

where, as before, all the σ terms are based on a given rupture scenario and are conditioned on $\ln(SAT1)$—e.g., $\sigma_{\ln(SAT_1)} = \sigma_{\ln(SAT_1)|\ln\,(SAT1),Rup}$, or $\sigma_{\ln(SA_{Ratio})} = \sigma_{\ln(SA_{Ratio})|\ln\,(SAT1),Rup}$ and so on and so forth. These terms were derived/defined previously. Having the covariance matrix as laid out in Eq. (4.22), the correlation coefficient matrix can be derived as follows

$$\rho_{(\ln(SAT_k),\ln(SA_{Ratio})|\ln\,(SAT1),Rup} =$$

$$\sigma^{-1}_{\ln(IM_{vector})|\ln\,(SAT1),Rup}\Sigma_{\ln(IM_{vector})|\ln\,(SAT1),Rup}\sigma^{-1}_{\ln(IM_{vector})|\ln\,(SAT1),Rup}. \tag{4.27}$$

4.5 DRAWING REALIZATION SAMPLES AND GM SELECTION

Given the conditional logarithmic median and standard deviation for each IM_i, and also the correlation between various $IM_i's$, all of which derived in the preceding section, a multivariate normal distribution can be fitted into the IM vector. Moreover, the marginal distribution of each IM_i, considering its respective correlation with the rest of $IM_i's$, can be obtained. One then can draw any desirable number of samples from the marginal distribution of each IM_i following the procedure laid out down below.

According to Bradley (2012), a two-level approach will be adopted herein to draw realization samples of each IM_i from the conditional multivariate distribution of various IM_i's, which was defined in the previous section. This is done first by obtaining a random rupture (Rup^{nsim}) from the disaggregation probability density function. Next, in order to draw samples from a multivariate distribution, first an uncorrelated standard normal random vector is defined (u^{nsim}) whose elements are drawn from a standard normal distribution, independently. Using this vector, the correlated vector can then be defined as

$$v^{nsim} = Lu^{nsim} \tag{4.28}$$

where L is the Cholesky decomposition of the correlation matrix, which is

$$\rho_{(\ln(SAT_k)|\ln(SAT1),Rup,\ln(SA_{Ratio})|\ln(SAT1),Rup)} = LL^T. \tag{4.29}$$

Using this, each of the realization sample for each IM_i can be obtained, as in

$$lnIM_i{}^{nsim} = \mu_{lnIM_i|Rup,\ln(SAT1)} + \sigma_{lnIM_i|Rup,\ln(SAT1)} v_i{}^{nsim} \tag{4.30}$$

where $v_i{}^{nsim} = v^{nsim}(i)$ is the *i*-th element in the v^{nsim} vector, and $Rup = Rup^{nsim}$.

4.5.1 Record selection

Once the properties of the hazard-consistent target distributions are obtained and the realization samples are drawn, a database of as-recorded GMs can be consulted to compile a suitable set. The aim is to select records for which the empirical distribution of various IM_i's match those of the realization targets drawn from the multivariate target distribution, so that one can claim that the empirical multivariate distribution of the selected records for various IM_i's matches those of the target. It is essential to note that, once a record is selected matching a realization target, that record will be removed from the database and will no longer be used.

To get started with this process, first, the entire records in the database should be scaled so that their response spectra at $T1$ match the conditioning $SAT1$, after restrictions on causal bounds have been applied. Note that, the value of SA_{Ratio} does not change with amplitude scaling, which can be easily inferred from Eq. (4.13).

4.5.1.1 Scaling

The amplitude scale factor is derived as follows

$$SF_m = \left(\frac{SAT1}{sat1^{m,unscaled}}\right)^{1/\alpha} \tag{4.31}$$

where $sat1^{m,unscaled}$ is the spectral acceleration at the fundamental period of the unscaled record. α is an integer, which, for intensity measures such as peak ground acceleration (PGA), peak ground velocity (PGV), and spectral acceleration (SA) that scale linearly with amplitude scale factor, is set to 1 (Bradley, 2012). The IM_i for each record is, therefore, scaled using

$$IM_i{}^{m} = IM_i{}^{m,unscaled}(SF_m)^{\alpha}. \tag{4.32}$$

4.5.2 Selection algorithm

The selection algorithm adopted herein is a least-squares approach suggested by (Bradley, 2012), which can be laid out as

$$r_{m,nsim} = \sum_{i=1}^{N_{IM_i}} w_i \left[\frac{lnIM_i{}^{nsim} - SF_{optimal}\, lnIM_i{}^{m}}{\sigma_{lnIM_i|Rup^{nsim},\ln\,(SAT1)}}\right]^2 \tag{4.33}$$

where,

$$SF_{optimal} = \exp\left(\frac{\sum_{i=1}^{N_{IM}}\left(\frac{\alpha_i}{\sigma_{lnIM_i|Rup^{nsim},\ln\,(SAT1)}{}^2}\right) ln\left(\frac{lnIM_i{}^{nsim}}{lnIM_i{}^{m}}\right)}{\sum_{i=1}^{N_{IM}}\left(\frac{\alpha_i}{\sigma_{lnIM_i|Rup^{nsim},\ln\,(SAT1)}}\right)^2}\right) \tag{4.34}$$

in which $lnIM_i{}^{nsim}$ is the logarithmic IMi of the realization target, $lnIM_i{}^{m}$ is the logarithmic IMi of the record, and $\sigma_{lnIM_i|Rup^{nsim},\ln\,(SAT1)}$ is the logarithmic standard deviation of the realization target. w_i is the normalized weight vector assigning importance weights to any desirable IM_i's to be considered during the selection phase. Other terms have already been defined in the text.

4.6 APPLICATIONS

In this section, the effects of two different methods of GM selection to match the spectral shape will be discussed. One of these is the traditional spectrum matching approach where a number of ground motions are selected to match the response spectrum realization samples drawn from a multivariate distribution of several IM_i's (see Eq. 4.17). In the traditional spectrum matching approach, which is adopted herein, the ground motions (GMs) are selected based on a generalized conditional intensity measure ($GCIM$) approach (see section 4.4), thereby they may still be deemed to have matched the spectral shape of the target response spectrum. That is because, based on the $GCIM$, ground motions records have all gotten the same $SAT1$ at the conditioning period ($T1$). Moreover, they are selected such that the empirical multivariate distribution of their spectra match those of the $GCIM$ theoretical target. As such, the effects of ε which can be deemed as one of the metrices representing the spectral shape of the ground motion records, has already been incorporated in defining the correlation coefficient matrix in the $GCIM$ which is one of the key parameters in defining the theoretical multivariate distribution. To render the difference between this method of spectral shape matching with another one, a second suite of earthquake records will be selected based on the procedure described in section 4.5. Accordingly, a GM suite will be selected whose empirical distribution of SA_{Ratio} matches the empirical target SA_{Ratio} distribution of the realization samples drawn from a multivariate distribution, as described in section 4.5. To study the corresponding effects of these two different GM suites on the seismic responses of structures, various types of ductile and non-ductile reinforced concrete (RC) structures will be analyzed next.

4.6.1 Ground motion records

In order to select ground motion records, a hypothetical site in the city of Los Angeles, CA (LONG-118.43; LAT34.053) with average shear-wave velocity for the upper 30 m depth of 760 m/sec, and a depth to a 2.5 km/sec shear-wave velocity horizon of $z_{2.5} = 1$ km, has been chosen. Hazard-consistency is enforced by considering a 2% probability of exceedance as the hazard level of interest for which the GM suites are selected. An IM vector consisting of only SAT

at multiple periods of vibration is adopted. The number of $SATs$ in the IM vector is set exactly the same as the number of $SATs$ for which hazard curves can be generated. Using the algorithm described in section 4.5, an IM vector corresponding to Eq. (4.17) is generated in which the intensity measures are SA_{Ratio} and multiple $SATs$ at various periods of vibration, respectively. The period interval $[T_{lb,}T_{ub}]$ to compute the SA_{Ratio} is chosen to be $T_{lb} = 0.20T1$, $T_{lb} = 3.0T1$ where $T1$ is the fundamental period of vibration for the specimen structure, based on (Chandramohan, 2016) and (Eads, et al., 2016).

Hereafter, following the algorithm described in section 4.5, two sets of earthquake records from the NGA-WEST2 database $(\text{Bozorgnia, et al.}, 2014)$ will be selected using a least-squares approach via Eq. (4.33). As such, one of the suites will be selected with more emphasis given to $SATs$ by assigning a 99% weight factor to the $SATs$ at multiple periods of vibration, which is distributed evenly among them. The remainder weight, i.e. 1%, is assigned to the SA_{Ratio}. The other suite will be selected by reversing the weight factors. Note that the scale factor during this phase (e.g., $SF_{optimal}$) is set to 1, so no scaling is required in order to make sure no improvement is enforced with respect to the spectrum matching approach, thereby isolating the effect of the traditional spectral shape matching approach. As for the causal parameters, the magnitude range of $M = [5\,,8]$, the closest source-to-site distance of $R_{jb}(km) = [0\,,100]$ and the $V_{s30}({}^{m}/_{sec}) = [300\,,1200]$ are adopted. The maximum scale factor is set to 4, and the number of records is set to 50. It is also worth noting that hazard-consistency is implemented by considering up to 2,000 rupture scenarios and their contributions to the conditioning intensity measure.

Figure 4.1(a) is response spectra of the records selected for a 4-story structure with $T1 = 1.3\ sec$. A 99% weight factor was assigned to the $SATs$ in the IM vector which results in a perfect match with respect to the statistics of the selected records shown in green as compared with those of the realization target shown in blue. Figure 4.1(b), on the other hand, shows a clear mismatch with respect to the other IM_i, namely, the SA_{Ratio}, which is the direct result of smaller weight factor (1%) which was assigned to it during the selection phase. This record set is deemed as the set to have been selected based on the traditional spectral shape matching approach as it is common.

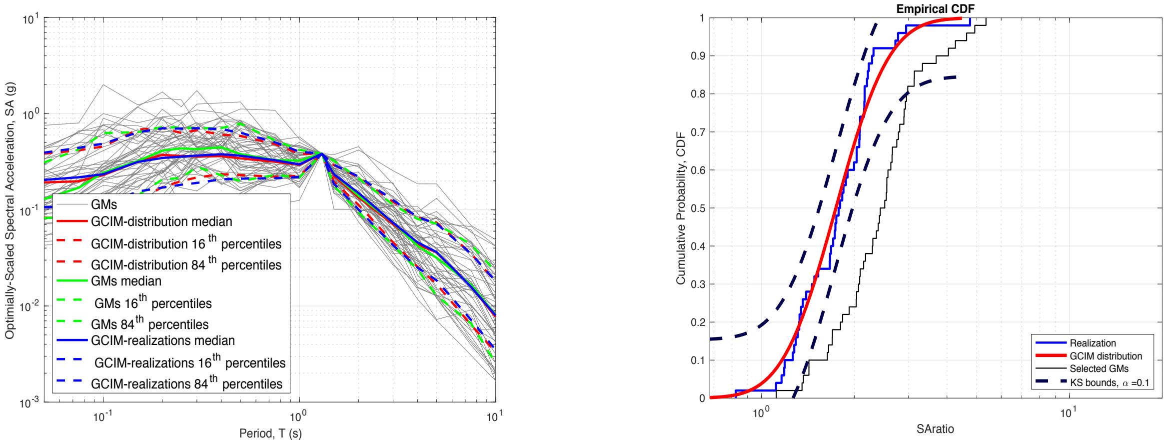
(a)

(b)

Figure 4.1. (a) Response spectra of the records selected based on 99% weight factor assigned to $SATs$. (b) Cumulative distribution of the $SA_{Ratio}{}'s$ of the selected records based on 1% weight factor.

The second suite of earthquake records is selected by assigning 99% importance weight to SA_{Ratio}. As such, 50 realization samples of SA_{Ratio}, whose empirical distribution is shown in blue in Figure 4.2(b), were drawn from the marginal target distribution of the SA_{Ratio} —i.e., based on a generalized conditional intensity measure ($GCIM$) approach (Bradley, 2012)—, the way described in section 4.5. The dashed curves are the confidence bounds. Next, earthquake records were selected such that the distribution of their $SA_{Ratio}{}'s$, shown in black in Figure 4.2(b), matches that of the target. As can be seen, a perfect match has been attained since the emphasis was given to the SA_{Ratio} matching during the selection phase. As such, the statistics of the selected record's spectra shown in green, in Figure 4.2(a), does not match those of the target shown in blue.

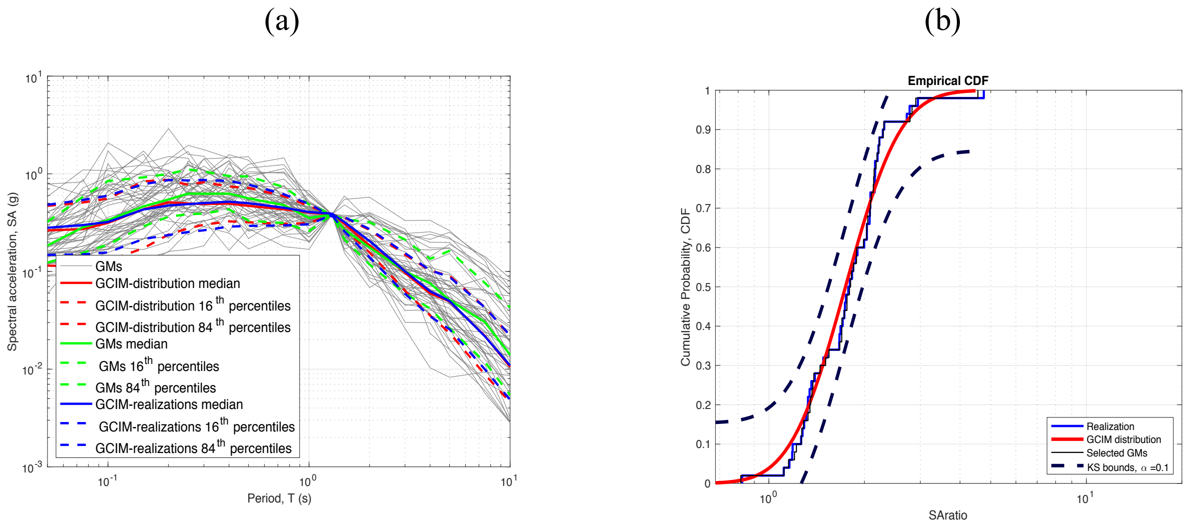

Figure 4.2. (a) Response spectrum of the records selected based on 1% weight factor assigned to $SATs$. (b) Cumulative distribution of the $SA_{Ratio}{}'s$ of the selected records based on 99% weight factor.

These ground motions suites were presented just as an example, herein, and for the sake of saving the space, the reminder of ground motions suites selected for the 8- and 12- story buildings to be used in this study, are omitted.

4.6.2 Ductile and Non-ductile reinforced concrete structures

Three buildings of various heights—i.e., 4, 8, and 12 stories—are modeled assuming either a ductile or non-ductile behavior so six structures are simulated, in total. Degree of non-ductility is enforced by ${}^{V_p}\!/_{V_n}$ where V_p is the shear corresponding to development of probable moment strengths and V_n is the nominal shear strength in accordance with ASCE/SEI 41-06 for low ductility demand. ${}^{V_p}\!/_{V_n}$ is set to one for the non-ductile buildings to be used in this study. The fundamental periods of vibration for these three buildings are $T1 = 1.30\ sec$, $T1 = 1.80\ sec$ and $T1 = 2.20\ sec$ for the 4-, 8- and 12-strory, respectively. The structures were modeled in OpenSees which is a finite element software and widely used for earthquake engineering simulations (McKenna, et al., 2000).

`

Properties of the ductile and no-ductile RC structures which are all modeled two-dimensionally are taken from (Galanis, 2014). Figure 4.4 shows the schematics of these three buildings. Figure 4.3 shows some of the elements and the material model which are utilized to simulate the ductile and non-ductile behaviors.

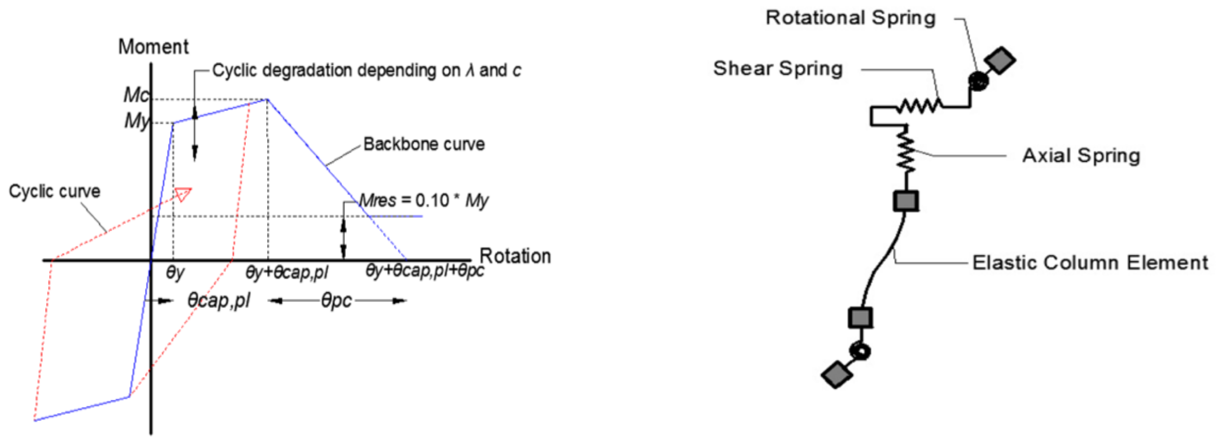
(a) (b)

Figure 4.3. (a) Ibarra backbone curve for the component model (b) zero length elements to be assigned to plastic hinges to simulate ductile and non-ductile behavior (in case of ductile members, the axial and shear springs are removed). Adopted from (Galanis, 2014).

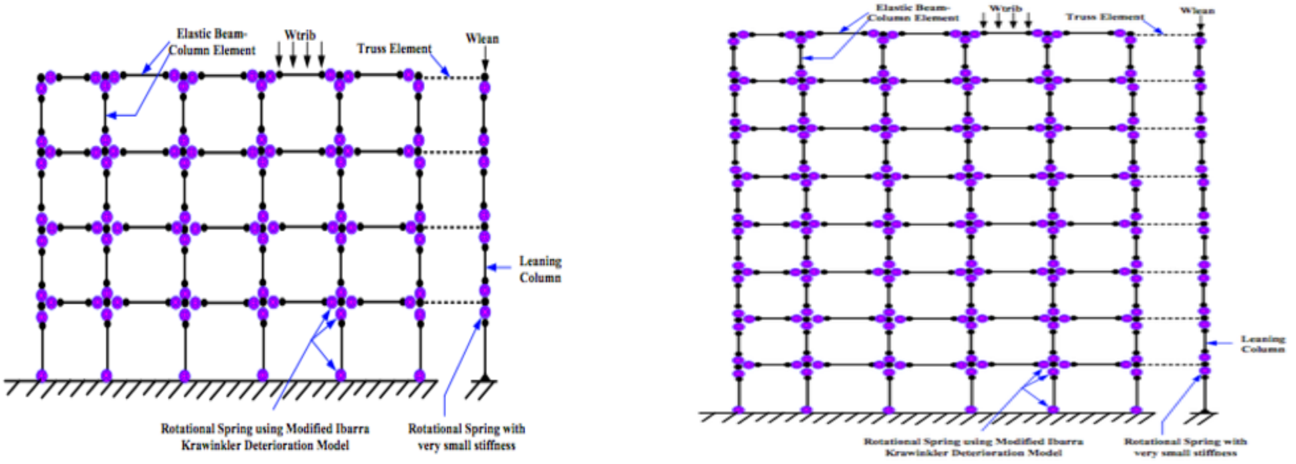
(a) (b)

(c)

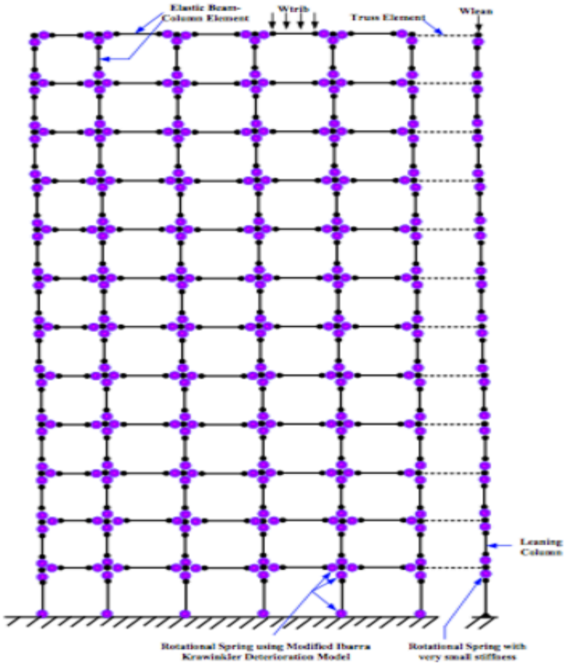

Figure 4.4. (a), (b) and (c) Schematic of a 4-, 8-, and 12-story building.

Figure 4.3(a) shows the backbone curve to be assigned to various plastic hinges in different elements, shown in purple in Figure 4.4, for various buildings based on (Ibarra, et al., 2005). To simulate the ductile behavior, an element such as the one shown in Figure 4.3(b), but without the shear and axial springs, will be assigned to plastic hinges within different columns and beams across multi levels for various buildings. As per non-ductile behavior, the element shown in Figure 4.3(b), including the shear and axial springs is assigned to plastic hinges whose properties to capture the shear and axial behavior are adopted from (Elwood, 2004). All the details regarding the structural elements being used in this study including the cross-sectional properties, definition of various parameters to be assigned to plastic hinges, and their properties both for simulating ductile and non-ductile behaviors have been adopted from (Galanis, 2014).

It is worth noting that given a very high computational cost of the nonlinear response history analyses for multiple suites of earthquake records as is the case for this study, a parallel computing approach is adopted. Therefore, all of the upcoming analyses are run on the $XSEDE$ supercomputing facilities—more specifically, the Stampede2 platform—, which is managed by the University of Texas at Austin. Stampede2 is a high-performance computational platform with 12,000,000 node-hour capacity, which makes it suitable for this study. Figure 4.5 demonstrates the schematics of the job submission procedures and the configuration of the platform. Figure 4.6 displays the algorithm utilized to run the required analyses on the Stampede2 platform.

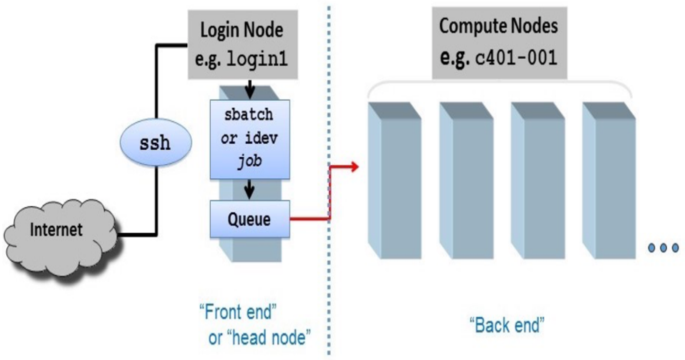

Figure 4.5. Schematic of the job submission process (e.g., batch submission) and the configuration of the supercomputing platform (adopted from https://portal.tacc.utexas.edu/user-guides/stampede2).

`

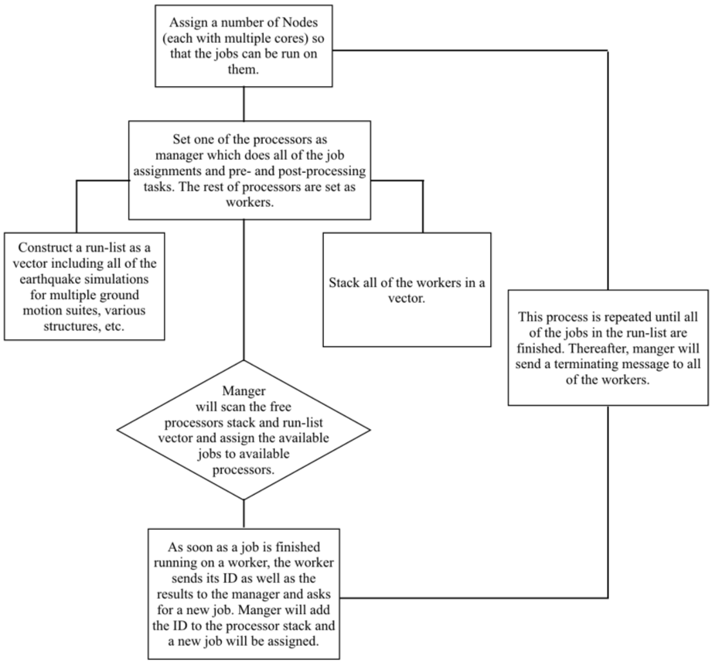

Figure 4.6. The parallel computing algorithm adopted in this study.

4.6.3 Analysis results

All of the structural models discussed in section 4.6.2 will be analyzed using the two suites of earthquake records, to be selected separately for each building type, considering two methods of the spectral shape matching as discussed in section 4.6.1. Two types of engineering demand parameters ($EDPs$), namely the inter-story drift ratio ($IDR(\%)$) and the peak floor acceleration (PFA) are set to be recorded for each $NRHA$. Figure 4.7 displays the results of the $NRHAs$ on an 8-story non-ductile building using a GM suite compiled by giving more emphasis to SA_{Ratio} during the selection phase. Note that, this is presented here only as an example. The statistics of the responses (shown in grey) for both IDR and PFA—namely, the median, and the 16- and 84-percentile are shown in red in both of the plots in Figure 4.7. Hereafter, these metrices will be used for comparison purposes.

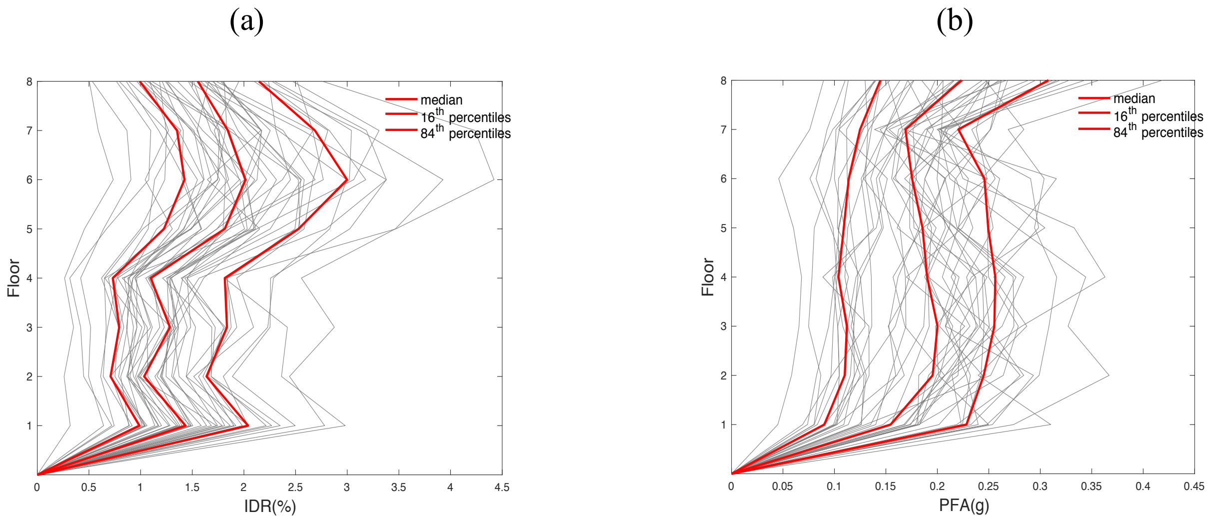

Figure 4.7. (a) and (b) $IDR(\%)$ and $PFA(g)$ responses for a 8-story non-ductile building using a ground motions suite selected based on giving more emphasis to SA_{Ratio} during the selection phase.

Figure 4.8 includes four plots which obtained by performing $NRHAs$ on a 4-story ductile and non-ductile RC structure using two different suites of earthquake records one of which selected based on the traditional spectral shape matching and the other one based on the SA_{Ratio} matching approaches, which is a novel (and arguably more appropriate) method of spectral matching, as discussed in section 4.5.

Figure 4.8(a) and Figure 4.8(b) show the comparison between the statistics of the $IDR(\%)$ obtained using the two different suites for a ductile and non-ductile building, respectively. Figure 4.8(c) and Figure 4.8(d) present identical things, but for the $PFA(g)$. As can be observed from all of the figures, using a suite selected based on the SA_{Ratio} matching approach, imposes higher median and percentile demands (see the blue lines) both for the $IDR(\%)$ and $PFA(g)$. This effect is more pronounced specially in the higher percentiles of the responses where the structure would already be in the nonlinear phase. Moreover, it can be found from Figure 4.8(a) and Figure 4.8(b) that using the suite selected based on the SA_{Ratio} matching approach in comparison with the one selected based on the traditional spectral shape matching (see the red lines), intensify the demands for the non-ductile case as opposed to the ductile one. It should also be noted from Figure 4.8 that, the soft story mode of failure seems to be dominant as the peak $IDR(\%)$ is at the first or second floor for the ductile and non-ductile scenarios, respectively.

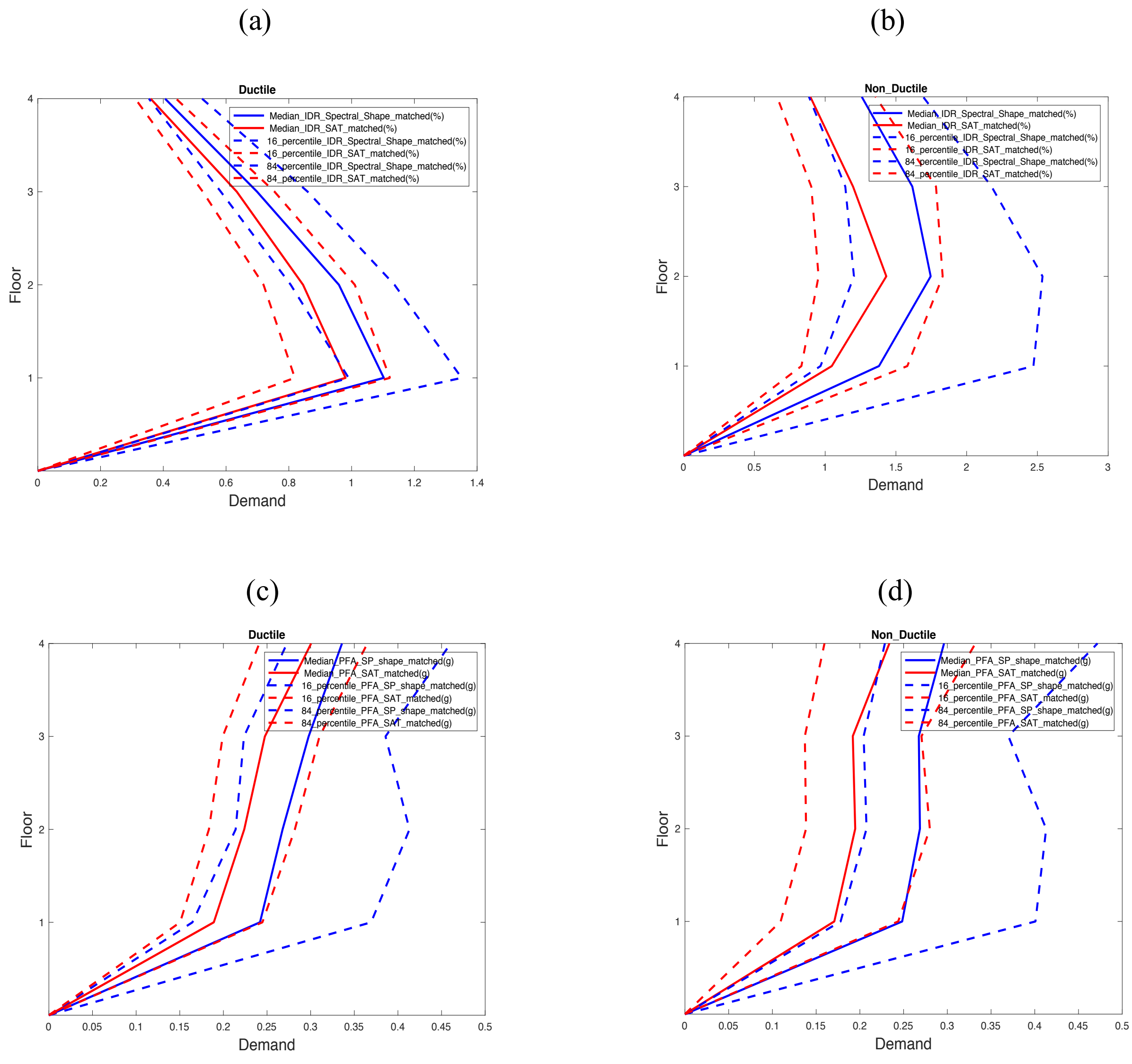
(a)

(b)

(c)

(d)

Figure 4.8. (a) and (b) Comparison between the statistics of the $IDR(\%)$ obtained using the two different suites for a ductile and non-ductile 4-story building, respectively. (c) and (d) Comparison between the statistics of the $PFA(g)$ obtained using the two different suites for a ductile and non-ductile building, respectively.

An identical task is performed on an 8-story RC building, considering both ductile and non-ductile behaviors and using the two suites of earthquake records selected for a 8-story RC building.

Figure 4.9 shows the results. It is evident from the plots of various demands presented in Figure 4.9 that the second ground motion set selected by giving more emphasis to SA_{Ratio} as the adopted metric of spectral shape, again imposes higher median and percentile demands (shown in blue) on the structure as opposed to the set selected based on the traditional way of spectral shape matching which is based on response spectrum matching (shown in red). This is more pronounced for the non-ductile building (shown in Figure 4.9(b)). However, the magnitude of this difference is not as high compared to the 4-story building. Moreover, it can be seen that that due to the contribution of the higher modes, the peak responses are shifted from the bottom floor to the upper ones which is in contrast with the 4-story.

(a)

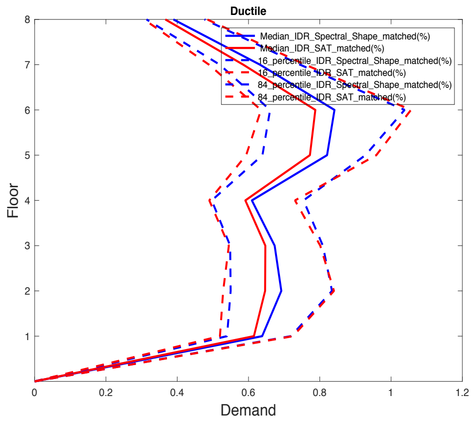

(b)

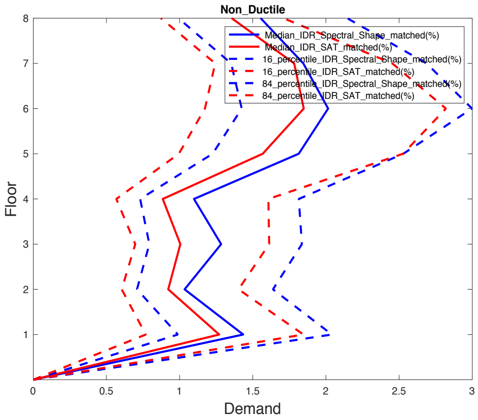

(c)

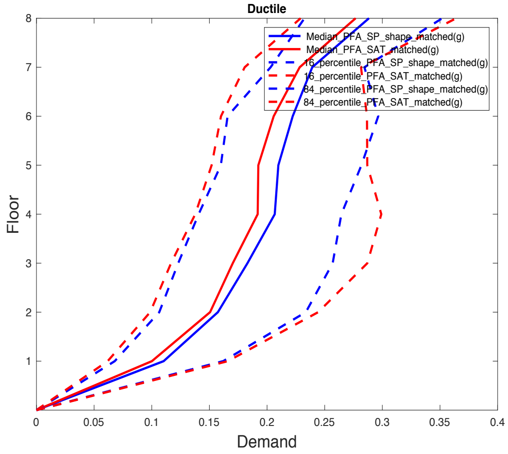

(d)

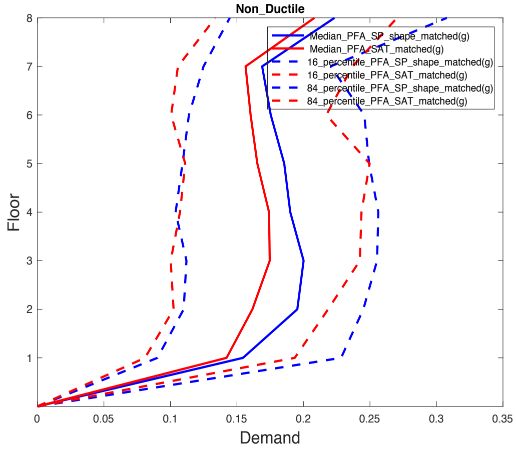

`

Figure 4.9. (a) and (b) Comparison between the statistics of the $IDR(\%)$ obtained using the two different suites for a ductile and non-ductile 8-story building, respectively. (c) and (d) Comparison between the statistics of the $PFA(g)$ obtained using the two different suites for a ductile and non-ductile building, respectively.

The last batches of analysis are carried out on a 12-story RC building considering both ductile and non-ductile behaviors and using the two suites of earthquake records selected for a 12-story RC building. The differences between demands obtained using the record sets produced by two different methods of spectral shape matching seems to be declined significantly compared to the 4-store case and quite a bit compared to the 8-story. It seems that as the building height goes up, this difference becomes less pronounced. One of the reasons for that would be that, as the number of stories and therefore the fundamental period goes up and multiple modes of vibration starts to contribute, other ground motion attributes, other than spectral shape begin to participate in capturing the seismic demand responses of the structure.

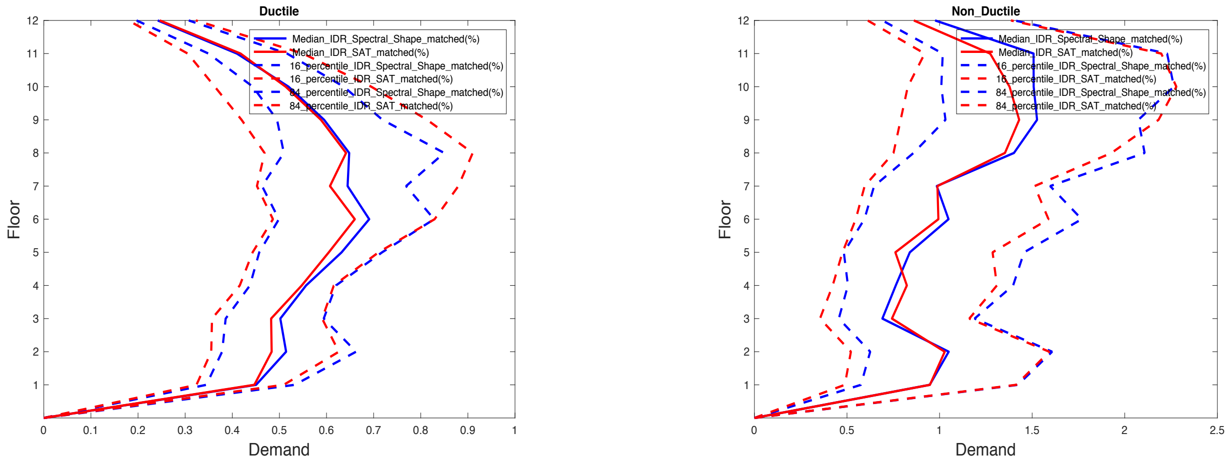
(a) (b)

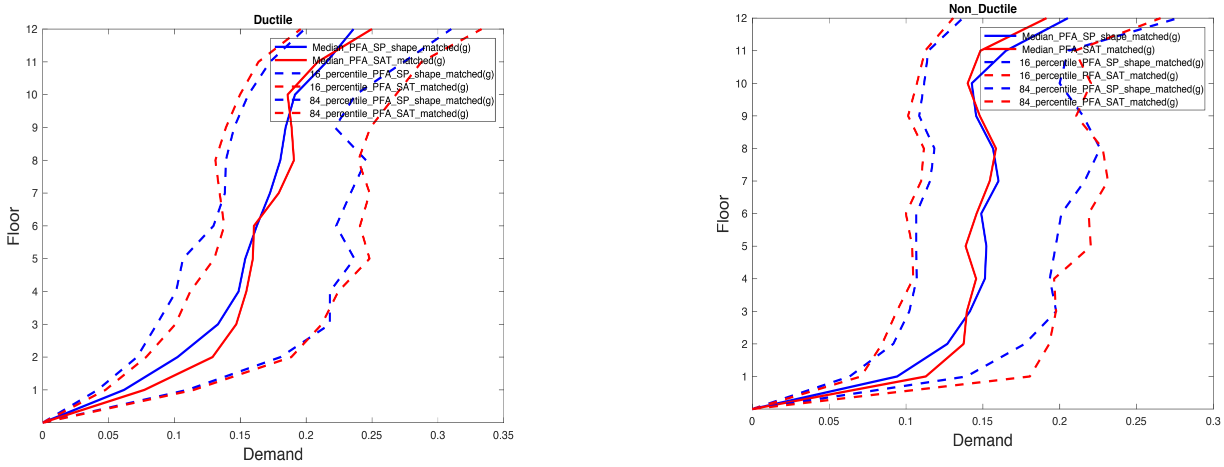

(c)

(d)

Figure 4.10. (a) and (b) Comparison between the statistics of the $IDR(\%)$ obtained using the two different suites for a ductile and non-ductile 12-story building, respectively. (c) and (d) Comparison between the statistics of the $PFA(g)$ obtained using the two different suites for a ductile and non-ductile building, respectively.

4.7 DISCUSSION

In this section, a set of incremental dynamic analyses ($IDAs$) are conducted using the two suites of ground motion records developed previously, one at a time. The goal is to study the effects of baseline ground motion suite to be used in IDA, on the damage fragilities given various levels of damage state. The effect will also be studied on the probability of collapse, separately.

The IDA (Vamvatsikos & Cornell, 2002) is a commonly used technique for this purpose. To perform IDA, one first needs to select a baseline suite of earthquake records consisting of several earthquake ground motion records. The ground motions in the suite are then scaled to various levels of shaking. The EDP response to be chosen to record the structural response is usually set as IDR. As such, when the ground motions in the suite are incrementally scaled up to higher levels of shaking, EDP increases accordingly. By scaling the ground motions to a higher level of shaking, one can potentially capture the state of structural collapse where for a small incremental increase in the level of shaking, the EDP response increases quite significantly.

Through performing the IDA, one can simulate the EDP distribution for various levels of shaking from which the damage fragility functions can be obtained assuming a range of damage limit states using

$$\text{Fragility} = \Phi\left(\frac{\ln(x/\theta)}{\beta}\right) \tag{4.35}$$

where, Φ represents a normal cumulative distribution, x is a damage limit state, θ is the median demand which is the peak inter-story drift ratio, and β is the logarithmic standard deviation of the peak inter-story drift ratio. The probability of collapse can also be obtained by fitting an empirical cumulative distribution function into the level of shakings causing the collapse (by setting the drift limit to 10%) assuming that all of the GMs in the suite have been scaled up to collapse. The IM representing the level of shaking is often picked as $SAT1$. In order to scale the GMs in the suite to a higher level of $SAT1$, it is common to use an amplitude scaling factor approach, such that the $sat1$ of each of the record in the site is scaled to match the $SAT1$.

IDA, which is based on the amplitude scaling of the earthquake records, does not make the earthquake records to be hazard-consistent for a given level of shaking to which the records have been scaled. This is the main drawback of IDA. In order to enforce the hazard-consistency for a level of shaking, other characteristics of the records—including frequency, duration, and cumulative characteristics —should also be hazard-consistent, instead of only being so for the spectral amplitude, as is the case with IDA.

To overcome this shortcoming of $IDA,$ Baker (2015) introduced a new way to derive fragility functions using a technique called "multiple-stripe analysis." According to this technique, a separate suite of hazard-consistent earthquake records is selected for each level of shaking. Although more efficient than IDA, this method has its own drawbacks. First, several suites of earthquake records need to be selected so that various states of damage can be captured, whereas in IDA only one baseline suite is required. Second, some of the earthquakes in multiple suites for different levels of shaking would be repetitive as some earthquakes can be hazard-consistent at multiple levels of shaking. This introduces some inconsistency/redundancy into the outcomes and complicate the interpretation of PBSA outcomes.

IDA is the method that is utilized throughout the present study. The baseline suites are selected according to section 4.6.1 with identical properties with the only difference in the hazard level. As such, a 50% probability of exceedance in 50 years is adopted as the hazard level and records are selected accordingly. As such, 25 earthquake records for each suite are set to be selected. The earthquakes selected for this hazard level are usually not that intense, so through IDA, and by scaling the records up, one can simulate various levels of structural damage quite accurately.

Figure 4.11 presents the damage fragilities at different states of damage for various types of structures. These are obtained one at a time using IDA, and by utilizing two sets of earthquake records for spectral shape matching purposes based on different methods as explained before.

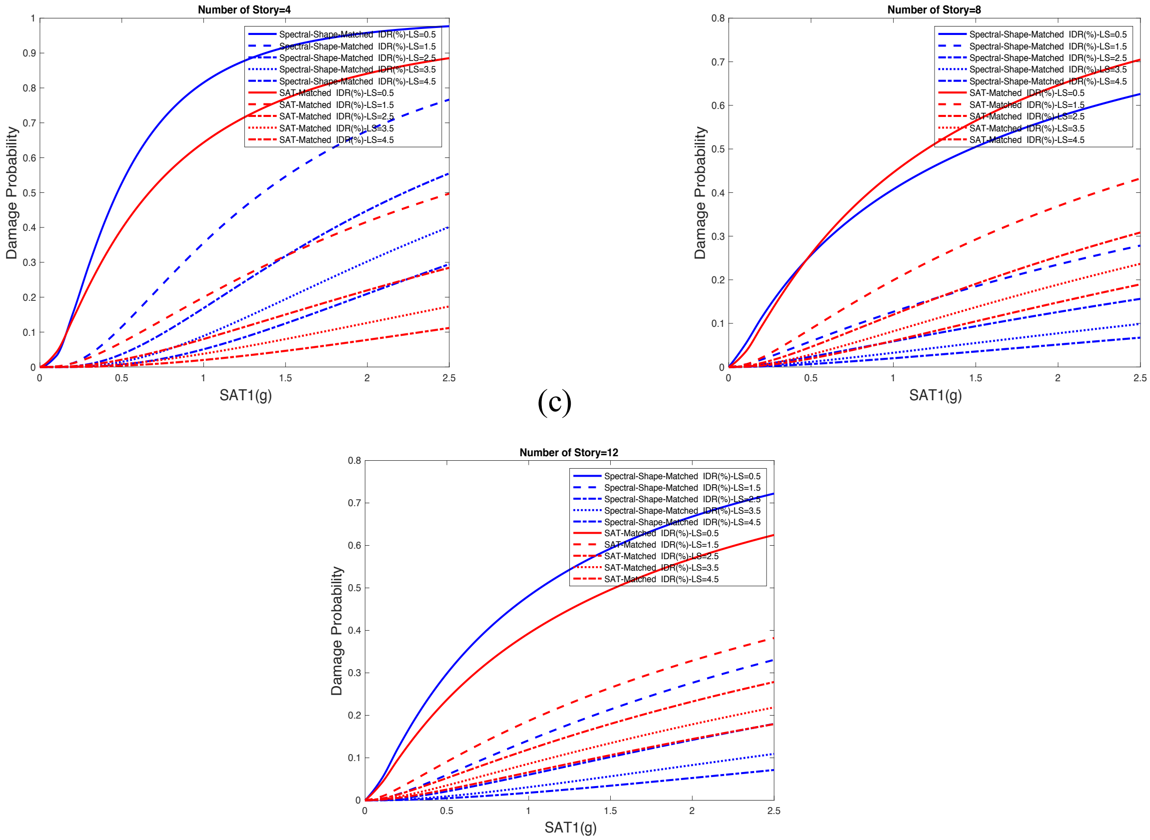
(a) (b) (c)

Figure 4.11. Comparison of damage fragilities for a range of damage limit states ($LS = IDR(\%)$) as indicated on the figures, obtained from $SA_{Ratio}-$ based method of spectral shape matching, with the SAT-based method of spectral shape matching for a (a) 4-, (b) 8- and (c) 12-story ductile building.

From Figure 4.11(a), it is clear that using SA_{Ratio}–based method of spectral shape matching will estimate the structure to be more fragile at all of the damage limit states. However, as the damage limit states increases, the probabilities of damage become closer with respect to using two different methods of spectral shape matching for the baseline earthquake suites. For the 8-story structure (see Figure 4.11(b)), this trend is reversed as the use of the SAT-based method of spectral shape matching produces more fragile curves compared to the other method (of spectral shape matching). Again, as the damage state increases, the difference in damage probabilities become less pronounced and the blue and red curves stand closer to each other.

Finally, for the 12-story structure as can be observed in Figure 4.11(c), for a very low level of damage where higher modes would not contribute much, the SA_{Ratio}-based method of spectral shape matching results in a higher damage probability (see blue curve at the damage limit state $LS = IDR(\%) = 0.50$). As the damage state increases, this trend gets reversed again, however, the difference between the damage fragilities obtained using two different ground motion suites are not that pronounced.

For collapse fragilities, Figure 4.12 shows the collapse cumulative distributions for different structures using two different suites of earthquake records as the baselines. Herein, the collapse limit state is set to be $LS = IDR(\%) = 10$. It can be observed that SA_{Ratio}-based method of spectral shape matching results in a slightly higher collapse fragility (blue curve). However, the difference between the red and blue curves are not that pronounced. This corroborates the conclusions made in the preceding paragraphs with respect to reduction in the differences between damage fragilities using two different suites, as the damage limit state increases. Moreover, at higher levels of damage, other attributes of the earthquake record other than the spectral shape begin to participate in capturing the seismic demand responses.

It should again be emphasized that using IDA, for the reasons discussed at the beginning of this section, is not the most accurate method, as only one suite of records is used throughout the entire process, and hazard-consistency is implemented by amplitude scaling alone. Using the multiple-stripe analysis method (Baker, 2015) would be more appropriate for this comparison. As such, the results obtained here may not be quite comparable with those of section 4.6.3 where a hazard-consistent sets of records had been selected.

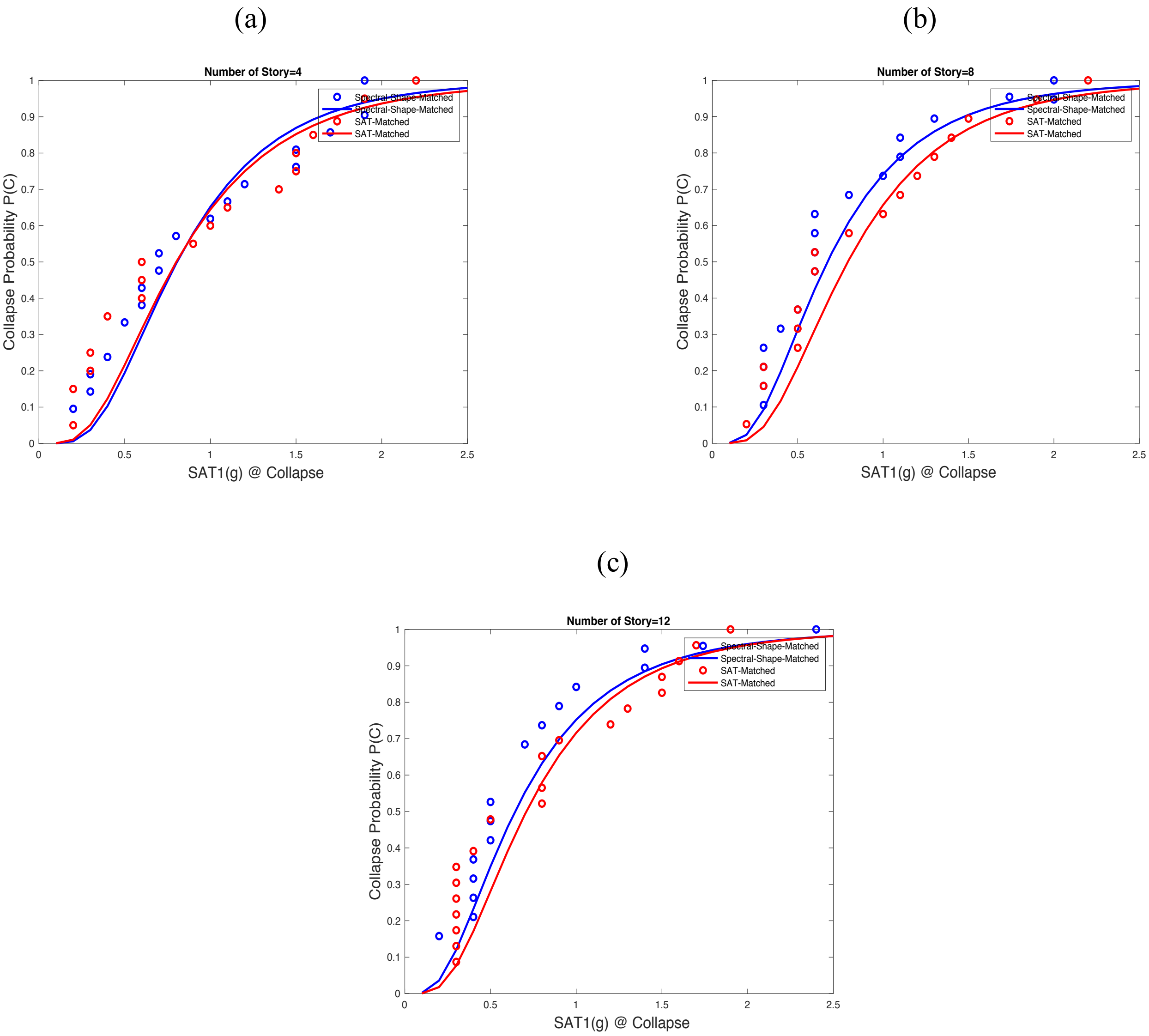
(a)

(b)

(c)

Figure 4.12. Comparison of the probability of collapse obtained from $SA_{Ratio}-$ based method of spectral shape matching, with the SAT-based method of spectral-shape matching for a (a) 4-, (b) 8- and (c) 12-story ductile building.

4.8 CONCLUDING REMARKS

A new GM selection algorithm was purposed to select ground motion earthquake records with emphasis on the spectral shape of the records. This method is based on defining a hazard-consistent target multivariate distribution for a vector of intensity measures including a new metric to represent the spectral shape. The marginal target distributions can ultimately be obtained by considering the cross-correlations between different intensity measures, including the aforementioned new metric defining the spectral shape. A desirable number of realization samples can then be drawn from the marginal distribution of each intensity measure. Finally, ground motion earthquake records can be selected considering different sets of importance weight factors to be assigned to different intensity measures during the selection phase. Therefore, the records could be selected such that the distributions of their intensity measures match those of the corresponding target distributions of the realization samples.

Accordingly, two sets of records were selected—one with respect to the new metric of spectral shape, and the other one based on the traditional spectral shape matching. A set of different types of ductile and non-ductile reinforced concrete structures have been adopted to study the effects of each of the selected earthquake suites on their seismic demand responses. It was concluded, in most cases, that the ground motion records selected based on the new spectral shape metric have a more destroying effect than those selected based on the traditional way.

To study the probability of damage given a wide range of damage limit states including collapse, a set of incremental dynamic analyses were performed using two baseline suites of ground motions selected based on two different ways of spectral shape matching. It was concluded that as the damage state grows, the difference between the damage probability obtained using different earthquake records becomes less pronounced. As such, the collapse probability distributions have become quite identical.

5 EFFECTS OF GM SELECTION ON SEISMIC RESPONSES OF DUCTILE AND NON-DUCTILE REINFORCED CONCRETE STRUCTURES

5.1 INTRODUCTION

Earthquake hazard imposes a significant risk on the safety of our societies. Experiences with past earthquakes prove that, in regions where there hadn't been a set of standards to consider the effects of earthquake on structures, consequences were devastating. Current seismic codes and provisions require all buildings constructed in any region to be designed for seismic loads in addition to gravity and other types of common loads. This is applied even to those places where seismic activities are not that pronounced where it is still necessary to apply a minimum seismic design requirement.

There are many sources of uncertainties in almost all aspects of seismic analysis, design and evaluation of structures which need to be quantified and considered in subsequent analyses. One of the major sources of variability in structural seismic responses can be attributed to earthquake ground motion records. Hence, in order to analyze a structure for seismic activities, ground motions to be utilized should actually represent the seismicity of a given site where the structure is located. That means that ground motion records should actually be hazard-consistent. Structural modeling is another important task which needs to be rigorously carried out for seismic analyses of structures. To this end, both component and material modeling would play some role in capturing the seismic demand responses.

There have recently been lots of progresses in the area of ground motion selection, scaling and modification. It is, therefore, very common to select a number of ground motion records (i.e.

a suite of earthquake records) rather than just a single record for the purpose of seismic analyses. It has also been known that in addition to the records in a suite, the methodology by which the suite itself is selected, would be a source of variability in the subsequent structural seismic responses. Hence, considering different ground motion selection criteria would end up with ground motion suites with different ground motion characteristics. As such, different types of structures would be sensitive to various earthquake characteristics and this would be a source of variability in seismic responses of structures which needs to be considered.

5.2 SCOPE AND MOTIVATION

Given recent advances in the area of probabilistic seismic hazard analysis, availability of databases of as-recorded ground motions and with the advent of new tools and methodologies to produce simulated (i.e. synthetic) earthquake records, seismic analysis and design of structures have become a much more mature task than would have been in the past. However, there is still a significant need for research works to be carried out specially in the area of ground motion selection, scaling and modification.

It is known that depending on structural characteristics, different contents of earthquake records would have different effects on seismic responses of structures. Structures which were designed based on recent seismic standards which are known as code-conforming or ductile are known to be more sensitive to specific ground motion contents such as amplitude and frequency contents, so that the inertia effects of earthquakes would play a key role in capturing the seismic responses of these types of structure. Whereas, existing structures especially those which are older and wouldn't have been designed based on rigorous seismic standards, would be sensitive to both amplitude- and cumulative-based contents of earthquakes. These structures which are known as none code-conforming or non-ductile are of paramount importance in the field of performance-based seismic risk assessments of structures. As such, failing to reevaluate the seismic performance of these types of structures based on the up-to-date seismic codes, would end up in devastating consequences in a real earthquake, which have been the case in many of the past earthquake events, due to significant damages that an earthquake could inflict on those types of structure.

Performing a reliable and accurate performance-based seismic risk evaluation of structures requires knowledges with regard to both computer simulation of structures and also ground motions, to enable users to capture the actual responses of structures corresponding to several modes of vibration. Computer modeling of structures, whether ductile or non-ductile, requires various linear and nonlinear structural components which would be capable of simulating the actual behavior of a given structure. Picking properties of material models to be assigned to these components, whether using experimental data or by following available codes, would also be deemed key for an accurate seismic risk assessment.

Given the importance of ground motion selection, scaling and modification in the area of seismic risk evaluation and design of both ductile and non-ductile, reinforced concrete (RC) structures, this study aims at shedding some more light on that area. To this end, not only the most recent advances in structural elements, and martial properties will be incorporated into the computer modeling (i.e. numerical simulation) of both ductile and non-ductile RC structures, but also a set of rigorous algorithms will be used for ground motion selection purposes to study the effects on the seismic performances of different structural systems. As such, the performance of various earthquake ground motion suites selected based on different criteria will be evaluated with respect to the statistical responses of different types of structures and appropriate conclusions will be drawn.

5.3 A REVIEW OF PRIOR STUDIES

5.3.1 Background

In recent years, there have been quite an extensive amount of studies on the area of efficiency and sufficiency of earthquake ground motion records to capture the seismic responses of structures in various modes of vibration. This has become even more common especially considering recent developments in the field of probabilistic seismic hazard assessment and ground motion selection using novel algorithms. As such, some of the most recent works on the effects of various ground motion selection criteria on the seismic performances of different structural systems will be reviewed. It is worth noting that, a compressive review along with developing a number of rigorous algorithms on ground motion selection, scaling and modification has already been conducted in Chapter 2.

(Baker & Cornell, 2008) developed a vector-valued ground motion intensity measure metric consisting of other intensity measures such as spectral shape and also ε (i.e. the number of standard deviations by which each of the record's spectrum is away from the median target spectrum) in addition to SAT, in order to see the effects on the uncertainty in structural demands. (Baker & Cornell, 2005) also used a vector-valued intensity measure metric consisting of SAT and ε, and concluded that failing to consider ε which can be deemed as a proxy to spectral shape would underestimate the structural response, quite significantly.

(Wong & Chopra, 2017) extended the generalized conditioning intensity measure ($GCIM$) approach, initially developed by (Bradley, 2010), to generate target distributions conditioned on two IM_j's rather than one. The reason for this is that in most of nonlinear response history analysis ($NRHA$) cases, ground motions conditioned on a single IM_j would not have sufficient contents to excite a given structure in various modes of vibration especially as the structure undergoes some level of damage and experiences changes in its fundamental period. Therefore, it would be necessary to select multiple suites of ground motions conditioned on multiple single IM_j's which increases the computational costs, quite significantly. Using two or more conditioning IM_j's, however, would require users to select only a single suite of earthquake records which would have sufficient contents to be able to capture the nonlinear behavior of structures in several modes of vibration.

(Wong & Chopra, 2016) also compared various ground motion selection, scaling and modification procedures using conditioning spectrum (CS), initially developed by (Lin, et al., 2013), and the $GCIM$ to evaluate biases in the evaluation of the seismic hazard demand curves ($SDHCs$) for a given structure at a specific site in comparison with a benchmark $SDHC$. (Wong, et al., 2015) developed an algorithm to select unscaled ground motion records to evaluate $SDHCs$. (Wong, et al., 2015) used various methods to generate synthetic earthquake ground motion records to evaluate the effect of various ground motion selection and modification procedures on the $SDHCs$.

(Kohrangi, et al., 2017) employed a conditional IM_i target generation approach by adopting an average of multiple SATs at various periods as IM_j rather than a single conditioning IM_j. Ground motion records were subsequently selected to match the new conditioning target IM_i and were utilized in $NRHA$s of structures which ensured increased sufficiency and efficiency in the estimation of the seismic demands. (Kohrangi, et al., 2017) studied the degree of site influence with respect to the adopted conditioning IM_j, on the seismic responses of structures. They concluded that using a single IM_j as the conditioning intensity measure (IM) results in a significant variability in the seismic demand responses from site to site. In contrasts, using an average-IM_j -

i.e. average of $SATs$ at multiple periods- helps to decrease the variability in the seismic demands from site to site.

(Wang, 2011) proposed a ground motion selection algorithm to select ground motions (GMs) to match a target median, standard deviation and correlation matrix conditioned on specific causal properties. He concluded that ground motions selected based on this procedure are more efficient and sufficient in capturing the seismic demand responses. (Weng, et al., 2010) proposed a ground motion selection and scaling method to consider the dominant modes of vibration with regard to the structural seismic demand responses. To this end, they proposed a multi-mode ground motion scaling method to combine various seismic demand responses in different modes to compute the peak response.

(Yang, et al., 2009) developed a rigorous performance-based methodology which considers seismic hazard, structural response, inflicted damage, and subsequent repair costs using a fully probabilistic approach. (Bradley, et al., 2015) utilized various methods of ground motion simulations instead of using the empirical ground motion prediction equations to generate a set of hazard-consistent synthetic records to study the seismic responses of engineered systems. (Tarbali, et al., 2018) investigated the effects of uncertainty in seismic hazard and ground motion selection methodologies, on the seismic responses of structures. (Shokrabadi & Burton, 2017) utilized a set of different intensity measures (IMs) to study the effects on the dispersion of seismic responses of two different structural systems, namely, a controlled rocking steel braced frame system with self-centering action and a rocking spine system for reinforced concrete infill frames.

Chandramohan et al. (2016) studied the duration effects on the collapse capacity of both steel and RC structures by using a pair of spectrally-equivalent long- and short-duration ground motion records. Chandramohan et al. (2016) studied the duration effects of ground motions on the seismic demands of various structural systems. As such, they used the $GCIM$ methodology to select ground motions whose cumulative distributions of duration metrices match those of the hazard-consistent target distributions.

Cantagallo et al. (2014) used two different ground motion selection strategies, one based on the response spectrum matching and another one by minimizing the amplitude scaling procedure. They, then, studied the effects on the seismic demand responses of RC strcutrues. Araujo et al. (2106) studied the effects of various code-based ground motion selection criteria on the seismic responses of steel structures with emphasis on the efficiency of the selected records. (Champion & Liel, 2012) studied the effects of forward directivity on the collapse capacity of RC structures using an incremental dynamic analysis (IDA) approach. Haselton et al. (2011) studied the collapse risk of ductile RC special moment-frame structures considering various seismic design provisions. Raghunandan & Liel (2013) studied the collapse risk of RC structures by considering the duration effects of the GMs as well as various properties for the structures. They used an IDA approach to derive the probability of collapse for various structures. They concluded that considering the duration effect would increase the collapse risk. Liel et al. (2011) studied the collapse risk of non-ductile RC structures considering various seismic design provisions. Raghunandan et al. (2015) studied the effects of subduction earthquakes (as compared to crustal earthquakes) on the probability of collapse of non-ductile RC structures.

5.3.2 The state of research

The main goal of this research is to compare the effects of various ground motion suites selected based on different methodologies, on the seismic demand responses of both ductile and non-ductile RC structures. These methodologies which are based on the algorithms developed in Chapter 2, can produce different hazard-consistent conditioning target $IM_i's$ by using some sampling methods to be applied to draw IM_i realization samples from the multivariate distribution of various $IM_i's$ assuming a single-, double- and multiple-IM_j. Ground motions will then be selected from a database of earthquake ground motion records considering a variety of importance weighs to be assigned to different $IM_i's$ during the selection phase. As such, numerous suites of ground motions will be selected with an emphasis on several characteristics of earthquake records ranging from amplitude- to cumulative- and duration-based characteristics.

In order to study the impacts of the aforementioned earthquake suites on the seismic responses of RC structures, a set of different ductile and non-ductile RC structures with a varying height will be modeled in OpenSees. These structures will then be analyzed using various ground motion suites and the statistics of the demand responses will be determined. A set of different comparisons will be made with respect to different parameters, namely, the conditioning $IM_j's$, the IM_i importance weight factors, various engineering demand parameters ($EDPs$), type of RC buildings, and the specimen buildings' height. The appropriateness of various ground motions suites will accordingly be evaluated and discussed.

5.4 APPLICATIONS

5.4.1 Ductile and Non-ductile reinforced concrete structures

Three buildings of various heights—i.e., 4, 8, and 12 stories—are modeled assuming either a ductile or non-ductile behavior so six structures are simulated, in total. Degree of non-ductility is enforced by ${V_p}/{V_n}$ where V_p is the shear corresponding to development of probable moment strengths and V_n is the nominal shear strength in accordance with ASCE/SEI 41-06 for low ductility demand. ${V_p}/{V_n}$ is set to one for the non-ductile buildings to be used in this study. The fundamental periods of vibration for these three buildings are $T1 = 1.30\ sec$, $T1 = 1.80\ sec$ and $T1 = 2.20\ sec$ for the 4-, 8- and 12-strory, respectively. The structures were modeled in OpenSees which is a finite element software and widely used for earthquake engineering simulations (McKenna, et al., 2000).

Properties of the ductile and no-ductile RC structures which are all modeled two-dimensionally are taken from (Galanis, 2014). Figure 5.2 shows the schematics of these three buildings. Figure 5.1 shows some of the elements and the material model which are utilized to simulate the ductile and non-ductile behaviors.

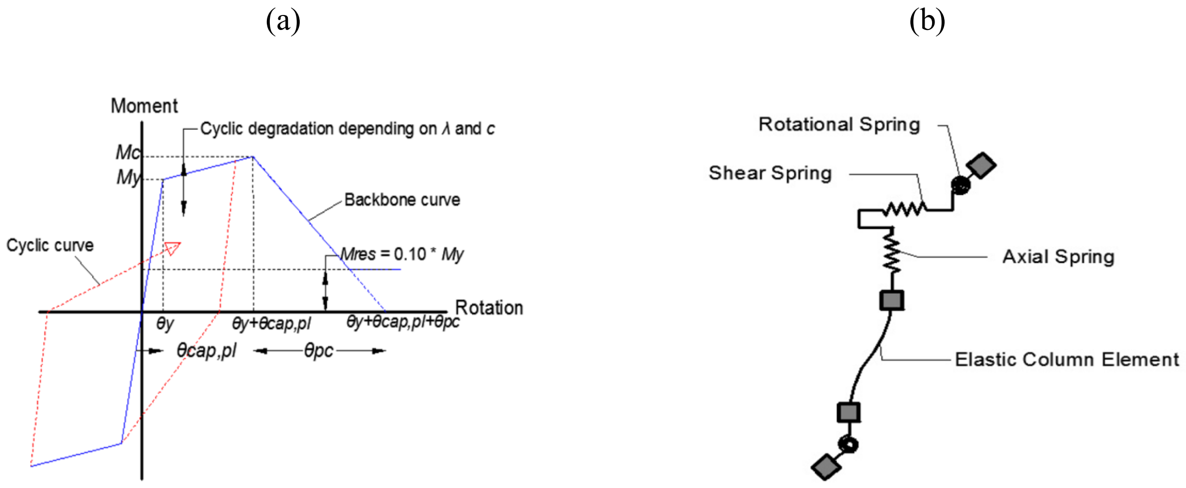

Figure 5.1. (a) Ibarra backbone curve for the component model (b) zero length elements to be assigned to plastic hinges to simulate ductile and non-ductile behavior (in case of ductile, the axial and shear springs are removed). (Adopted from (Galanis, 2014)).

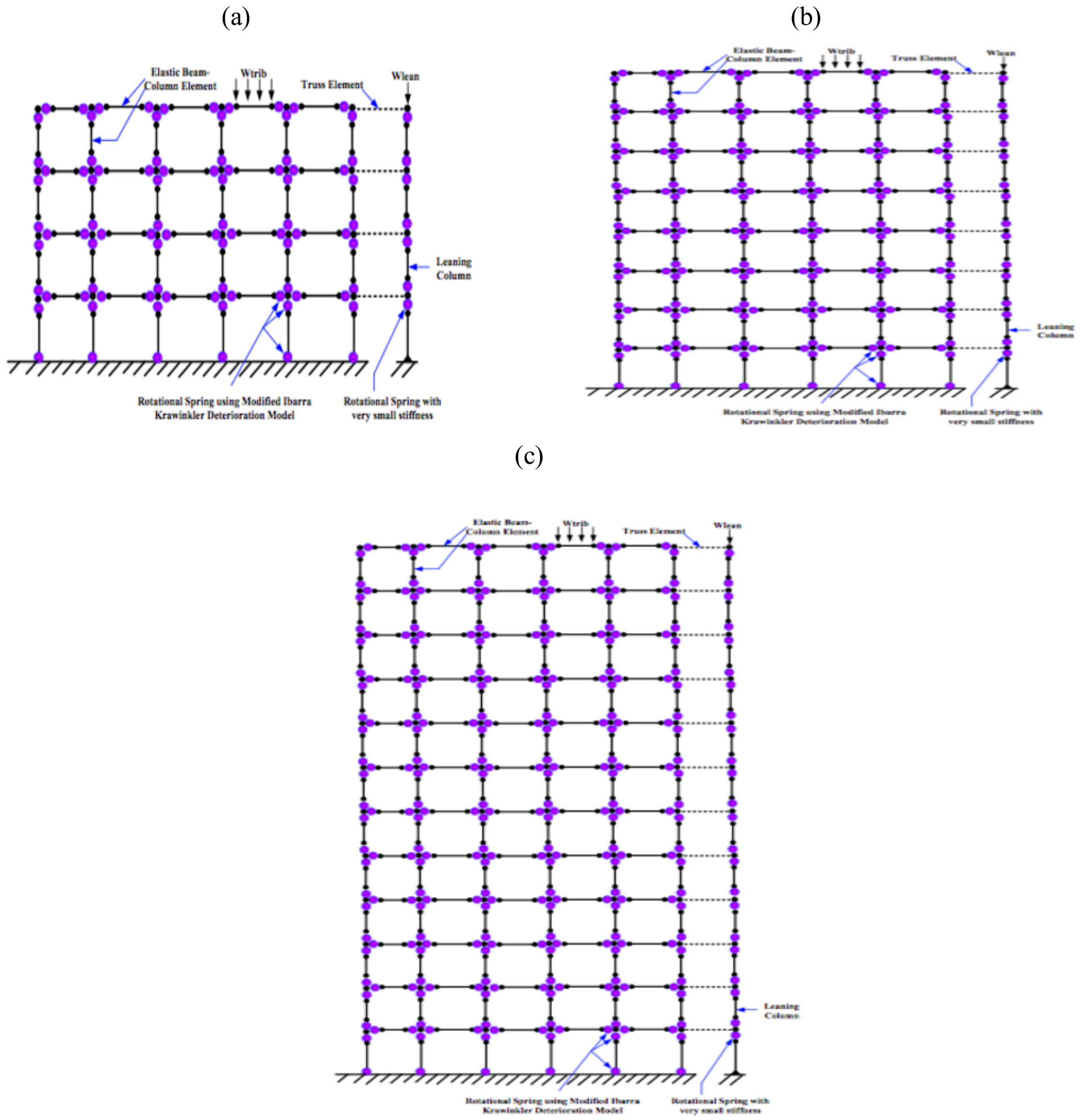

Figure 5.2. (a), (b) and (c) Schematic of a 4-, 8-, and 12-story building.

Figure 5.1(a) shows the backbone curve to be assigned to various plastic hinges in different elements, shown in purple in Figure 5.2, for various buildings based on (Ibarra, et al., 2005). To simulate the ductile behavior, an element such as the one shown in Figure 5.1(b), but without the shear and axial springs, will be assigned to plastic hinges within different columns and beams across multi levels for various buildings. As per non-ductile behavior, the element shown in Figure 5.1(b), including the shear and axial springs is assigned to plastic hinges whose properties to capture the shear and axial behavior are adopted from (Elwood, 2004). All the details regarding the structural elements being used in this study including the cross-sectional properties, definition of various parameters to be assigned to plastic hinges, and their properties both for simulating ductile and non-ductile behaviors have been adopted from (Galanis, 2014).

It t is worth noting that given a very high computational cost of the nonlinear response history analyses for multiple suites of earthquake records as is the case for this study, a parallel computing approach is adopted. Therefore, all of the upcoming analyses are run on the $XSEDE$ supercomputing facilities—more specifically, the Stampede2 platform—, which is managed by the University of Texas at Austin. Stampede2 is a high-performance computational platform with 12,000,000 node-hour capacity, which makes it suitable for this study. Figure 5.3 demonstrates the schematics of the job submission procedures and the configuration of the platform. Figure 5.4 displays the algorithm utilized to run the required analyses on the Stampede2 platform.

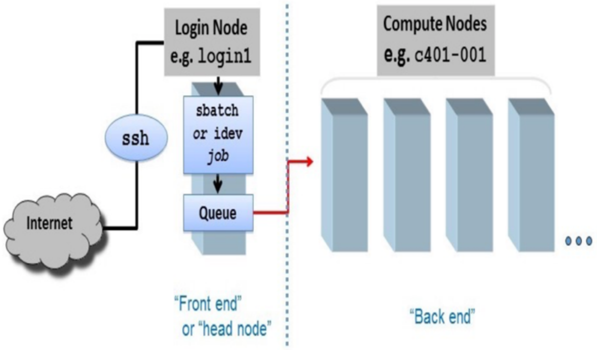

Figure 5.3. Schematic of job submission process (e.g. batch submission) and the configuration for the platform. (Adopted from https://portal.tacc.utexas.edu/user-guides/stampede2).

`

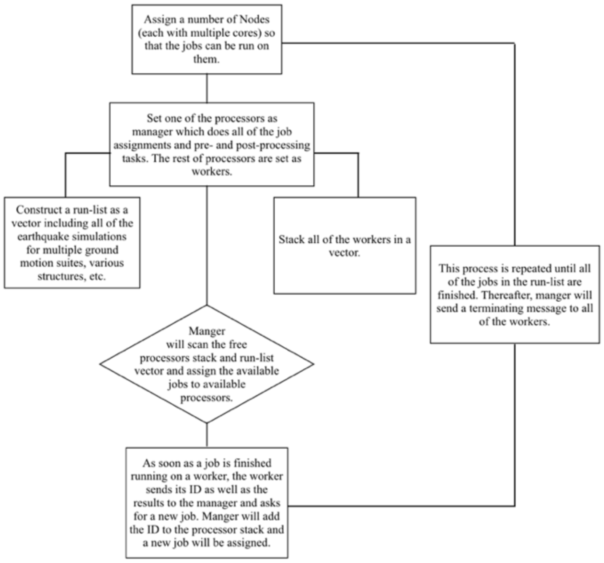

Figure 5.4. The parallel computing algorithm adopted in this study.

5.4.2 Ground motions

The ground motion suites to be used for the subsequent structural analyses, are briefly described here. The full list of ground motion suites and more detailed information with regard to the algorithms these ground motions have been selected based upon, can be found in Chapter 2.

First, $IM_i = \{SA(T), AI, CAV, Ds575, Ds595\}$ is set as the target IM_i intensity measure vector where AI, CAV, $Ds575$ and $Ds595$ are defined as, arias intensity, cumulative absolute velocity, 5-75%, and 5-95% significant durations, respectively. For computation of $SA(T)$, 21 different periods identical to those for which hazard curves can be generated, have been chosen. The goal would, then, be to select ground motion records with matching contents as those in the target IM_i vector.

In order to select ground motion records, a hypothetical site in the city of Los Angeles, CA (LONG-118.43; LAT34.053) with average shear-wave velocity for the upper 30 m depth of 760 m/sec , and a depth to a 2.5 km/sec shear-wave velocity horizon of $z_{2.5} = 1\ km$, is chosen.

`

Using the relationships developed in Chapter 2, a set of different ground motion earthquake suites are selected based on different conditioning criteria and IM_i importance weight factors. Hence, various suites selected based on giving different weights to different IM_i's in the IM_i vector. As such, weight factors of $70\%\,,99\%,1\%$ for the $SATs$, and consequently weight factors of $30\%\,,1\%,99\%$ for the non-$SATs$ are considered. The weights to be assigned to either of SAT or non-SAT intensity measures are evenly distributed among all of them during the selection phase. Hence, the sum of the SAT and non-SAT weights equals one. A separate ground motions suite is also selected solely based on the duration as an independent metric considering an interval of $T(sec) = [40\,,300]$. As for causal parameters, the magnitude range of $M = [5\,,8]$, the closest source-to-site distance of $R_{jb}(km) = [0\,,100]$, and the $V_{s30}(\text{m/sec}) = [300\,,1200]$ are adopted. The maximum scale factor is set to 4. It is also worth noting that hazard-consistency is implemented by considering up to 2,000 rupture scenarios and their contribution to different types of conditioning intensity measures.

5.4.2.1 An example of selected ground motion suites

In this section, some of the information related to the selected ground motion suites conditioned on a single, two and multiple conditioning intensity measures ($IM_j's$) based on 1% SAT and 99% non-SAT weigth factors is provided for a 8-story structure, just as an example. The structural fundamental period is $T1 = 1.80$ sec. Hence, the IM_j is turned out to be $SA(T1 = 1.80\text{ sec})$ throughout this study, which will be derived from the hazard curve for a 2% probability of exceedance in 50 years.

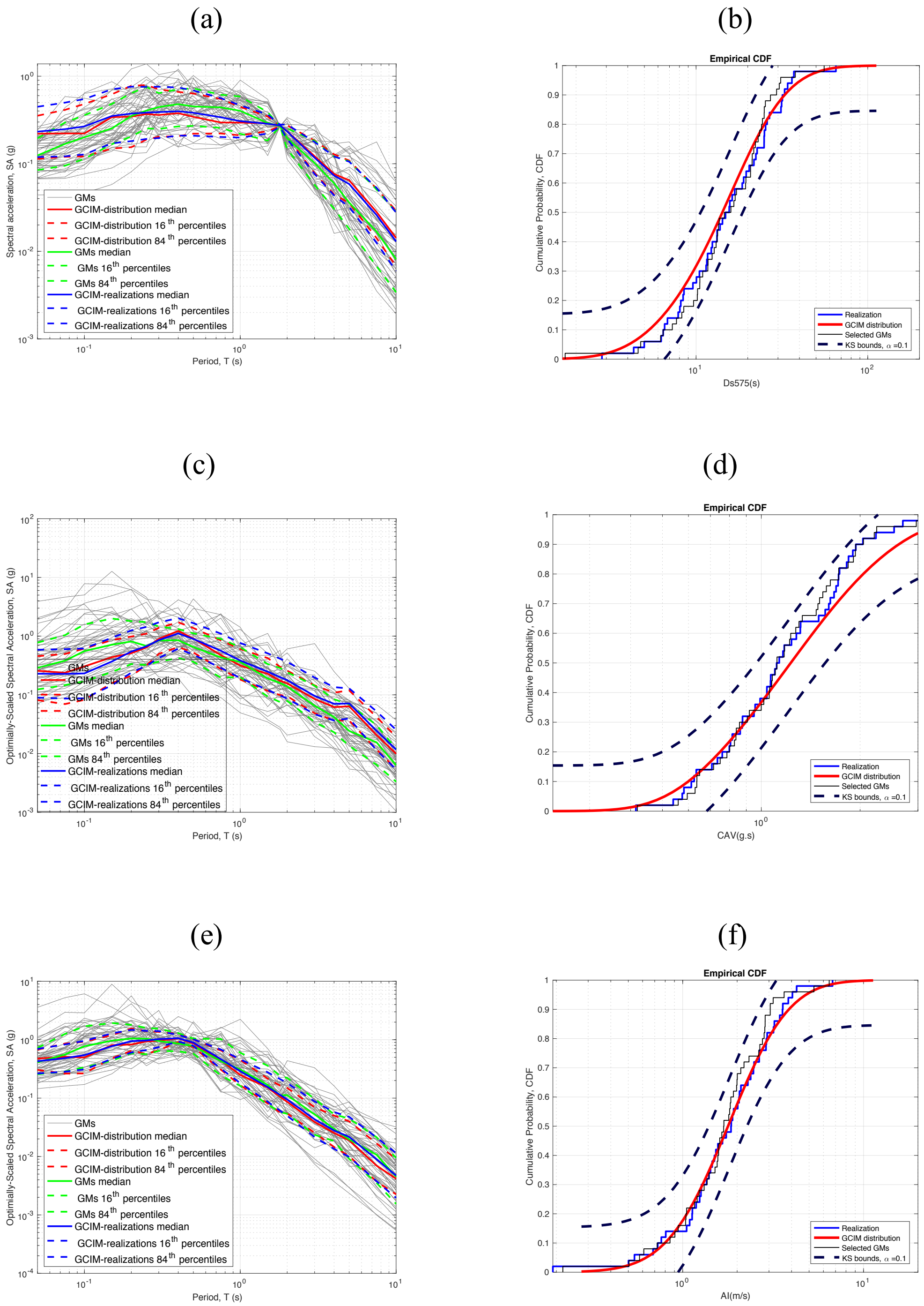
(a) (b) (c) (d) (e) (f)

Figure 5.1. (a), (c), and (e) Response spectra of the selected records for a single-, two-, and multiple- IM_j. (b), (d) and (f) empirical distribution of $Ds575, CAV$, and AI for the selected records.

When it comes to multiple conditioning $IM_j's$, the lower and upper bound coefficients of 0.20 and 3.0 were, respectively, applied to derive IM_{j1} and IM_{j2} based on (Eads, et al., 2016) and

`

(Chandramohan, 2016). Thus, $T1$, $T2$ were set to 0.40 sec and 5.0 sec , respectively. Hence, IM_{j1} and IM_{j2} are turned out to be $SA(T = 0.4\ sec)$ and $SA(T = 5.0\ sec)$, respectively. Using the algorithm described in Chapter 2, 50 earthquake records from the NGA-WEST2 database $(\text{Bozorgnia, et al., } 2014)$ are selected based on various conditioning criteria. (see Figure 5.5)

As observed in Figure 5.5, since more emphasis was given to the non-SAT intensity measures during the selection phase, it is clear from the figures (e.g. ,Figures 5.5(b), 5.5(d), 5.5(f)) that the ground motions are richer in cumulative- and duration-based contents with respect to the hazard-consistent targets as opposed to amplitude-based contents, as can be observed from the response spectra (e.g., Figures 5.5(a), 5.5(c), 5.5(e)). It is worth noting that on all of the plots presented in Figure 5.5, the grey curves represent the response spectra of the selected records, the green curves are the statistics of the selected record's spectra, the blue curves are the statistics of the realizations drawn from a generalized conditioning intensity measure ($GCIM$) (shown in red) for which the matching records (gray curves) have been selected, and the red curves are the statistics of the theoretical target distribution obtained using the $GCIM$ approach as described in Chapter 2. Finally, the black curves (in the CDF plots) are the cumulative distributions of the non-SAT intensity measures which belong to the selected records.

Figure 5.5 is presented, herein, just an example of the ground motion suites that will be used for the subsequent structural analyses, and the rest of them (for example those that are selected based on different importance weight factors, etc.) are omitted here for the sake of brevity but can be found in Chapter 2.

As per the reason why various conditioning criteria are picked, a brief description is provided herein. As it is known, selecting GMs matching a uniform hazard spectrum (UHS) is deemed to be overly conservative. The UHS is obtained directly from hazard curves for various

$SATs$ over a range of periods. All the ordinates of UHS are, therefore, hazard-consistent and have the same return period. In reality, few as-recorded earthquakes can produce a response spectrum which is hazard-consistent at all periods without applying unrealistic amplitude scaling. One way to mitigate this problem is to choose the target response spectrum to be hazard-consistent only at specific ordinates of the spectrum instead of all.

A quick comparison of median response spectra obtained using various conditioning methods can be seen in Figure 5.6, which is obtained for a hypothetical site in the city of Los Angeles, CA (LONG-118.43; LAT34.053) with average shear-wave velocity for the upper 30 m depth of $760\ \mathrm{m/sec}$, and a depth to a $2.5\mathrm{m/sec}$ shear-wave velocity horizon of $z_{2.5} = 1$ km. The structural fundamental mode period is set to $T1 = 1$ sec.

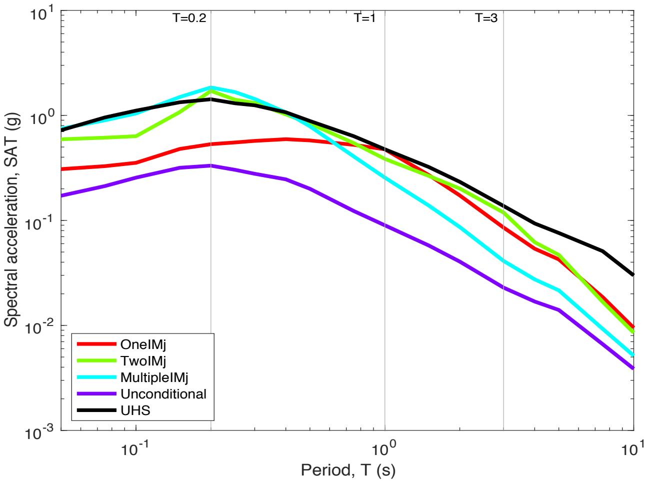

Figure 5.6. Comparison of median spectra obtained from various methods of conditioning target generation, with the target spectrum obtained based on UHS.

As it can be observed from this figure, selecting earthquake records matching the UHS target spectrum (shown in black) will result in a very conservative set of records, simply because these records are going to be very intense at the entire set of structural periods of vibration. On the other hand, the response spectrum obtained from the new methods proposed earlier, as well as the response spectrum using an unconditional approach, all fall below the UHS at most period values. However, record selection based on an unconditional approach is highly non-conservative and produces hazard-inconsistent $SATs$ for any period of vibration, and therefore it is not recommended. The target conditioned on a single intensity measure (shown in red) produces a target that is hazard-consistent at a single IM_j (i.e. $SAT = 1$ sec) and falls below UHS at all of the other $SATs$. Here, it can be argued that records selected matching this target spectrum may not be sufficient if the structure goes into a highly nonlinear phase. Therefore, one would have to repeat this process for a few times to generate conditional targets using new $IM_j's$ each time, which then increases the computational burden significantly.

Selecting records matching a target to be hazard-consistent over a range of conditioning periods—which has been the case for the proposed two-IM_j and multiple-IM_j methods—seems to have mitigated the aforementioned problems. As it can be observed in Figure 5.6, the target spectrum conditioned on two-IM_j (shown in green) intercepts the UHS over a range of periods between IM_{j1} and IM_{j2}— here, $SAT(T = 0.2\text{sec})$ and $SAT(T = 3.0\text{sec})$, respectively—, which necessarily brackets and includes $SAT1$ ($SAT = 1.0\ sec$). Thus, the selected records matching this target *will* have sufficient intensity to excite the structure at its many modes (controllable by selecting the IM_{j1} and IM_{j2}) rather than only $T1$. This, then, obviates the use of multiple suites, thereby reducing the computational burden significantly.

The records selected based on multiple-IM_j conditioning (shown in cyan in Figure 5.6) produces but a more intense spectrum at a lower vibration periods than other methods, but a less intense spectrum around $SAT1$, eventually diminishing into the unconditional spectrum at longer periods.

5.4.3 Structural analysis results

Given the variety of GM selection algorithms described briefly in the previous section, a comprehensive range of nonlinear response history structural analyses ($NRHAs$) are performed on the cloud and various comparisons are made with respect to multiple sets of importance weights assigned to both SAT and non-SAT intensity measures, different methods of conditioning, and finally various structural systems (see section 5.4.1). As such, once a $NRHA$ is carried out on a structural system using a GM suite, the results will be post-processed just like what can be seen in Figure 5.7. In this figure, the gray curves are the results from the entire $NRHAs$ using the records in the suite. Hence, the statistics of both the inter-story drift ratio (IDR) and peak floor acceleration (PFA)—namely, the median, 16- and 84 percentiles—will be estimated, which are shown in red in both of the plots in Figure 5.7. Hereafter, these metrices will be used for comparison purposes.

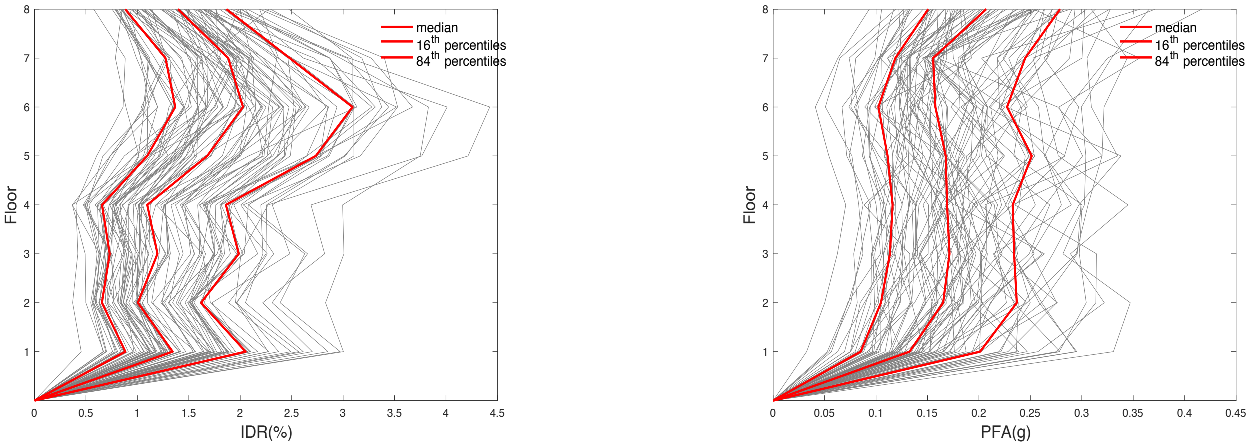
(a) (b)

Figure 5.2. (a) and (b) $IDR(\%)$ and $PFA(g)$ responses for a 8-story non-ductile building using a ground motions suite.

5.4.3.1 Effects of importance weight factors

In this section, the effects of varying importance weight factors to be assigned to both SAT and non-SAT intensity measures, on different engineering demand parameters ($EDPs$) for various types of structural systems, will be investigated. Hence, a set of different weight factors as mentioned in section 5.4.2 will be adopted to study the effects of the amplitude-, frequency-, cumulative-, and duration-based characteristics of the earthquake records on the statistics of the structural $EDPs$.

5.4.3.1.1 Ductile reinforced concrete (RC) structrues

This section will study the effects of varying importance weight factors on the statistics of the $EDPs$ for ductile RC structures with varying heights.

Figure 5.8. demonstrates the median (solid lines) and 16th and 84th percentiles (dashed lines) of $IDR(\%)$ and $PFA(g)$ for a 4-story ductile RC structure. The basis of comparisons, herein, is in accordance with different sets of importance weight factors. Hence, comparing the effects of records selected based on different conditioning algorithms on the statistics of the responses will be discussed in another section.

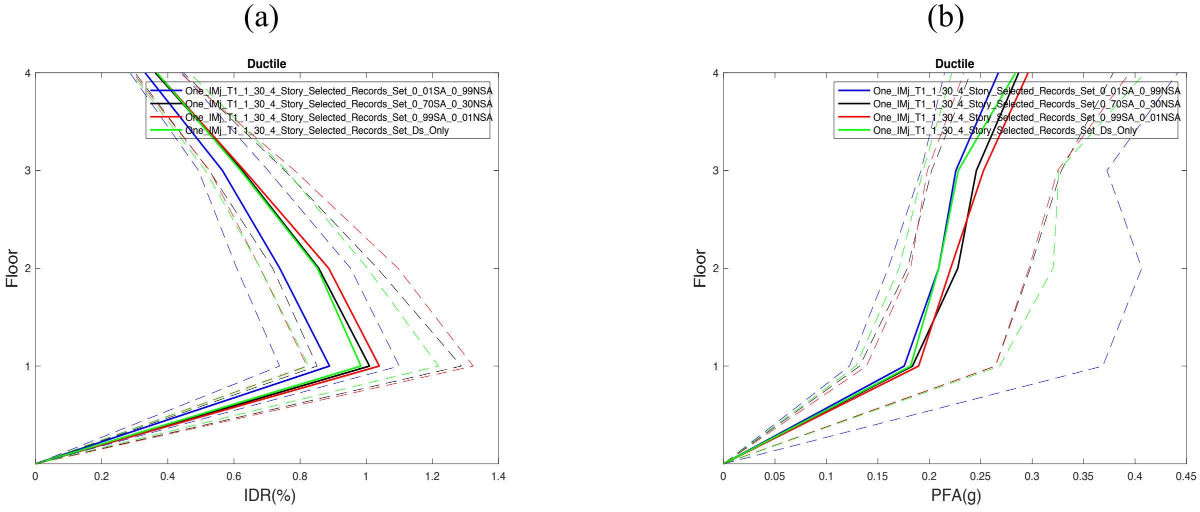

Figure 5.3. (a) and (b) Median (solid curves) and 16^{th} and 84^{th} percentiles (dashed curves) of $IDR(\%)$ and $PFA(g)$ for a 4-story ductile RC structure.

From Figure 5.8(a), it can be observed that giving more emphasis to the cumulative characteristics of the records during the selection phase underestimated the response with respect to both of the median and percentiles (see the blue curves). That makes sense as the structure is ductile or code-conforming, thereby it is not supposed to undergo large nonlinear deformation and therefore the response will mostly be governed by the inertia effects of the records. Hence, the records with more inertia- or amplitude-based contents should perform better in capturing the actual response of this structure. This can be clearly observed in Figure 5.8(a) as the median as well as the percentile responses of $IDR(\%)$ are all capped by the red curves which are obtained using the records where the majority of emphasis or weight was given to their amplitude-based contents during the selection phase. This is also clear from the black curves in Figure 5.8(a) for which the underlying records were selected by giving the majority of weights (i.e. 70%) to their amplitude-based contents, which stands in the second place after the red curves in capturing the response. The effects of selected records with emphasis on duration given an interval of $T(sc) = [40\,,300]$, on the $IDR(\%)$ response can also be seen in Figure 5.8(a) (see green curves). Although, it appears that the records selected based, solely, on a duration interval have been able to capture the actual responses as accurate as the red and black curves, the results, herein, would be affected by an insufficient number of records with long durations available in the $NGA-WEST2$ database. Besides, since the records were selected only by setting bounds on the duration, it is suspected that the records could be rich in amplitude-based contents as well which would magnify the responses. It is, however, worth mentioning that a hazard-consistent effect of duration has also been incorporated into the ground motion selection phase as the significant duration was set as one of the $non-SAT$ intensity measures. Given that, giving more weight to this metric during the record selection phase does not seem to be effective in capturing the drift as can be seen from the blue curves in Figure 5.8(a) which was discussed earlier as well.

$PFA(g)$ is another very important EDP which is considered in this study. Figure 5.8(b) shows the variation of $PFA(g)$ with respect to different sets of weight factors during the record selection phase. Comparing the median $PFA(g)$ demands shows that records selected based on different weight factors resulted in almost identical median $PFA(g)$ demands. However, at the 84th percentile, giving more weights to non-SAT contents, results in a larger demand as can be seen from the dashed blue curve. The reason why this record set estimates the largest of $PFA(g)$, among all of the other methods could be attributed to its contents which have imposed more variability on the structural response.

A similar type of analysis was performed on a 8-story ductile RC structure for which sample results are provided in Figure 5.9

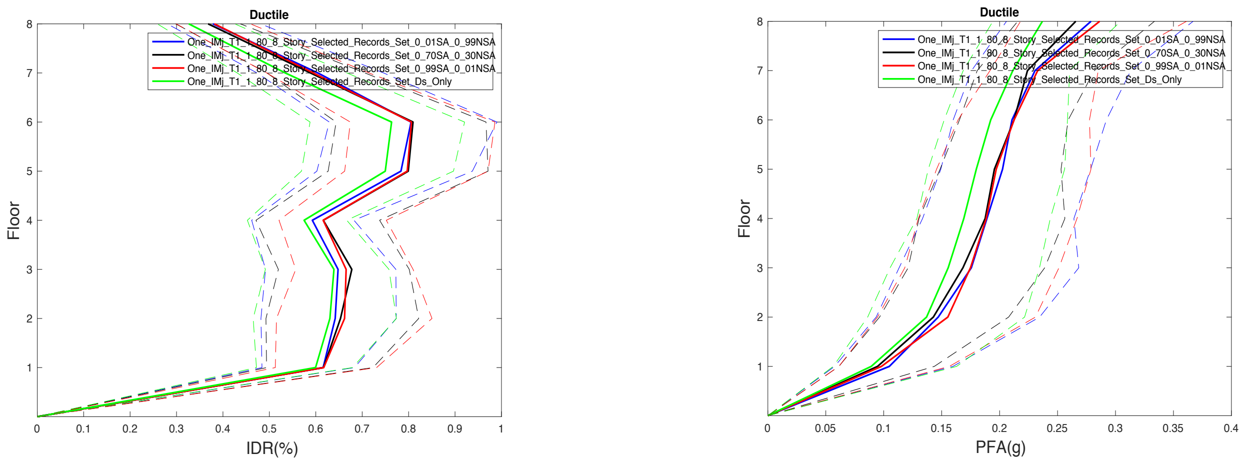
(a)

(b)

Figure 5.4. (a) and (b) Median (solid curves) and 16th and 84th percentiles (dashed curves) of $IDR(\%)$ and $PFA(g)$ for a 8-story ductile RC structure.

Figure 5.9(a) includes the statistics of the $IDR(\%)$ which shows that variation in weight factors did not significantly affect the median response as the demands are very close. Hence, the red and black curves which are the $IDR(\%)$ obtained using records where most of emphasis was given to SAT contents during the selection phase, are slightly larger than the rest. The duration-based set whose associated $IDR(\%)$ response shown in green seems to impose the smallest response among all. However, by looking at other percentiles of the response shown with dashed curves, especially the 84th percentile on the far-right hand side of the graph, there is a more sensible variation in the responses obtained by using different record sets with various weight factors. This proves that as the $IDR(\%)$ level increases and the structure begins to experience some level of damage, in other word as the structure goes into the nonlinear phase, the effects of different weight factors stand out and various earthquake record attributes begin to contribute.

Similar conclusions can too be drawn for $PFA(g)$ as compared with IDR . Hence, as can be observed in Figure 5.9(b) the median PFA obtained using various sets of records with different weight factors are identical for most of the sets expect for the one which had been selected solely based on a duration interval. The underlying reasons for this have already been discussed. At the 84th percentile, though, there is a variation as the structure undergoes a larger level of deformation.

Similar types of analysis were carried out on a 12-story ductile RC structure for which the results are presented as follows.

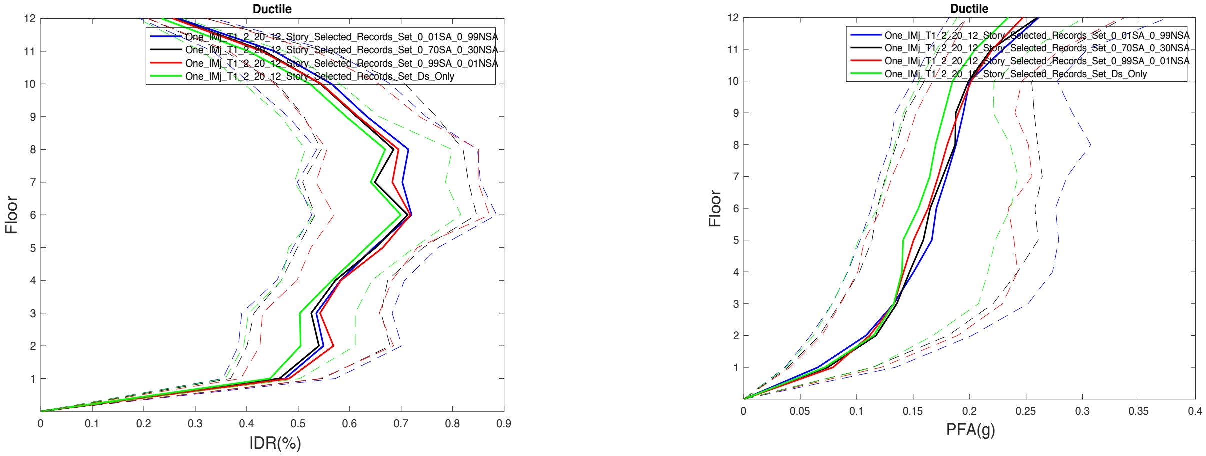
(a)

(b)

Figure 5.5. (a) and (b) Median (solid curves) and 16th and 84th percentiles (dashed curves) of $IDR(\%)$ and $PFA(g)$ for a 12-story ductile RC structure.

Looking at the median drift and acceleration plots in Figures 5.10(a) and (b), one could notice that as the height of structure increases, the effects of different weight factors do not play a tangible role especially for code-conforming structures where median demands are not that high. Once the structure starts going into the nonlinear phase and multiple modes of vibration begin to contribute, this trend starts to change and there is a variation in the demand responses as can been seen in the 84th percentiles of both plots shown with dashed curves on the far right-hand side of the graphs. Moreover, it is worth noting that by looking at the median IDR, the ground motion records with more cumulative characteristics impose a larger demand compared to other sets (see blue curve in Figure 5.10(a)). This difference is not that noticeable, though, as all of the sets impose identical demands. Lastly, in Figure 5.10(b) just like for the 4- and 8-story, the records selected with higher weights assigned to $non-SAT$s predict the largest 84th percentile in $PFA(g)$ demands. This is specifically more noticeable from the blue curve in the 84th percentile of Figure 5.10(b).

5.4.3.1.2 Non-Ductile reinforced concrete (**RC**) structrues

A similar type of analysis which was carried out for the ductile RC structures, will be conducted for the non-ductile RC structures, herein, and the results will be presented. Figure 5.11 demonstrates the outcomes for a 4-story non-ductile RC structure.

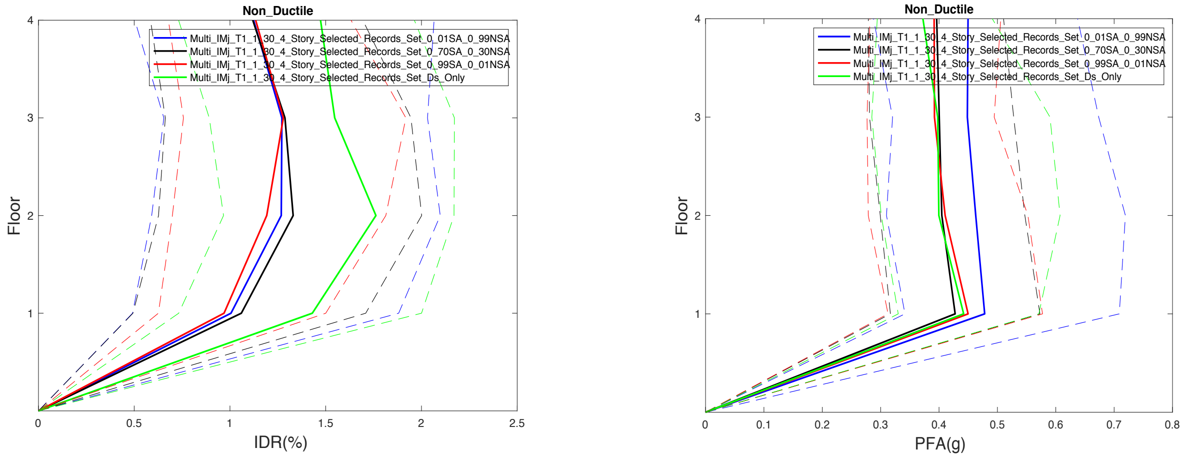

(a)

(b)

`

Figure 5.6. (a) and (b) Median (solid curves) and 16th and 84th percentiles (dashed curves) of $IDR(\%)$ and $PFA(g)$ for a 4-story non-ductile RC structure.

From Figure 5.11(a) and by looking first at the median responses (i.e. solid curves), it can clearly be observed that the record selected based on restricting the duration by setting a duration interval, has imposed the largest demand (see the green curve). That makes sense as in non-ductile structures, damage will be accumulated at lower level of drift so given the shear and axial failure in columns and generation of plastic hinges in various elements, the long-duration records would impose more severe damage due to continuous deterioration in various structural elements. Moreover, other records selected by giving emphasis to different contents of earthquake records have pretty much produced identical median responses, however, it can still be observed that records with more cumulative- and duration-based characteristics (see the blue and black curves) have produced a larger median demand compared to those which were solely selected based on the amplitude-based contents (see the red curve). This fact can be clearly noticed from the 84th percentile on Figure 5.11(a) where due to a larger level of drift and more nonlinearity, demand variation imposed by using different records is clearly noticeable. Moreover, it can again be noticed that the records selected solely based on duration and those selected based on giving more weights to the $non-SAT$ contents have produced a larger variability in demand (see the 84th percentile dashed curves).

When it comes to PFA (see Figure 5.11(b)), as can be seen from both of the medians and percentiles, the records selected by giving more emphasis to cumulative effects have imposed a larger demand variability which can be noticed from blue solid and dashed curves. This corroborates the results obtained earlier by studying the ductile buildings.

Similar analyses were conducted on a 8-story non-ductile RC structure for which the results are presented in Figure 5.12. In Figure 5.12(a) it can, again, be noticed that with respect to both of the medians and percentiles of the drift, the records selected based on giving more weights to the duration and cumulative effects, have imposed a larger median and variability, respectively. Hence, duration-based records (see the green curves) have imposed the largest demand and those selected based on giving more emphasis to cumulative characteristics (see blue curves) are next. This again could be due to the cumulative damage at lower level of drifts and contribution of multiple modes which distinguishes the non-ductile structures from those of the ductile where the amplitude effects of the records were more pronoucned. As per PFA, as can be seen in Figure 5.12(b), giving more emphasis to cumulative characteristics during the record selection phase, resulted in a higher median PFA and PFA variability which is more pronounced in the 84th percentile (see the blue curves).

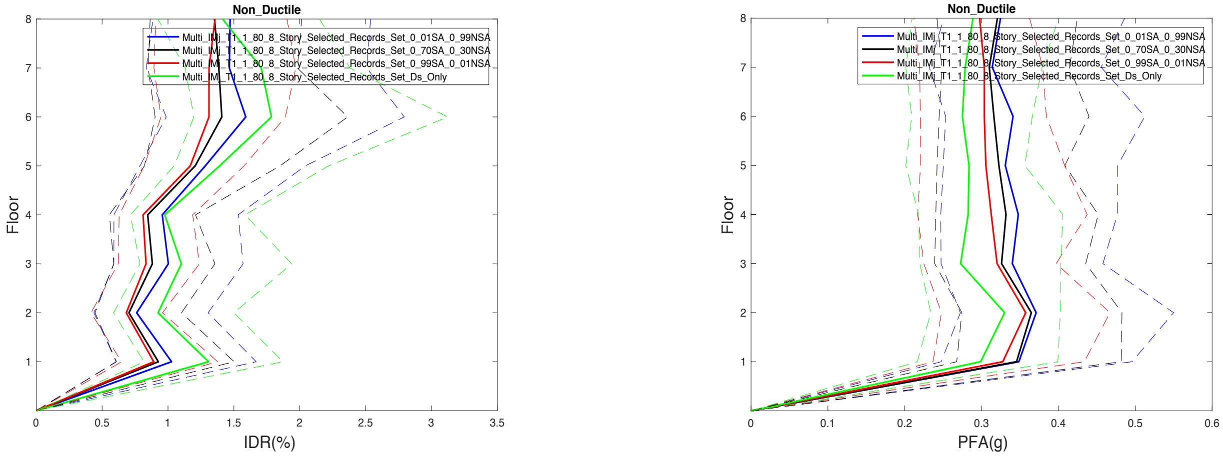

(a)

(b)

Figure 5.7. (a) and (b) Median (solid curves) and 16th and 84th percentiles (dashed curves) of $IDR(\%)$ and $PFA(g)$ for a 8-story non-ductile RC structure.

Last but not the least, a 12-story non-ductile RC structure is studied for which the results are presented in Figure 5.13. From Figure 5.13(a), it can, again, be observed that the records selected based on giving more emphasis to duration and cumulative characteristics resulted in larger median demand and variability in demand which can be noticed from the green, and blue curves. The variation in percentile responses is more tangible especially in the 84th percentile which is due to a more nonlinearity at higher drift levels.

When it comes to PFA as can be observed from Figure 5.13(b), again, the records selected based on cumulative effects have imposed a larger median demand and variability in demand as can be seen from the blue curves. Hence, identical trends were observed for all the previous structures as well.

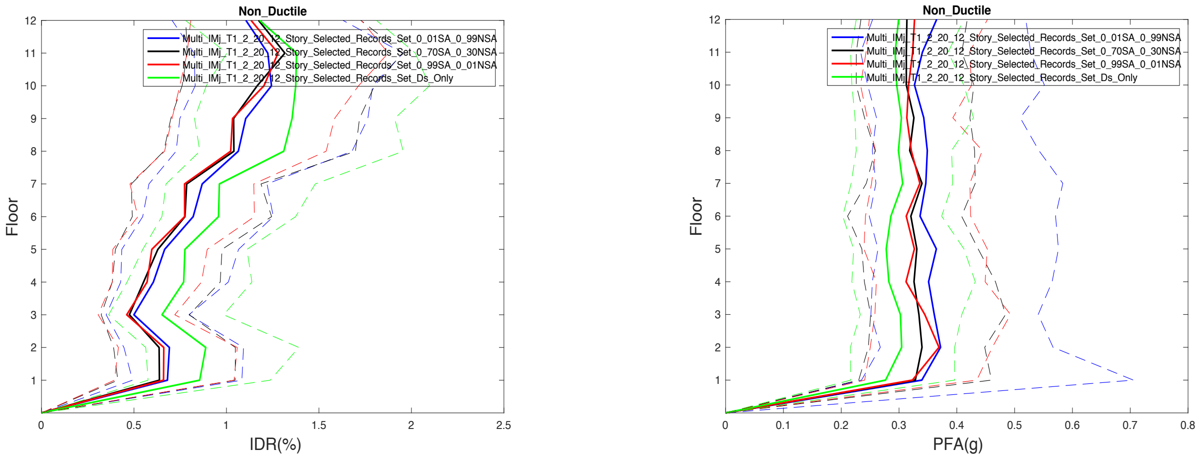
(a)

(b)

Figure 5.8. (a) and (b) Median (solid curves) and 16th and 84th percentiles (dashed curves) of IDR(%) and $PFA(g)$ for a 12-story non-ductile RC structure.

5.4.3.2 *Effects of conditioning intensity measure* (IM_j)

In this section the effects of ground motion records selected based on different conditioning algorithms (e.g. single-, double- and multiple-IM_j) on the statistics of various $EPDs$ will be studied. It should be noted that comparisons will be made using a specific set of weight factors based on which the records have been selected using different conditioning approaches. A thorough study of the effects of weights with respect to different contents of records were conducted in the previous section. Moreover, for the single conditioning record selection, in addition to the main IM_j which is $SAT1$, two additional suites will also be selected for which the IM_j is set as $SA(T = 0.2T1)$ and $SA(T = 3.0T1)$, respectively. Hence, average of responses obtained from these three sets will be computed. This could help to mitigate the drawback associated with the single suite selected conditioned on a single IM_j, which would not have sufficient contents to capture the seismic demand responses due to contribution of multiple modes.

5.4.3.2.1 Ductile reinforced concrete (RC) structures

Figure 5.14 demonstrates median (solid curves) and 16th and 84 percentiles (dashed curves) of the $IDR(\%)$ and $PFA(g)$ responses for a 4-story ductile RC structure with respect to different record sets selected based on various conditioning criteria.

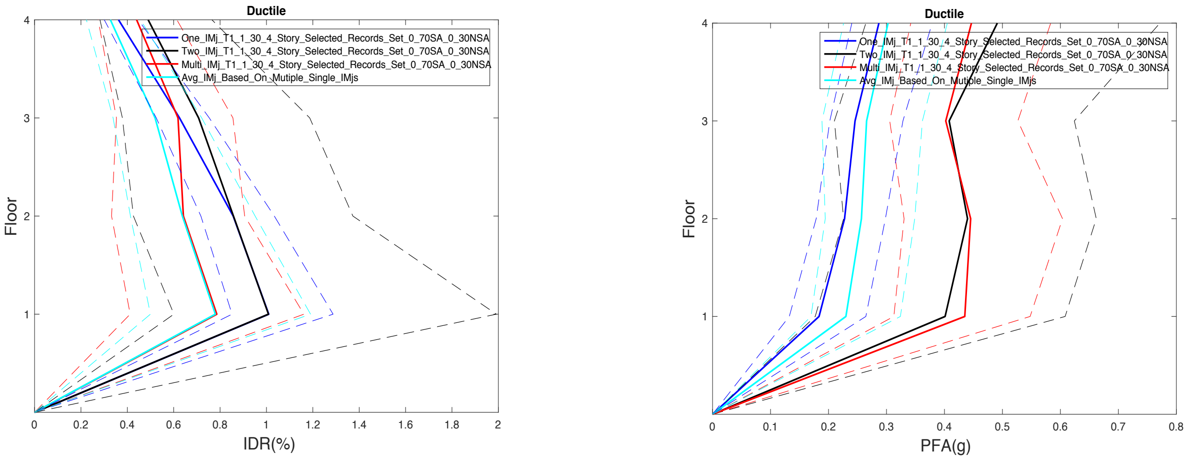
(a)

(b)

Figure 5.9. (a) and (b) Median (solid curves) and 16th and 84th percentiles (dashed curves) of $IDR(\%)$ and $PFA(g)$ for a 4-story ductile RC structure.

From Figure 5.14(a), it can be noticed that the record sets selected based on single- and double-IM_j impose a larger demand and variability in demand with respect to both median and percentile demands (see the blue and black curves). Hence, the records selected based on multiple IM_j and an average-based approach (i.e. average of demands obtained using multiple single-IM_j

suites) could predict the lowest demand. This makes sense for a ductile structure with a lower level of drift demand where the first mode of vibration is dominant. Hence, records selected based on single IM_j (i.e. $SAT1$) have sufficient contents to capture the response in the first mode. The suite selected based on two-IM_j imposes similar demands as the one with single IM_j and that's mainly because those records have been selected to be hazard-consistent over a range of periods including the fundamental period, so they have sufficient contents to capture the response in the dominant mode of vibration as well. An average-based approach whose results can be seen as the cyan curve and also a multiple-IM_j approach shown in red have both underestimated the response since they would lack the necessary contents to capture the response in the dominant mode.

From Figures 5.14(a) and (b), one could easily notice that when it comes to higher percentiles (e.g. 84th) there is more variation imposed using different suites which is stemmed from the fact that as the drift level increases, multiple modes of vibration begin to contribute as the structure starts undergoing some level of damage.

When it comes to PFA, the selected suites based on different conditioning approaches have slightly different impact as compared with the IDR which can clearly be noticed from Figure 5.14(b). As such, the suites selected based on two and multiple IM_j's have imposed the largest demand with respect to both of the medians and percentiles of the PFA. This clearly proves the contribution of multiple modes of vibration to predict the demand responses.

A similar study was carried out, this time however, on a 8-story ductile RC structure. Figure 5.15 presents the results. As can be noticed from Figure 5.15(a), the records selected based on one -and two-IM_j imposed the largest median and percentile demands. This was the case for the 4-story structure as well for which the underlying reasons were discussed. As per PFA, a similar conclusion as made for the 4-story can be made here as well. As can be seen in Figure 5.15(b), the suites conditioned on two and multiple $IM_j's$ impose the largest median and percentile demands (see the red and black curves).

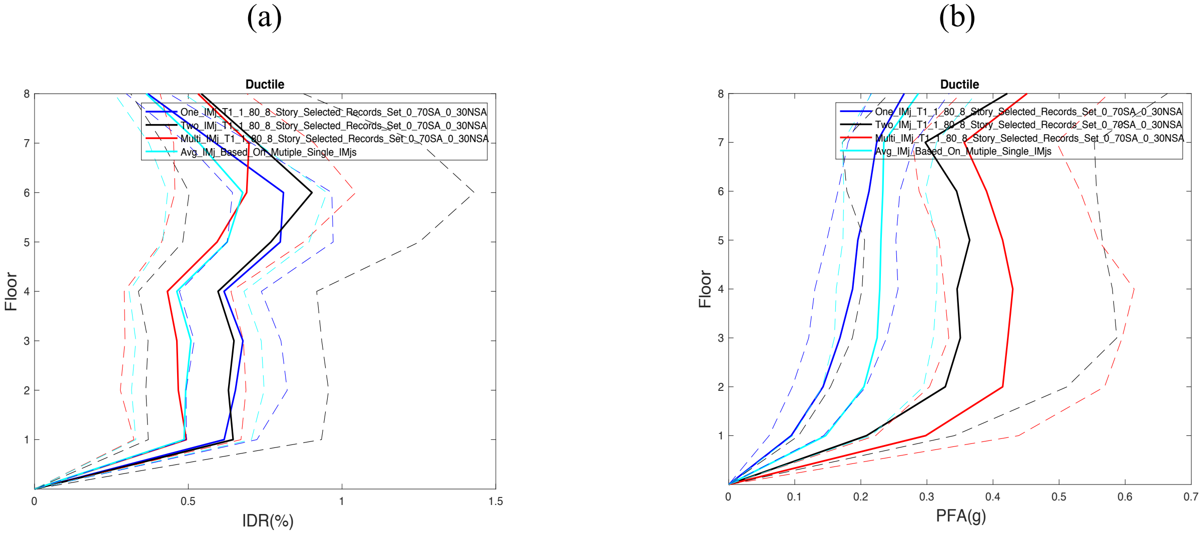
(a)

(b)

Figure 5.10. (a) and (b) Median (solid curves) and 16th and 84th percentiles (dashed curves) of $IDR(\%)$ and $PFA(g)$ for a 8-story ductile RC structure.

Last but not the least, a 12-story ductile RC structure is studied for which the results are presented in Figure 5.16. From Figure 5.16(a) it can be noticed that, again, the suites selected based on single- and two- IM_j have imposed the largest median and percentile demands, which can be noticed from the blue and black curves, respectively. This is consistent with the outcomes which have already been discussed so for the sake of brevity will no longer be discussed herein. As per PFA, similar conclusions drawn for the 4- and 8-story, can be made for the 12-story as well. As such, the suites selected based on multiple and two conditioning approaches imposed the largest median and percentile demands as can be noticed from the red and black curves in Figure 5.16(b).

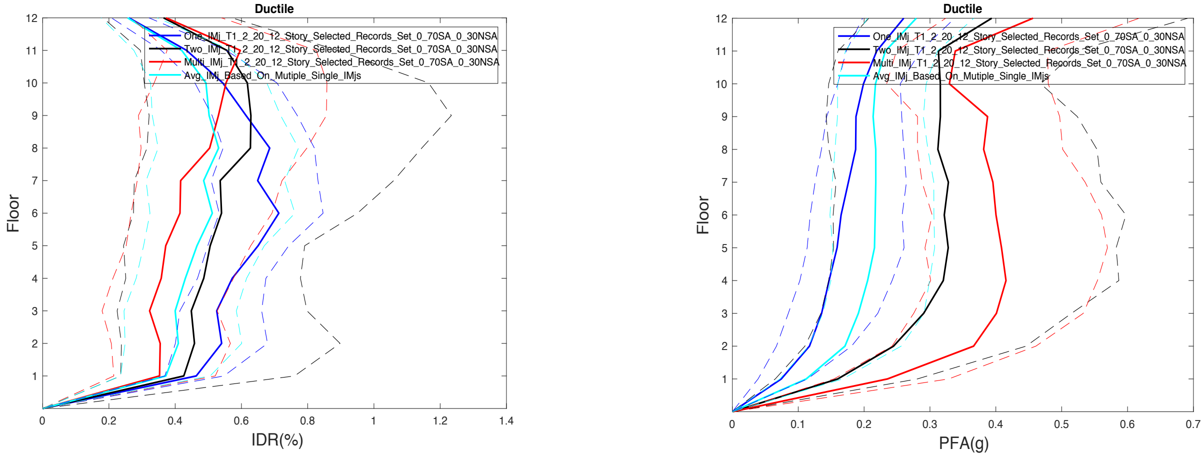
(a)

(b)

Figure 5.11. (a) and (b) Median (solid curves) and 16th and 84th percentiles (dashed curves) of $IDR(\%)$ and $PFA(g)$ for a 12-story ductile RC structure.

5.4.3.2.2 Non-Ductile reinforced concrete (RC) structrues

A similar type of analysis carried out for the ductile RC structures, will be conducted for the non-ductile RC structures, herein, and the results will be presented. Figure 5.17 demonstrates the outcomes for a 4-story non-ductile RC structure.

As can be observed from Figure 5.17(a). the suite selected based on two-IM_j has imposed the largest median and percentile demands (see the back curves). After that, the suites selected based on one and multiple conditioning $IM_j's$ impose the largest demands. The demand obtained using an average-based approach seems again to have underestimated the response. The efficiency of the records conditioned on two-IM_j in estimating the median response stems from the fact that as the non-ductile structures starts to experience some level of damage at a lower drift level, multiple modes of vibration would come to play a role, thereby those suites that are hazard-consistent over a range of periods including the fundamental period would perform better in capturing the median demand as is the case for the records selected based on two-IM_j approach.

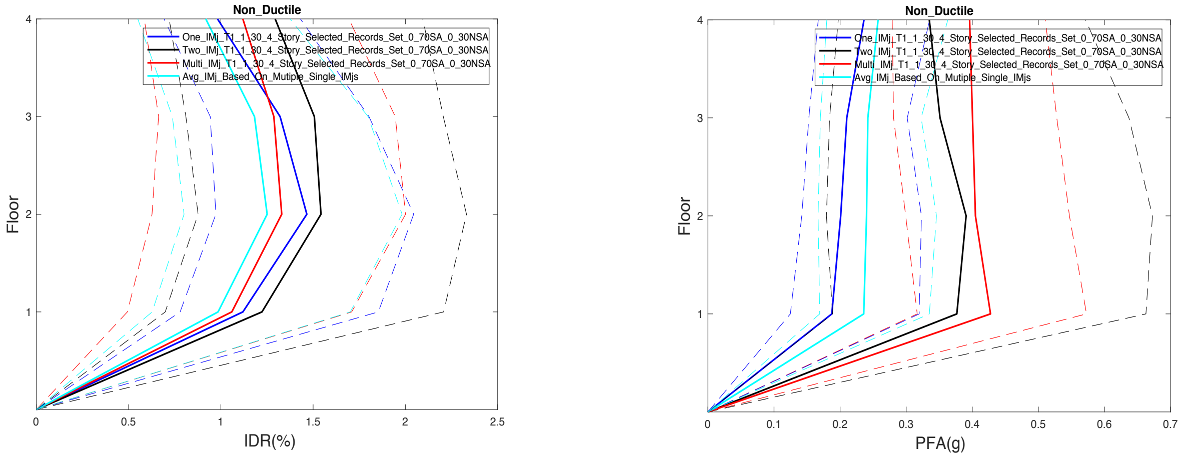
(a)

(b)

Figure 5.12. (a) and (b) Median (solid curves) and 16th and 84th percentiles (dashed curves) of IDR(%) and $PFA(g)$ for a 4-story non-ductile RC structure.

As per the PFA, as demonstrated in Figure 5.17(b), just like the ductile case, the suites selected based on multiple and two $IM_j's$ have imposed the largest median and percentile demands. As such the single-IM_j conditioning suite, as can be noticed from the blue curve, has underestimated the demand. This proves the efficiency of the records selected with respect to the hazard-consistency over a range of conditioning periods rather than just a single one as is the case with the single IM_j conditioning approach.

A similar study was carried out, this time however, on a 8-story non-ductile RC structure. Figure 5.18 presents the results. As can be noticed from Figure 5.18(a), the suites selected based on the single- and two-IM_j approaches have produced the largest median IDR demands, which can be noticed from the blue and black curves, respectively.

As per PFA, the multiple- and two-IM_j conditioning approach have, once again, produced the largest median and percentile demands.

`

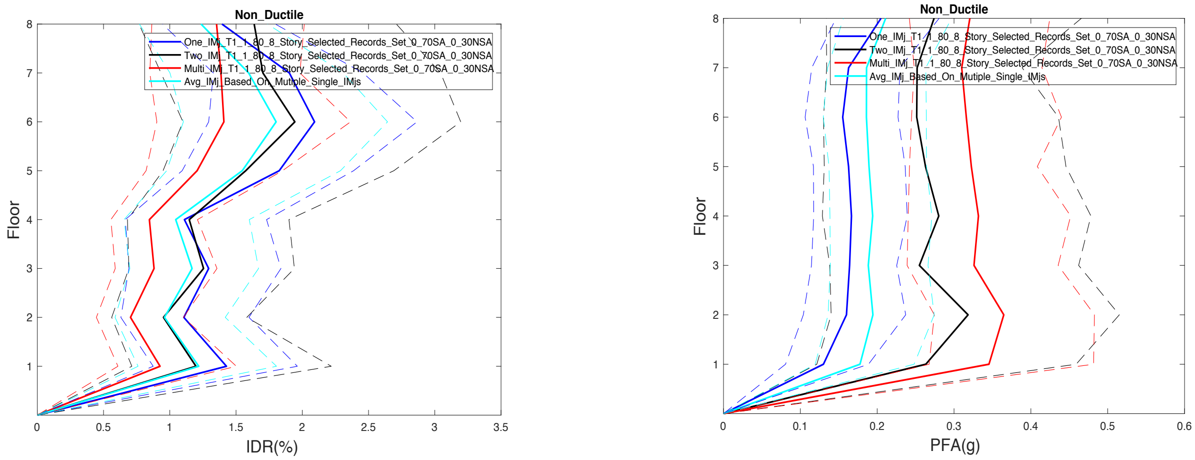
(a)

(b)

Figure 5.13. (a) and (b) Median (solid curves) and 16th and 84th percentiles (dashed curves) of $IDR(\%)$ and $PFA(g)$ for a 8-story non-ductile RC structure.

Lastly, a 12-story non-ductile RC structure is studied for which the results are presented in Figure 5.19. Figure 5.19(a) shows the median and 16th and 84th percentiles of IDR and Figure 5.19(b) shows the same things but this time for the PFA. From Figure 5.19(a), it can, once again, be noticed that the suites selected based on single- and two-IM_j approaches have been able to impose the largest median and percentile demands. As per the PFA, it can be observed from Figure 5.19(b), again, that the suites selected based on multiple and two conditioning approaches have been able to impose the largest demands, which was the case for all the structures that were studied in the preceding sections.

It should also be added that the poor performance of the suites selected base on multiple-IM_j could be attributed to the fact that those suites were not hazard-consistent at the structural fundamental period (see the cyan curve in Figure 5.6 in Chapter 5). As such, they underestimated the drift demand responses due to the inertia effects and the contribution of the first mode.

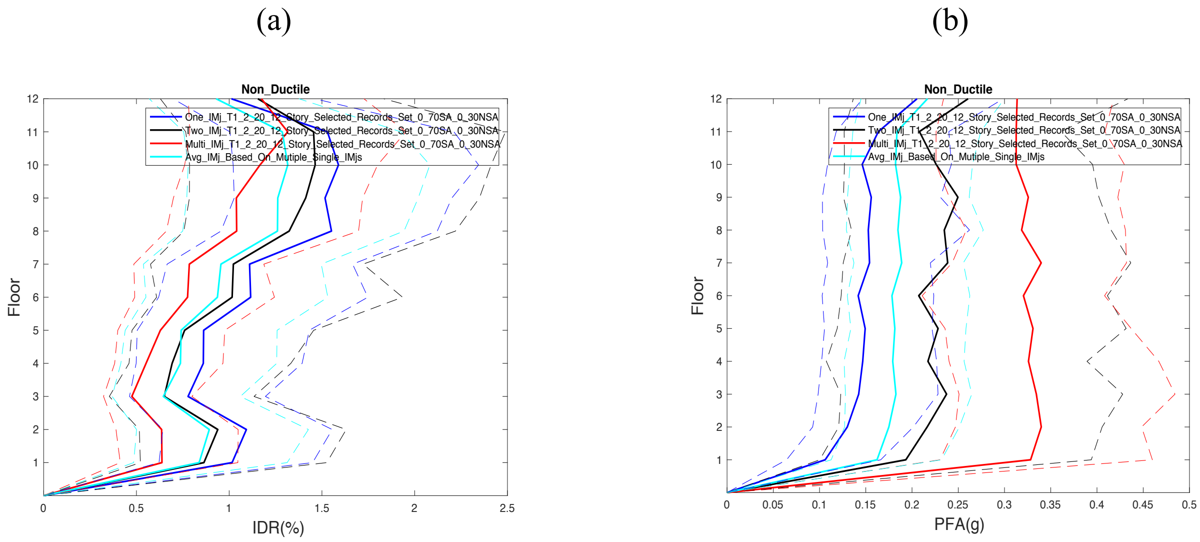

Figure 5.14. (a) and (b) Median (solid curves) and 16th and 84th percentiles (dashed curves) of $IDR(\%)$ and $PFA(g)$ for a 12-story non-ductile RC structure.

5.4.3.3 Ductile versus non-ductile RC structures

Figures 5.20-5.22 are presented here to render the effects of building type (i.e. ductile versus non-ductile) with respect to various demands for a 4-, 8- and 12-story RC structure, respectively. It is worth noting that all of the respective comparisons with respect to importance weights, conditioning methods, etc. have already been carried out in the preceding sections. As such, the following figures are presented herein just for the sake of demonstration and the rest of results are omitted for the sake of saving the space.

As can be observed from all of the figures listed below, the median demands and also the associated percentiles are both larger for non-ductile cases compared with those of the ductile. The median demands are more similar for both building types in the plots of PFA compared to those of the IDR. It can also be noticed that non-ductile cases have a wider range in the percentiles response as opposed to those of the ductile proving a higher level of nonlinearity that non-ductile structures experience at lower levels of drift demand.

(a) (b)

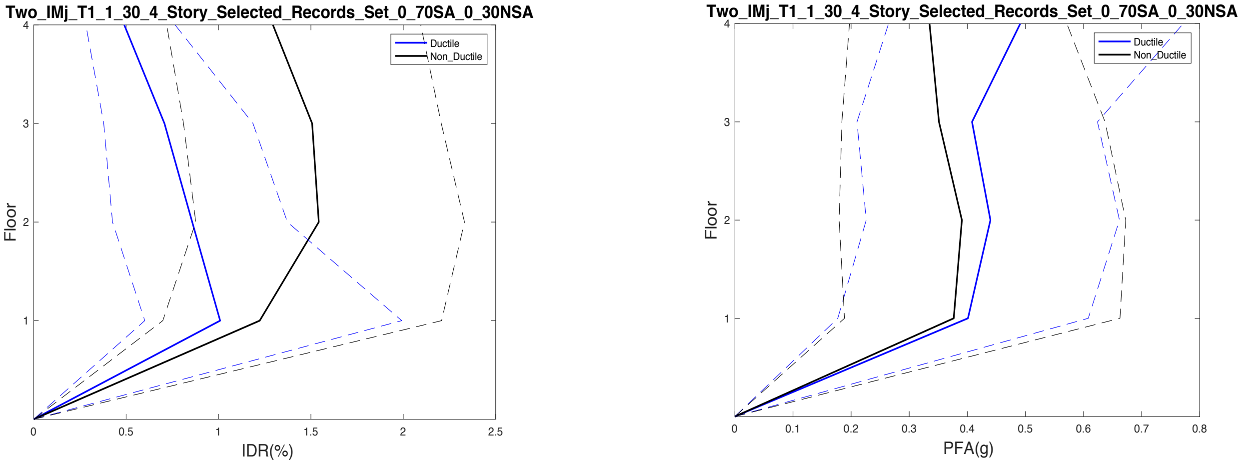

Figure 5.15. (a) and (b) Median (solid curves) and 16th and 84th percentiles (dashed curves) of $IDR(\%)$ and $PFA(g)$ for 4-story ductile and non-ductile RC structures.

(a) (b)

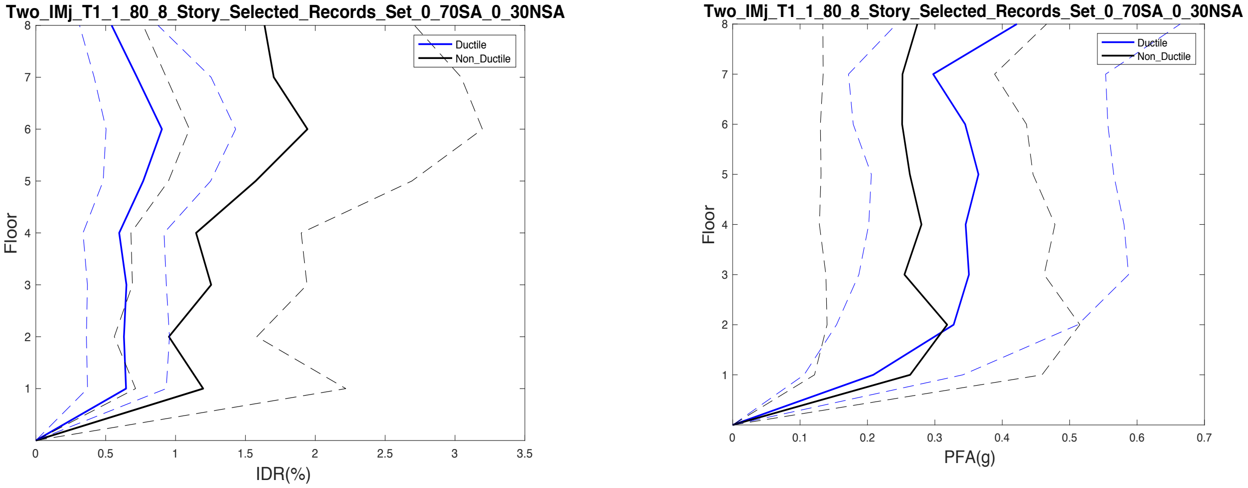

Figure 5.16. (a) and (b) Median (solid curves) and 16th and 84th percentiles (dashed curves) of $IDR(\%)$ and $PFA(g)$ for 8-story ductile and non-ductile RC structures.

`

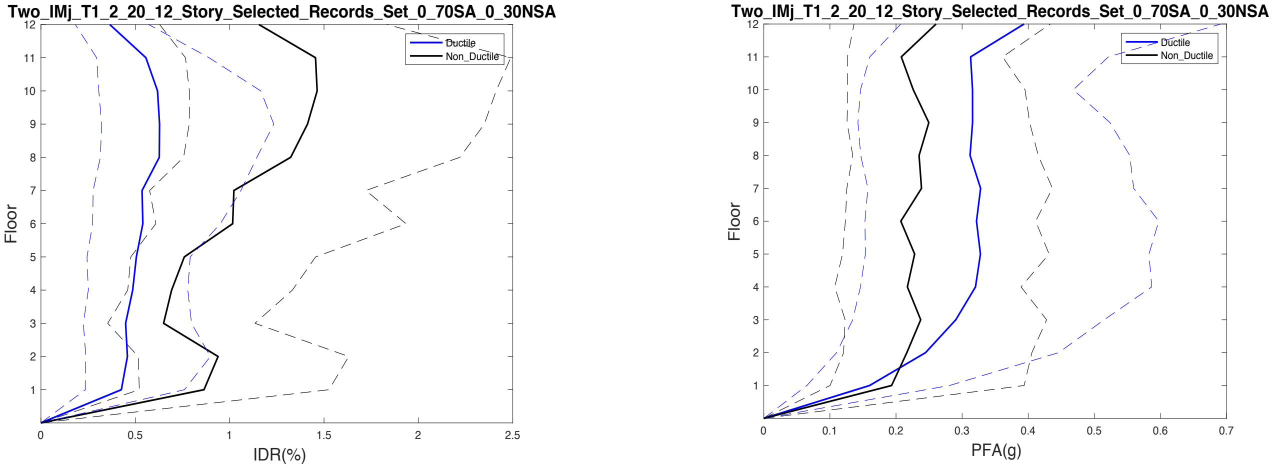
(a) (b)

Figure 5.17. (a) and (b) Median (solid curves) and 16th and 84th percentiles (dashed curves) of $IDR(\%)$ and $PFA(g)$ for 8-story ductile and non-ductile RC structures.

5.5 DISCUSSION

So far, the effects of a set of different parameters on the statistics of various demand responses for a set of different structures have been studied for both ductile and non-ductile RC structures. One of the approaches, which was utilized to mitigate the potential drawback with using records conditioned on a single IMj, was to use multiple suites of earthquake records selected based on multiple single IMj's and then take the mean of the structural response obtained by using each of those suites. That approach, however, in most of the cases, as seen in pervious sections ended up with producing results which underestimated the responses compared to other conditioning algorithms which were also used to select earthquake records.

To explore this further, another approach is adopted here based on taking the maximum of the responses to be obtained using multiple single- IMj suites which is called the maximum- IMj approach, hereafter.

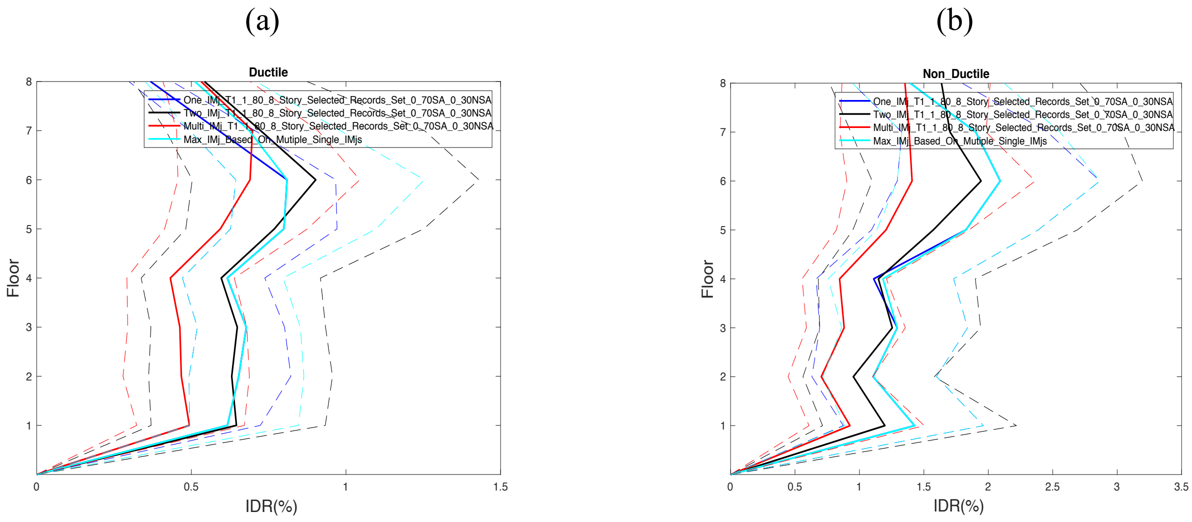

Figure 5.18. (a) and (b) Median (solid curves) and 16th and 84th percentiles (dashed curves) of $IDR(\%)$ for a ductile and non-ductile 8-story RC structure.

Figure 5.23 shows the IDR outcomes for a ductile and non-ductile 8-story RC structure. It should be added that the exactly identical results were obtained for the 4- and 12-story which are not repeated here. As can be seen from both graphs in Figure 5.23, the maximum-IMj approach results in a demand which is exactly identical to the results based on a single IMj approach, in both ductile and non- ductile cases. That means that of three record sets with different conditioning $IMj's$ (e.g. $SA(T = 0.3T1), SAT1 \; and \; SA(T = 3.0T1)$, the record conditioned on $SAT1$ produces the maximum demand. This proves that the other sets produce much smaller demands so that in the average-IMj approach, the average of responses obtained from the three sets became small, in most of the cases as observed in the previous sections. Another conclusion that can be made here would be that the structures are not sensitive to the spectral contents at the very short and long periods and therefore will not be excited by those records selected based on a very low or high conditioning periods so that the associated demands will be lower as opposed to the suite which was conditioned on $SAT1$.

`

As per PFA demand, Figure 5.24 presents the results for a 8-story ductile and non-ductile structure.

As can be observed from both graphs in Figure 5.24, the maximum- IMj approach produces larger PFA demands, very close to those obtained using the record conditioned on multiple- IMj. Whereas, the average- IMj approach, as observed previously, underestimated the PFA by producing the smallest demands as compared with the rest of conditioning methods.

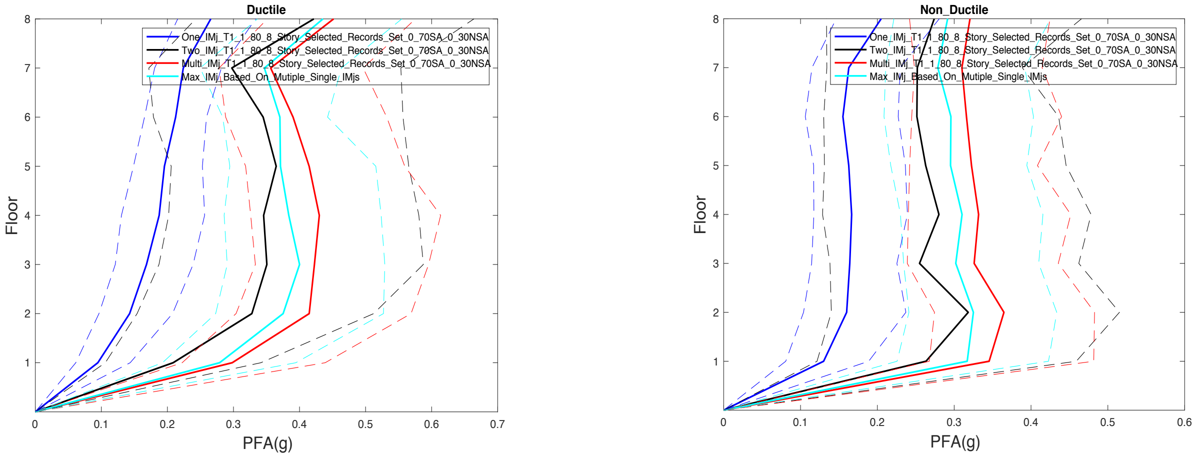
(a) (b)

Figure 5.19. (a) and (b) Median (solid curves) and 16th and 84th percentiles (dashed curves) of $PFA(g)$ for a ductile and non-ductile 8-story RC structure.

In summary, it can be concluded that the maximum-IMj approach is superior over average- IMj, as it produces more reasonable demands with respect to both drift and acceleration for ductile and non-ductile buildings.

5.6 CONCLUDING REMARKS

Applications of various ground motion selection, scaling and modification techniques on estimating the seismic responses of a set of different types of structures were explored. Different conditioning approaches in selecting hazard-consistent suites of earthquake records have been adopted and the effects on the seismic responses of both ductile and non-ductile RC structures with varying heights, were investigated. It was concluded that depending on the type of structure and the level of demand the structure undergoes, the ground motion suites selected to be hazard-consistent over a range of spectral ordinates including the one associated with the fundamental period of the structure, have been able to capture the seismic demand responses, in a more realistic way. As such, one of the major conclusions that can be made is that the two-IMj conditioning approach could probably be deemed as the most reliable approach for ground motion selection purposes to produce unbiased demands. Moreover, dispersion in the demand responses with respect to both median and percentiles of the demands had increased in non-ductile structures as opposed to those of the ductile. This can be a direct consequence of higher drift level that the non-ductile structures would undergo as a result of cumulative damage. As such, multiple modes of vibration begin to contribute, thereby other contents of earthquake records come to play role in capturing the demand responses. This would be the main reason for the observed contrast which was observed between the demand responses using different suites.

Moreover, the effects of considering different characterizations of earthquake record, through selection of multiple suites, on the seismic responses of different types of structures were explored. It was concluded that for ductile structures using suites selected based on giving more emphasis to their amplitude-based contents ended up in a better estimation of demand responses. Moreover, it was found that when the drift demand is low, as is the case for the ductile structures, assigning various weight factors to different intensity measures during the selection phase does not make a noticeable difference, in most cases, especially when multiple modes of vibration do not contribute much. Whereas, for the non-ductile structures where the cumulative- and duration-based characteristics of records begin to contribute, a larger contrast was observed between the responses especially at the higher percentiles.

Last but not the least, a maximum-based approach was suggested over an average-based, to compute the demands when multiple suites of records conditioned on different $IMj's$ had been utilized. This approach was mainly proposed to compensate for a potential drawback of the single-IMj approach in estimating the demands especially for those structures which experience changes in their fundamental period.

6 APPLICATION OF DIFFERENT SAMPLING TECHNIQUES FOR DEVELOPING HAZARD-CONSISTENT TARGET INTENSITY MEASURES

6.1 INTRODUCTION

Due to various sources of uncertainty in the fields of probabilistic seismic hazard analysis ($PSHA$) and ground motion selection, scaling and modification, using probability density functions for different contributing parameters are very common. As such, various parameters which would be deemed as uncertain are often represented by probability distribution functions ($PDFs$) from which one could draw any desirable number of realization samples using different sampling techniques.

In $GMSSM$, it is common that the ground motion earthquake records are selected with respect to the hazard-consistency meaning that the seismicity of any site of interest for which the ground motion records are selected are fully incorporated into the ground motion selection phase.

Ground motions need often to be selected for the purpose of seismic evaluation and design of different types of structures. It is common to select a number of earthquake records rather than only a single record for the purpose of seismic evaluation of buildings, and that is mainly due to the aleatoric variability in earthquake records. Moreover, given the type of structure being analyzed, different characteristics of an earthquake record would play role in capturing the structural response over multiple modes of vibration of the structural system. As such, ground motion selection phase is of paramount importance so that records which can properly excite a structural system and predict the seismic demand responses over multiple periods of vibration, need to be selected.

6.2 SCOPE AND MOTIVATION

An earthquake record contains a set of different characteristics (e.g. amplitude-, frequency-, cumulative- and duration-based) which need to be considered during the selection phase. It is very common that various characteristics of an earthquake records are often represented with different intensity measures ($IM_i's$). In the field of earthquake engineering, these $IM_i's$ are considered as uncertain whose uncertainties can be quantified by using the so-called ground motion prediction equations ($GMPEs$) (e.g. (Campbell & Bozorgnia, 2012)) which provide essential parameters to define the distribution of $IM_i's$. These $IM_i's$ are also often correlated and there are empirical relationships (e.g. (Bradley, 2011)) to provide the correlation coefficients between them. Hence, one could fit a multivariate distribution into a number of $IM_i's$ knowing the distribution of each from a $GMPEs$ and the cross correlation between them from some empirical relationships.

The number of $IM_i's$ to be utilized for the purpose of ground motion selection is dependent on the type of structural system for which the ground motions are selected. As such, after setting forth a number of $IM_i's$ and by forming the multivariate distribution given the information provided in the preceding paragraph, one could draw any desirable number of samples from the corresponding marginal distributions of different $IM_i's$. Hence, the application of different sampling techniques has to be incorporated in this stage. Thus, any sampling technique providing a more identical empirical distributions of the realization samples with respect to those of the theoretical marginal distribution from which these samples were drawn, is deemed suitable. Hence, the last stage of ground motion selection would be to select earthquake records whose characteristics are identical to those of the realization samples.

Given the information provided in the preceding paragraph, this research is aimed to investigate the application of different sampling techniques in the area of ground motion selection, scaling and modification. The prime goal would then be to apply these sampling techniques to generate realization samples for various hazard- consistent target $IM_i's$ which will be utilized in $GMSSM$.

6.3 A REVIEW OF PRIOR STUDIES

6.3.1 Background

Of different sampling techniques which are commonly used to draw realization samples from any type of distribution, the Monte Carlo (MC) and the Latin Hypercube Sampling (LHS) techniques will be utilized herein. The Monte Carlo (MC) sampling method which can be deemed as a brute-force technique, has been widely used in several engineering fields including the earthquake engineering. As such (Bradley, 2010), (Bradley, 2012) (Tarbali & Bradley, 2015), (Tarbali & Bradley, 2016), and (Tarbali, et al., 2018) have all utilized the MC in order to draw realization samples from various distributions associated with different $IM_i's$ which were ultimately used for the purpose of ground motions selection.

The LHS, though, has not been broadly used in the field of earthquake engineering despite of its wide application in various other fields of engineering. (Vorechovsky & Novák, 2009) combined the MC and LHS in order to draw a smaller number of samples from a multivariate distribution of various parameters to match the theoretical marginal distribution of each parameter as well as the covariance matrix of all the parameters. (Dolsek, 2009) utilized the LHS to draw realization samples from the PDF of various structural modeling parameters to consider the epistemic variability in those parameters in addition to the variability in ground motions to perform a set of incremental dynamic analyses. (Chouna & Elnashai, 2010) utilized a simplified method based on modifying the quantile athematic methodology in comparison with the MC, in order to consider the epistemic variability associated with different parameters involved in seismic loss assessment of structures. (Zhongxian, et al., 2014) studied the effects of variability in ground motions and also some of the structural modeling parameters on the probabilistic seismic response of bridges. They used the LHS to consider the effects of epistemic variability in structural modeling parameters. (Decò & Frangopol, 2013) used the LHS to generate random earthquakes for the purpose of life-cycle risk assessment of bridges. (Celarec & Dolšek, 2013) studied the effect of variability in structural modeling parameters on the probabilistic seismic risk of reinforced concrete (RC) structures by using a first- order-second-moment ($FOSM$) reliability approach combined with LHS.

(Decò, et al., 2013) utilized the MC and LHS to consider the effects of uncertainty associated with expected damage, restoration process, and rehabilitation costs with respect to the resilience-based seismic assessment of bridges. (Kosič, et al., 2014) studied the probabilistic response of RC structures using a single degree of freedom ($SDOF$) structural system instead of modeling the entire structural system. They used the LHS to consider the effects of structural modeling parameters and also used a suite of ground motion records in order to incorporate the effects of record-to-record variability in ground motions. (Vamvatsikos & Fragiadakis, 2010) performed an incremental dynamic analysis (IDA) on a 9-story moment-frame steel structure considering the effects of epistemic variability in structural modeling parameters and also variability in ground motion earthquake records. They used different methods such as MC mixed with LHS as well as $FOSM$ to consider the effects of aforementioned variability.

(Bucher, 2009) used the MC mixed with LHS for the purpose of optimization and design of seismic isolation devices to be incorporated into various structural systems. (Pan, et al., 2007) utilized the LHS and a restricted pinning approach in considering the uncertainty in various modeling parameters of the steel bridges. They also considered the simultaneous effects of variability in ground motion earthquake records and studied the corresponding impacts of both sources of uncertainty on the seismic demand fragilities for various components of the bridges. (Tubaldi, et al., 2012) utilized the MC mixed with LHS for the purpose of uncertainty propagation into the structural models, in order to perform seismic damage assessments on multi-span continuous bridges with dissipative piers and a steel-concrete composite deck. (Vamvatsikos, 2014) adopted the MC mixed with LHS to incorporate the effects of uncertainty in structural modeling parameters on the IDA which is used to assess seismic response of structures at various damage limit states.

6.3.2 The state of research

The main purpose of this research is to study the application of both MC and LHS techniques in the area of ground motion selection, scaling and modifications. As such, these methods will be utilized to draw realization samples form a multivariate distribution of various IM_i's. In order to do so, a comprehensive and robust algorithm to generate hazard-consistent targets of various $IM_i's$, which was developed in Chapter 2, will be utilized. A set of comparisons will then be made to compare the efficiency of the aforementioned sampling methods with respect to the statistics of the realization samples drawn from the theoretical marginal distribution of each IM_i.

6.4 MONTE CARLO AND LATIN HYPERCUBE SAMPLING TECHNIQUES

The underlying framework to which different sampling techniques will be applied which is the main focus of this study, was developed in Chapter 2 and will not be repeated, herein. Hence, the goal is to apply both of the MC and LHS sampling methods in order to draw realization samples for various $IMi's$ which can be represented with a theoretical multivariate distribution.

6.4.1 Monte Carlo sampling technique

Given the conditioning logarithmic median, and standard deviation of each IM_i and also the correlation between various $IM_i's$, all derived in Chapter 2, a multivariate normal distribution can be fitted into an IM_i vector consisting of several $IM_i's$. Moreover, marginal distribution of each IM_i considering its correlation with others can be obtained. One could then draw any desirable number of samples from the marginal distribution of each IM_i following the procedure listed below.

Following Bradley (2012), a two-level approach will be adopted herein, to draw realization samples of each IM_i from conditional multivariate distribution of various IM_i's, which was defined in Chapter 2 based a single-, two-, and multiple-IM_j. This is done first by obtaining a random rupture probability (Rup^{nsim}) from a disaggregation density function. Then, to draw samples from a multivariate distribution, an uncorrelated standard normal random vector is defined (u^{nsim}) whose elements are drawn from a standard normal distribution, independently. Using this vector, a correlated vector can thus be defined as

$$v^{nsim} = Lu^{nsim} \tag{6.1}$$

where, L is the Cholesky decomposition of the correlation matrix which is

$$\rho_{lnIM|IM_{j,Rup}} = LL^T \tag{6.2}$$

where $\rho_{lnIM|IM_{j,Rup}}$ is the conditional correlation coefficient matrix given a specific rupture scenario. Using this, the realization sample for each IMi can be obtained through a MC-based approach as follows

$$lnIM_i^{nsim} = \mu_{lnIM_i|Rup,IM_j} + \sigma_{lnIM_i|Rup,IM_j} v_i^{nsim} \tag{6.3}$$

where $\mu_{lnIM_i|Rup,IM_j}$ and $\sigma_{lnIM_i|Rup,IM_j}$ are the logarithmic median and standard deviation of IM_i for a given rupture scenario (Rup) and conditioning intensity measure (IM_j), $v_i^{nsim} = v^{nsim}(i)$ is the ith element in v^{nsim} vector and $Rup = Rup^{nsim}$.

6.4.2 Latin Hypercube sampling technique

The Latin hypercube sampling (LHS) can be applied through a stratified sampling approach (see Figure 6.1). In order to draw realization samples from a distribution of an IM_i , its domain is stratified into N equally-spaced and non-overlapping intervals. Next is to randomly draw a sample from each of the interval. Hence, by utilizing a random permutation approach, a set of random LHS samples can be obtained. As such, the application of LHS to draw samples from a theoretical multivariate distribution of multiple $IM_i's$ can be summarized as:

1. Sample from the actual marginal distribution of each IM_i using LHS (Zhang & Pinder, 2003).
2. Derive the correlation matrix of the sampled realizations of various $IM_i's$.

3. Get the Cholesky decomposition of a Hermitian positive-definite matrix (L) of the correlation coefficient matrix (see Eq. 6.2). If L is not positive definite apply methods such as the one introduced by (Higham, 2002) to find the nearest PD matrix.
4. Add dependency between the independent samples drawn using LHS by transforming their governing normal distribution into a uniform distribution (this transformation preserves the dependency between the variables).
5. Map each of the $IM_i{}'s$ uniform distribution onto the associated probability distribution of each defined by a $GMPE$.
6. Obtain the correlation between the new realization samples in order to compare it with the original correlation of the multivariate distribution to make sure they are identical.

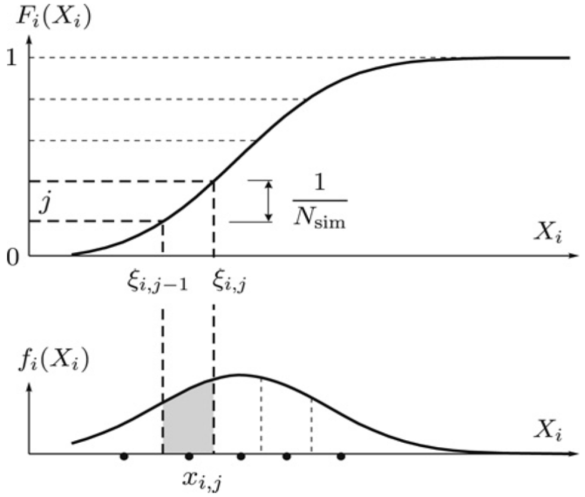

Figure 6.1. Schematic of the stratification of a variable distribution's domain using LHS (Adopted from (Vorechovsky & Novák, 2009)

6.5 APPLICATIONS

Applications of the methods described in the preceding sections are discussed in this section. For this purpose, first an IM_i vector has to be populated. As suggested by (Bradley, 2012), $IM_i = \{SA(T), AI, CAV, Ds575, Ds595\}$ where $AI, CAV, Ds575, Ds595$ are defined as Arias intensity, cumulative absolute velocity, 5-75% significant duration, and 5-95% significant duration, respectively. For computation of $SA(T)$, 21 different periods identical to those for which hazard curves can be generated, have been chosen. The $GMPE$s which are used to define the distribution of each of the IM_i in the IM_i vector are, (Boore & Atkinson, 2008) for $SA(T), PGA\ and\ PGV$, (Campbell & Bozorgnia, 2012) for AI , (Campbell & Bozorgnia, 2010) for CAV, and (Bommer, et al., 2009) for $(Ds575, Ds595)$.

In order to generate the multivariate distribution of IM_i's in the IM_i vector, a correlation matrix defining the cross correlation between various IM_i's should be obtained in addition to the median and standard deviation of each IM_i. For that, one would refer to Table. 1 in (Bradley, 2012).

As laid out in Chapter 2, three different algorithms were proposed to generate hazard-consistent target $IM_i's$ based on different conditioning approaches, namely, the single-, two-, and multiple-conditioning approach. As such, three different multivariate distributions for various $IM_i's$ can be generated with respect to different conditioning intensity measures $(IM_j's)$. The MC and LHS will then be utilized to draw 50 realization samples from the marginal distribution of each IM_i given their multivariate distribution and the performance of each method of sampling will be evaluated. Figure 6.2 shows the realization samples (blue curves) of response spectrum ($SA(T)$ at multiple periods) conditioned on a set of different $IM_j's$. The LHS was utilized to draw samples from the theoretical distribution of $SA(T)$ whose median (see the red solid curve), 16th and 84th percentiles (see the red dashed curves) are also shown in the figures. It is worth noting that the underlying algorithm to derive the theoretical multivariate distribution of various $IM_i{}'s$ is called the generalized conditioning intensity measure ($GCIM$) approach based on (Bradley, 2010) which is thoroughly explained in Chapter 2. It is also worth noting that the hazard-consistency is implemented by considering up to 2,000 rupture scenarios and their contribution to different conditioning intensity measures.

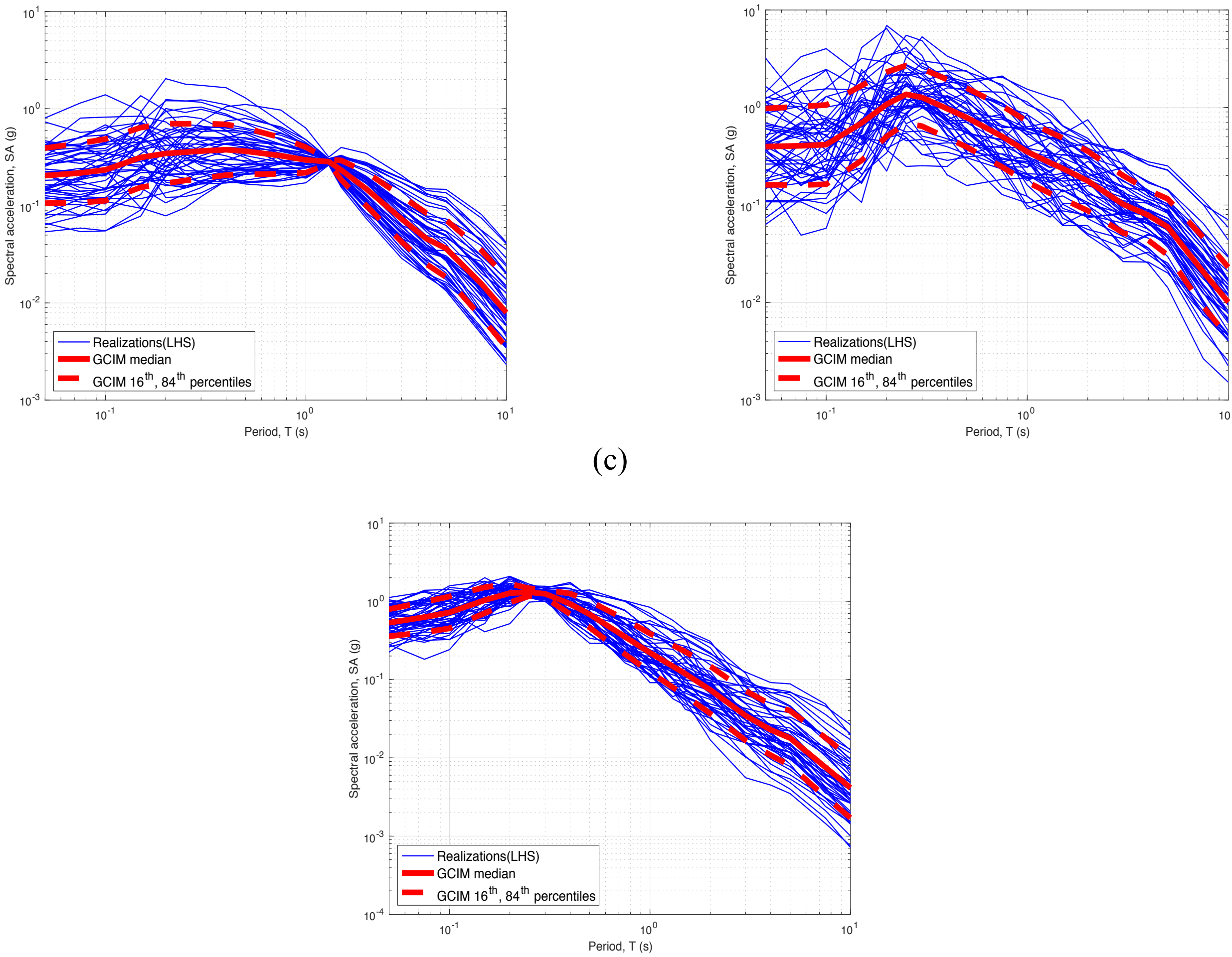
(a)

(b)

(c)

Figure 6.2. Theoretical distribution (red solid and dashed curves) as well as realizations samples (blue curves) for (a) single- , (b) two- , and (c) multiple-conditioning approach.

Figure 6.3 shows the comparison between empirical distributions of (a) $SA(T)$, (b) CAV, (c) AI and (d) $Ds595$ obtained using MC (shown in blue) and LHS (shown in red) with respect to the theoretical distribution ($GCIM$) (shown in black) for a single conditioning intensity measure case. As can be noticed from all the graphs, LHS performed better compared to MC with the same sample size. Hence, MC can be improved by increasing the sample size or repeating the procedure for a few more times to get better results.

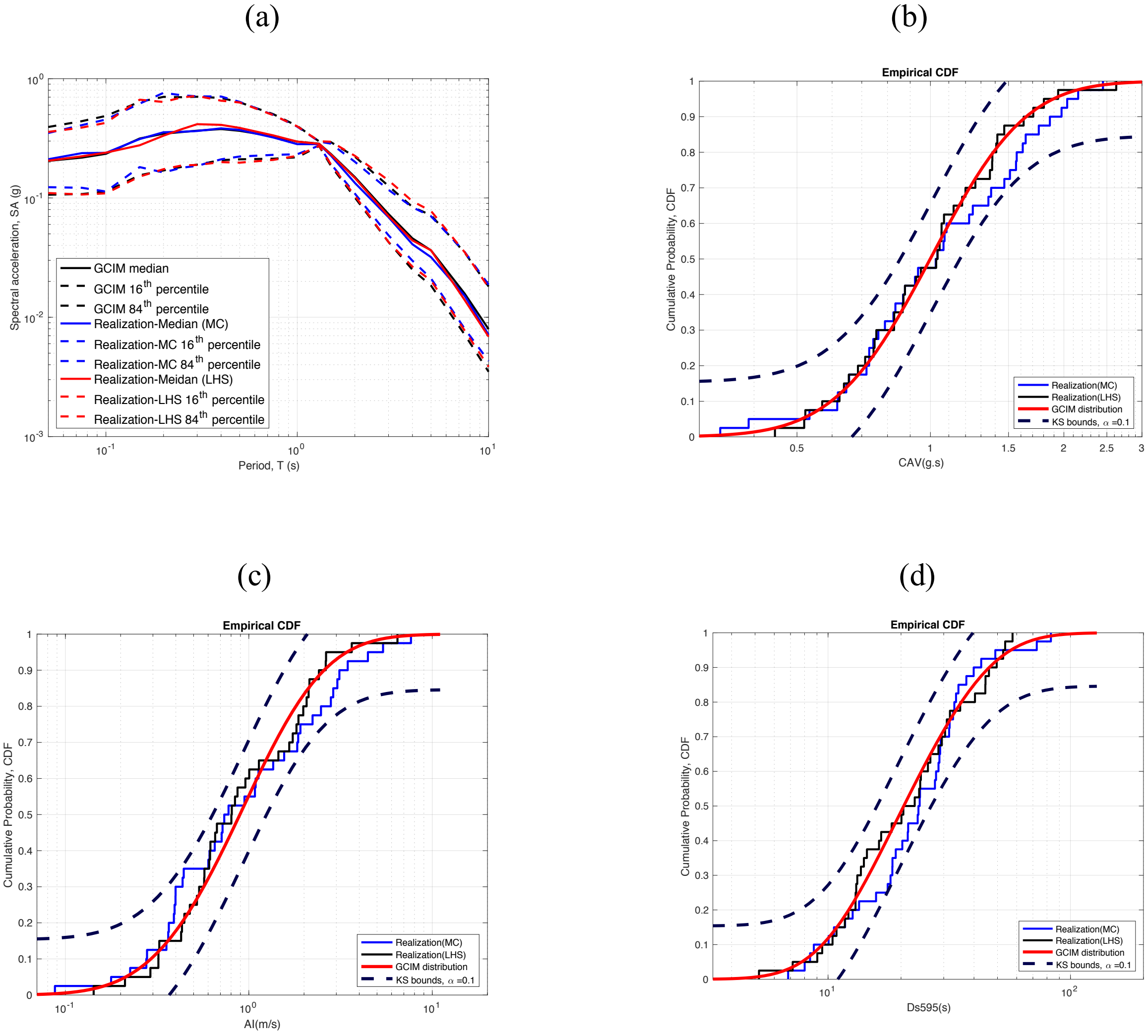
(a)
(b)
(c)
(d)

Figure 6.3. Comparison between empirical distributions of (a) $SA(T)$, (b) CAV, (c) AI and (d) $Ds595$ obtained using MC and LHS with respect to the theoretical distribution for a single-conditioning intensity measure case.

Figure 6.4 shows the comparison between empirical distributions of (a) $SA(T)$, (b) AI, (c) $Ds595$ and (d) $Ds575$ obtained using MC and LHS with respect to the theoretical distribution for a two-conditioning intensity measure case. Again, LHS performed better as is clear from all the graphs, as opposed to MC.

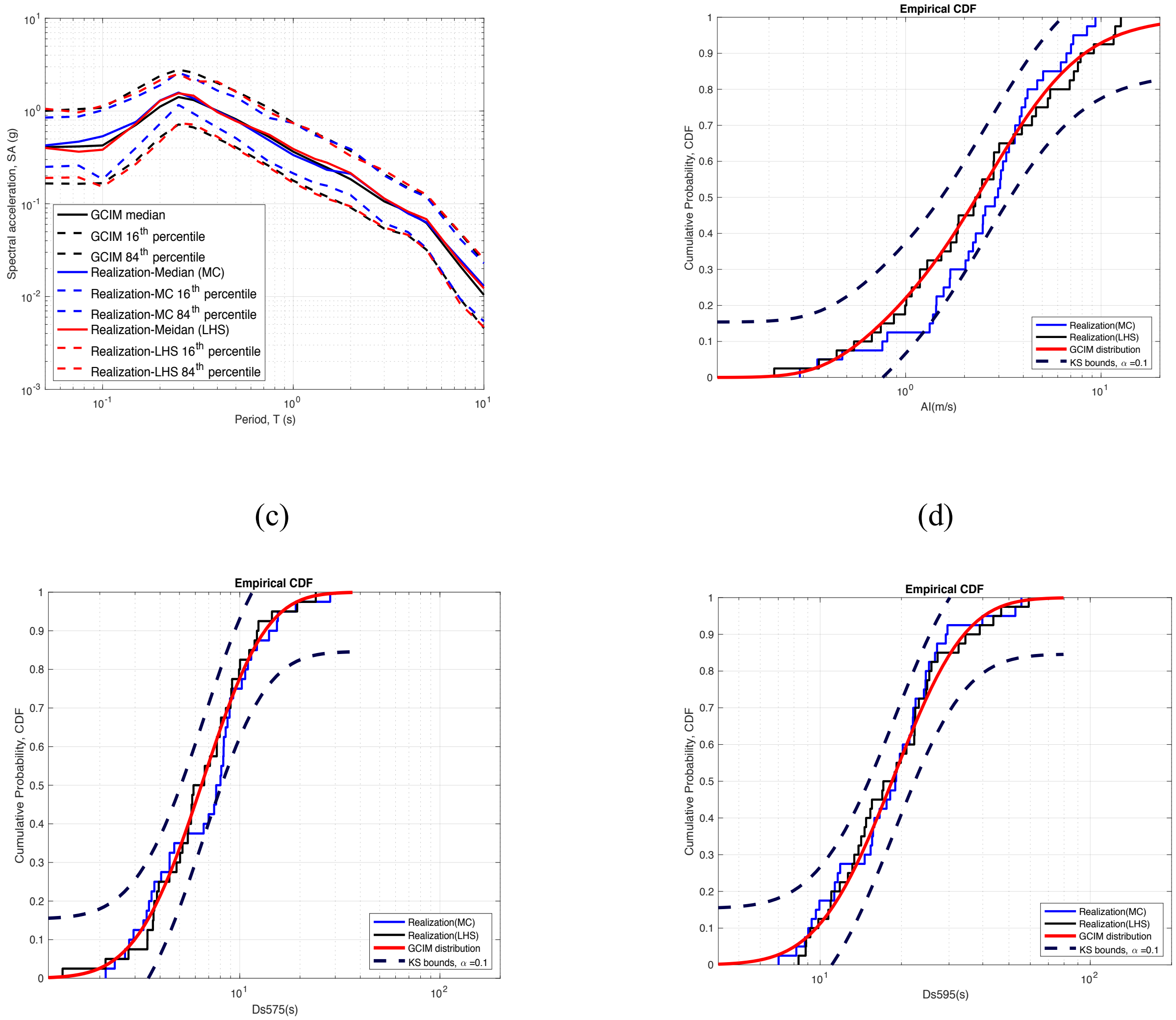
(a)

(b)

(c)

(d)

Figure 6.4 Comparison between empirical distributions of (a) $SA(T)$, (b) AI, (c) $Ds575$ and (d) $DS595$ obtained using MC and LHS with respect to the theoretical distribution for a two-conditioning intensity measure case.

Figure 6.5 shows the comparison between empirical distributions of (a) $SA(T)$, (b) AI, (c) $Ds575$ and (d) $Ds595$ obtained using MC and LHS with respect to the theoretical distribution for a multiple-conditioning intensity measure case. In case of multiple-conditioning intensity measure, LHS has again performed better than MC.

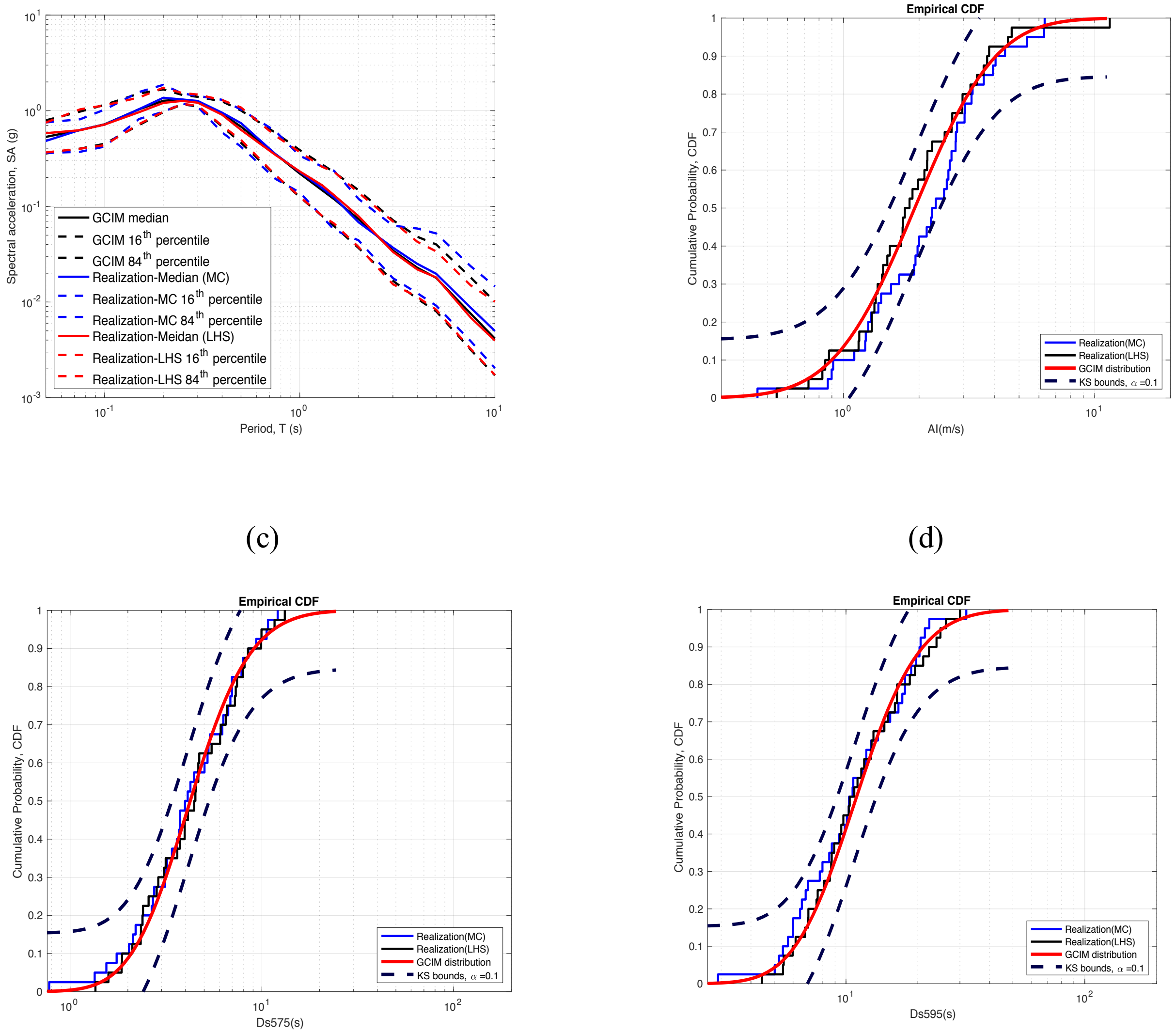
(a)

(b)

(c)

(d)

Figure 6.5. Comparison between empirical distributions of (a) $SA(T)$, (b) AI, (c) $Ds575$ and (d) $DS595$ obtained using MC and LHS with respect to the theoretical distribution for a multiple-conditioning intensity measure case.

In some of the graphs, it was seen that the blue curve which is obtained using MC intercepted the confidence bounds (dashed curves) meaning that those samples must be rejected.

However, none of the cumulative distributions obtained by LHS (see the black curves) hit the confidence bounds which means all of them are accepted.

The main reason why LHS performed better in all of the above cases can be attributed to the stratification strategy which made it possible to draw samples from the entire domain of distribution. Whereas in MC, since the samples are randomly drawn, as the number of samples are low, there is no guarantee that samples are drown uniformly from the entire distribution domain. Increasing the number of samples or executing the MC for a few more times would mitigate this problem.

6.6 CONCLUDING REMARKS

Application of two sampling techniques, namely the monte Carlo (MC) and the Latin hypercube sampling (LHS) was investigated in the field of earthquake engineering. As such, a multivariate distribution for a range of intensity measures ($IM_i's$) were defined and these sampling techniques were applied to draw realization samples from the marginal distribution of each IM_i. Different cases were investigated considering a range of different conditioning intensity measures. A thorough comparison was then made with respect to the application of these two methods to evaluate the performance of each for all of the cases being considered. It was observed, in all of the cases, that LHS performed better than MC assuming the same number of samples and executions for each sampling methods.

7 PERFORMANCED-BASED SEISMIC DESIGN OPTIMIZATION OF RC STRUCTURES

7.1 INTRODUCTION

Earthquake is a viable threat to the safety of our societies which could seriously put both of the people and infrastructure at risk. As such, there is a need for any type of building to be designed in accordance with the regional seismic codes and provisions, and those which are already in service must be reevaluated to assess their seismic performance. Due to various sources of uncertainty in seismic evaluation and design of structure, a probabilistic approach needs to be adopted. Hence, only through a probabilistic approach, it is possible to first quantify all sources of uncertainty involved in various stages of seismic evaluation and design of structures, and then take them into account in any type of structural analysis and design strategy.

There are several key ingredients in seismic evaluation and design of structures. Hence, ground motion earthquake records are one of the main components and an essential part of performance-based seismic evaluation and design of structures. Uncertainty in ground motions is called the record-to-record or aleatory variability in earthquake records. This indicates that, for instance, two earthquake records that seem identical in some of their characteristics, may differ in others. These differences in characteristics would impose variability on structural seismic demand responses. The only way to quantify this variability is to employ a ground motion suite consisting of several earthquake records rather than just a single record. It is also necessary that the ground motion suite is selected to be representing the actual seismicity of a site where the records are selected for in order to utilize them in seismic evaluation of a given structure located at that site.

Besides ground motion earthquake records, there is a variability in structural modeling parameters which is essential to be considered in performance-based seismic evaluation and design of structures as well. The simplified numerical models for various types of structures is key in an accurate estimation of seismic demand responses. Different types of structures would behave differently when they are subjected to ground motion earthquake records. There is a wide range of responses (e.g. linear elastic to nonlinear) that a structure would undergo depending on how well it was designed to withstand the seismic loads. Therefore, this needs to be incorporated in any structural modeling and various types of material models should be assigned to different elements across a given structure to enable an accurate seismic response assessment. As such, there is a considerable number of parameters, called the structural modeling parameters, which are the main ingredients of those material models.

Quantifying the uncertainty in structural modeling parameters are often carried out through experiments. As such, different components of a structure or a prototype model of it, will be simulated in a lab under identical gravity and seismic loads, as those the structure would actually be subjected to in real life, in order to calibrate the modeling parameters for a range of prescribed seismic performances. This, in itself, is subjected to uncertainties, associated with various ingredients of the experimental protocol.

It is often known that the variability in structural modeling parameters in the presence of the aleatory variability in earthquake records, would impact seismic responses of a given structure in different modes of vibration. Accordingly, along with the aleatory variability in earthquake records, the variability in structural modeling parameters would also have to be considered in any performance-based seismic evaluation and design of structures. It is also essential to find practical strategies to reduce the impact of this variability on seismic responses. This would be possible whether through improving the methodologies by which this type of uncertainty is quantified, or by using advanced methods of structural analysis integrated with different optimization techniques in order to minimize the effects of this variability.

7.2 SCOPE AND MOTIVATION

As explained in the previous section, the effects of both aleatory variability in ground motion earthquake records and also variability in structural modeling parameters would have to be considered in performance-based seismic evaluation and design of structures. Adopting appropriate strategies with regard to both trying to quantify these sources of uncertainty and also to reduce their impacts on the seismic responses of structures is of paramount importance. This is an essential task which needs to be undertaken for an accurate performance-based seismic evaluation and design of structures which is key for the subsequent damage and loss assessments.

As stated previously, performance-based seismic evaluation and design of structures has several key ingredients of which the ground motions are of paramount importance. Failing to accurately quantify the uncertainty associated with them as well as the underlying impact, would impose a considerable amount of dispersion on the seismic responses of various types of structural systems. As such, one or multiple hazard-consistent suites of earthquake records would often have to be selected for the purpose of the performance-based seismic evaluation and design of structures.

After ground motion earthquake records, the effects of structural modeling and the underlying parameters are of prime importance in the performance-based seismic evaluation and design of structures. With the advent of various numerical software which are available and being utilized in computer molding of various structural systems, the task of structural modeling would have never been as straightforward as is today. Hence, accurate modeling of structural components to actually enable users to capture the actual responses, has still remained a challenging task, especially when it comes to the seismic analysis and design of structures. As such, there is a considerable number of simplifying assumptions which need to be made in order to develop numerical models of structures. These assumptions could range anything from, using various structural elements with a set of different material types to capture a range of structural responses from elastic to nonlinear, or sticking to two-dimensional ($2D$) rather than three-dimensional ($3D$) modeling strategies. These assumptions, although often quite erroneous, would still be necessary as continuum modeling of a structure similar to the as-built condition is not an easy task if not impossible, or very costly in terms of computational resources to be utilized for this purpose.

In addition to the strategies to be adopted for structural modeling purposes, the properties of various materials to be utilized in different elements across a structure are key in an accurate performance-based seismic evaluation and design of structures. These are known as the structural modeling parameters which often are deemed as uncertain. Given the uncertainty associated with these parameters, it is often necessary to take a probabilistic approach rather than a deterministic one. As such, these uncertainties would have to be quantified and propagated into any performance-based seismic evaluation and design of structure. The effects of these uncertainties along with those which are due to ground motion earthquake records would often be undesirable as they cause dispersion, often quite significant, in structural demand responses which would impact the subsequent seismic damage assessment and loss evaluation.

As such, this research is aimed to study the effects of both uncertainties associated with the earthquake ground motion records and those due to structural modeling parameters on performance-based seismic evaluation and design of RC structures. An emphasis would be given to reducing the effects of uncertainty in structural modeling parameters through a performance-based optimization framework by which new designs with respect to various modeling parameters will be proposed given a set of different performance levels.

7.3 A REVIEW OF PRIOR STUDIES

7.3.1 Background

Pervious works on the effects of epistemic variability in structural modeling parameters are quite handful both in quantity and scope, especially when it comes to quantifying and somehow reducing this source of variability.

7.3.1.1 Effects of epistemic variability in structural modeling parameters

(Dolsek, 2009) utilized a sampling technique, namely, the Latin hypercube sampling (LHS) to draw realization samples from probability distributions ($PDFs$) of various structural modeling parameters to consider the epistemic variability in those parameters in addition to variability in ground motions to perform a set of incremental dynamic analyses. (Chouna & Elnashai, 2010) utilized a simplified method based on modifying the quantile athematic methodology in comparison with the Monte Carlo (MC) sampling technique in order to consider the epistemic variability associated with different parameters involved in seismic loss assessment of structures. (Zhongxian, et al., 2014) studied the effects of variability in ground motions and also some of the structural modeling parameters on the probabilistic seismic response of bridges. They used LHS to consider the effects of epistemic variability in structural modeling parameters. (Celarec & Dolšek, 2013) studied the effect of variability in structural modeling parameters on the probabilistic seismic risk of reinforced concrete (RC) structures by using a first- order-second-moment reliability approach ($FOSM$) combined with the LHS.

(Decò, et al., 2013) utilized the MC and LHS to consider the effects of uncertainty associated with expected damage, restoration process, and rehabilitation costs with respect to resilience-based seismic assessment of bridges. (Kosič, et al., 2014) studied the probabilistic response of RC structures using a single degree of freedom ($SDOF$) structural system instead of modeling the entire structural system. They used LHS to consider the effects of structural modeling parameters and also used a suite of ground motion records in order to incorporate the effects of record-to-record variability in ground motions. (Vamvatsikos & Fragiadakis, 2010) performed an incremental dynamic analysis (IDA) on a 9-story moment-frame steel structure with considering the effects of epistemic variability in structural modeling parameters and also the variability in ground motion earthquake records. They used different methods such as MC mixed with LHS as well as $FOSM$ to consider the effects of the aforementioned variability.

(Bucher, 2009) used the MC mixed with LHS for the purpose of optimization and design of seismic isolation devices to be incorporated into various structural systems. (Pan, et al., 2007) utilized LHS and a restricted pinning approach in considering the uncertainty in various steel bridges' modeling parameters and studied the corresponding effects as well as the simultaneous effects of the variability in ground motion earthquake records, on the seismic demand fragilities for various components of the bridges. (Tubaldi, et al., 2012) utilized MC mixed with LHS for the purpose of uncertainty propagation into the structural models, in order to perform seismic damage assessments on multi-span continuous bridges with dissipative piers and a steel-concrete composite deck. (Vamvatsikos, 2014) adopted the MC mixed with LHS to incorporate the effects of uncertainty in structural modeling parameters on the IDA which is used to assess the seismic response of structures in various damage limit states. (Gokkaya, et al., 2016) studied the effects of epistemic variability on the seismic response of a range of different ductile and non-ductile RC strcutures.

7.3.1.2 Application of optimization strategies

There have been some advances in the application of various optimization algorithms in the minimization of multiple, and often contradicting, objective functions in the field of performance-based seismic evaluation and design of structures. This would be the strategy to be adopted, herein, in order to reduce the effects of epistemic variability in structural modeling parameters, on the performance-based seismic evaluation and design of RC structures. As such, some of the past research works, which have been conducted in this area, will be reviewed, herein.

(Bai, et al., 2016) utilized an optimization framework for uniform damage design of RC moment resisting buildings using a consecutive modal pushover analysis and by incorporating the performance-based earthquake engineering methodology. (Fragiadakis & Papadrakakis, 2008) developed a performance-based optimization framework for optimum seismic design of RC structures based on a deterministic and also a probabilistic approach.

(Liu, et al., 2005) investigated the performance-based seismic design optimization of steel special moment-resisting frame structures as a multi-objective optimization problem with a set of different contradicting objectives, which reflect the present capital investment as well as the future seismic risk. They also considered a set of different design constraints on the structural modeling parameters as well as response demands. (Paya, et al., 2008) used a simulated-annealing optimization algorithm for the purpose of design of RC structures considering multiple contradicting objectives, namely, the economic cost, the constructability, the environmental impact, and the overall safety of RC framed structures. (Liu, et al., 2013) incorporated the effects of uncertainty in structural modeling parameters for special moment-resisting frames. They, then, developed an optimization framework to generate a new set of optimum designs with respect to the modeling parameters by incorporating the performance-based earthquake engineering and also by considering multiple contradicting objectives.

(Foley, et al., 2007) and (Alimoradi, et al., 2007) developed a performance-based seismic design optimization methodology utilizing a set of different contradicting objectives and multiple hazard-consistent demand limits by using the genetic algorithm as the optimization tool. (Pourzeynali & Zarif, 2008) utilized a non-dominated sorting genetic algorithm ($NSGA - II$) in order to optimize the modeling parameters of the base isolation devices utilized for the purpose of seismic rehabilitation of tall buildings given two different objectives, namely, the roof and the base isolator displacement. (Saadat, et al., 2016) utilized a performance-based optimization framework for optimum design of steel structures considering the seismic performance of both structural and non-structural components where the minimization of initial cost and expected annual loss were set to be the objectives of their framework.

7.3.2 The state of research

Given the importance of structural modeling parameters in performance-based seismic evaluation and design of structures, this research will be aimed at shedding some more light on this topic. To this end, a set of different RC ductile structures will be modeled. Moreover, twelve different structural modeling parameters simulating a range of structural behavior, from linear-elastic to nonlinear, will be considered as uncertain to be assigned to different plastic hinges across various structural components. These parameters would play a key role in capturing a range of structural behavior from linear-elastic to nonlinear. A set of probability distribution functions will be utilized to quantify the variability in the aforementioned parameters. A sampling technique will then be adopted to draw realization samples from these distributions to be utilized as the structural input parameters.

As per incorporating the performance-based earthquake engineering methodology, two different suites of earthquake records will be selected to be hazard-consistent at two different hazard levels. Ultimately an optimization framework will be utilized to be integrated with a structural simulation software in order to generate optimum designs for the structures with respect to modeling parameters. As such, the initial population of design variables obtained by drawing realization samples from various distributions of structural modeling parameters will be utilized to generate performance-based objectives at two different performance levels for which two suites of ground motion had been selected. Thereafter, an optimization framework will be incorporated with the aim of reducing the effects of uncertainty in structural modeling parameters on the structural seismic demand responses, in an iterative fashion. Finally, the effects of optimum design variables will be studied on the seismic damage fragility of different types of structures.

7.4 A FRAMEWORK FOR OPTIMUM DESIGN OF RC STRUCTURES

In this section an optimization framework will be developed for the purpose of optimum design of reinforced concrete (RC) structures based on two objectives, namely, the median peak inter-story drift ($IDR(\%)$) at immediate occupancy (IO), and collapse prevention (CP) performance levels, respectively. It should be noted that the immediate occupancy and collapse prevention performance levels are enforced by simultaneously subjecting the structures to two suites of earthquake records corresponding to a 50- and 2-percent probability of exceedance in 50 years.

The algorithm for the optimization framework is demonstrated in Figure 7.1. As can be observed, two different software programs, namely the OpenSeesMP (McKenna, et al., 2000) and

Matlab (*https://www.mathworks.com/products/matlab.html*) will be integrated for this purpose. Median drift demands at two performance levels to be obtained by performing nonlinear response history analysis ($NRHA$) on the cloud, are set as the objectives. They are generated using OpenSeesMP on Stampede2 platform (see Figure 7.2 and Figure 7.3) by iteratively running the $NRHAs$ for a population of design variables using two suites of ground motion records. The design variables which are actually the structural modeling parameters for which an optimum design is sought, are iteratively updated through a non-dominated sorting genetic algorithm ($NSGA-II$) (Deb, et al., 2002). This process continues until convergence is reached based on an internal convergence criterion or a user-defined maximum number of iterations.

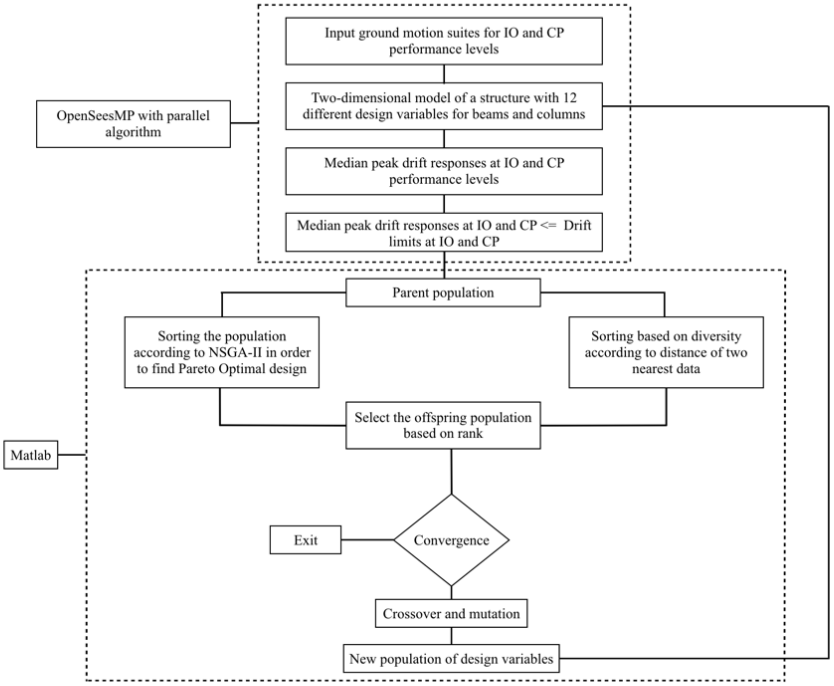

Figure 7.1. An optimization-based algorithm for optimum design of reinforced concrete structures.

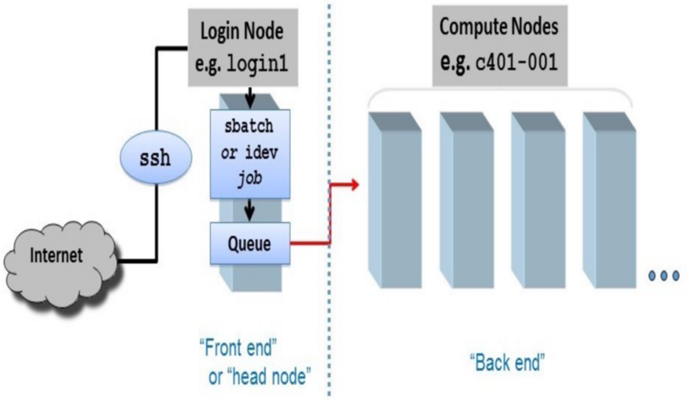

Figure 7.2. Schematic of job submission process (e.g. batch submission) and the configuration for the platform. (Adopted from https://portal.tacc.utexas.edu/user-guides/stampede2)

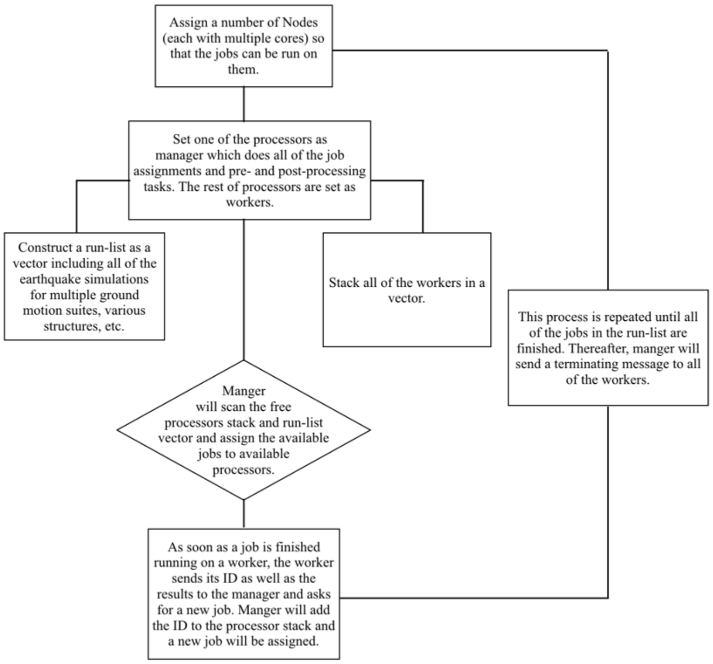

Assign a number of Nodes (each with multiple cores) so that the jobs can be run on them.

Set one of the processors as manager which does all of the job assignments and pre- and post-processing tasks. The rest of processors are set as workers.

Construct a run-list as a vector including all of the earthquake simulations for multiple ground motion suites, various structures, etc.

Stack all of the workers in a vector.

Manger will scan the free processors stack and run-list vector and assign the available jobs to available processors.

As soon as a job is finished running on a worker, the worker sends its ID as well as the results to the manager and asks for a new job. Manger will add the ID to the processor stack and a new job will be assigned.

This process is repeated until all of the jobs in the run-list are finished. Thereafter, manger will send a terminating message to all of the workers.

Figure 7.3. The parallel computing algorithm adopted in this study.

7.4.1 A multi-objective optimization algorithm

A non-dominated sorting genetic algorithm ($NSGA - II$) based on (Deb, et al., 2002) will be utilized, herein. This algorithm produces a set of solutions (Pareto Optimal set) which are not dominated by other solutions in the solution space. Domination in a minimization problem means that a possible solution dominates another solution if all its components are smaller or equal to the components in the other solution and at least one of the components is absolutely smaller (Xie, 2017). After achieving the Pareto Optimal solutions set which provides a set of optimum design variables, choice of selecting a single design would totally be up to analyst based on various choices of tradeoff.

The way the algorithm shown in Figure 7.1 works is to first generate an initial population of design variables and then derive the parent populations (drift demands) associated with them thorough running $NRHAs$. Thereafter, using $NSGA - II$, a solution with lower rank (i.e. non-dominated) will be picked. Moreover, in order to sort out the solutions in the less crowded area, the distance between two nearest data points are computed and ranked. Hence, the sorting protocol guarantees convergence to Pareto optimal solutions and the distance ranking maintains diversity among populations. A set of classic genetic operator, namely, the mutation and crossover will be used to generate offspring populations so that better genes of the parent population and the population diversity can be maintained. As such, a default value of 20% and 80% will be assigned to each of these parameters, herein.

7.5 APPLICATIONS

The optimization framework described in the previous section is utilized, herein, to generate optimum design variables for a set of three different ductile RC structures. To compute the objectives at two different performance levels (e.g. IO and CP), two sets of ground motion earthquake records are selected for which the details will be provided in the next section.

7.5.1 Ground motions

The ground motion suites to be used for the subsequent structural analyses, are briefly described here. A more detailed information on the algorithms these ground motions have been selected based upon, can be found in Chapter 2.

First, $IM_i = \{SA(T), AI, CAV, Ds575, Ds595\}$ is set as the intensity measure (IM_i) vector where AI, CAV, $Ds575$ and $Ds595$ are defined as, arias intensity, cumulative absolute velocity, 5-75%, and 5-95% significant durations, respectively. For computation of $SA(T)$, 21 different periods identical to those for which hazard curves can be generated, have been chosen. The goal would, then, be to select ground motion records with matching characteristics identical to those in the IM_i vector, which are generated based on a generalized conditioning intensity measure ($GCIM$) approach.

In order to select ground motion records, a hypothetical site in the city of Los Angeles, CA (LONG-118.43; LAT34.053) with average shear-wave velocity for the upper 30 m depth of 760 m/sec, and a depth to a 2.5 km/sec shear-wave velocity horizon of $z_{2.5}$ = 1 km, is chosen. Using the relationships developed in Chapter 2, a set of different ground motion earthquake suites are selected based on the two-IM_j approach. The ground motions selected based on this approach are hazard-consistent over a range of intensity measures, and thus they have sufficient content to capture a range of structural behavior corresponding to multiple modes of vibration (see Chapter 5).

Weight factors of 70% for the amplitude-based and 30% for the cumulative-based intensity measures have been considered, which are enforced during the selection phase. Since ductile RC structures are analyzed, the majority of importance weight is given to the amplitude-based contents as these structures are not expected to undergo significant nonlinearity and the inertia mode seems to be dominant. The weights to be assigned to either of the amplitude- or cumulative-based intensity measures are evenly distributed among all of them during the selection phase. As for causal parameters, the magnitude range of $M = [5\,,8]$, the closest source-to-site distance of $R_{jb}(\text{km}) = [0\,,100]$ and the $V_{s30}(\text{m/sec}) = [300\,,1200]$ are adopted. The maximum scale factor is set to 4.

7.5.1.1 An example of selected ground motion suites

In this section, some of the information with regard to two ground motion suites selected at the IO and CP performance levels will be presented. While separate suites were selected for different buildings (e.g., 4-, 8-, and 12-story), only the ground motions suites selected for the 4-story ductile RC building are presented here for brevity. The structural fundamental period of that building is $T1 = 1.30$ sec. The spectral acceleration at the fundamental period ($SAT1$) is picked as the IM_j. Since the two-IM_j approach is adopted, the lower- and upper-bound coefficients of 0.20 and 3.0 were applied to determine IM_{j1} and IM_{j2} based on (Eads, et al., 2016) and (Chandramohan, 2016). Thus, $T1$, and $T2$ were set to 0.25 sec, and 4.0 sec, respectively. Hence, IM_{j1} and IM_{j2} are adopted as $SA(T = 0.25 \text{ sec})$ and $SA(T = 4.0 \text{ sec})$, respectively. Finally, using the algorithm described in Chapter 2, 25 earthquake records are selected from the $NGA - WEST2$ database $(\text{Bozorgnia, et al.}, 2014)$. It is also worth noting that hazard consistency is implemented by considering up to 2,000 rupture scenarios and their contribution to different types of conditioning intensity measures.

Figures 7.4(a) and (b) demonstrates the response spectra of the selected records (shown in gray) for two different hazard levels, respectively. Since the statistics of the select records shown in green match those of the realization target (drawn from the $GCIM$ distribution shown in red) shown in blue, one could claim that the hazard-consistency has been fully enforced.

In addition to response spectrum, the empirical distribution of two other cumulative metrices, namely, the CAV and $Ds575$ are presented in Figures 7.4(c) and (d), respectively. These metrices would represent the cumulative characteristics of the records for which a 30% importance weight had been initially assigned during the selection phase. As can be seen, despite the lower weight, still a good match can be observed between the empirical distributions of the selected records (shown in black) and those of the realization targets shown in blue. It should be noted that the empirical distributions of the realization targets were initially drawn from the $GCIM$ distribution whose statistics are provided on the figures which are shown in red.

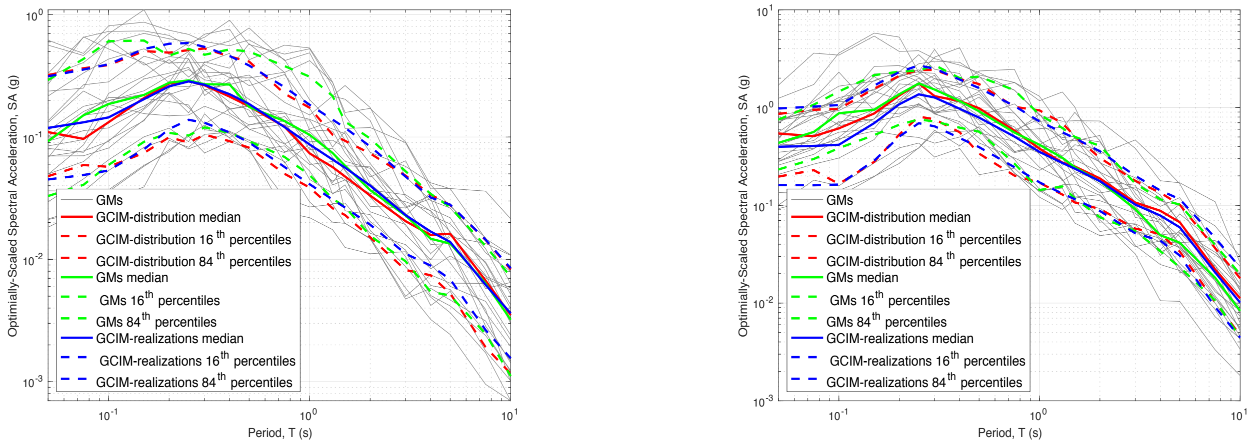
(a)

(b)

(c) (d)

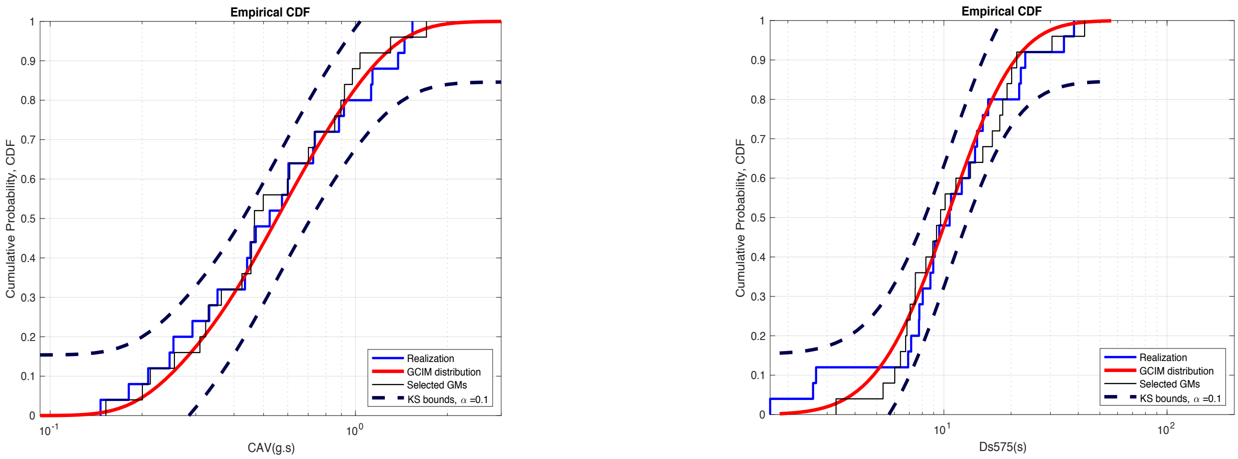

Figure 7.4. (a) and (b) Response spectra of the selected records at the IO and CP performance levels, respectively. Empirical distributions of the (c) CAV and (d) $Ds575$ of the selected records at the IO performance level.

7.5.2 Ductile reinforced concrete structures

Three buildings of various heights—i.e. 4, 8, and 12 stories—are modeled assuming a ductile behavior. The fundamental periods of vibration for these three buildings are $T1 = 1.30\ sec$, $T1 = 1.80\ sec$ and $T1 = 2.20\ sec$ for the 4-, 8- and 12-strory, respectively. The structures were modeled in OpenSeesMP which is a finite element software and widely used for earthquake engineering simulations (McKenna, et al., 2000). Figure 7.5 shows the schematics of these three buildings.

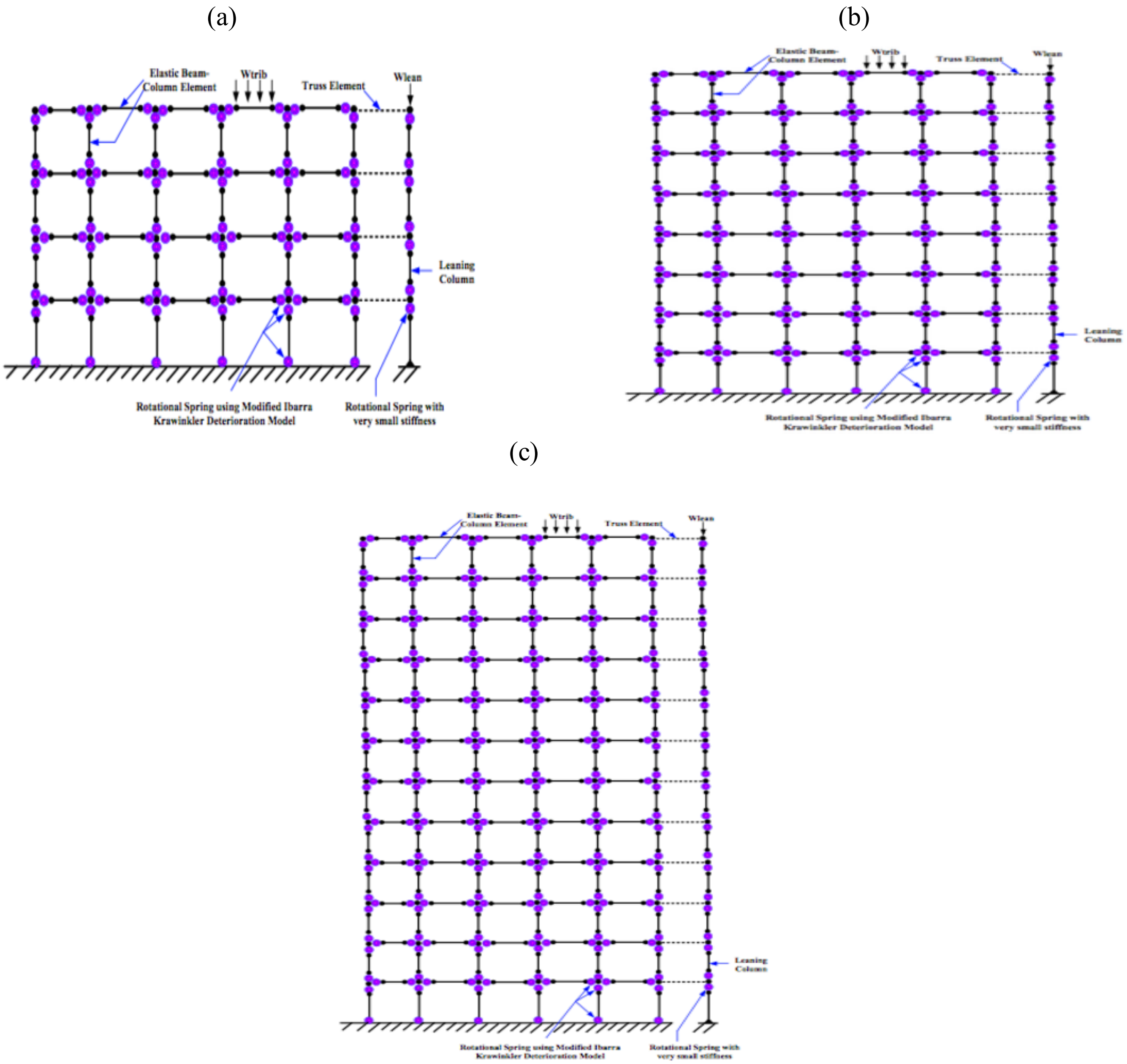

Figure 7.5. (a), (b) and (c) Schematic of a 4-, 8, and 12-story building.

As discussed before, the main goal of this study is to reduce the variability in structural seismic demand responses due to the uncertainty in the structural modeling parameters, using an optimization algorithm. As such, 12 different modeling parameters simulating the ductile behavior, are recognized as uncertain. These parameters are actually the properties of the backbone curves to be assigned to plastic hinges across different beam and column elements within the structure (see Figure 7.6(b)). They are defined as flexural strength (M_y), ratio of maximum moment and yield moment capacity (M_c/M_y), effective initial stiffness which is defined as the secant stiffness to 40% of yield force ($EI_{stf,40}/EI_g$), plastic rotation capacity ($\theta_{cap,pl}$), post-capping rotation capacity (θ_{pc}) and energy dissipation capacity for cyclic stiffness and strength deterioration (λ). These parameters are identical for both of the beam and column elements.

Since the aforementioned parameters will be utilized to generate initial population of design variables to be used in the initial stage of the optimization framework (see Figure 7.1), they first need to be quantified. Hence, various probability distribution functions whose properties are obtained from (Gokkaya, et al., 2016) and (Haselton, et al., 2008) will be adopted to quantify the uncertainty associated with those parameters. In addition to the variability in each parameter, the correlation between the parameters will be considered as well. Hence, according to (Gokkaya, et al., 2016), it was assumed that parameters between beams and between columns within a building are fully correlated. Moreover, parameters between beams and columns and those within each component model (e.g. within a beam or column) of a building are partially correlated. Figure 7.6(a) clarifies the definition of various correlation types- e.g. between or within components.

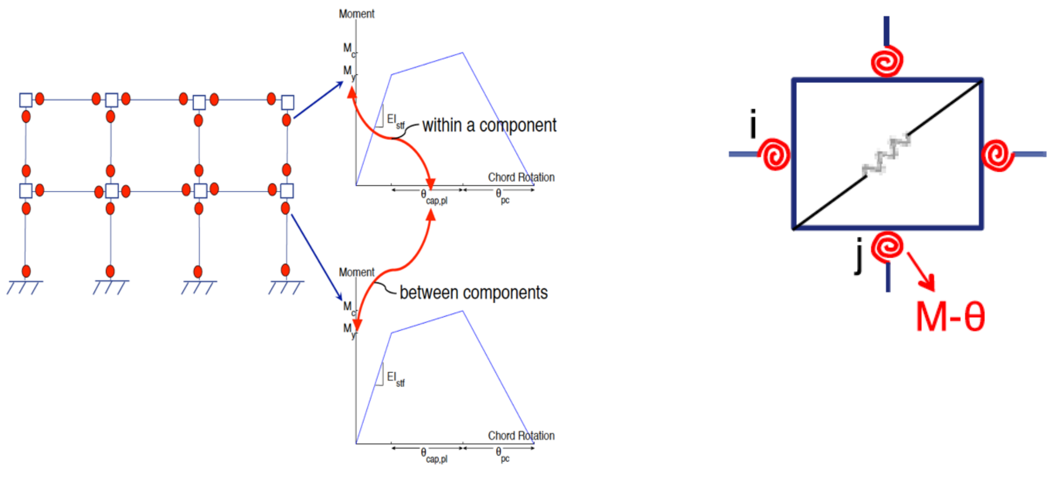
(a)
(b)

Figure 7.6 (a) Definition of various correlation types- e.g. between or within components (b) zero length elements to be assigned to plastic hinges to simulate a ductile behavior. (Adopted from (Gokkaya, et al., 2016))

Given the information provided in the preceding paragraph, 12 parameters are defined as the design variables of which six belong to the beam and the reminder to the column elements. Given the marginal distribution of each of these parameters as well as the cross correlation between them which were obtained according to (Gokkaya, et al., 2016)- see Tables I and II- and (Haselton, et al., 2008), one could draw any number of realization samples using a sampling technique. As such, the Latin Hypercube Sampling (Vorechovsky & Novák, 2009), which was discussed in Chapter 6, is utilized to draw 200 realization samples from the multivariate distribution of the design parameters. This is called the so-called design population which will be utilized as the initial population to be fed into the optimization algorithm in the very initial stage (see Figure 7.1).

7.6 APPLICATIONS

The information provided in the preceding sections have been applied to all the three RC ductile structures. It is worth noting that on average more than 250,000 $NRHAs$ were conducted on each of the building type. The average runtime, on Stampede2 platform, to get the optimization done for each of these buildings is approximately one day and half which is a reasonable runtime given the tremendous number of dynamic analyses being performed. If this was to be done on a personal computer or on a sequential machine with only multiple cores, it would have taken months to get the optimization done for these buildings, so the necessity and effectiveness of parallel commuting can easily be noticed here.

The objectives of the optimization framework were set as the median peak IDRs at two different performance levels, namely, the IO and CP. Moreover, drift limits of 1.5% for the IO and 6.5% for the CP levels were implemented which were enforced throughout the optimization.

7.6.1 4-story ductile RC structure

Figure 7.7 presents the net outcome of the optimization framework on a 4-story ductile RC structure. As can be seen from this figure, the epistemic variability in structural modeling parameters, had imposed a large scatter on the response which can be noticed from the blue circles. It should be added that since the building is a ductile RC, the drift level is low at both of the performance levels. In any case, it can easily be noticed that the optimization framework has had a very positive impact on shrinking the scatter due to epistemic variability in the design variables. As such, scatter in the red circles which show the responses (the Pareto-front solutions) due to the optimum design population, compared to the initial population (blue circles) have considerably shrunk. Reducing the effects of epistemic variability on the nonlinear response of structures have never been an easy task, but as it is observed from Figure 7.7, the optimization framework has succeeded in this matter and reduced this effect, quite significantly.

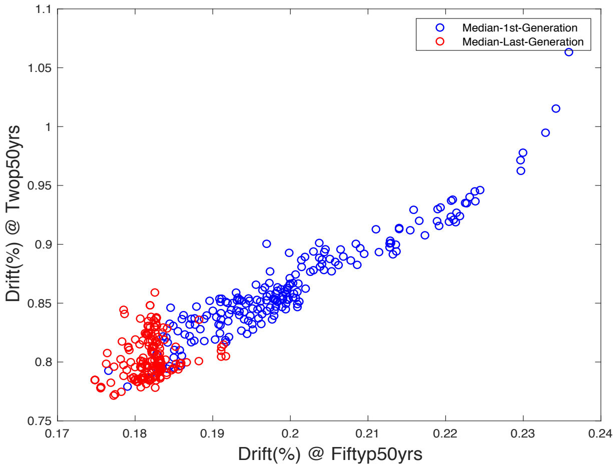

Figure 7.7. Effect of epistemic variability in structural modeling parameters before (see the blue circles) and after (see the red circles) optimization.

In order to, separately, study the effect of the optimization framework on the statistics of the responses at two different performance levels, another effort was made. Figure 7.8 shows the median IDR for both of the initial and last design populations which are plotted along with the entire height of the building.

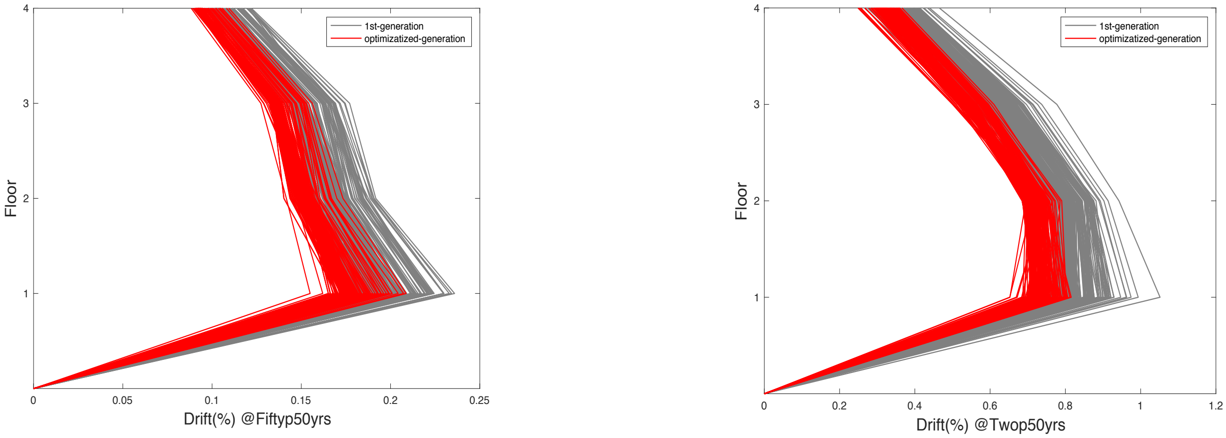
(a)

(b)

Figure 7.8. The responses obtained using the initial and last population of design variables at (a) IO and (b) CP performance levels.

Figure 7.9(a) demonstrates the median as well as 16th and 84th percentile responses (see Figure 7.8) for both the initial (shown in gray) and optimum design populations (shown in red) at the IO performance level. Figure 7.9(b) displays the same information, however this time at the CP performance level. As can be observed from these plots, both of the median and percentile responses associated with the Pareto-front solutions (red curves) have decreased with respect to those associated with the initial design population (gray curves). The difference is not that significant as the overall drift level is low, since a ductile structure is being analyzed; however, it shows the effectiveness of the optimization algorithm being utilized in reducing the effects of epistemic uncertainty in design variables on the structural responses.

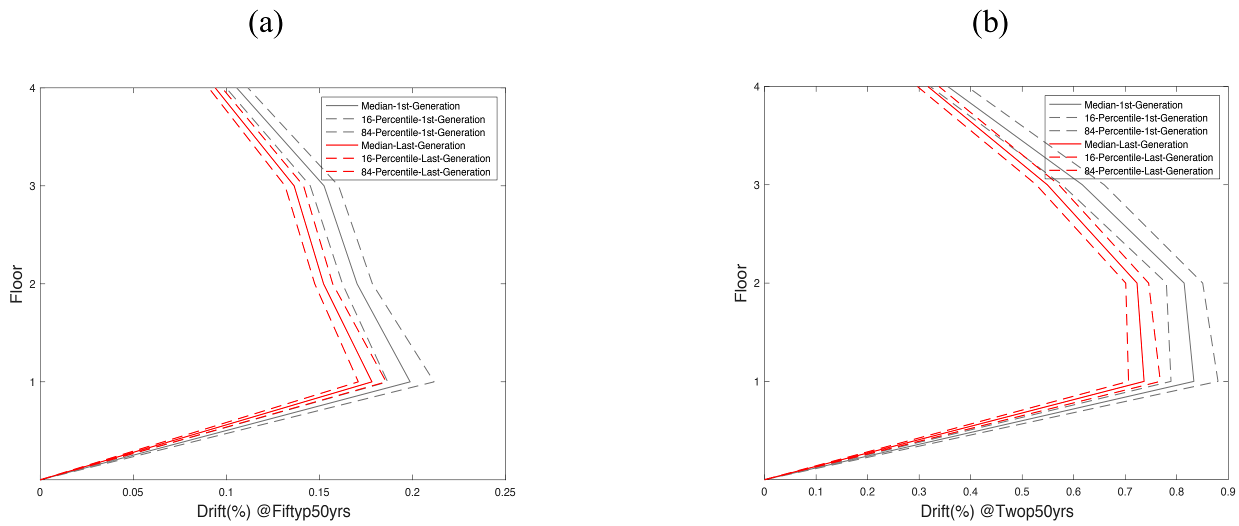

Figure 7.9. Median as well as 16- and 84-percentile of responses at (a) IO and (b) CP performance levels.

7.6.2 8-story ductile RC structure

In this section, a similar type of analysis which was carried out in section 7.6.1, will be repeated, however this time for a 8-story ductile RC structure.

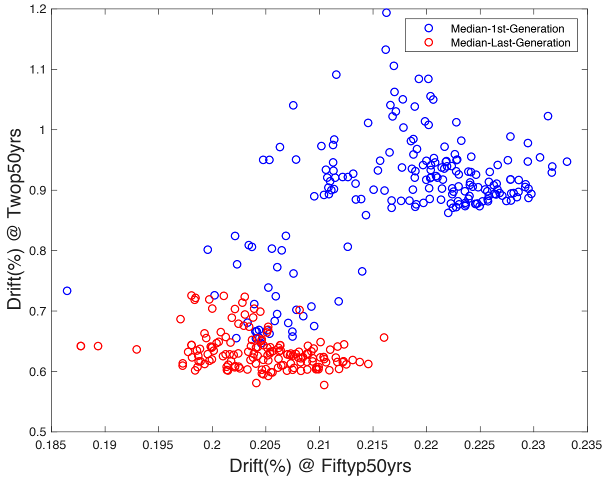

Figure 7.10. Effect of epistemic variability in structural modeling parameters before (see the blue circles) and after (see the red circles) optimization.

As can be noticed from Figure 7.10, the optimization framework has again had a significant impact in reducing the effects of epistemic uncertainty in structural modeling parameters, on the structural seismic demand responses. As such, the scatter in the Pareto-front solutions shown in red has shrunk as opposed to the one in the initial design solutions which is shown in blue.

Figure 7.10(a) demonstrates the median as well as 16th and 84th percentile responses for both of the initial (shown in gray) and optimum design populations (shown in red) at the IO performance level. 7.10(b) shows the same things, however this time at the CP performance level.

Overall, the optimization framework has again done a great job in reducing the effects of epistemic variability in structural modeling parameters, on the structural seismic demand responses at both of the performance levels. As such, both of the median and percentile responses have decreased for the Pareto-front solutions as opposed to those of the initial designs.

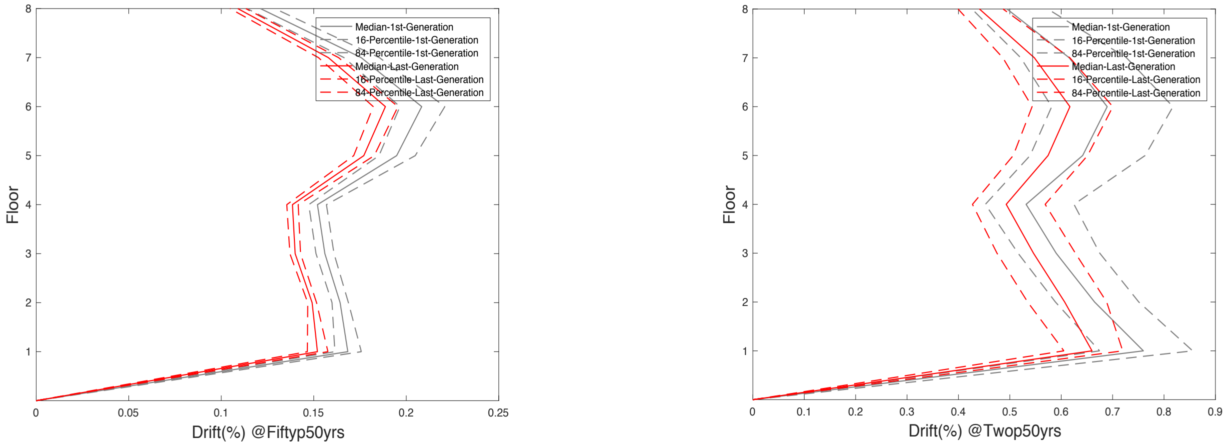
(a)

(b)

Figure 7.11. Median as well as 16- and 84- percentile of responses at (a) IO and (b) CP performance levels.

`

7.6.3 12-story ductile RC structure

In this section a similar set of analyses will be carried out on a 12-story ductile RC structure. Figure 7.12 shows the scatter in the structural responses at two different performance levels due to the optimum design population (see the red circles) as well as initial design population (see the blue circles). It is clear that the optimization framework has shrunk the initial scatter, significantly.

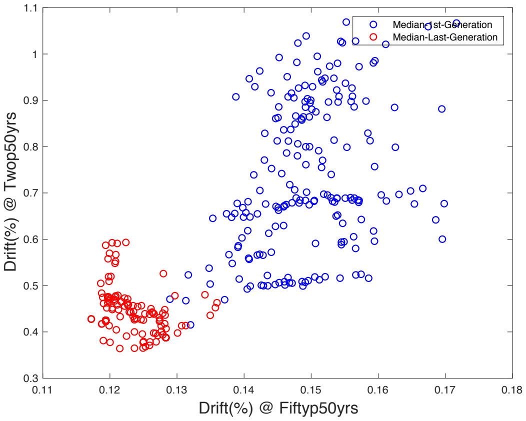

Figure 7.12. Effect of epistemic variability in structural modeling parameters before (see the blue circles) and after (see the red circles) optimization.

In order to study the effects of the optimization algorithm on the statistics of the responses at two different performance levels, Figure 7.13 has been generated. As can be seen from the plots in Figure 7.13, both of the median and percentile responses have decreased for the optimum design population (see the red lines) comparing to the initial designs (see the gray lines). This, again, proves the capability and effectiveness of the optimization framework in reducing the effect of epistemic variability in structural modeling parameters on the structural responses at multiple performance levels.

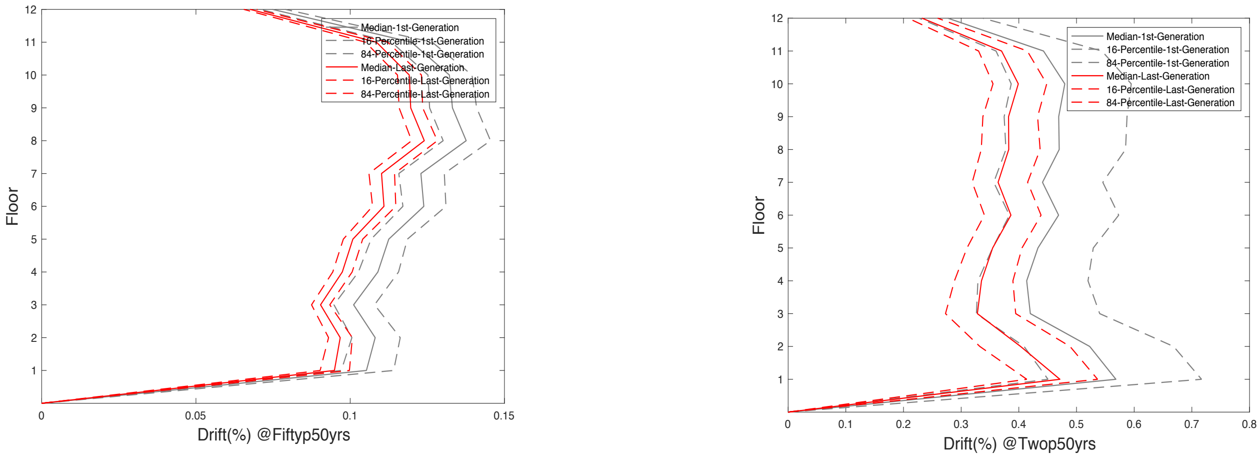

(a)

(b)

Figure 7.13. Median as well as 16- and 84-percentile of responses at (a) IO and (b) CP performance levels.

7.7 DISCUSSION

In this section the effects of epistemic variability on damage fragilities with respect to both of the initial and optimum designs will be discussed. Hence, by assuming a normal distribution for median peak drift demands and given the logarithmic medians and standard deviations obtained from the previous sections, damage fragilities (based on Eq. 7.1) will be generated for all of the three structures discussed in the previous sections.

$$Fragility = \Phi\left(\frac{\ln\,(x/\theta)}{\beta}\right) \tag{7.1}$$

where, Φ represents a normal cumulative distribution, x is a damage limit state, θ is the median demand which is the peak inter-story drift ratio, herein, and finally β is the logarithmic standard deviation of the peak inter-story drift ratio.

Additionally, some information with regard to the statistics of the optimum and initial design variables will be included in the end of this section as well.

7.7.1 4-story ductile RC structure

Figures 7.14(a) and (b) show the probability of exceedance of various levels of damage with respect to the initial and optimum design populations at IO and CP performance levels, respectively. As can be noticed from these figures, utilizing the optimum designs is ended up with a less fragile structure (see the red curves) as opposed to the initial designs (see the gray curves). In other word, when the effect of epistemic variability is reduced by utilizing the optimization framework, the structure becomes less fragile for a given damage limit state. This is a considerable achievement with regard to isolating the effect of epistemic variability in the probabilistic seismic response of a 4-story RC structure.

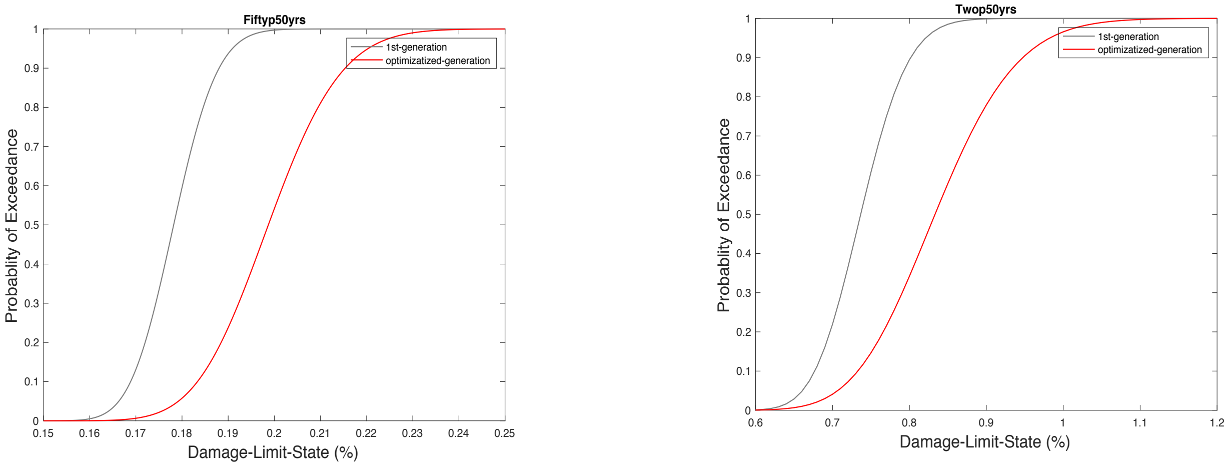
(a) (b)

Figure 7.14. Damage fragilities for the initial and optimum design populations at (a) IO and (b) CP performance levels.

7.7.2 8-story ductile RC structure

A similar type of analysis is repeated for an 8-story ductile RC structure for which the damage fragilities are presented in Figure 7.15 at two different performance levels.

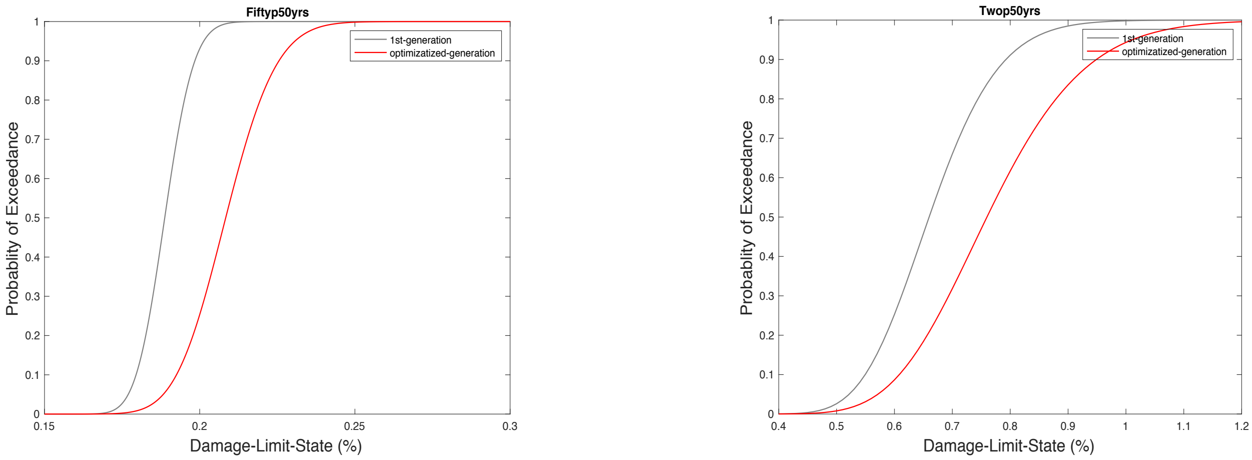
(a)

(b)

Figure 7.15. Damage fragilities for the initial and optimum design populations at (a). IO and (b). CP performance levels.

As can be noticed from both of the plots presented in Figure 7.15, the optimization algorithm has again had a positive impact with regard to reducing the effects of epistemic variability in structural modeling parameters, on damage fragilities for various levels of damage. As such, the optimum designs are more reliable with regard to performing any type of probabilistic damage and subsequent loss assessments on this structure.

7.7.3 12-story ductile RC structure

Last but not the least, a set of comparisons has been made with regard to the effects of optimization of the design variables on the damage fragilities of a 12-story ductile RC structure which can be observed from Figure 7.16. The optimum designs whose fragilities are shown in red at both of the performance levels have made the structure less fragile as opposed to the initial population designs (see the gray curves). This is, again, a positive impact that the optimization framework has had in reducing the effects of epistemic variability in design variables on the damage fragilities of a 12-story ductile RC structure.

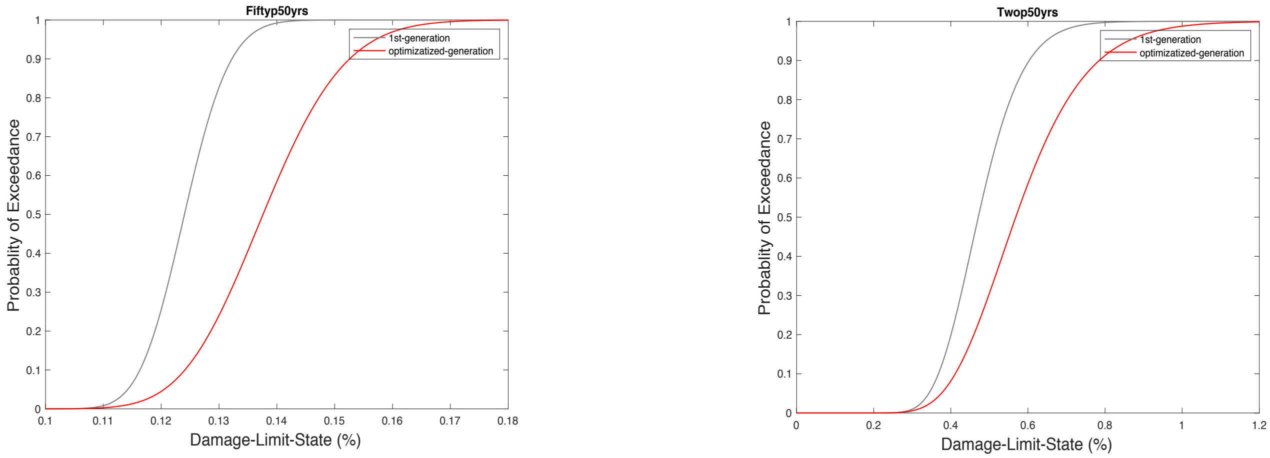
(a)

(b)

Figure 7.16. Damage fragilities for the initial and optimum design populations at (a) IO and (b) CP performance levels.

7.7.4 Design variables

This section presents the histograms of some of the design variables as defined in section 7.5.2 with respect to both of the initial and optimum design populations. The histograms are derived for both of the beams and columns design variables.

Figure 7.17 demonstrates the histograms of initial and optimum design populations for some of the structural modeling parameters belonging to a 4-story ductile RC structure, as defined in section 7.5.2. variables. The same type of information is available for various design parameters belonging to different types of structural systems which were utilized here in this study, however they are omitted for brevity.

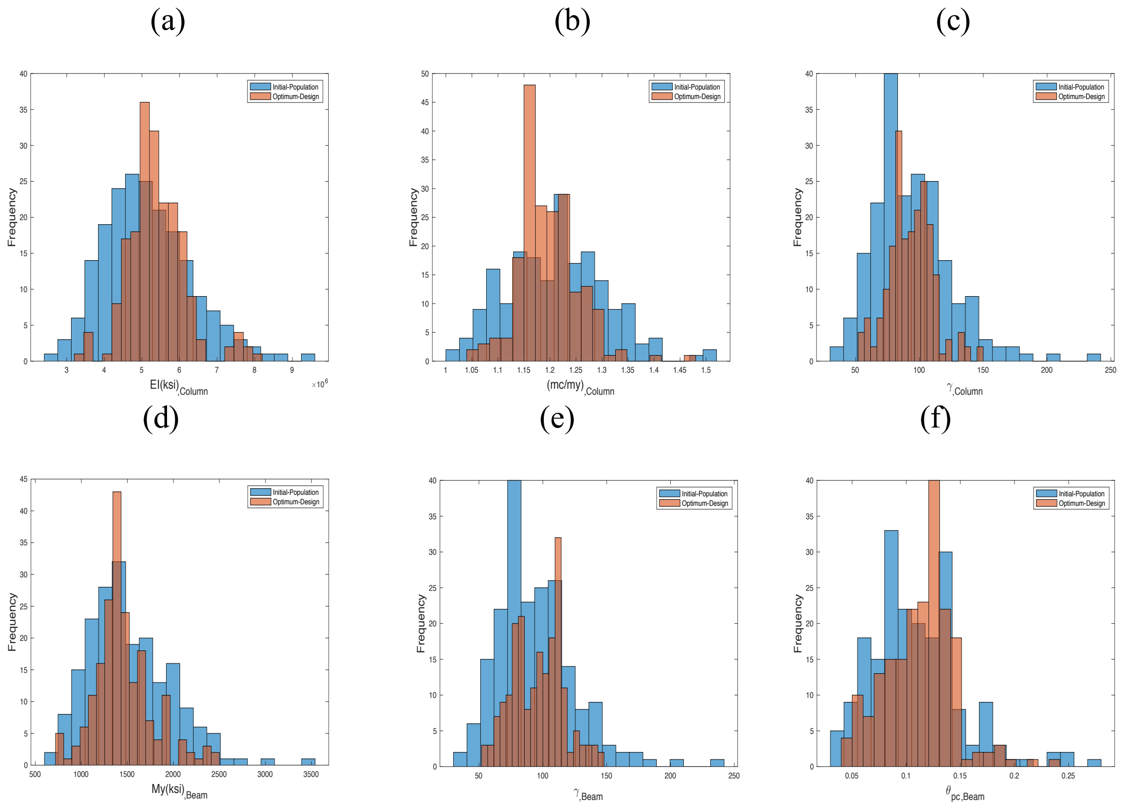

Figure 7.17. Histograms of initial and optimum design populations for some of the structural modeling parameters belonging to a 4-story ductile RC structure.

As can be observed from Figure 7.17, some of the variables are more optimized than the others in order to achieve an optimum design with respect to two simultaneous objectives which were the median peak inter-story drift ratios at two different performance levels.

7.8 CONCLUDING REMARKS

An optimization framework was developed to reduce the effects of epistemic uncertainty in structural modeling parameters, on the structural seismic demand responses. An initial population of 12 different design variables were drawn from a multivariate distribution using a sampling technique, namely, the Latin hypercube sampling. Hence, up to 200 realizations of the structure were generated for each of the three types of reinforced concrete structure with various heights.

Two sets of earthquake ground motion records were selected at two different hazard levels based on a two-conditioning intensity measure approach. The structural realizations were then analyzed using these two sets of ground motions and the median peak demand responses (i.e. inter-story drift) were computed. As such, the initial designs and the corresponding median responses were used as an initial population to be fed into the optimization algorithm, namely the non-dominated sorting genetic algorithm to update the design variables based on two objectives. Hence, the two objectives were set as the minimization of the inter-story drift ratios at two different performance levels.

A set of different scatter and statistics plots were generated using the optimum and initial design populations. It was observed that the optimum designs have reduced the scatter in the responses at different performance levels. They have also done so with respect to the statistics of the median drifts at both performance levels. As such, it can be concluded that the optimization framework had a very positive impact in reducing the effects of epistemic variability in structural modeling parameters, on the structural responses. This is clear especially when the results are compared with respect to the initial designs.

A set of different fragilities have also been generated for all of the structures with respect to the comparison of the effects of optimum and initial designs. It was observed that the optimum designs which were achieved by using the optimization framework, have made, all of the structures being analyzed, less fragile compared to the initial designs. This can be deemed as a noticeable outcome since reducing the effects of epistemic variability in structural modeling parameters, on damage fragilities is extremely important and will have a positive impact on the subsequent loss assessments.

8 CONCLUSIONS

A comprehensive list of conclusions has already been drawn and included in the end of each chapter which will not be repeated, herein. However, a bullet list of concluding remarks as well as some recommendations for future studies in this area are presented in this chapter.

8.1 SUMMARY & CONCLUDING REMARKS

1. Various probabilistic algorithms were developed to select ground motions with respect to a range of different conditioning methods, and by giving emphasis to different characteristics of the earthquake records.
2. A temporal aftershock probabilistic seismic hazard assessment (APSHA) framework was developed to assist with aftershock ground motion selection, scaling and modification (GMSSM).
3. After performing a range of nonlinear response history analyses on both single- and multi-degree of freedom structural systems, it was concluded that using a two-IMj conditioning method was superior in estimating the demands, over the single- or multiple-IMj approach.
4. It was also concluded that including the cumulative and duration-based characteristics of earthquake records rather than amplitude-based contents during the selection phase, are important in capturing the inelastic responses of ductile and non-ductile reinforced concrete structures.
5. A probabilistic framework was developed to select ground motion records matching a new metric for spectral shape. Also, a wide range of structural analyses were performed using two sets of earthquake records—one selected based on the traditional way of

spectral shape matching (a.k.a. response spectrum matching) and the other one based on the newly developed algorithm for spectral shape matching. It was observed that the latter had more destructive effects on the examined structures in most cases.

6. Efficiency of different sampling techniques in drawing a desirable number of realization samples from a multivariate distribution of various parameters, with respect to both its application in earthquake engineering as well as structural modeling was investigated.
7. The effect of variability in structural modeling parameters and ground motion records, on seismic responses of different structural types were studied. Moreover, an efficient multi-objectives optimization algorithm was developed with a main goal of reducing the effect of epistemic variability in structural modeling parameters, on structural seismic response. As such, various types of ductile reinforced concrete structures were studied to test the application of the optimization framework which resulted in a significant reduction in epistemic variability with respect to median peak inter-story drift ratios at two different performance levels.
8. It was also concluded that by generating optimum designs with respect to a set of different structural modeling parameters and given multiple objectives at two different performance levels, damage probability or fragility has decreased with respect to the initial design population.
9. Parallel computing was widely utilized throughout this study by developing various algorithms to help run numerous jobs on the cloud which resulted in saving a significant amount of computational expenses.

8.2 RECOMMENDATIONS FOR FUTURE STUDIES

The following items are identified as potential future studies as a follow up to those presented in this dissertation:

1. The aftershock framework developed in Chapter 3 can be applied to a real site with actual neighboring faults. Depending on data availability, a validation study can be carried out.
2. The assumption of aftershock rupture occurring at the end of mainshock rupture zones can be implemented, and the effects on aftershock probabilistic seismic hazard assessment can be investigated.
3. Application of various GMSSM methodologies developed in this dissertation can be repeated for three-dimensional models of reinforced concrete structures. There are likely new things to discover regarding GMSSM when torsional irregularities are considered. Moreover, even for structures with regular geometry and configuration, uneven generation of damage can induce torsional irregularities at lower performance levels.
4. The variability imposed using various sets of ground motion records can be quantified, using a cloud-based approach to define and compare dispersions in each scatter plot with respect to different GM suites being used.
5. A deterministic approach based on a vector of intensity measures can be investigated with respect to efficiency of ground motion records in capturing seismic responses. This approach can then be compared with the probabilistic approach developed in this study.

6. Additional measures can be considered when constructing the objective function in the PBSD optimization framework such as initial cost and/or the mean annual rate of exceedance of various levels of loss, for different structural types.

Appendix A: NGA-WEST2 Database

Various properties of the NGA-WEST2 (Bozorgnia, et al., 2014) database are presented.

(a) (b)

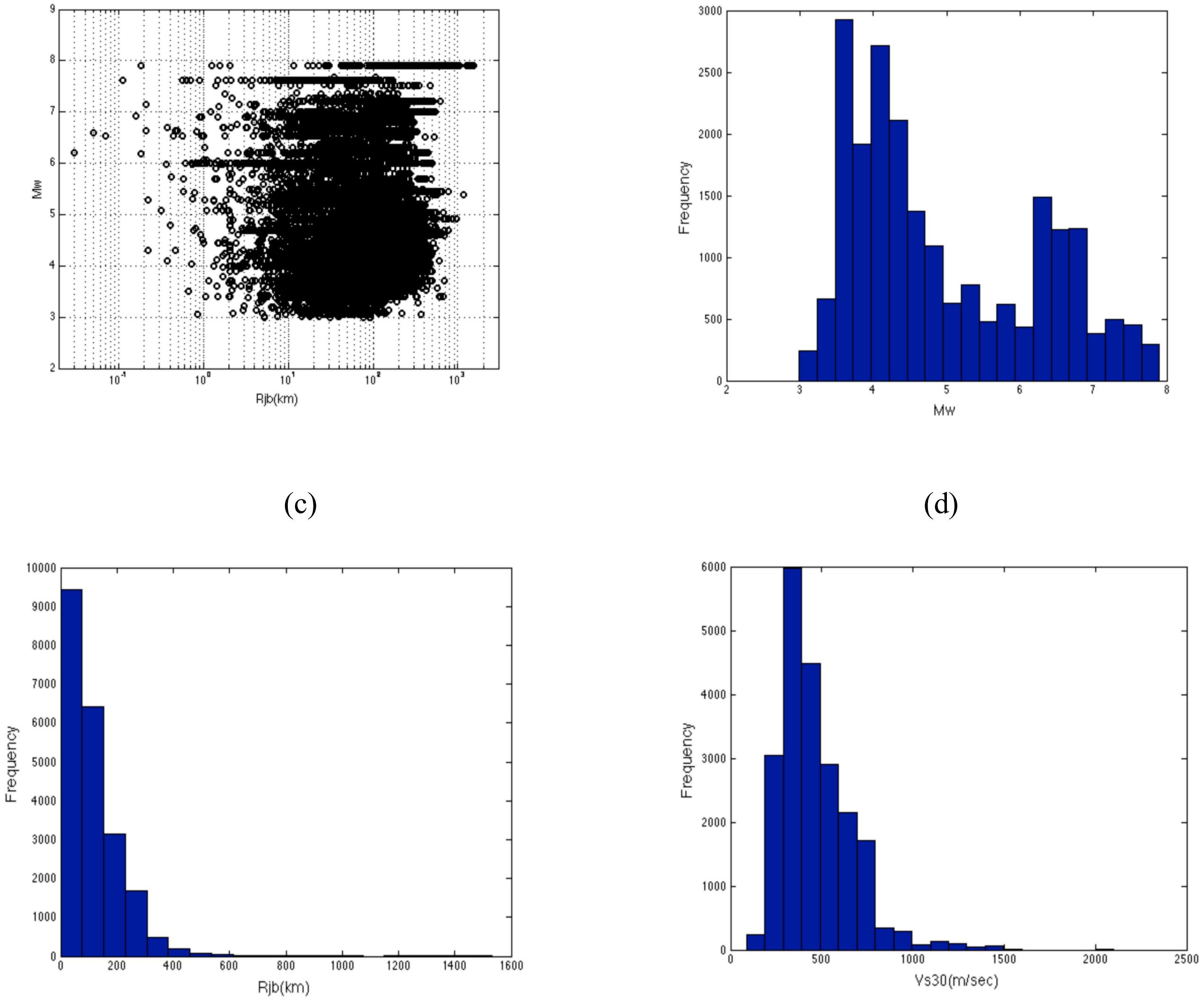
(c) (d)

Figure A.1. Various causal properties of $NGA - WEST2$ database.

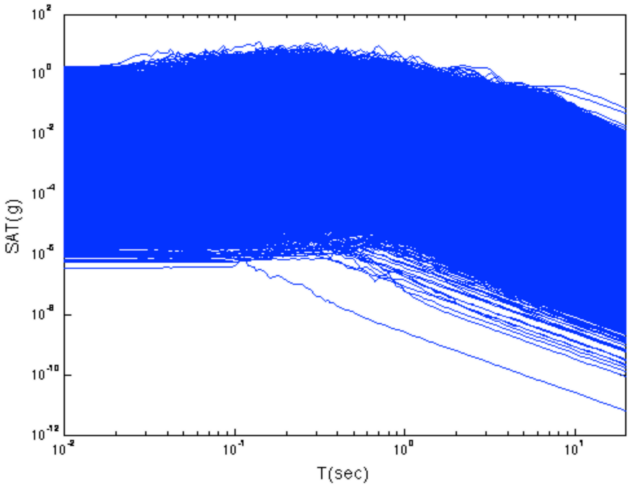

Figure A.2. Response spectra of all the available records in $NGA - WEST2$ database.

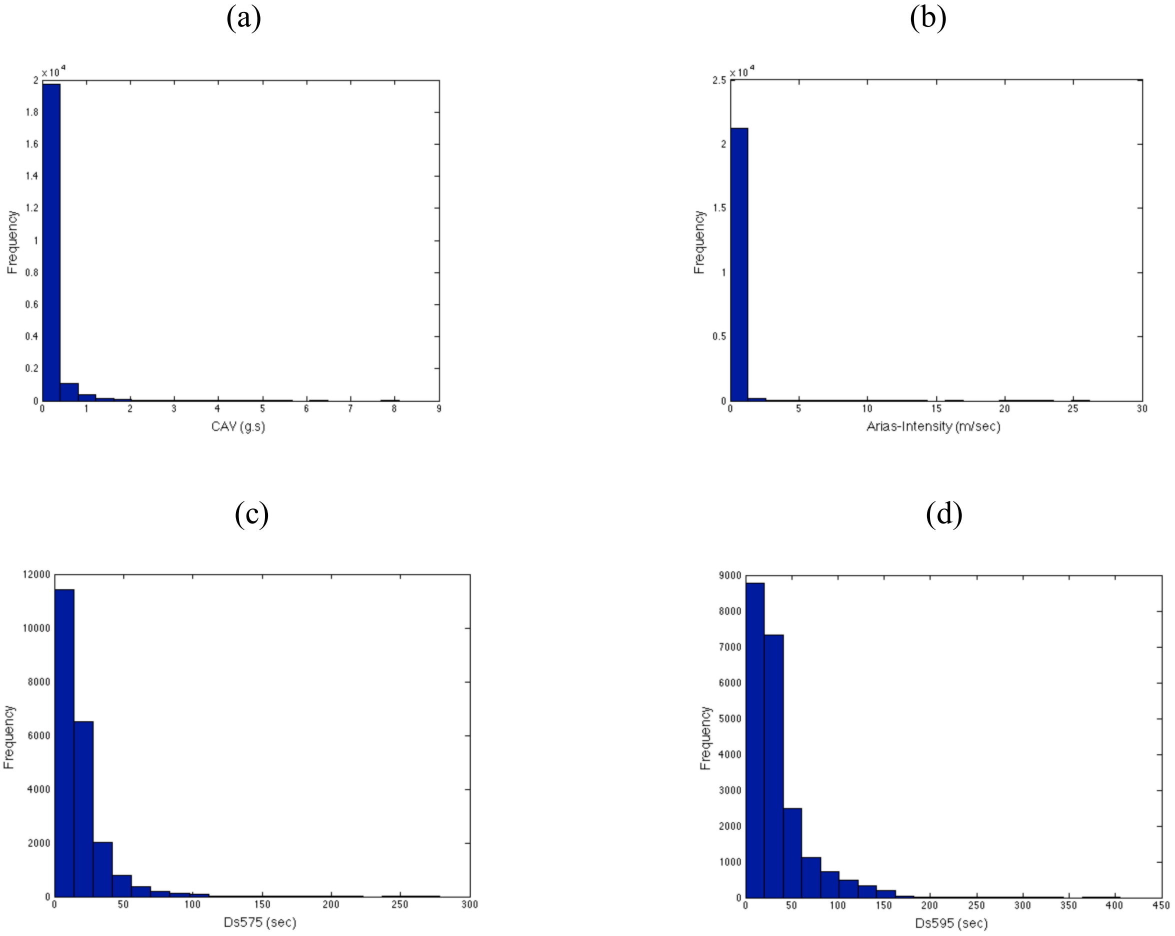
(a)

(b)

(c)

(d)

Figure A.3. Histograms of various cumulative- and duration -based characteristics of $NGA - WEST2$ database.

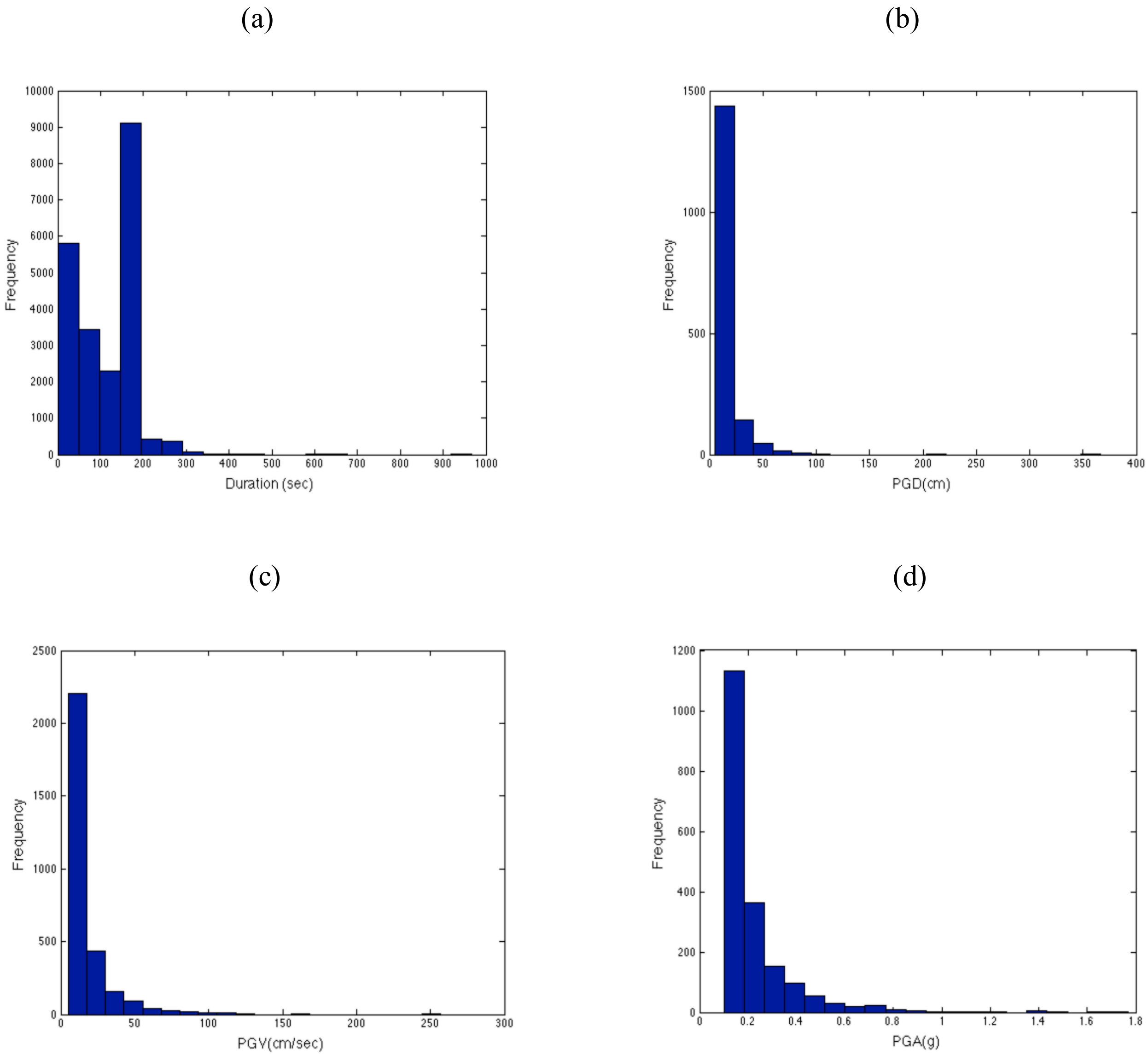

Figure A.4. Histograms of various amplitude- and duration -based contents of $NGA - WEST2$ database.

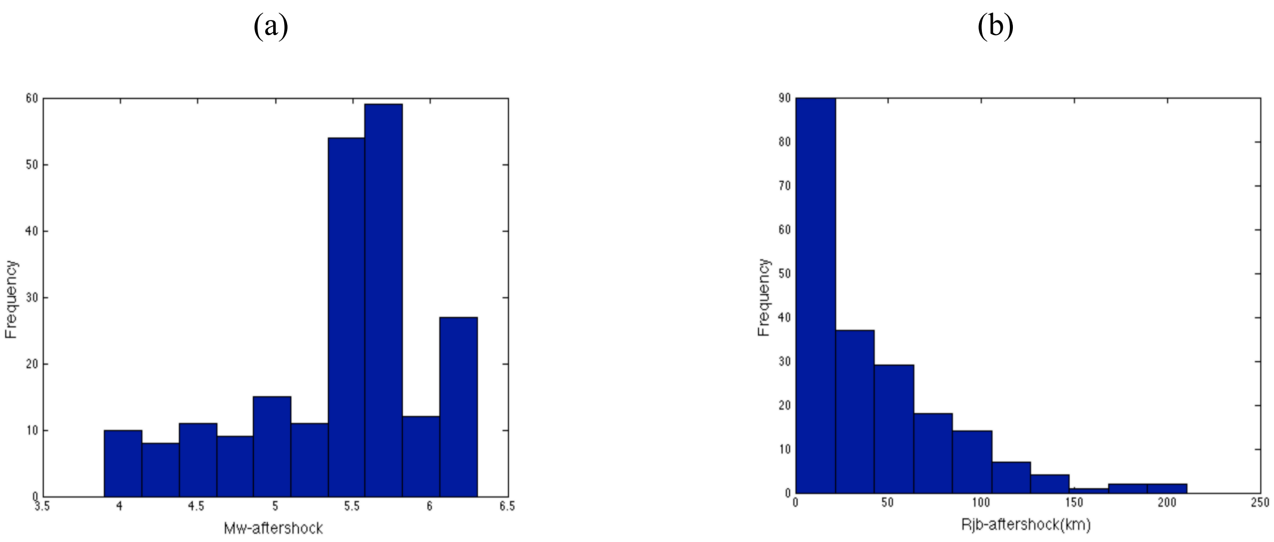

Figure A.5. Histograms of the (a) magnitude, and (b) closest source-to-site distance of aftershock records in $NGA - WEST2$ database.

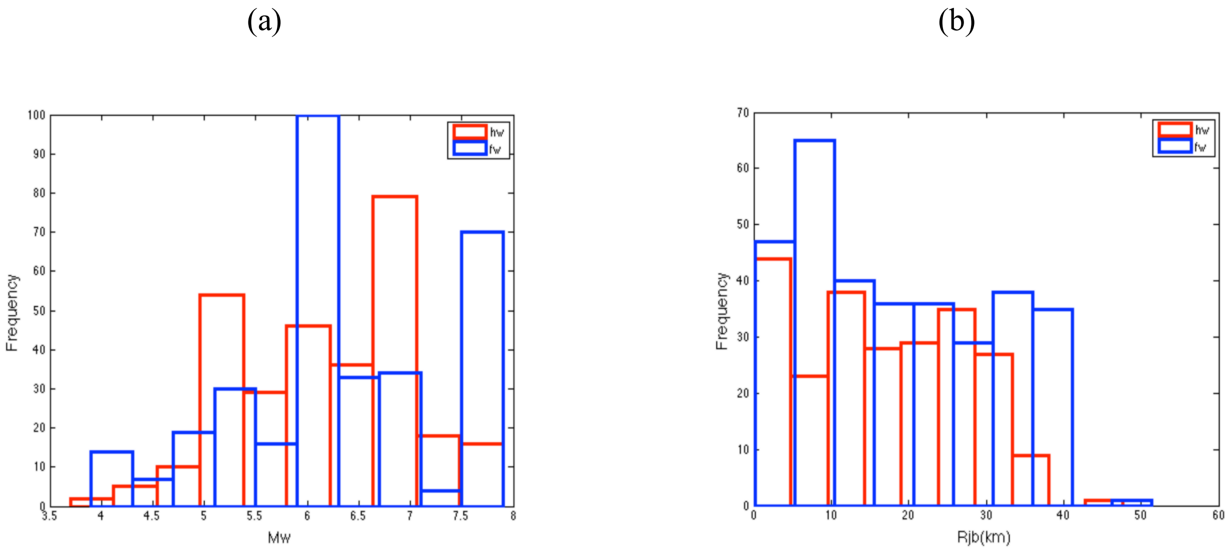

Figure A.6. Histograms of (a) magnitude, and (b) closest source-to-site distance of the records influenced by footwall (fw) and hanging wall (hw) effects, in $NGA - WEST2$ database.

REFERENCES

Alimoradi, A., Pezeshk, S. & Foley, M. C., 2007. Probabilistic Performance-Based Optimal Design of Steel Moment-Resisting Frames. II: Applications. *Journal of Structural Engineering,* 133(6), pp. 767-776.

Araújo, M., Macedo, L., Marques, M. & Castro, M. J., 2106. Code-based record selection methods for seismic performance assessment of buildings. *Earthquake Engng Struct. Dyn.,* Volume 45, p. 129–148.

Armstrong, R. J., 2016. Procedure for selecting and modifying earthquake motions to multiple intensity measures. *Soil Dynamics and Earthquake Engineering,* Volume 89, p. 91–99.

Bai, J., Jin, S., Zhang, C. & Ou, J., 2016. Seismic optimization design for uniform damage of reinforced concrete moment-resisting frames using consecutive modal pushover analysis. *Advances in Structural Engineering ,* 19(8), p. 1313–1327.

Baker, J. W., 2011. Conditional Mean Spectrum: Tool for Ground-Motion Selection. *Journal of Structural Engineering,* pp. 322-331.

Baker, J. W. & Cornell, A., 2008. Vector-valued Intensity Measures Incorporating Spectral Shape For Prediction of Structural Response. *Journal of Earthquake Engineering,,* Volume 12, p. 534–554.

Baker, J. W. & Cornell, A. C., 2005. A vector-valued ground motion intensity measure consisting of spectral acceleration and epsilon. *Earthquake Engng Struct. Dyn.,* Volume 34, p. 1193–1217.

Baker, J. W. & Lee, C., 2018. An Improved Algorithm for Selecting Ground Motions to Match a Conditional Spectrum. *Journal of Earthquake Engineering,* 22(4), pp. 708-723.

Baker, W. J., 2015. Efficient Analytical Fragility Function Fitting Using Dynamic Structural Analysis. *Earthquake Spectra,* 31(1), pp. 579-599.

Bojórqueza, E. & Iervolinob, I., 2011. Spectral shape proxies and nonlinear structural response. *Soil Dynamics and Earthquake Engineering,* 31(7), pp. 996-1008.

Bommer, J. J., Stafford, J. P. & Alarcón, E. J., 2009. Empirical equations for the prediction of the significant, bracketed, and uniform duration of earthquake ground motion.. *Bulletin of the Seismological Society of America,* 99(6), p. 3217–3233.

Boore, M. D. & Atkinson, A. G., 2008. Ground-Motion Prediction Equations for the Average Horizontal Component of PGA, PGV, and 5%-Damped PSA at Spectral Periods between 0.01 s and 10.0 s. 24(1), pp. 99-138.

Bozorgnia, Y., Abrahamson, A. A., Atik, A. L. & Authors, O., 2014. NGA-West2 Research Project. *Earthquake Spectra,* 30(3), pp. 973-987.

Bradley, A. B., 2009. Site specific and spatially distributed prediction of acceleration spectrum intensity. *Bulletin of the Seismological Society of America,* 100(2), p. 792–801.

Bradley, A. B., 2010. A generalized conditional intensity measure approach and holistic ground-motion selection. *Earthquake Engng Struct. Dyn.,* Volume 39, p. 1321–1342.

Bradley, A. B., 2011. Empirical equations for the prediction of displacement spectrum intensity and its correlation with other intensity measures.. *Soil Dynamics and Earthquake Engineering,* 31(8), p. 1182–01191.

Bradley, A. B., 2012. A ground motion selection algorithm based on the generalized conditional intensity measure approach. *Soil Dynamics and Earthquake Engineering,* Volume 40, p. 48–61.

Bradley, A. B., Burks S, L. & Baker, W. J., 2015. Ground motion selection for simulation-based seismic hazard and structural reliability assessment. *Earthquake Engng Struct. Dyn.,* Volume 44, p. 2321–2340.

Bradley, A. B., Cubrinovski, M. & Prasad, D. R., 2009. Ground motion prediction equation for spectrum intensity from spectral acceleration relationships. *Bulletin of the Seismological Society of America,* 99(1), p. 277–285.

Bucher, C., 2009. Probability-based optimal design of friction-based seismic isolation devices. *Structural Safety ,* Volume 31, p. 500–507.

Burton, V. H. & Sharma, M., 2017. Quantifying the Reduction in Collapse Safety of Main Shock–Damaged Reinforced Concrete Frames with Infills. *Earthquake Spectra ,* 33(1), pp. 25-44.

Burton, V. H., Sreekumar, S., Sharma, M. & Sun, H., 2017. Estimating aftershock collapse vulnerability using mainshock intensity, structural response and physical damage indicators. *Structural Safety ,* Issue 68, p. 85–96.

Campbell, W. K. & Bozorgnia, Y., 2010. A ground motion prediction equation for the horizontal component of cumulative absolute velocity (CAV) based on the PEER-NGA strong motion database. *Earthquake Spectra,* 26(3), p. 635–650.

Campbell, W. K. & Bozorgnia, Y., 2012. A Comparison of Ground Motion Prediction Equations for Arias Intensity and Cumulative Absolute Velocity Developed Using a Consistent Database and Functional Form. *Earthquake Spectra.,* 28(3), pp. 931-941.

Cantagallo, C., Camata, G. & Spaconea, E., 2014. Seismic Demand Sensitivity of Reinforced Concrete Structures to Ground Motion Selection and Modification Methods. *Earthquake Spectra,* 30(4), p. 1449–1465.

Celarec, D. & Dolšek, M., 2013. The impact of modelling uncertainties on the seismic performance assessment of reinforced concrete frame buildings. *Engineering Structures ,* Volume 52, p. 340–354.

Champion, C. & Liel, A., 2012. The effect of near-fault directivity on building seismic collapse risk. *Earthquake Engng Struct. Dyn.,* Volume 41, p. 1391–1409.

Chandramohan, R., 2016. *DURATION OF EARTHQUAKE GROUND MOTION: INFLUENCE ON STRUCTURAL COLLAPSE RISK AND INTEGRATION IN DESIGN AND ASSESSMENT PRACTICE,* Stanford: Stanford University.

Chandramohan, R., Baker, W. J. & Deierlein, G. G., 2016. Quantifying the Influence of Ground Motion Duration on Structural Collapse Capacity Using Spectrally Equivalent Records. *Earthquake Spectra,* 32(2), p. 927–950.

Chandramohan, R., Baker, W. J. & Deierlein, G. G., 2106. Impact of hazard-consistent ground motion duration in structural collapse risk assessment. *Earthquake Engng Struct. Dyn,* Volume 45, p. 1357–1379.

Chouna, Y.-S. & Elnashai, S. A., 2010. A simplified framework for probabilistic earthquake loss estimation. *Probabilistic Engineering Mechanics 25 (2010) ,* Volume 25, p. 355–364.

Cordova, P., Deierlein, G., Mehanny, S. & Cornell, C., 2000. *Development of a two-parameter seismic intensity measure and probabilistic assessment procedure.* Sapporo, Hokkaido, Japan, The Second U.S.–Japan Workshop on Performance-Based Earthquake Engineering Methodology for Reinforced Concrete Building Structures.

Dai, Z., Li, X. & Hou, C., 2014. An optimization method for the generation of ground motions compatible with multi-damping design spectra. *Soil Dynamics and Earthquake Engineering ,* Volume 66, p. 199–205.

Deb, K., Pratap, A., Agarwal, S. & Meyarivan, T., 2002. A Fast and Elitist Multiobjective Genetic Algorithm: NSGA-II. *IEEE TRANSACTIONS ON EVOLUTIONARY COMPUTATION,* 6(2), pp. 182-197.

Decò, A., Bocchini, P. & Frangopol, M. D., 2013. A probabilistic approach for the prediction of seismic resilience of bridges. *Earthquake Engng Struct. Dyn,* Volume 42, p. 1469–1487.

Decò, A. & Frangopol, M. D., 2013. Life-Cycle Risk Assessment of Spatially Distributed Aging Bridges under Seismic and Traffic Hazards. *Earthquake Spectra,* 29(1), p. 127–153.

Dolsek, M., 2009. Incremental dynamic analysis with consideration of modeling uncertainties. *Earthquake Engng Struct. Dyn,* Volume 38, p. 805–825.

Eads, L., Miranda, E. & Lignos, D., 2016. Spectral shape metrics and structural collapse potential. *Earthquake Engng Struct. Dyn.,* 45(10), pp. 1643-1659.

Ebrahimian, H., Azarbakht, A., Tabandeh, A. & Golafshani, A. A., 2012. The exact and approximate conditional spectra in the multi-seismic-sources regions. *Soil Dynamics and Earthquake Engineering 39 ,* Volume 39, p. 61–77.

Ebrahimian, H. et al., 2014. A performance-based framework for adaptive seismic aftershock risk assessment. *Earthquake Engng Struct. Dyn,* Volume 43, p. 2179–2197.

Elwood, J. K., 2004. Modelling failures in existing reinforced concrete columns. *Can. J. Civ. Eng. ,* Volume 32, p. 846–859 .

Foley, M. C., Pezeshk, S. & Alimoradi, A., 2007. Probabilistic Performance-Based Optimal Design of Steel Moment-Resisting Frames. I: Formulation. *Journal of Structural Engineering,* 133(6), pp. 757-766.

Fragiadakis, M. & Papadrakakis, M., 2008. Performance-based optimum seismic design of reinforced concrete structures. *Earthquake Engng Struct. Dyn.,* Volume 37, p. 825–844.

Galanis, P., 2014. *Probabilistic Methods to Identify Seismically Hazardous Older-Type Concrete Frame Buildings,* Berkeley: University of California, Berkeley.

Goda, K. & Taylor, A. C., 2012. Effects of aftershocks on peak ductility demand due to strong ground motion records from shallow crustal earthquakes. *Earthquake Engng Struct. Dyn,* Volume 41, p. 2311–2330.

Goda, K., Wenzel, F. & De Risi, R., 2015. Empirical assessment of non-linear seismic demand of mainshock–aftershock ground-motion sequences for Japanese earthquakes. *Front. Built Environ,* Volume 1, pp. 1-17.

Gokkaya, U. B., Baker, W. J. & Deierlein, G. G., 2016. Quantifying the impacts of modeling uncertainties on the seismic drift demands and collapse risk of buildings with implications on seismic design checks. *Earthquake Engng Struct. Dyn.,* 40(10), pp. 1661-1683.

Han, R., Yue, L. & van de Lindt, J., 2015. Assessment of Seismic Performance of Buildings with Incorporation of Aftershocks. *J. Perform. Constr. Facil.,* 29(3), pp. 1-17.

Haselton, B. C., Jack, B. W., Liel, B. A. & Deierlein, G. G., 2011. Accounting for Ground-Motion Spectral Shape Characteristics in Structural Collapse Assessment through an Adjustment for Epsilon. *Journal of Structural Engineering ,* 137(3), p. 332–344.

Haselton, B. C. et al., 2011. Seismic Collapse Safety of Reinforced Concrete Buildings. I: Assessment of Ductile Moment Frames. *J. Struct. Eng.,* 137(4), pp. 481-491.

Haselton, B. C., Liel, B. A., Lange, T. S. & Deierlein, G. G., 2008. *Beam-Column Element Model Calibrated for Predicting Flexural Response Leading to Global Collapse of RC Frame Buildings,* Berkeley: PACIFIC EARTHQUAKE ENGINEERING RESEARCH CENTER.

Ha, S. J. & Han, S. W., 2016. An efficient method for selecting and scaling ground motions matching target response spectrum mean and variance. *Earthquake Engng Struct. Dyn.,* Issue 45, p. 1381–1387.

Higham, J. N., 2002. Computing the nearest correlation matrix-A problem for finance. *IMA Journal of Numerical Analysis,* Volume 22, pp. 329-343.

Ibarra, F. L., Medina, A. R. & and Krawinkler, H., 2005. Hysteretic models that incorporate strength and stiffness deterioration. *Earthquake Engng Struct. Dyn.,* 34(12), pp. 1489-1511.

Jalayer, F. & Ebrahimian, H., 2017. Seismic risk assessment considering cumulative damage due to aftershocks. *Earthquake Engng Struct. Dyn. ,* Volume 46, p. 369–389.

Jayaram, N., Lin, T. & Baker, J. W., 2011. A Computationally Efficient Ground-Motion Selection Algorithm for Matching a Target Response Spectrum Mean and Variance. *Earthquake Spectra,* 27(3), p. 797–815.

Jeon, J.-S., DesRoches, R., Lowes, N. L. & Brilakis, I., 2015. Framework of aftershock fragility assessment–case studies: older California reinforced concrete building frames. *Earthquake Engng Struct. Dyn. ,* Volume 44, p. 2617–2636.

Kennedy, R. et al., 1984. *Engineering characterization of ground motion. Task I: Effects of characteristics of free-field motion on structural response.,* Washington, DC: U.S. Nuclear Regulatory Commission.

Kohrangi, M., Bazzurro, P. & Vamvatsikos, D., 2016. Vector and Scalar IMs in Structural Response Estimation, Part I: Hazard Analysis. *Earthquake Spectra,* 32(3), p. 1507–1524.

Kohrangi, M., Bazzurro, P. & Vamvatsikos, D., 2016. Vector and Scalar IMs in Structural Response Estimation, Part II: Building Demand Assessment. *Earthquake Spectra,* 32(3), p. 1525–1543.

Kohrangi, M., Bazzurro, P., Vamvatsikos, D. & Spillatura, A., 2017. Conditional spectrum-based ground motion record selection using average spectral acceleration. *Earthquake Engng Struct. Dyn.,* 46(10), pp. 1667-1685.

Kohrangi, M., Vamvatsikos, D. & Bazzurro, P., 2017. Site dependence and record selection schemes for building fragility and regional loss assessment. *Earthquake Engng Struct. Dyn.,* 46(10), pp. 1625-1643.

Kosič, M., Fajfar, P. & Dolšek, M., 2014. Approximate seismic risk assessment of building structures with explicit consideration of uncertainties. *Earthquake Engng Struct. Dyn. ,* Volume 43, p. 1483–1502.

Kottke, A. & Rathje, E. M., 2008. A Semi-Automated Procedure for Selecting and Scaling Recorded Earthquake Motions for Dynamic Analysis. *Earthquake Spectra,* 24(4), p. 911–932.

Liel, B. A., Haselton, B. C. & Deierlein, G. G., 2011. Seismic Collapse Safety of Reinforced Concrete Buildings. II: Comparative Assessment of Nonductile and Ductile Moment Frames. *J. Struct. Eng., 2011,* 137(4), pp. 492-502.

Lin, T., Harmsen, S. C., Baker, J. W. & Luco, N., 2013. Conditional Spectrum Computation Incorporating Multiple Causal Earthquakes and Ground-Motion Prediction Models. *Bulletin of the Seismological Society of America,* 103(2A), p. 1103–1116.

Li, Q. & Ellingwood, B. R., 2007. Performance evaluation and damage assessment of steel frame buildings under main shock–aftershock earthquake sequences. *Earthquake Engng Struct. Dyn,* Volume 36, p. 405–427.

Liu, M., Burns, A. S. & Wen, K. Y., 2005. Multiobjective optimization for performance-based seismic design of steel moment frame structures. *Earthquake Engng Struct. Dyn,* Volume 34, p. 289–306.

Liu, Z., Atamturktur, S. & Juang, H. C., 2013. Performance based robust design optimization of steel moment resisting frames. *Journal of Constructional Steel Research 89 (2013)* , Volume 89, p. 165–174.

McKenna, Fenves, L. G. & Scott, H. M., 2000. *Open system for earthquake engineering simulation,* Berkeley: University of California, Berkeley.

Mousavi, M., Ghafory-Ashtiany, M. & Azarbakht, A., 2011. A new indicator of elastic spectral shape for the reliable selection of ground motion records. *Earthquake Engng Struct. Dyn.,* 40(12), pp. 1403-1416.

Nazari, N. L. J. W. v. d. & Y, L., 2015. Effect of Mainshock-Aftershock Sequences on Woodframe Building Damage Fragilities. *J. Perform. Constr. Facil.,* 29(1), pp. 1-7.

Pan, Y., Agrawal, K. A. & Ghosn, M., 2007. Seismic Fragility of Continuous Steel Highway Bridges in New York State. *J. Bridge Eng.,* 12(6), pp. 689-699.

Paya, I., Yepes, V., Gonzalez-Vidosa, F. & Hospitaler, A., 2008. Multiobjective Optimization of Concrete Frames by Simulated Annealing. *Computer-Aided Civil and Infrastructure Engineering ,* Volume 23, p. 596–610.

Pourzeynali, S. & Zarif, M., 2008. Multi-objective optimization of seismically isolated high-rise building structures using genetic algorithms. *Journal of Sound and Vibration ,* Volume 311, p. 1141–1160.

Raghunandan, M. & Liel, B. A., 2013. Effect of ground motion duration on earthquake-induced structural collapse. *Structural Safety ,* Volume 41, p. 119–133.

Raghunandan, M., Liel, B. A. & Luco, N., 2015. Aftershock collapse vulnerability assessment of reinforced concrete frame structures. *Earthquake Engng Struct. Dyn. ,* Volume 44, p. 419–439.

Raghunandan, M., Liel, B. A. & Luco, N., 2015. Collapse Risk of Buildings in the Pacific Northwest Region due to Subduction Earthquakes. *Earthquake Spectra,* 31(4), p. 2087–2115.

Ruiz-García, J. & Aguilar, D. J., 2015. Aftershock seismic assessment taking into account postmainshock residual drifts. *Earthquake Engng Struct. Dyn. ,* Volume 44, p. 1391–1407.

Saadat, S., Camp, V. C. & Pezeshk, S., 2016. Probabilistic Seismic Loss Analysis for the Design of Steel Structures: Optimizing for Multiple-Objective Functions. *Earthquake Spectra,* 32(3), p. 1587–1605.

Sadeghi, M., Ghafory-Ashtiany, M. & Pakdel-Lahiji, N., 2017. Multi-objective optimization approach to define risk layer for seismic mitigation. *Journal Geomatics, Natural Hazards and Risk ,* 8(1), pp. 257-270 .

Sewell, R., Toro, G. & McGuire, R., 1996. *Impact of ground motion characterization on conservatism and variability in seismic risk estimates,* Washington, DC.: U.S. Nuclear Regulatory Commission .

Shokrabadi, M. & Burton, H., 2018. Building service life economic loss assessment under sequential seismic events. *Earthquake Engng Struct Dyn,* 47(9), pp. 1864-1881.

Shokrabadi, M. & Burton, H., 2018. Risk-based assessment of aftershock and mainshock-aftershock seismic performance of reinforced concrete frames. *Structural Safety ,* Volume 73, p. 64–74.

Shokrabadi, M. & Burton, V. H., 2017. Ground Motion Intensity Measures for Rocking Building Systems. *Earthquake Spectra,* 33(4), pp. 1533-1554.

Smerzini, C., Galasso, C., Iervolino, I. & Paolucci, R., 2014. Ground Motion Record Selection Based on Broadband Spectral Compatibility. *Earthquake Spectra,* 30(4), p. 1427–1448.

Sunasaka, Y. & Kiremidjian, S. A., 1993. *sequences, a method of structural safty eveluation uder mainshock-aftershock earthquake,* Standord : Stanford University .

Tarbali, K., Bradley, A. B. & Baker, W. J., 2018. Consideration and Propagation of Ground Motion Selection Epistemic Uncertainties to Seismic Performance Metrics. *Earthquake Spectra.,* 34(2), pp. 587-610.

Tarbali, K. & Bradley, B. A., 2015. Ground motion selection for scenario ruptures using the generalised conditional intensity measure (GCIM) method. *Earthquake Engng Struct. Dyn.,* Volume 44, p. 1601–1621.

Tarbali, K. & Bradley, B. A., 2016. The effect of causal parameter bounds in PSHA-based ground motion selection. *Earthquake Engng Struct. Dyn.,* 45(9), pp. 1515-1535.

Tubaldi, E., Barbato, M. & Dall'Asta, A., 2012. Influence of Model Parameter Uncertainty on Seismic Transverse Response and Vulnerability of Steel–Concrete Composite Bridges with Dual Load Path. *J. Struct. Eng.,* 138(3), pp. 363-374.

Vamvatsikos, C. D. & Cornell, A., 2005. Developing efficient scalar and vector intensity measures for IDA capacity estimation by incorporating elastic spectral shape information.. *Earthquake Engng Struct. Dyn.,* 34(13), pp. 1573-1600.

Vamvatsikos, D., 2014. Seismic Performance Uncertainty Estimation via IDA with Progressive Accelerogram-Wise Latin Hypercube Sampling. *J. Struct. Eng.,* 140(8), p. A4014015.

Vamvatsikos, D. & Cornell, C. A., 2002. Incremental dynamic analysis. *Earthquake Engng Struct. Dyn.,* Volume 32, p. 491–514.

Vamvatsikos, D. & Fragiadakis, M., 2010. Incremental dynamic analysis for estimating seismic performance sensitivity and uncertainty. *Earthquake Engng Struct. Dyn. ,* Volume 39, p. 141–163.

Vorechovsky, M. & Novák, D., 2009. Correlation control in small-sample Monte Carlo type simulations I: A simulated annealing approach. *Probabilistic Engineering Mechanics,* Volume 24, p. 452–462.

Wang, G., 2011. A ground motion selection and modification method capturing response spectrum characteristics and variability of scenario earthquakes. *Soil Dynamics and Earthquake Engineering ,* Volume 31, p. 611–625.

Wang, G. et al., 2017. Damage demand assessment of mainshock-damaged concrete gravity dams subjected to aftershocks. *Soil Dynamics and Earthquake Engineering ,* Volume 98, p. 141–154.

Wells & Coppersmith, J. K., 1994. New Empirical Relationships among Magnitude, Rupture Length, Rupture Width, Rupture Area, and Surface Displacement. *Bulletin of the Seismological Society of America,* 84(4), pp. 974-1002.

Weng, Y.-T., Tsai, K.-C. & Ya-Ran, Y.-R., 2010. A Ground Motion Scaling Method Considering Higher-Mode Effects and Structural Characteristics. *Earthquake Spectra,* 26(3), p. 841–867.

Wong, N. S. K. & Chopra, A., 2016. Evaluation of the exact conditional spectrum and generalized conditional intensity measure methods for ground motion selection. *Earthquake Engng Struct. Dyn.,* Volume 45, p. 757–777.

Wong, N. S. K. & Chopra, A., 2017. A Generalized Conditional Mean Spectrum and its application for intensity-based assessments of seismic demands. *Earthquake Spectra,* 33(1), pp. 123-143.

Wong, N. S. K., Chopra, A. & McGuire, R. K., 2015. A ground motion selection procedure for enforcing hazard consistency and estimating seismic demand hazard curves. *Earthquake Engng Struct. Dyn. ,* Volume 44, p. 2467–2487.

Wong, N. S. K., Chopra, A. & McGuire, R. K., 2015. Evaluation of ground motion selection and modification procedures using synthetic ground motions. *Earthquake Engng Struct. Dyn. ,* Volume 44, p. 1841–1861.

Xie, Y., 2017. *Seismic Modeling, Quantifying and Protection of Highway Bridges Considering Shaking and Lateral Spreading,* Los Angeles : PhD Dissertation, UCLA..

Yaghmaei-Sabegh, S. & Makaremi, S., 2017. Development of duration-dependent damage-based inelastic response spectra. *Earthquake Engng Struct. Dyn.,* Volume 46, p. 771–789.

Yang, T., Moehle, J., Stojadinovic, B. & Der Kiureghian, A., 2009. Seismic Performance Evaluation of Facilities: Methodology and Implementation. *J.Struct. Eng.,* 135(10), pp. 1146-1154.

Yeo, G. L. & Cornell, C. A., 2005. *Stochastics characterization and decsion bases under time-dependent aftershock risk in performance-based earthquke engineering,* Stanford : Stanford University .

Yeo, G. L. & Cornell, C. A., 2009. A probabilistic framework for quantification of aftershock ground-motion hazard in California: Methodology and parametric study. *Earthquake Engng Struct. Dyn. ,* Volume 38, p. 45–60.

Yeo, G. L. & Cornell, C. A., 2009. Building life-cycle cost analysis due to mainshock and aftershock occurrences. *Structural Safety,* Volume 31 , p. 396–408.

Yeo, G. L. & Cornell, C. A., 2009. Equivalent constant rates for post-quake seismic decision making. *Structural Safety ,* Volume 31, p. 443–447.

Yeo, G. L. & Cornell, C. A., 2009. Post-quake decision analysis using dynamic programming. *Earthquake Engng Struct. Dyn. ,* Volume 38, p. 79–93.

Yue, L., Song, R. & Van De Lindt, W. J., 2014. Collapse Fragility of Steel Structures Subjected to Earthquake Mainshock-Aftershock Sequences. *J. Struct. Eng.,* 140(2), pp. 1-10.

Zhang, Y. & Pinder, G., 2003. Latin hypercube lattice sample selection strategy for correlated random hydraulic conductivity fields. *WATER RESOURCES RESEARCH,* 39(8), pp. 1-11.

Zhongxian, L., Yang, L. & Ning, L., 2014. Vector-intensity measure based seismic vulnerability analysis of bridge structures. *Earthq Eng & Eng Vib ,* Volume 13, pp. 695-705.